EVALUATION OF REDOX ACTIVE ORGANIC MOLECULES FOR USE IN NONAQUEOUS FLOW BATTERIES

by

Jeffrey A. Kowalski

Bachelor of Science in Chemical Engineering (Materials)
California Institute of Technology, 2013

Master of Science in Chemical Engineering Practice
Massachusetts Institute of Technology, 2015

Submitted to the Department of Chemical Engineering
in partial fulfillment of the requirements for the degree of

Doctor of Philosophy in Chemical Engineering

at the

Massachusetts Institute of Technology

June 2019
© 2019 MIT

Author .... Signature redacted
Department of Chemical Engineering
January 30th, 2019

Certified by .... Signature redacted
Fikile R. Brushett
Cecil and Ida Green Career Development Chair
Thesis Supervisor

Accepted by... Signature redacted
Patrick S. Doyle
Robert T. Haslam (1911) Professor of Chemical Engineering, Graduate Officer
Chairman, Committee for Graduate Student

1

Evaluation of Redox Active Organic Molecules for Use in Nonaqueous Flow Batteries

by

Jeffrey A. Kowalski

Submitted to the Department of Chemical Engineering in January 2019, in partial fulfillment of
the requirements for the degree of
Doctor of Philosophy in Chemical Engineering

Abstract:

Technical advances in grid energy storage are of critical importance to facilitate the integration of intermittent renewables and improve the efficiency, reliability, and resiliency of the existing fossil fuel infrastructure. Redox flow batteries (RFBs) are an electrochemical technology well suited for stationary energy storage due to independently addressable power and energy components, simplified manufacturing, and long operating lifetimes. While state-of-the-art RFBs utilizing transition metal salts in acidic, aqueous electrolytes have found some success, further cost reductions are needed, motivating research into organic redox couples dissolved in nonaqueous electrolytes. Nonaqueous electrolytes offer the advantages of wider electrochemical stability windows and compatibility with a broader palette of charge-storage materials. Redox active organic molecules can be modified through targeted functionalization to impart desired properties and consist of earth abundant elements, which may enable scalable, low cost synthesis routes.

This thesis focuses on organic molecules intended for use as positive active materials in nonaqueous RFBs. The two redox active cores examined are substituted dialkoxybenzenes and phenothiazines. Both molecules served as learning platforms and were systematically functionalized, with one or more substituent groups, to elucidate structure-function relationships with particular emphasis on increasing solubility, gravimetric capacity, and redox potential. Initial efforts focused on the modification of 2,5-di-tert-butyl-1,4-bis(2-methoxyethoxy)benzene through subtractive engineering to identify stable minimal structures. Next, the impact of halidization was examined leading to a 300 – 400 mV increase in redox potential but severe reductions in cyclability. Due to limitations of the stability of the substituted dialkoxybenzenes, subsequent efforts were undertaken using N-ethylphenothiazine. Through an iterative approach of targeted functionalization, (1) solubility was increased and (2) the second electron transfer was stabilized resulting in redox active electrolytes with a volumetric charge storage capacity approaching the range envisioned for economically viable RFBs.

While the moderate stability of the substituted dialkoxybenzenes appears to limit their applicability as active materials, they have utility as model compounds suitable for supporting the development and standardization of testing protocols for RFBs. As organic materials are emergent for RFB applications, standardized testing protocols and benchmarking techniques are not established, frustrating quantitative comparisons between new materials. To this end, new electrochemical methods are introduced to evaluate and report the stability of redox active materials at dilute conditions, using bulk electrolysis cycling, and at concentrated conditions, using time-dependent microelectrode voltammetry, which are validated using dialkoxybenzenes.

Thesis Supervisor: Fikile R. Brushett, Associate Professor of Chemical Engineering
Title: Cecil and Ida Green Career Development Chair

ACKNOWLEDGEMENTS:

Table of Contents:

List of Figures

13

supporting electrolytes of 1 M LiTFSI in DME and 1 M LiTFSI in PC, respectively. All data was

collected with a scan rate of 20 mV/s with 0.010 M active species. The working, counter, and

reference electrodes used were a 3 mm glassy carbon disk, a gold coil, and a fritted lithium foil.

Figure 23: Cyclic voltammograms using a microelectrode of saturated solutions of 25DDB (black),

25FDB (red), 25ClDB (blue), 25BrDB (purple), and 25IDB (orange) in 1 M LiTFSI in DME (a)

and 1 M LiTFSI in PC (b). The working, counter, and reference electrodes are a carbon fiber,

Figure 24: Bulk electrolysis voltage profiles for the second through sixth cycles of 0.001 M

25DDB (a), 25FDB (b), 25ClDB (c), and 25BrDB (d) each in 1 M LiTFSI in 1:1 weight ratio of

EC:DMC. The concentration of active species was 0.001 M and the charge/discharge current was

Figure 25: Bulk electrolysis charging capacity of 0.001 M of 25DDB (black, circles), 25FDB (red,

squares), 25ClDB (blue, triangles), and 25BrDB (purple, diamonds) each in 1 M LiTFSI in 1:1

EC:DMC. All experiments were conducted in duplicate. 25IDB was not insoluble in this

Figure 26: Coulombic efficiency as a fuction of cycle number for each of the materials cycled for

Figure 27: Calculated HOMO by DFT of 25DDB (a), 25DDB$^+$ (e), 25FDB (b), 25FDB$^+$ (f),

Figure 28: The ^{19}F NMR (a) and ^{1}H NMR (b) both before cycling (red) and after cycling (dark

List of Tables

1 Introduction to Redox Flow Batteries

This chapter provides the need for grid storage and why flow batteries are a promising technology. It is partially reprinted from "Recent Developments and Trends in Redox Flow Batteries" by Liang Su, **Jeffrey A. Kowalski**, Kyler J. Carroll, and Fikile R. Brushett in Rechargeable Batteries: Materials, Technologies and New Trends (2015, editors: Zhengcheng Zhang and Sheng Shui Zhang)[1]. Permission for reproduction of the work was obtained on January 1, 2019 through Copyright Clearance Center's RightsLink® service. Next technoeconomic analysis is performed on both aqueous and nonaqueous flow batteries and provides performance metrics to reach economically viable flow batteries. It is partially reprinted from "Pathways to low-cost electrochemical energy storage: a comparison of aqueous and nonaqueous flow batteries" by Robert M. Darling, Kevin G. Gallagher, **Jeffrey A. Kowalski**, Seungbum Ha, and Fikile R. Brushett from *Energy and Environmental Science* (2014, 7, 3459-3477)[2].

1.1 The Need for Grid Scale Energy Storage

A major challenge of the 21st century is the development of efficient and sustainable means of energy conversion, distribution, and storage on a global scale. Presently, fossil fuel technologies make up the backbone of our energy economy, notably transportation and bulk generation for electrification. The International Energy Agency (IEA) reported that, in 2012, of the total energy consumed worldwide, around 70.8 % was derived from fossil fuel sources (oil, natural gas, coal, etc.), with the majority of energy consumption and demand growth coming from developing nations[3]. In the United States, the 2011 Energy Information Administration (EIA) annual review reported that around 78 % of the total energy consumed was derived from fossil fuel sources (i.e.,

oil, coal, and natural gas), and the two largest consumption sectors are electricity (38 %) and transportation (27 %), both of which are dominated by fossil fuel sources[4,5]. However, in the future, this energy mix will not be feasible[6]. Rising population and continuing economic growth in the developing world are projected to double global energy consumption by 2050[5]. Non-renewable fossil fuel reserves, which took millennia to accumulate, are finite and rapidly disappearing. Moreover, the continued and increasing generation of anthropogenic carbon dioxide (CO_2) from fossil fuel combustion will likely have negative implications for the global climate[7]. Analysis by the Intergovernmental Panel on Climate Change (IPCC) indicated that to stabilize the atmospheric concentration of CO_2 at 350–400 ppm (near its current level), global CO_2 emissions would need to be tapered by 2050 to a level of 20–50 % of the 2000 emissions[8]. Thus a tremendous need exists for scientific and technological advances to address these grand challenges, sparking worldwide investment in low-carbon/carbon-neutral power generation, carbon capture and storage, and system-wide energy efficiency[9].

Stationary energy storage systems (ESS) will play a pivotal role in the widespread integration of renewable, non-dispatchable electricity generators (e.g., solar photovoltaic (PV), wind) and in the improvement of energy efficiency of the electric grid[10,11]. Indeed, increased energy storage assets can enhance energy security, reduce carbon emissions, and introduce new revenue streams for a range of stakeholders[12,13]. In cases where no transmission or distribution constraints exist, grid-connected ESS are not required to be co-located with the energy source, providing the flexibility to optimize storage performance characteristics and minimize costs. Where constraints exist (e.g., developing economies, island nations), coupling energy storage with local generation resources (e.g., solar PV, fuel cells, micro-turbines) can enable the development of robust micro-grids. Services provided by ESS and their remuneration create the incentive for

adopting energy storage. These services can be broadly classified as bulk energy, ancillary, transmission and distribution (T&D), renewables integration, and customer energy management (Table 1)[14,15]. However, despite this promise, only ~ 2.5 % of total electric production in the US relies on grid energy storage with the principal barrier to widespread installation being the system cost[16]. Therefore, the development of cost-competitive energy storage technologies with validated reliability and safety is of paramount importance to the continued evolution of the electric power sector in the US and worldwide.

Table 1: Key characteristics of storage systems for selected energy services adapted from the International Energy Agency technology roadmap: energy storage[15]

Services	Size (MW)	Discharge duration	Cycles (typical)	Response time	Output (electricity 'e', thermal 't')
Bulk energy services					
Seasonal storage	500–2000	d–mo	1–5/y	d	e, t
Arbitrage	100–2000	8–24 h	0.25–1/d	>1 h	e
Ancillary services					
Frequency regulation	1–2000	1–15 min	20–40/d	1 min	e
Load following	1–2000	15 min–1 d	1–29/d	<15 min	e, t
Voltage support	1–40	1–60 s	10–100/d	0.001–1 s	e
Black start	0.1–400	1–4 h	<1/y	<1 h	e
Spinning reserve	10–2000	15 min–2 h	0.5–2/d	<15 min	e
Non-spinning reserve	10–2000	15 min–2 h	0.5–2/d	>15 min	e
Transmission and distribution infrastructure services					
Transmission and distribution congestion relief	10–500	2–4 h	0.14–1.25/d	>1 h	e, t
Transmission and distribution investment deferral	1–500	2–5 h	0.75–1.25/d	>1 h	e, t
Renewable and other integration services					
Variable Supply Resource Integration	1–400	1 min–h	0.5–2/d	<15 min	e, t
Waste Heat Utilization	1–10	1–24 h	1–20/d	<10 min	t
Combined Heat and Power	1–5	min–h	1–10/d	<15 min	t
Customer energy management services					
Demand shifting and peak reduction	0.001–1	min–h	1–29/d	<15 min	e, t
Off-grid	0.001–	3–5 h	0.75–1.5/d	<1 h	e, t

34

While a range of ESS options exist to meet the aforementioned services, no single technology is suitable for all applications. Present storage technologies vary in their performance characteristics, level of technological maturity, and, most importantly, cost. The applicability of different technologies based on their associated attributes is shown in Figure 1, an adaptation from a recent Sandia National Laboratory report[17]. The storage technology comparison shown divides the applications roughly into three broad segments based on the discharge time and system power requirements: uninterruptible power supply, T&D grid support-load shifting, and bulk management. Both cost and bulk-storage-relevant attributes have resulted in pumped hydroelectric storage (pumped hydro) being responsible for over 97 % of the worldwide energy storage capacity (ca. 127 GW) in 2010[18]. Pumped hydro however suffers from constraints arising from geographical settings, licensing, environmental regulations, and uncertainty in long-term electric markets[12,19]. Though they presently constitute a significantly smaller installed capacity (ca. 400 MW), electrochemical energy storage technologies have a number of desirable characteristics including high power/energy density, high round-trip efficiency, rapid response time, and terrain-independence. However, the economics of grid storage are challenging. In a 2013 report, the United States Department of Energy (DOE) has outlined a near-term system capital cost goal of $250/kWh for grid storage systems with a long term reduction to $150/kWh[12]. Other DOE programs have proposed more aggressive cost targets. For example, the Advanced Research Projects Agency-Energy (ARPA-E) Grid-Scale Rampable Intermittent Dispatchable Storage (GRIDS) program has set a target of less than $100/kWh for new storage technologies[20]. Further, the Joint Center for Energy Storage Research (JCESR), a DOE-funded Energy Innovation Hub, aims to develop battery prototypes that, when scaled to manufacturing, are projected to reach battery price levels to enable widespread market adoption (e.g., $100 per useable kWh)[21]. These

stringent targets reflect the low cost of electricity in the United States, but market penetration may be realized in global regions with higher electricity costs (e.g., Europe, Japan[3]) or through niche applications where higher system costs can be offset by the value of provided services.
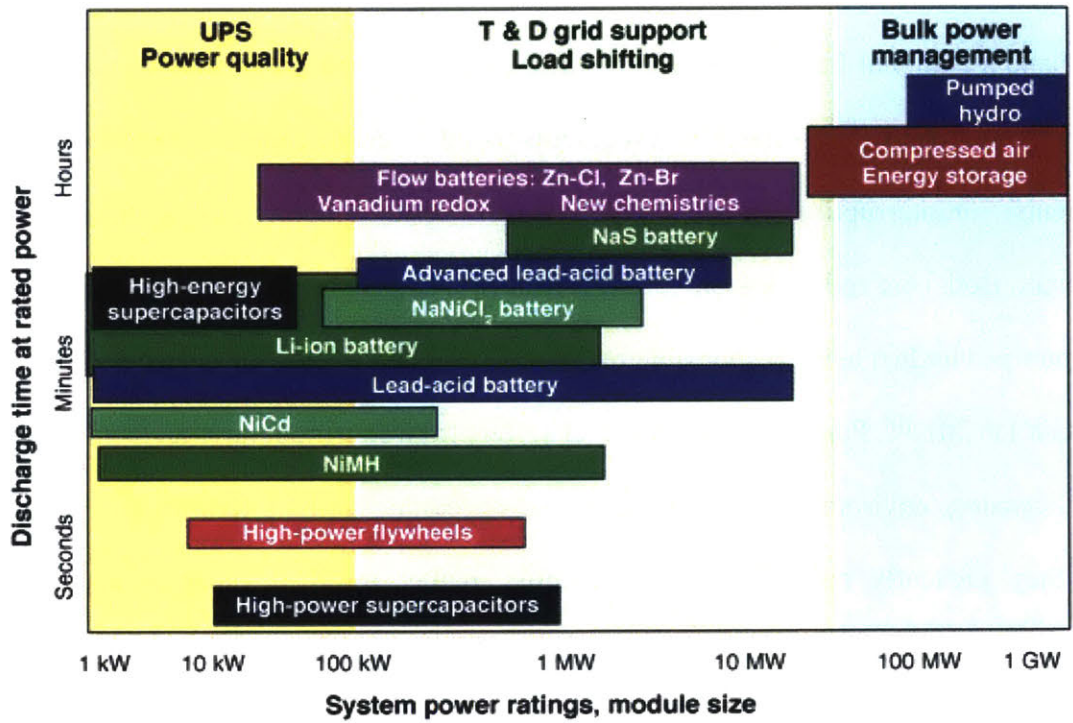
Figure 1: Comparison of select storage technologies and associated addressable services broadly divided into three categories: uninterruptible power supply (UPS)-power quality, transmission and distribution (T&D) grid support-load shifting, and bulk power management services, T&D grid support-load shifting to ancillary services, T&D infrastructure services, renewable and other integration services, while bulk power management can be related to bulk energy services. Figure adapted from DOE/EPRI 2013 electricity storage handbook[17]. Reproduced with permission. Copyright 2010 Electric Power Research Institute

Redox flow batteries (RFBs) have attracted considerable academic and industrial interest based on their favorable combination of performance, cost, and safety. Over the past few years, several comprehensive reviews have been published on RFBs with detailed assessments of individual components (i.e., membranes[22–24] and electrodes/bipolar plates[25–27]) and of utility for stationary ESS applications[28–33].

36

A redox flow battery (RFB) is a rechargeable electrochemical device that utilizes the reversible

redox reactions of two soluble electroactive species for energy storage. Figure 2 shows a simplified

schematic of a flow battery. The system includes electrochemical reactors, storage vessels,

circulation pumps, a heat exchanger, and power conditioning equipment. The positive and negative

electrolytes (also referred to as the posolyte and negolyte) are fed to one or more electrochemical

reactors, where the active species are oxidized or reduced to alternately charge or discharge the

battery. Within an electrochemical cell, each electrolyte reacts on the corresponding positive or

negative electrodes, which are separated by either an ion-selective membrane or a nanoporous

separator. These generic reactions are shown below (assuming a 1-electron transfer process):

Positive Electrode: $X^{n+} + e^- \rightleftharpoons X^{(n-1)+}$ E_1
Negative Electrode: $Y^{m+} + e^- \rightleftharpoons Y^{(m-1)+}$ E_2
Total Reaction: $X^{n+} + Y^{(m-1)+} \rightleftharpoons X^{(n-1)+} + Y^{(m-1)+}$ $E_{cell} = E_1 - E_2$
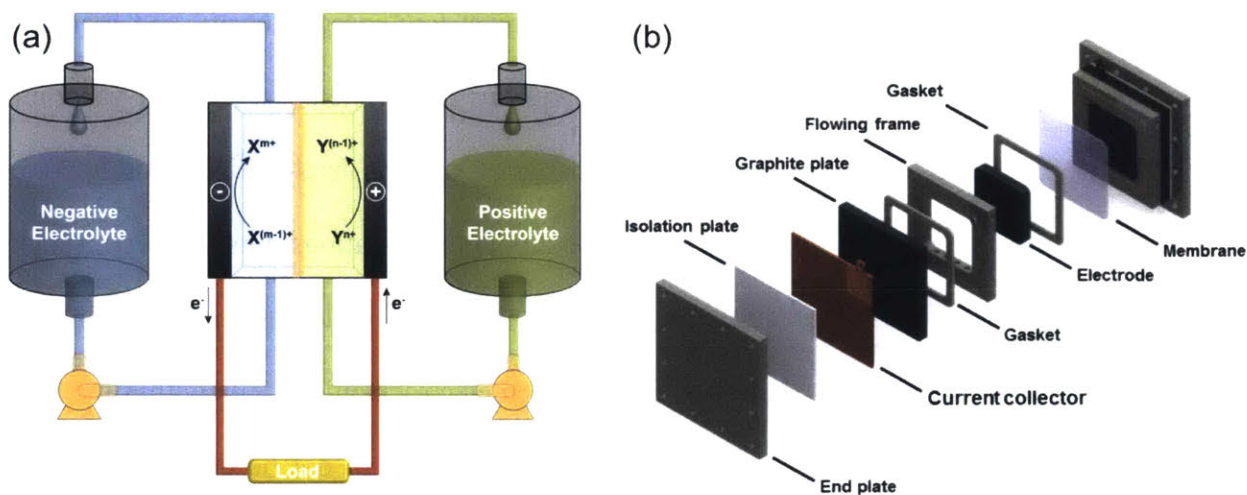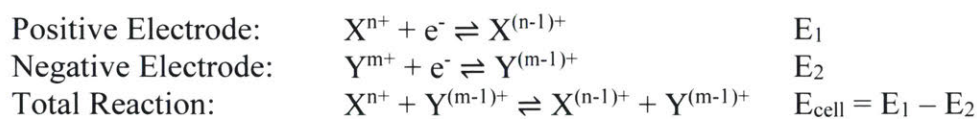
Figure 2: Schematic of a redox-flow cell during discharge (a). Exploded view of components in a redox flow cell (b).

As compared to enclosed batteries, the RFB architecture has several compelling features including:

- Independent power (W) and energy (Wh) due to separate tank and electroreactor configurations, which enables modular flexibility.

- Long life cycle with deep charge capabilities as storage is based on facile solution-phase redox reactions where the electrodes serve as a source or sink of electrons. Indeed, Skyllas-Kazacos et al. reported that durability generally exceeds 5000 deep cycles for flow batteries[33].

- Superior safety as reactants are contained in physically separated tanks with a relatively small volume in close proximity within the reactor stack.

- Simplified manufacturing and lower cell-to-cell variability due to simple electrode and stack construction. Further, replacement costs are likely to be lower.

- High active-to-inactive materials ratios are possible, especially for long duration storage where the battery cost asymptotically approaches the cost of redox solutions.

However, these advantages must be balanced against low energy density and increased system complexity. The energy densities of common aqueous flow systems, such as all-vanadium redox (VRFB), are lower than those of enclosed batteries such as lead-acid and lithium-ion. Fortunately, this deficiency can be tolerated in many stationary applications. Flow battery systems require pumps to circulate the electrolytes, resulting in parasitic losses and complicating independent operation on the grid. Shunt currents between electrochemical cells within the stack also lead to efficiency losses. These system-level considerations will not be discussed, but we direct the interested reader to references for the estimation of system efficiency in the presence of shunt currents and pumping losses[34].

At present, RFBs are broadly considered too expensive for widespread deployment. While materials cost reductions can be expected through manufacturing scale and learning by doing, and additional contributions to price will decrease through competition and volume, new redox couples, electrolytes, and reactor configurations are likely needed to meet the DOE cost targets. As battery costs ($/kWh) are proportional to materials costs ($/kg) and inversely proportional to materials requirements (kWh/kg), two approaches can be taken to lower the system cost: cheaper storage materials and higher energy density (less material required).

1.3   Technoeconomic Analysis for Redox Flow Batteries

Cost estimates of various sophistication have been reported previously for aqueous flow batteries[34–38]. This work seeks to build upon the knowledge disseminated in those works and examine the technological potential of aqueous, and for the first time, nonaqueous flow batteries in achieving cost objectives. The approach is to utilize the simplest model that maintains the essential performance and cost factors, enabling broad and meaningful discussions regarding material and system requirements. The analysis is intended to be flexible enough to facilitate comparison of different systems. Sources for performance and cost parameters are provided within the analysis where pertinent. Through a comparative analysis, we examine trends as well as areas of strength and future research needs. The exact values of system price presented here, which can be challenged on various grounds, are of secondary importance to our goals.

The goal of this work is to examine the relationships among the cost and performance of the components and the final system price for flow batteries in a general way. This work begins with a brief discussion of the economics of energy storage that provides an appreciation for the implications of price targets. This is followed by a mathematical description of the contributions to the price of a flow battery. The model is employed to determine sets of chemical and reactor

costs, as well as area-specific resistance (ASR) and thermodynamic potential that yield a target battery price. These results are interpreted in the context of existing and conceptual aqueous and nonaqueous flow batteries. Solubility targets for the active species in nonaqueous batteries are derived from the chemical costs.

1.3.1 Economics of Energy Storage

A variety of techniques are available to evaluate the economic prospects of an engineering project. These include evaluations of discounted cash flow, net present worth, capitalized costs, payback time, and rate of return on initial investment. The first three methods account for the time value of money, while the last two do not, and are therefore less reliable. For the sake of simplicity, we assume continuous, uniform payments and continuous compounding in our analysis. Given these assumptions, the economics of the project can be described by a simple, first-order differential equation relating the principle, the net revenue stream, and the internal rate of return. Newman et al. presented an analysis of energy-storage systems subject to the above constraints and we follow their approach in this work[39].

Newman et al. described the economics of energy storage with the equation[39]:

$$P_0 - N \frac{1 - \exp(-rt_L)}{r} = 0 \tag{1}$$

where P_0 is the price of the installed energy storage system in dollars, N is the net revenue in \$ per year, t_L is the life of the battery in years, and r is an inflation-adjusted rate of return in per year. The variable r is often referred to as the "internal rate of return" (IRR). The ratio P_0/N is a simple payback time in years, and the factor $r/(1 - \exp(-rt_L))$, referred to as the capital recovery factor for continuous payments and compounding, accounts for the time value of money. An IRR of 30% per year, which yields a payback time of 3.3 years in the limit of large t_L, is a reasonable benchmark

for an industrial process with moderate technical risk[40]. An IRR of 10% per year is commonly used when establishing the economics of different energy storage scenarios[17]. Electric utilities often work with longer time horizons than other industrial and commercial concerns. Both battery price and net revenue can be normalized by the discharge energy of the battery to create intrinsic values.

The net revenue for a battery that stores energy purchased at a low price to be sold later at a higher price is given by:

$$N = (p_d E_d - p_c E_c)\omega = p_d E_d \omega \left(1 - \frac{p_c}{\varepsilon_{e,rt} p_d}\right) \tag{2}$$

The variable N is the net revenue in $ per year, p is the price of electricity in $/kW h (or $/J), E is energy in kW h (or J), and ω is the frequency of deep cycling in per year. The subscript d denotes discharge, c denotes charge, and rt denotes round trip; $\varepsilon_{e,rt}$ is the round trip energy efficiency of the battery system. Equation 2 uses the energy discharged by the battery as a basis, while Newman et al. used charging energy[39]. This choice dictates where the energy efficiency appears in the equation, but is mathematically equivalent. The term in brackets on the right side of the equation indicates that the energy efficiency must exceed the ratio of electricity prices in order to achieve positive net revenue. Clearly, energy storage is most attractive when there is a large difference between peak and off-peak electricity prices. Excluded from our analysis are sources of revenue other than arbitrage, like managing demand charges, that may be available to batteries connected to the grid.

Equations 1 and 2 may be combined to calculate how much storing energy in a battery adds to the cost of electricity:

$$p_d - p_c = \frac{P_0}{E_d \omega} \frac{r}{1 - \exp(-r t_L)} + p_c \left(\frac{1}{\varepsilon_{e,rt}} - 1\right) \tag{3}$$

Casting the energy storage costs in this form was suggested by Poonpun and Jewell[41]. The cost added to the price of electricity, $p_d - p_c$, has the benefit that it is easily understood by all consumers who receive electric bills. The first term on the right shows that the price increase is proportional to the intrinsic capital cost of the battery, and inversely proportional to the cycling frequency. The second term on the right side of the equation shows how the cost and efficiency of charging affect the price increase. This term tends to be small because the factor in brackets tends to zero at high efficiency, and cheap electricity is typically used to charge the battery. For example, the final term is just $0.0167 per kW h for p_c = $0.05 per kW h and $\varepsilon_{e,rt}$ = 75%. This analysis does not contemplate battery replacements because flow batteries should be able to achieve the required number of cycles and longevity, as cited in the Introduction.

Figure 3 shows the relationship between capital cost and the increase in electricity price for various internal rates of return. The electricity price increase at a particular capital cost rises with internal rate of return. For example, the electricity price increase at $100 per kW h and 30% per year is identical to the price increase at $200 per kW h and 10% per year. A storage device achieving a capital cost of $100 per kW h would add $0.08 per kW h to the electricity cost at an IRR of 10% per year. Average industrial and residential electricity rates in the United States were $0.070 per kW h and $0.118 per kW h in 2012, respectively[42]. Peak wholesale prices of approximately $0.25 per kW h were observed in the Northeast and Mid-Atlantic regions of the United States in January 2014[43]. Electricity rates in many European countries and Japan are considerably higher than those in the United States, making energy storage potentially more valuable in these markets[42]. For example, industrial and residential rates in Japan were $0.18 per kW h and $0.26 per kW h in 2012[1]. Figure 3 was drawn for ω = 250 per year, roughly equal to one

cycle per weekday. Cycling daily or more frequently moderates the increase in electricity price associated with storage.
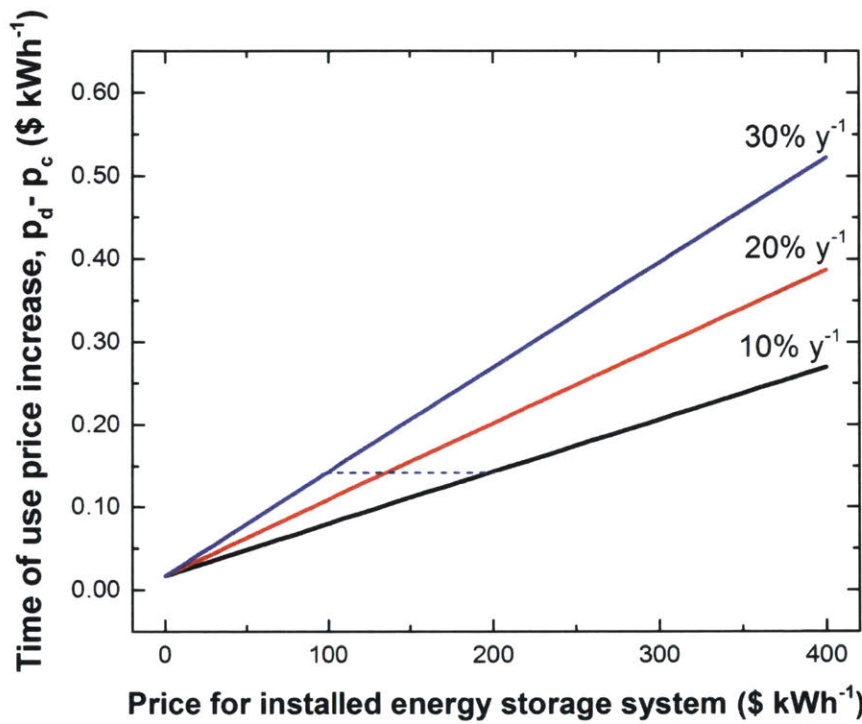
Figure 3: Relationship between capital cost and electricity price increase for various internal rates of return. Calculations done with: $\varepsilon_{e,rt} = 75\%$, $t_L = 10$ years, $\omega = 250$ per year, and $p_c = \$0.05$ per kW h. The dashed line illustrates the doubling of allowable capital costs when comparing a 10% per year return to a 30% per year at a price increase of $0.14 per kW h.

The simplicity and transparency of the preceding analysis help to clarify the cost of storage in arbitrage applications. More comprehensive analyses of the markets for energy storage devices that include other applications and sources of revenue have been published. Sandia National Laboratories has reported discharge durations, addressable market sizes, and anticipated economic benefits for nineteen segments of the energy storage market[44]. The benefits are presented as present worths in units of $/kW based on 10 years of life at a discount rate of 10% with 2.5% escalation. Present worth in $/kW was converted to $ per kW h by dividing by average discharge time. Reported values include $245 per kW h for managing time-of-use energy costs and $73 per kW h

for managing demand charges. A flow battery could potentially accomplish both of these tasks for a building owner. Bundling services significantly reduces the cost barrier to market entry.

1.3.2 Mathematical Description of Capital Cost

The price of a flow battery system can be apportioned into terms that scale with reactor area and electrolyte mass, as well as system costs that scale with power. Thus, the system price may be expressed as:

$$P_0 = c_a A + \left(c_{add} + c_{bop}\right)E_d t_d^{-1} + \sum_i c_{m,i} m_i \tag{4}$$

where P_0 is the initial system price in \$, c_a is the reactor cost per unit area in \$/m^2, A is the electrode area in m^2, c_{bop} is the cost for balance-of-plant components in \$/kW, c_{add} is the addition to the capital cost to reach the system price in \$/kW, E_d is the energy discharged by the battery system in kW h (or J), t_d is the discharge time of the battery in h, $c_{m,i}$ is the cost per unit mass of electrolyte species i in \$/kg, and m_i is the required mass of species i in kg. Power conditioning equipment, controls, sensors, pumps, pipes, fans, filters, valves, and heat exchangers are included in c_{bop}. The cost of the electrolyte storage vessels is absorbed into the electrolyte mass term. The additional contribution to price, c_{add}, includes factors such as depreciation, labor, overhead, and margin. Installation costs, which tend to be site and project specific and highly variable, are excluded from the price. Aqueous systems will tend to be larger, while nonaqueous systems may require additional environmental controls. Sandia provides example installation costs for various battery systems[17]. Estimation methods based on multipliers established from a ratio of installation and service costs to the costs of purchased equipment are commonly used in the chemical processing industries. A flow battery resembles a small, simple chemical plant in many respects.

The cost analysis is limited to the price of the electrochemical reactors, the mechanical and electrical balance of plant, and the chemicals leaving the factory.

In this analysis, reactor area is determined by the discharging half cycle. The time available for charging is expected to exceed the discharge time in most applications, and thus discharging power density is the limiting attribute. Achieving high power density is typically easier on charge because the voltage is higher, even though the upper voltage is often limited to avoid deleterious side reactions. The area is determined by dividing the output power by the power density of the electrochemical reactor. These quantities are assumed to be constant during discharge for the sake of simplicity. Practically, the power density of the reactor will decline as the battery discharges, and the active species are consumed. System losses associated with auxiliaries that include electrolyte pumps and power conversion equipment force the electrochemical reactor to discharge more energy than appears in the external circuit. Accounting for these losses, the area of the electrochemical reactor can be calculated from the formula:

$$A = \frac{E_d}{\varepsilon_{sys,d} i_d V_d t_d} \tag{5}$$

where $\varepsilon_{sys,d}$ is an efficiency that accounts for losses associated with auxiliary equipment, including power conversion, electrolyte pumps, and heat exchanger fans, during discharge. The subscript d is needed because the efficiencies of the auxiliary equipment may differ on charge and discharge. The current density and voltage of the reactor are denoted i_d and V_d, respectively. Their product is the power density of the reactor in W/cm^2 or kW/m^2. Pumping losses typically contribute less than 1% in a properly designed system [34,45]. However, the flowing electrolyte also takes the role of cooling the reactor. Other architectures without pumps will then be required to take on the burden of blowing cooled air or pumping a coolant. Shunt currents that reflect the losses due to the required manifolds of flow batteries are reflected in the coulombic efficiency as presented below.

45

A key factor that distinguishes enclosed battery designs from those based on flow architectures is the relationship between power and energy. For flow batteries, the reactors may be independently sized to meet power and efficiency requirements regardless of the energy requirements. By contrast, stationary electrodes in enclosed and hybrid cells are commonly limited by transport within the electrode or other phenomena that scale with current density. For example, in hybrid cells that utilize a metal electrodeposition and dissolution reaction at the negative electrode, the current density is constrained below a maximum on charge to ensure that the desired plating morphology is obtained (i.e., no dendrites). The reactor area is determined by either life or energy constraints rather than the target voltage efficiency. This typically results in larger reactors that are more expensive, albeit more efficient.

The round-trip energy efficiencies of the battery system and the electrochemical reactor are related by the equations:

$$\varepsilon_{rt} = \frac{E_d}{E_c} = \varepsilon_{sys,c}\varepsilon_{sys,d}\frac{E_{d,reactor}}{E_{c,reactor}} \tag{6}$$

where E_c and E_d are the charge and discharge energies of the battery system observed at the connection to the external power grid, and $E_{c,reactor}$ and $E_{d,reactor}$ are those energies observed at the electrical connections to the reactor. The energy ratios are round-trip energy efficiencies. In general, $\varepsilon_{sys,d}$ will depend on how the battery is operated. For example, pumping losses will increase with increasing flow through the system, and heat exchange losses will increase in proportion to ambient temperature in systems that require active cooling to maintain temperature below a prescribed maximum. Trading ε_{sys} with the efficiency of the reactor is an important aspect of design. For the simplified analysis presented in this paper, $\varepsilon_{sys,d}$ is treated as a constant.

The amounts of the electrochemically active species needed can be found by application of Faraday's law. Conservatively, the amount of electrolyte that must be stored in the system is determined

by the charging requirements, since coulombic inefficiency results in $Q_d < Q_r < Q_c$, where Q is charge capacity in coulombs, and the subscripts d, r, and c denote discharge, reversible, and charge, respectively. The mass of the positive active material, for example, is given by:

$$m_+ = \frac{M_+ s_+ Q_c}{n_e F \chi} = \frac{M_+ s_+ Q_d}{\varepsilon_{q,rt} n_e F \chi} = \frac{M_+ s_+ E_d}{\varepsilon_{sys,d} \varepsilon_{q,rt} n_e F \chi V_d} \tag{7}$$

where m_+ is the mass of positive active species required to charge the battery, M_+ is the molecular weight, s_+ is the stoichiometry of the positive active species in the energy storage reaction, n_e is the number of electrons, F is the Faraday constant, and χ is the allowable state of charge (SOC) range. The SOC range is limited in order to avoid unwanted side reactions and disproportionately large flows in the system. With regard to flows, decreasing the minimum SOC from 20% to 10% requires a doubling of the pumping and plumbing capacities in order to maintain a constant stoichiometric excess. We replaced Q_c with Q_d in order to put all cost terms on the same basis. This change introduces the round-trip coulombic efficiency, $\varepsilon_{q,rt}$. Finally, the charge capacity was replaced with the ratio of energy to voltage. This introduces the energy efficiency of the system, $\varepsilon_{sys,d}$, to account for losses associated with supporting equipment. Equation 7 shows that the mass of electrolyte is inversely proportional to the discharge voltage. Thus, operating at low voltages is undesirable from the perspective of electrolyte cost.

The electrolyte is expected to make a significant contribution to the total cost of a nonaqueous flow battery. The electrolyte, in our terminology, includes a dissociated acid, base, or salt in a solvent, but excludes the active material. Explicitly accounting for the electrolytes and active species on the positive and negative sides yields:

$$\sum_i c_{m,i} m_i = \frac{E_d}{\varepsilon_{sys,d} \varepsilon_{q,rt} n_e F V_d} \left[\frac{s_+ M_+}{\chi_+} \left(c_{m,+} + \frac{c_{m,e,+}}{S_+} \right) + \frac{s_- M_-}{\chi_-} \left(c_{m,-} + \frac{c_{m,e,-}}{S_-} \right) \right] \tag{8}$$

47

The subscripts + and − denote the positive and negative active species, and the subscripts e+ and e−

refer to the positive and negative electrolytes. S_+ is the solubility of the positive active species per unit

mass of electrolyte in kg/kg. The solubility of a redox species is typically a function of oxidation state.

The minimum of the solubilities for the oxidized and reduced forms should be used with enough margin

to ensure that concentration polarization does not lead to deposits in the electrodes that hinder

performance. A conflict between the solubilities of the salt and active species is likely to occur in

practice. Expanding the expression for chemical costs to explicitly include the solvent and salt is

straightforward, if justified.

A polarization equation relating i_d and V_d and relationships describing the system and

coulombic efficiencies are needed to proceed with the analysis. A flow battery must operate

efficiently, $\varepsilon_{e,rt} > p_c/p_d$, in arbitrage applications. It is, therefore, reasonable to expect a linear polarization

response for a successful flow battery over the economically viable range of efficiencies:

$$V_d = U - i_d R_i \tag{9}$$

where the potential intercept, U, corresponds to the thermodynamically reversible or open-circuit

potential, and R is the area-specific resistance (ASR) in Ω cm^2. The ASR includes ohmic losses in the

bipolar plates and separator, as well as kinetic, ohmic, and transport losses in the electrodes. The

potential intercept and the ASR generally depend on SOC. For example, the variation in U for a redox

pair separated by one oxidation state that follows the Nernst equation is 113 mV between 10% and 90%

SOC at 25 °C. The potential intercept and ASR are treated as constants in this work. Two important

sources of coulombic inefficiency in flow batteries are crossover of active species through the

membrane by diffusion and migration, and shunt currents in the manifolds connecting adjacent cells.

The inefficiency caused by crossover decreases with increasing current density, while the inefficiency

caused by shunt current decreases with decreasing voltage. Using thicker membranes will tend to reduce

the crossover of active species at the expense of higher ASR. Using less conductive electrolytes will tend to reduce shunt currents. The effect on ASR is less straightforward in this case. The above mentioned effects are ignored in this work.

Combining expressions for reactor, electrolyte, and system costs and introducing the discharge voltage efficiency, $\varepsilon_{v,d} = V_d/U$, to simplify notation yields the following equation for the total system price for useable energy:

$$\frac{P_0}{E_d} = \frac{c_a R}{\varepsilon_{sys,d} U^2 \varepsilon_{v,d}(1 - \varepsilon_{v,d})t_d} + \frac{1}{\varepsilon_{sys,d}\varepsilon_{q,rt}n_e F \varepsilon_{v,d} U}\left[\frac{s_+ M_+}{\chi_+}\left(c_{m,+} + \frac{c_{m,e,+}}{S_+}\right) + \frac{s_- M_-}{\chi_-}\left(c_{m,-} + \frac{c_{m,e,-}}{S_-}\right)\right] + \frac{c_{add} + c_{bop}}{t_d} \qquad (10)$$

The contribution of the reactor to the system cost is a minimum at $\varepsilon_{v,d} = 0.5$ and monotonically increases as $\varepsilon_{v,d}$ either increases or decreases according to Equation 10. Practically, the assumption of linear polarization will probably fail at low voltage efficiency as mass-transport effects become more important. The cost of the chemicals is a minimum at $\varepsilon_{v,d} = 1$ and increases monotonically with decreasing $\varepsilon_{v,d}$. There is a voltage efficiency that yields a minimum total price for any set of component cost and performance parameters, according to Equation 10. In the limit of long discharge times, the total system price approaches the chemical cost.

1.3.3   Analysis to Reach Cost Targets

We are seeking to establish the performance and cost objectives necessary to achieve cost competitive energy storage for aqueous and nonaqueous flow batteries. While market opportunities currently exist at battery prices greater than $200 per kW h[44], we focus on aggressive targets that could enable dramatic penetration worldwide. First, we map a broad set of pathways to meet an aggressive metric of $120 per kWh for an energy storage system, not including installation costs. This value is in line with the rolled up installed capital cost target of $150 per kWh suggested by the U.S. DOE Office of Electricity Delivery and Energy Reliability[12]. Then we examine the likelihood of achieving the necessary technological and economic values. The areal

costs for each flow battery include a flow field plate, an electrically insulating frame, a separator, seals, and two electrodes for each cell, and balance of stack materials such as end plates and tie rods. Component costs vary widely and depend on the materials used and the production volume considered. Table 2 lists the costs used in the analysis for 2014 and a mature, high-volume future state. To establish a frame of reference for "future state" cases, we calculate the annual production volume for flow batteries if used to store 1% of the electricity produced worldwide for five hours each day. In 2009, 20,000 TW h of electricity was produced worldwide[10]. Assuming daily use, 1% of electricity stored, and a 10 year battery life, $\sim$10 GW h of new energy storage systems is required annually. This equates to 2 GW of power and thus $\sim$$10^6$ m^2 of active area. For our calculations, values are taken from published literature on flow batteries and polymer electrolyte fuel cells where possible. Polymer electrolyte fuel cells and flow batteries share many design features and materials of construction. Fuel cells generally contain precious metal catalysts that are absent in flow batteries, conversely most fuel cells do not have insulating frames. The cost and performance characteristics of fuel cells have received considerable scrutiny because they are viewed as possible primary power sources for automobiles. When utilizing engineering estimates, we employed a comparison to similar high volume products and/or a bottom-up cost rationalization to determine long-run, high-volume costs.

Table 2: Component cost factors for flow batteries

Material	Year 2014 cost, $/m^2$	Reference	Future State cost, $/m^2$	Reference
Graphite flow field plate	55	34	25-35	34
Stainless-steel flow field plate	40	46,47	10-20	46,47
Carbon-fiber felt/paper electrodes	70	34	10-30	46,47
Fluorinated ion-exchange membrane	500	34	25-75	46–49
Polyolefin nanoporous separator	10	34	1-3	Est.
Fames, seals, and manifolds total	6	Est.	1-3	Est.

The likelihood of achieving the low costs in the future state case is highly uncertain. We present the values here as one possible pathway to dramatically reduced energy storage costs that may be reached in the future. We note that both benefits from manufacturing scale and engineering advancements will likely be required to reach the optimistic values. However, we also note that the cited studies estimate even lower material costs for items like ion-exchange membranes and carbon-paper electrodes than the values used in this study when annual production volumes exceeding those considered in this analysis are reached[46–48].

The analysis of the price of the battery system is presented in terms of the average chemical cost factor, c_m, needed to reach a system price of $120 per kW h as a function of open-circuit potential, U, with the product $c_a R$ as a parameter. The appearance of the product $c_a R$ indicates that an expensive, high performance reactor and a cheap, low performance reactor may be equivalent in economic terms. The chemical cost factor is given by:

$$c_m = \frac{\varepsilon_{q,rt} n_e F U \chi}{2sM} \left[\varepsilon_{v,d} \varepsilon_{sys,d} \left(\frac{P_0}{E_d} - \frac{c_{add} + c_{bop}}{t_d} \right) - \frac{c_a R}{U^2 (1 - \varepsilon_{v,d}) t_d} \right] \tag{11}$$

The positive and negative active species are assumed to be identical in terms of cost, molecular weight, ratio of s/n_e, and SOC range. The electrolyte cost factor, c_m, can be interpreted as the cost of the active material in a free electrolyte solution, or the cost of the combination of active material and electrolyte in a nonaqueous battery. Aqueous acidic solutions approach the ideal free electrolyte. For nonaqueous electrolytes, the solubility required to reach a given value of c_m can be calculated for prescribed values of $c_{m,+}$ and $c_{m,e+}$ from the equation:

$$c_m = c_{m,+} + \frac{c_{m,e+}}{S_+}$$

(12)

The subscripts + and − are interchangeable as we have assumed that the two electrolytes have identical properties. The contribution of the chemical costs was cast in the form of c_m to enable comparison with commodity chemical prices.

Table 3 summarizes the parameters used in the simulations presented in Figure 4, where P_0/E_d is the target system price, \$120 per kW h, excluding installation. The discharge time of 5 h matches the average given by Sandia for time-of-use energy management[44]. The SOC range is typical of vanadium flow batteries. The coulombic efficiency, $\varepsilon_{q,rt}$, was set to 0.97 to capture both crossover and shunt current losses. The system efficiency was assumed to be $\varepsilon_{sys,d} = \varepsilon_{sys,c} = 0.94$. The voltage efficiency, $\varepsilon_{v,d} = 0.916$, was calculated to give $\varepsilon_{e,rt} = 0.75$, assuming that the magnitude of the discharging current density is twice that for charging. The corresponding voltage efficiency during charging is 0.96. The oxidized and reduced forms of the active species were assumed to differ by one oxidation state. Species that can transfer more than one electron offer a considerable theoretical benefit. The assumed molecular weight of 0.1 kg/mol is a compromise that is higher than metals like Fe and V and lower than organic molecules like benzoquinone. A rough optimistic limit for organics is 1 electron equivalent per benzene ring, which yields an equivalent weight of $n_e M_i/s_i = 0.078$ g/(mol e⁻).

Table 3: Parameters used in system price calculations

P_0/E_d	t_d	χ	$\varepsilon_{sys,d}$	$\varepsilon_{q,rt}$	$\varepsilon_{V,d}$	$c_{add}+c_{bop}$	s/n_e	M
\$120/kWh	5h	0.8	0.94	0.97	0.916	\$300/kW	1	100 g/mol
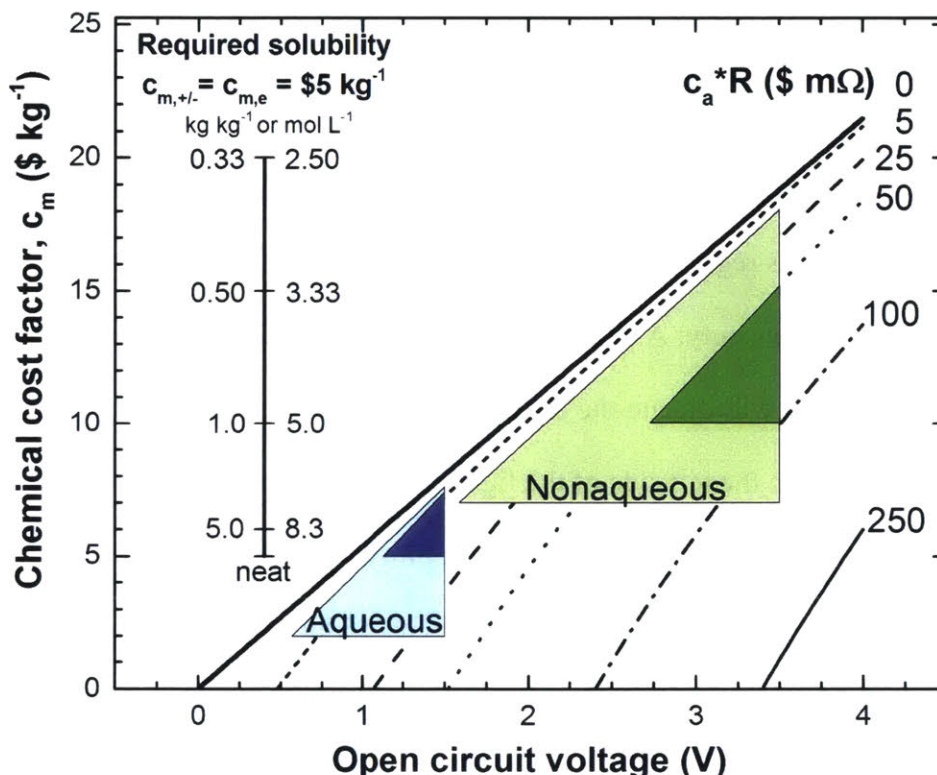
Figure 4: Allowable chemical cost factor on an active material basis (in \$/kg) *versus* open-circuit voltage for a range of reactor costs (c_aR in \$ mΩ). All points on a line give a system price of \$120 per kW h with the parameters given in Table 3. The region $U < 1.5$ V is considered to be available to aqueous systems. The dark shaded triangles are considered to have a higher likelihood of achievability compared to the larger lighter shaded triangles. The leftmost inset vertical scale shows the required solubility (in kg/kg) of a nonaqueous active species when solvent and solute cost \$5/kg. The rightmost inset vertical scale on the right shows the molar concentration, assuming specific volumes of 1 L/kg.

Figure 4 illustrates lines of constant system price, \$120 per kW h, for the parameters in Table 3, and the combinations of c_aR listed in the figure. The abscissa is the open-circuit potential, U. Aqueous batteries should be possible for $U < 1.5$ V. This exceeds the thermodynamic stability window of water in recognition of the fact that oxygen and hydrogen evolution are sluggish on carbon. Higher voltages likely require nonaqueous, aprotic electrolytes like those used in Li-ion batteries. Lead–acid and zinc–bromine batteries, with $U > 1.7$ V, are notable exceptions

to this heuristic. The aqueous region is marked with two triangles in the lower left of the figure. The nonaqueous region is identified in a similar fashion, towards the upper right of the figure. The darkly shaded triangles are considered to have a higher likelihood of achievement compared to the larger and lightly shaded triangles. The left ordinate is the chemical cost factor, c_m, in \$/kg. This cost factor is an average of the positive and negative sides and includes the active material, salt, solvent, and storage vessel costs on a mass of active material basis. The electrolyte should be inexpensive in the aqueous region; thus, c_m should correspond essentially to the sum of the active material and storage vessels only. A practical guideline for a minimum c_m for aqueous systems is \$2/kg. Commodity prices will dictate the exact cost contribution, which will probably be higher. The vertical scales inset on the left side of the figure aid in the interpretation of c_m for nonaqueous systems. The inner leftmost scale shows the solubility in kg/kg required to achieve a given chemical cost factor if active material and electrolyte cost \$5/kg each. The rightmost scale converts the solubility to a concentration of active species, assuming specific volumes of 1 L/kg. The sloped, dashed lines represent different reactor costs, parameterized by the product $c_a R$.

The future cost of nonaqueous electrolytes and tailored molecules is difficult to forecast at the scale of a combined gigawatt hours of energy storage around the world. However, the commodity chemical industry provides some clues as to what a reasonable price for materials might be[50,51]. Annual production of a 3 V nonaqueous flow battery providing a combined 10 GW h of storage requires $\sim 10^4$ metric tons per year of electrolyte and active material and $\sim 10^6$ m^2 of membrane annually. Prices of commodities of similar or larger scale such as acetonitrile, propylene carbonate, triethylene glycol, and ethyl ether fall in the \$1–5/kg[50,52]. Based on the trends observed for these, we selected \$5/kg as a reasonable material price that could be achieved if volumes of electrolyte and active material on the order of 10^4 metric tons are demanded by the market. World-

wide production of acetonitrile was near 10^5 metric tons in 2011, although only a portion of that amount was isolated and refined for resale[50]. An electrolyte includes both solvent and salt contributions, for which the salt is likely to be more expensive than the solvent, particularly if fluorinated and only used in a few industrial applications. The assumption of $5/kg for the electrolyte could be considered as $2/kg for the solvent and $20/kg for a salt at 1 M concentration; however, we lump the values together as a reflection of the inherent uncertainty contained in this analysis.

In Figure 4, the top line, $c_aR = 0$, corresponds to a free reactor and gives the maximum possible chemical cost that yields the system price target of $120 per kW h, subject to the parameters in Table 3, as a function of open-circuit voltage. This line prevails at long discharge times, as the contributions of the reactor and balance of plant diminish to zero. The lower lines correspond to higher reactor costs. The line at 5 $ mΩ is consistent with an ASR of 0.5 Ω cm^2 and a reactor cost of $100/m^2. These values appear to be achievable with aqueous flow batteries having ion-exchange membranes and carbon bipolar plates for a high-volume, large-market future state. For the sake of comparison, ASR values as low 0.23 Ω cm^2 have been measured for H$_2$/Br flow batteries with thin membranes[53]. Elimination of the ion-exchange membrane in favor of a nanoporous separator, if technically palatable, would certainly reduce costs at lower production volumes. Nanoporous is taken here to mean pore sizes less than 100 nm. Thus, an aqueous system meeting the $120 per kW h target is possible with a chemistry that costs $5/kg and operates at 1.5 V. The line drawn for $c_aR = 50$ $ mΩ represents a nonaqueous reactor cost of $100/m^2 and ASR of 5 Ω cm^2 [54]. The ASR is expected to be higher in nonaqueous batteries compared to aqueous electrolytes because of a lower electrolyte conductivity in the separator and within the electrodes. High-power Li-ion cells have pulse-power ASR >5 Ω cm^2 with more common values near 20 Ω

cm^2 [55,56]. Today's Li-ion batteries have area cost factors of approximately \$6/m^2 and potentially

lowering to \$2–5/m^2 for higher volumes. This is at least a factor of 20 smaller than the optimistic

future state area cost of flow batteries at \$100/m^2. The larger voltage window of nonaqueous

electrolytes allows for a wider range of c_aR values. As mentioned previously, power density scales

with the square of voltage. In addition, stamped metal plates will likely replace the graphite flow

fields, resulting in a net increase in c_aR over aqueous that is less than a factor of 10. The dark

shaded region bounds the most likely set of parameters yielding a nonaqueous flow battery with a

system price of \$120 per kW h. This region suggest $U > 3$ V and $S > 0.8$ kg/kg (a concentration of

>4.4 mol/L with $M = 0.1$ kg/mol and a specific volume of 1 L/kg) with an active material that costs

less than \$12/kg and is compatible with an electrolyte costing \$5/kg. These values are inexact, but

they provide guidance regarding the combinations of potential, solubility, and performance that

must be achieved in order to create a successful nonaqueous flow battery for storing grid energy.

The quantities in Table 3 should be adjusted once a particular electrolyte and active material couple

has been identified to improve accuracy.

Figure 4 indicates that nonaqueous electrolytes enable a potentially wider range of cell

voltages compared to aqueous electrolytes. Nonetheless, one must also consider two additional

factors that potentially counteract this perceived advantage. First, the lead–acid battery teaches us

that while the thermodynamic stability window of water is 1.2 V, a 2.0 V aqueous cell is possible

when the kinetics of water splitting is slow. The products of water decomposition, H_2 and O_2, may

be recombined advantageously to reform water. Energy storage systems based on enclosed

architectures such as lead–acid and nickel–metal hydride are designed to promote this

recombination[57]. An open architecture could also mitigate the loss of water by electrolysis with

the addition of water to the reservoir, assuming that the gases escape from the system. Conversely,

nonaqueous electrolytes generally undergo irreversible decomposition when pushed outside of their stability window, which results in various gas molecules, soluble compounds, and precipitants [58,59]. The precipitant is commonly associated with increased resistance to electron transport from the conducting surfaces (i.e., passivity). If passivity is not achieved, the irreversible reaction will continue to consume the electrolyte, thereby dramatically increasing the battery impedance and shortening the useable life. The second consideration is the higher cost of nonaqueous compared to aqueous electrolytes. Current Li-ion electrolytes are reported to cost \$15–20/kg, albeit at a relatively low production volume relative to commodity chemicals[55,56]. Conversely aqueous electrolytes cost significantly less than \$1/kg[60].

Figure 5 illustrates the sensitivity of the required solubility to the cost and equivalent weight of the active material for an electrolyte that costs \$5/kg and a battery price of \$120 per kW h. For low molecular weights and low active material costs, the required solubility is below 0.5 kg/kg. However, a solubility at or above 1 kg/kg is required for the target active material cost of \$5/kg and a more reasonable equivalent weight of 100 g/(mol e$^-$). The sensitivity to molecular weight raises an important issue related to the counter ion required by a tailored molecule. When a molecule undergoes a redox reaction, the newly formed charge is balanced with a cation or anion in the electrolyte. If a molecule is transformed to a net positive valence, then an anionic counter ion is needed. In nonaqueous electrolytes, PF_6^- or BF_4^- might be considered as counter ions. Unfortunately, these fluorine-based anions are expensive constituents of current electrolytes. Additionally, the anions have large molecular weights and will quickly shrink the available design space to nothing. In contrast, aqueous systems may utilize inexpensive salts such as sulfur (i.e., H_2SO_4). For aqueous electrolytes, an anion-paired tailored molecule would likely be reasonable. A commodity counter ion such as sulfur may also be possible in a nonaqueous battery, assuming

57

a high enough conductivity is reached. However, cation-associating molecules are most likely to achieve the cost target.
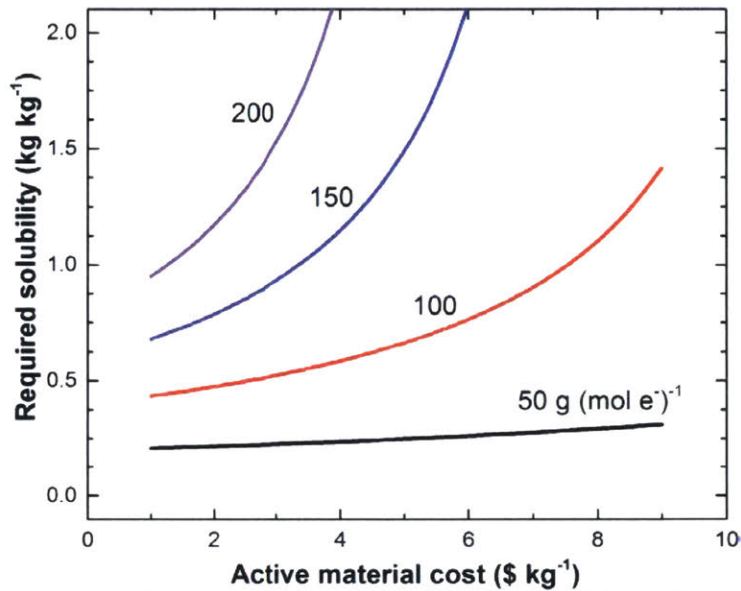
Figure 5: Solubility requirements for a nonaqueous redox flow battery. Lines of constant equivalent weight are shown.

1.3.4   Properties of Aqueous and Nonaqueous Flow Batteries

To assess the likelihood of achieving the estimated performances and costs, we compare key measured physical, transport, and kinetic properties of aqueous and nonaqueous electrolytes. Figure 6 shows properties for a number of nonaqueous electrolytes. The properties have been normalized by dividing by the quantity appropriate for the VO^{2+}/VO_2^+ positive electrode couple of a VRFB; the separator is assumed to be a Nafion ion-exchange membrane. The selected properties are pertinent to kinetic, ohmic, and mass transport losses in the electrochemical reactor as well as pumping losses and, indirectly, electrolyte cost. The arrows indicate better properties. Nonaqueous electrolytes have conductivities approximately two orders of magnitude lower than aqueous electrolytes. This difference drives comparatively higher ASR, although the additional losses may be less than proportional because, in cell designs without a gap, the ohmic losses

58

associated with the electrolyte occur in a porous electrode that, in many designs, contains a highly conductive solid phase. The second column in Figure 6 shows the relative conductivity of the separator between the electrodes. The separators include Nafion exposed to different organic electrolytes, which give conductivities differing by an order of magnitude, and ceramic electrolytes. The ohmic loss through the separator makes a proportional contribution to ASR; therefore, this difference between aqueous and nonaqueous batteries is particularly important. Whether or not an ion-exchange membrane is required in either an aqueous or nonaqueous system with two flowing electrolytes is an open question. Clearly, minimizing transport of active species across the separator is desirable in order to maintain high coulombic efficiency and to eliminate the need for separation processes. However, a combination of tailored active species and membranes with low hydraulic conductivity may possibly satisfy these requirements for either aqueous or nonaqueous systems. For reference, a lithium battery electrolyte in a polypropylene separator has conductivity near the maximum shown in Figure 6.
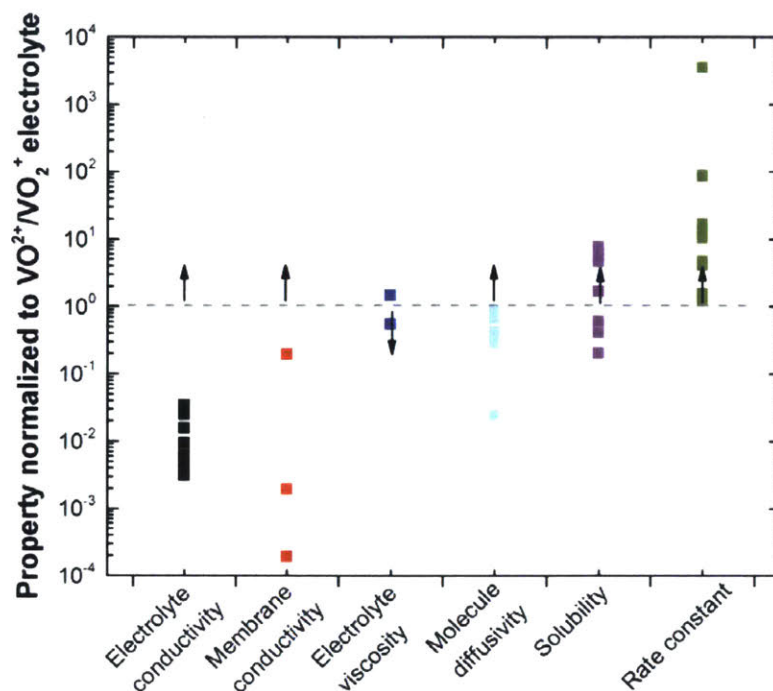
Figure 6: Physical properties of select nonaqueous electrolytes normalized by the quantity describing the VO^{2+}/VO_2^+ couple of a VRFB. A Nafion membrane is assumed for VRFBs. The arrows indicate the direction of beter nonaqueous properties.

As shown in the third column of Figure 6, nonaqueous viscosities range near aqueous values, indicating that it should be possible to achieve similar pumping losses. Nonaqueous active species tend to have lower diffusion coefficients than metal ions like vanadium. The higher mass transport losses may not be important because nonaqueous cells will tend to operate at lower current densities than aqueous cells because of ohmic losses. Transport losses can usually be addressed by increasing intra-electrode velocity, at the expense of higher pumping losses. The solubility of a nonaqueous active species must be high because the supporting electrolyte is relatively expensive. The data in column 5 indicate that high solubility is possible in some nonaqueous systems. The final column indicates that high rate constants can be achieved in nonaqueous systems.

60

1.3.5 Conclusions and the Path Forward

Materials-level performance and cost requirements are presented in Table 4. Both aqueous and nonaqueous electrolyte platforms would benefit from tailored molecules with low equivalent weights, fast kinetics, and cell voltages that stretch the electrolyte stability window. The active material and electrolytes must both be inexpensive. Nonaqueous electrolytes should be no greater than $5/kg, and aqueous electrolytes must be almost free. Targets for the concentrations of active materials are 5 mol/L and 2 mol/L for nonaqueous and aqueous systems, respectively. Finally, the sensitivity of the nonaqueous system to salt cost and the equivalent weight of the active material suggests that successfully tailored molecules will utilize cation-based counter ions.

Table 4: Performance and cost parameters required to meet cost effective energy storage

	U_{ave}, V	Equivalent weight g/(mol·e⁻)	Solubility mass basis, kg/kg	Solubility molar basis, mol/L	Material c_m, $/kg	Electrolyte c_e, $/kg
Nonaqueous	3	150	0.8	~4-5	5	5
Aqueous	1.5	150	0.05	~1-2	5	0.1

Nonaqueous flow batteries are far from a commercial reality at the time of this archival publication (2014) and subsequent thesis chapter (2019). This analysis provides the first quantitative guidance for researchers to consider in their exploration of chemical systems that, through maturation, may provide cost-effective energy storage. Unlike aqueous flow batteries, an archetype nonaqueous redox couple is not yet established. Examples of intriguing pathways for nonaqueous redox electrolytes that are aligned with the above goals could follow disparate routes. Reducing the unneeded molecular complexity of known redox structures to minimize equivalent weight (e.g., modifying Li-ion overcharge protection molecules) can reduce cost and may lead to increased charge carrier concentration. Conversely, suspensions of electroactive polymers with

multiple redox moieties can be created to achieve required charge carrier concentration and potentially obviate the need for an ion exchange membrane.

Both aqueous and nonaqueous flow batteries have pathways to reach long-term objectives for cost-effective energy storage. The design space for nonaqueous appears to be broader than that of aqueous systems. However, the constraints for nonaqueous systems of active material solubility and electrolyte cost create additional hurdles that must be overcome before a system of technological interest can be developed. Additionally, lower risk existing technologies that require less development like C-PbAcid, Li-ion, and VRFB will reach cost effective system price levels for many applications if large enough production volumes are demanded by the marketplace.

1.3.6 Relevant Nomenclature for Technoeconomic Model

a	Interfacial area per unit volume, 1/cm
A	Electrode area, m^2
c	Cost factor, use specific units
E_c	Energy to charge battery, kW h
E_d	Energy to discharge battery, kW h
F	Faraday constant, C/(mol e$^-$)
i	Current density, A/cm^2
i_0	Exchange current density, A/cm^2
L	Thickness, cm
M	Molecular weight, kg/mol
n	Number of electrons
N	Net revenue, $ per year
p	Electricity price, $ per kW h
P_0	System price, $
Q	Charge, C
r	Internal rate of return, per year

R	Area-specific resistance, Ω cm^2
R	Universal gas constant, J/mol/K
s	Stoichiometric coefficient
S	Solubility, kg/kg
t	Time, h or year
T	Temperature, C or K
U	Potential intercept, V
V	Voltage, V
χ	State-of-charge
ε	Efficiency
ω	Deep discharge cycles, per year

Subscripts

a	Area
add	Additional contributions to price
bop	Balance of plant
c	Charge
d	Discharge
e	Electrolyte
i	Species i
L	Life
m	Material
q	Coulombic
rt	Round trip
sys	System
v	Voltage
+	Positive electrolyte
-	Negative electrolyte

2 Flow Battery Active Materials

This second introductory chapter provides background on flow battery active materials that are typically used to store energy in flow battery systems. Four different categories of active materials are examined: inorganic materials in aqueous electrolytes, organic materials in aqueous electrolytes, metal-centered coordination complexes in nonaqueous electrolytes, and organic materials in nonaqueous electrolytes. The first three sections are partially reprinted from "Recent Developments and Trends in Redox Flow Batteries" by Liang Su, **Jeffrey A. Kowalski**, Kyler J. Carroll, and Fikile R. Brushett in <u>Rechargeable Batteries: Materials, Technologies and New Trends</u> (2015, editors: Zhengcheng Zhang and Sheng Shui Zhang)[1]. Permission for reproduction of the work was obtained on January 1, 2019 through Copyright Clearance Center's RightsLink® service. The section on organic materials in nonaqueous electrolytes is partially reprinted from "Recent advances in molecular engineering of redox active organic molecules for nonaqueous flow batteries" by **Jeffrey A. Kowalski**, Liang Su, Jarrod D. Milshtein, and Fikile R. Brushett from *Current Opinions in Chemical Engineering* (2016, 13, 45-52)[61]. The last section of this chapter provides general information about the remaining content of this thesis.

2.1 *Inorganic Redox Active Compounds in Aqueous Electrolytes*

The application of inorganic electroactive compounds in aqueous RFBs have been the subject of the vast majority of the literature to date. Table 5 summarizes the standard electrode potentials of common redox couples while Table 6 highlights prominent cell chemistries based on combinations of these redox couples. Of these chemistries, iron–chromium (ICB)[62], polysulfide–bromide (PSB)[16], and all-vanadium (VRFB)[33] systems have yielded industry-level demonstrations

(order of 100 kW–10 MW). Below, these RFB chemistries are introduced in some detail with key advantages, disadvantages, and challenges highlighted.

Table 5: Electrochemical series for redox flow batteries[63]

Electrode reaction	E^0 (V)
$Li^+ + e^- \rightleftharpoons Li$	−3.040
$2H_2O + 2e^- \rightleftharpoons H_2 + 2OH^-$	−0.828
$Zn^{2+} + 2e^- \rightleftharpoons Zn$	−0.762
$Cr^{3+} + e^- \rightleftharpoons Cr^{2+}$	−0.407
$S_4{}^{2-} + 2e^- \rightleftharpoons 2S_2{}^{2-}$	−0.265
$V^{3+} + e^- \rightleftharpoons V^{2+}$	−0.255
$Pb^{2+} + 2e^- \rightleftharpoons Pb$	−0.126
$TiOH^{3+} + H^+ + 2e^- \rightleftharpoons Ti^{3+} + H_2O$	−0.055
$2H^+ + 2e^- \rightleftharpoons H_2$	0.000
$O_2 + 2H_2O + 4e^- \rightleftharpoons 4OH^-$	0.401
$I_3{}^- + 2e^- \rightleftharpoons 3I^-$	0.536
$Fe^{3+} + e^- \rightleftharpoons Fe^{2+}$	0.771
$VO_2{}^+ + 2H^+ + e^- \rightleftharpoons VO^{2+} + H_2O$	0.991
$Br_2 + 2e^- \rightleftharpoons 2Br^-$	1.807
$O_2 + 4H^+ + 4e^- \rightleftharpoons 2H_2O$	1.229
$PbO_2 + 4H^+ + 2e^- \rightleftharpoons Pb^{2+} + 2H_2O$	1.455
$Mn^{3+} + e^- \rightleftharpoons Mn^{2+}$	1.542
$Ce^{4+} + e^- \rightleftharpoons Ce^{3+}$	1.720

Here E^0 represents the standard electrode potential.

Table 6: Summary of major aqueous redox flow battery chemistries

Chemistry	Cell voltage (V)	Electrolyte (positive/negative)	Current density (mA/cm²)	Efficiency	Reference
Fe/Ti	0.826	1 M $FeCl_3$ + 0.5 M HCl	$\leq$ 25	CE $\approx$ 100 %	64
		1 M $TiCl_3$ + 6 M HCl		EE = 40 %	
Fe/V	1.026	1.25 M $FeCl_2$ + 1.25 M VCl_3 + 2.3 M HCl	50	CE = 97 %	65
		1.25 M $FeCl_2$ + 1.25 M VCl_3 + 2.3 M HCl		EE = 78 %	
Fe/Cr	1.178	1.25 M $FeCl_2$ + 2.3 M HCl + 1.25 M $CrCl_3$	40	CE = 97 %	66
		1.25 M $FeCl_2$ + 2.3 M HCl + 1.25 M $CrCl_3$		EE = 73 %	
VRFB	1.246	1.5 M $VOSO_4$ + 2 M H_2SO_4	40	CE = 90 %	67
		1.5 M $VOSO_4$ + 2 M H_2SO_4		EE = 73 %	
Bromide/ polysulfide	1.352	4.0 M NaBr	40	EE = 64 %	68
		1.3 M Na_2S_4			
Polyhalide/ V	~1.43	1 M NaBr + 1 M HCl	20	CE = 83 %	69
		1 M VCl_3 + 1.5 M HCl		EE = 66 %	
Mn/V	1.797	0.3 M Mn(II) + 5 M H_2SO_4	20	CE = 69 %	70
		0.3 M V(III) + 5 M H_2SO_4		EE = 63 %	
Ce/V	1.975	0.5 M Ce(III) + 1 M H_2SO_4	22	CE = 87 %	71
		0.5 M V(III) + 1 M H_2SO_4			

Here, CE and EE represent coulombic efficiency and energy efficiency, respectively

As the first modern RFB, the Fe–Cr system was proposed by NASA in 1973 and triggered considerable research activity on electrodes, membranes, and catalysts for optimizing performance and durability throughout the 1980s[72]. Furthermore, a 1 kW/13 kWh ICB system with 8 × 39-cell

stacks was prototyped as the energy storage device for a photovoltaic array in the early 1980s[73].

The electrode reactions are:

Positive Electrode: $Fe^{3+} + e^- \rightleftharpoons Fe^{2+}$ $\qquad E^0 = 0.771$ V
Negative Electrode: $Cr^{3+} + e^- \rightleftharpoons Cr^{2+}$ $\qquad E^0 = -0.407$ V
Total Reaction: $Fe^{3+} + Cr^{2+} \rightleftharpoons Fe^{2+} + Cr^{3+}$ $\qquad E_{cell} = 1.178$ V
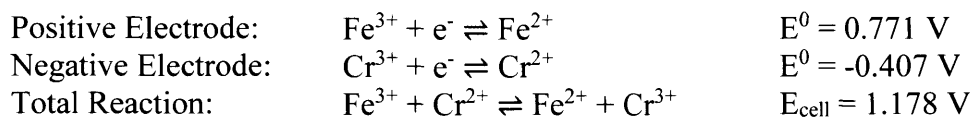
Hydrochloric acid and a cation or anion-selective membrane are commonly employed in the system. While the ferrous/ferric (Fe^{2+}/Fe^{3+}) redox couple demonstrates facile kinetics on carbonaceous surfaces, the kinetics of the chromous/chromic (Cr^{2+}/Cr^{3+}) couple are fairly sluggish, requiring a relatively high overpotential to drive the reaction. Thus, the hydrogen evolution reaction (HER) inevitably becomes a concern at these low potentials, resulting in parasitic losses on the negative electrode. A gold-lead bimetallic electrocatalyst has been shown to effectively mitigate the problem as lead suppresses HER while gold catalyzes the redox reaction of Cr^{2+}/Cr^{3+} [73]. However, the incorporation of gold is undesirable as it dramatically increases the capital cost. Moreover, for these systems, rebalancing the system due to side reactions and active species crossover (through the membrane) is necessary for long-term use, which adds to the overall operating expenses.

The polysulfide-bromine flow battery is an attractive chemistry due to the low cost, high abundance, and high solubility of both polysulfide and bromine in aqueous electrolytes. Considered applicable in MW/MWh class installations, this chemistry has been extensively studied since the earlier 1990s with several large-scale demonstration undertaken by various companies (e.g., Regenesys Technology)[16]. The electrode reactions are:

Positive Electrode: $Br_3^- + 2e^- \rightleftharpoons 3Br^-$ $\qquad E^0 = 1.087$ V
Negative Electrode: $S_4^{2-} + 2e^- \rightleftharpoons 2S_2^{2-}$ $\qquad E^0 = -0.265$ V
Total Reaction: $Br_3^- + 2S_2^{2-} \rightleftharpoons 3Br^- + S_4^{2-}$ $\qquad E_{cell} = 1.352$ V
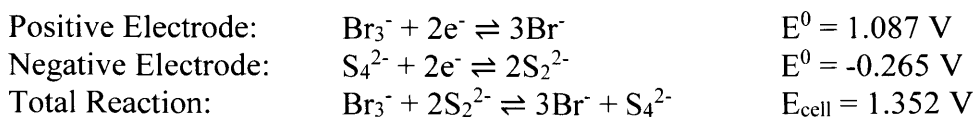
A cation exchange membrane is typically used with a sodium ion shuttling between the positive and negative electrolytes containing NaBr and Na_2S_4, respectively. Nickel[74] and cobalt[68] have been found to catalyze the negative electrode reaction. Further, the use of activated carbon/polyolefin composite electrodes has been shown to increase charging voltages, from 1.7 to 2.1 V, due to bromine adsorption[33]. However, as with ICBs, species crossover during the operating life dramatically decreases the efficiency and capacity of the cell. Moreover, side reactions may lead to the formation of toxic gases (i.e., Br_2, H_2S) and insoluble insulating precipitants. Therefore, the system requires stringent maintenance to separate the electrolyte and to recover the reactants, which substantially increases the operating cost. Despite the favorable kinetics, the mass transfer overpotential on the positive electrode limits the discharge performance of the battery[75]. Scamman and co-workers developed a numerical model for PSBs, and showed that there would still be a net loss for arbitrage applications even if operated under optimum conditions. However, if the total capital cost were reduced by 20–30 % or the buy and sell price difference for electrical energy were increased, the system could become economically feasible[76].

As arguably the most well-known RFB chemistry, all vanadium RFBs take advantage of the four oxidation states of vanadium within the stability window of water. This enables operation with the same element as an electroactive species as both negative and positive electrolytes and limits concerns about solution crossover and the associated permanent deleterious effects (e.g., capacity fade, irreversible side reactions). Since the initial electrochemical studies of the V(IV)/V(V) and the V(II)/V(III) redox couples in 1985[77,78] and the first demonstration of an all-vanadium redox flow cell in 1986[79] by Skyllas-Kazacos and co-workers, VRFBs have been the focus of intensive research, development, demonstration, and deployment activities for more than

two decades. These efforts have culminated in several pilot plant scale or utility scale installations worldwide[33]. The electrode reactions of a VRFB are:

Positive Electrode: $VO_2^+ + 2H^+ + e^- \rightleftharpoons VO^{2+} + H_2O$ $E^0 = 0.991$ V
Negative Electrode: $V^{3+} + e^- \rightleftharpoons V^{2+}$ $E^0 = -0.255$ V
Total Reaction: $VO_2^+ + V^{2+} + 2H^+ \rightleftharpoons VO^{2+} + V^{3+} + H_2O$ $E_{cell} = 1.246$ V
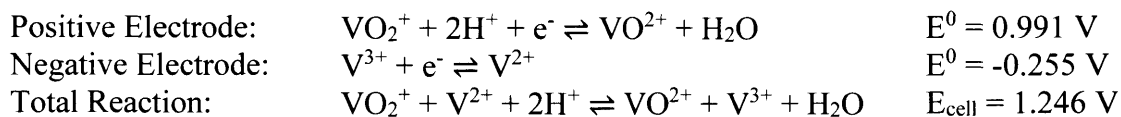
This system typically uses sulfuric acid as the electrolyte with a proton exchange membrane. While a porous separator could be used, for high efficiency operation, ion-selective membranes are generally preferred as vanadium crossover leads to losses in coulombic efficiency. At present, Nafion is the membrane of choice as V(V) is a powerful oxidizing agent, which can attack cheaper hydrocarbon-based ion selective membranes[23]. The redox reactions of different vanadium species have displayed reversibility and high activity on carbon based electrodes. Moreover, Li et al. discovered the catalytic effects of bismuth nanoparticles on V(II)/V(III)[80] and of niobium oxide nanorods on both V(II)/V(III) and V(IV)/V(V)[81], which have been shown to further enhance the energy efficiency of the VRFB by more than 10 %.

One challenge of VRFBs is the low energy density (<25 Wh/L), which is, at least partially, restricted by the low solubility of $VOSO_4$ (<1.7 M), which is sensitive to both acid concentration (3–4 M H_2SO_4) and solution temperature (10–40 °C)[82]. Recently, Li et al. developed sulfate-chloride mixed acid electrolyte that solubilizes V(V) in the form of $VO_2Cl(H_2O)_2$ up to 2.5 M, which corresponds to a 70 % improvement of the battery capacity compared to the conventional sulfate based electrolyte[83]. A 1 kW/1 kWh prototype VRFB system using the mixed acid electrolyte has been demonstrated and the underlying patents are being licensed by several companies[84]. A second challenge for VRFB technologies is the high cost of vanadium, reportedly 43 % of total cost for 1 MW/4 MWh mixed acid system[34]. This may set a floor for the potential

system costs despite reductions enabled by mass production and engineering improvements. Alternative approaches are exploring the use of bromine polyhalide positive electrolytes, which leverages the higher solubility of vanadium in the presence of halides and the lower cost of bromine-based electrolytes[32,33]. However, the aforementioned challenges with ICB and PSB systems; namely species crossover and bromine toxicity, are re-introduced.

2.2   Organic Redox Active Compounds in Aqueous Electrolytes

Recently, electroactive organics have been explored as active materials in aqueous RFBs and may open new avenues to meet the stringent grid storage cost targets. Indeed, organic molecules offer several advantages over inorganic molecules. First, they are often comprised of earth-abundant elements (carbon, hydrogen, oxygen, nitrogen, sulfur, etc.), and thus, their cost and availability is less constrained by the production and reserves of key elements (e.g., vanadium). Moreover, while transition metals must be mined and purified from ore, organic materials may be synthesized in a sustainable fashion using green chemistry routes[85]. Second, while inorganic redox couples are restricted by the known periodic table, a broader array of organic redox-active molecules are available, allowing for the realization of new redox couples. Third, key electrochemical and physical properties (e.g., redox potential, solubility) can be tailored via modification of the redox moiety or the surrounding molecular structure. Further, a number of organics are known to undergo 2-electron transfer (e.g., quinones), which may lead to higher intrinsic capacities and thus, higher cell energy densities. These design degrees of freedom allow for a wide array of potential storage materials to be contemplated and for high throughput computational tools to be leveraged to drive the discovery and development process. However, as

71

with any emerging materials, a number of unanswered questions exist including organic stability

in acidic electrolytes and the organic solubility in aqueous media.

Huskinson et al. studied the electrochemistry of 9,10-anthraquinone-2,7-disulphonic acid

(AQDS) and demonstrated its applicability as the low potential compound in a AQDS-bromide

aqueous redox flow cell[86]. AQDS undergoes a reversible, 2-electron transfer process on the glassy

carbon electrode. Excitingly, the reported reaction kinetics were one to three orders of magnitude

faster than many common redox couples (Fe^{2+}/Fe^{3+}, Cr^{2+}/Cr^{3+}, VO^{2+}/VO_2^+, V^{2+}/V^{3+}, Br_2/Br^-,

S_4^{2-}/S_2^{2-}) on similar carbon surfaces. The electrode reactions are:

Positive Electrode:	$Br_2 + 2e^- \rightleftharpoons 2Br^-$	$E^0 = 1.087$ V
Negative Electrode:	$AQDS + 2H^+ + 2e^- \rightleftharpoons AQDSH_2$	$E^0 = 0.213$ V
Total Reaction:	$Br_2 + AQDSH_2 \rightleftharpoons 2Br^- + AQDS + 2H^+$	$E_{cell} = 0.874$ V
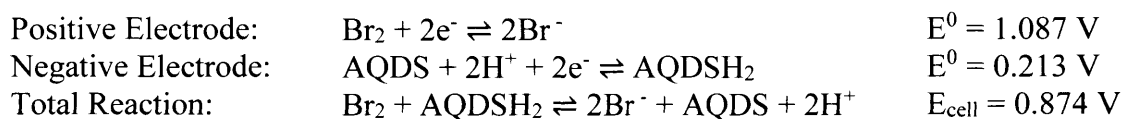
Promising cycling performance and capacity retention was obtained using a benchtop cell

(Figure 7). Specifically, the cell was operated at a large current density (0.5 A/cm^2) with a high

current efficiency (~99 %) and low capacity degradation (0.78 %/cycle). Since energy density is

directly proportional to the number of electrons transferred by the redox active compound, the

2-electron transfer redox event of AQDS is highly favorable in the application of RFBs. Moreover,

via DFT-informed molecular design, the researchers were able to identify a more promising second

generation AQDS derivative with one hydroxyl group on each benzene ring (1,8-dihydroxy-9,10-

anthraquinone-2,7-disulphonic acid). Compared to AQDS, the derivative displayed a lower redox

potential (consequently, a higher cell voltage) and a higher kinetic rate constant, which not only

produces a more favorable low potential compound, but also validates the applicability of

computationally directed research for RFBs. Based on this work, the authors further explored the

long-term cycling performance of the AQDS/Br$_2$ cell containing 0.1 L of 1 M AQDS and 1 M

H_2SO_4 on the negative side and 0.12 L of 0.5 M Br_2 and 3 M HBr on the positive side with a

Nafion 115 membrane separating the electrolytes[87]. The cell showed good stability at 100 % state-

of-charge and 0.75 A/cm^2 over 750 cycles with an average discharge capacity retention and current

efficiency as high as 99.84 and 98.35 %, respectively.
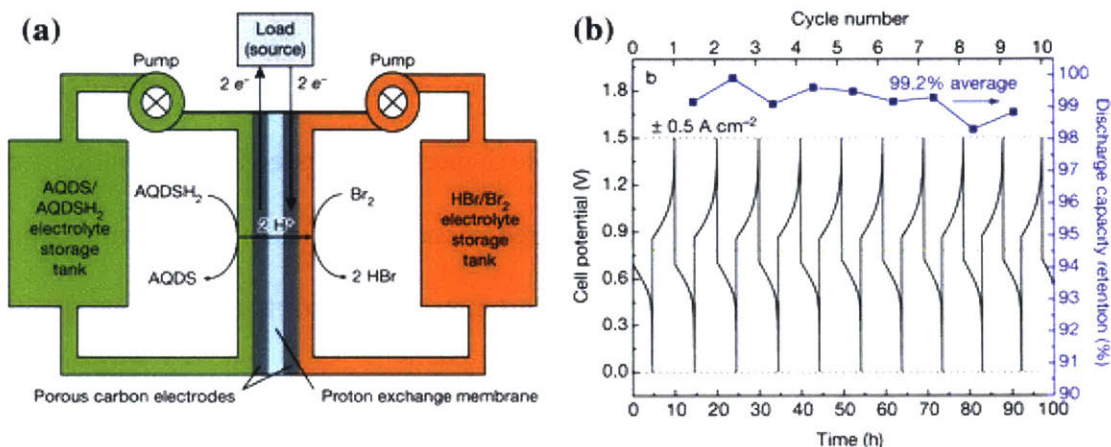
Figure 7: Cell schematic (a). Discharge mode is shown; the arrows are reversed for electrolytic/charge mode. AQDSH$_2$ refers to the reduced form of AQDS. Constant-current cycling (0.5 A/cm^2) at 40 °C using a 3 M HBr + 0.5 M Br$_2$ solution on the positive side and a 1 M AQDS + 1 M H$_2$SO$_4$ solution on the negative side (b). Discharge capacity retention is indicated for each cycle[86]. Reproduced with permission. Copyright 2014 Nature

Beyond anthraquinone, the fundamental electrochemistry of other quinonoid compounds

such as benzoquinone and naphthoquinone in aqueous systems have been thoroughly studied,

paving the way for their new applications in RFBs[88,89]. Huskinson et al. reported the cyclic

voltammetry results of 1,4-benzoquinone in neutral solution with high reversibility on both glassy

carbon and platinum disc electrodes[90]. Moreover, they also studied the cycling performance of

0.1 M benzoquinone as the positive electrolyte couple with hydrogen reduction reaction with a

theoretical cell voltage of ~0.70 V in acidic electrolyte using I-V polarization curve. The authors

pointed out that the cell performance was primarily restricted by mass transport of benzoquinone

due to its limited solubility, as a higher flow rate improved the peak power density and limiting

current density. Xu et al. investigated the electrochemical behavior of 4,5-dihydroxybenzene-1,3-disulfonic acid disodium salt (Tiron) as a high potential compound in the application of aqueous redox flow batteries. Constant current electrolysis (vs. a lead counter electrode) was performed on 0.05 M Tiron in 3 M H_2SO_4[91]. The proposed reaction mechanism involves a reversible 2-electron transfer process followed by the addition of a hydroxyl group and a subsequent reversible 2-electron transfer process, which is also known as an ECE (electrochemical–chemical–electrochemical) process (Figure 8). The reversible 2-electron transfer redox reaction between compound 3 and compound 4 at 0.96 V makes this redox couple an ideal high potential compound for aqueous RFBs. Tiron, herein, serves as a starting material due to its commercial availability and low price.
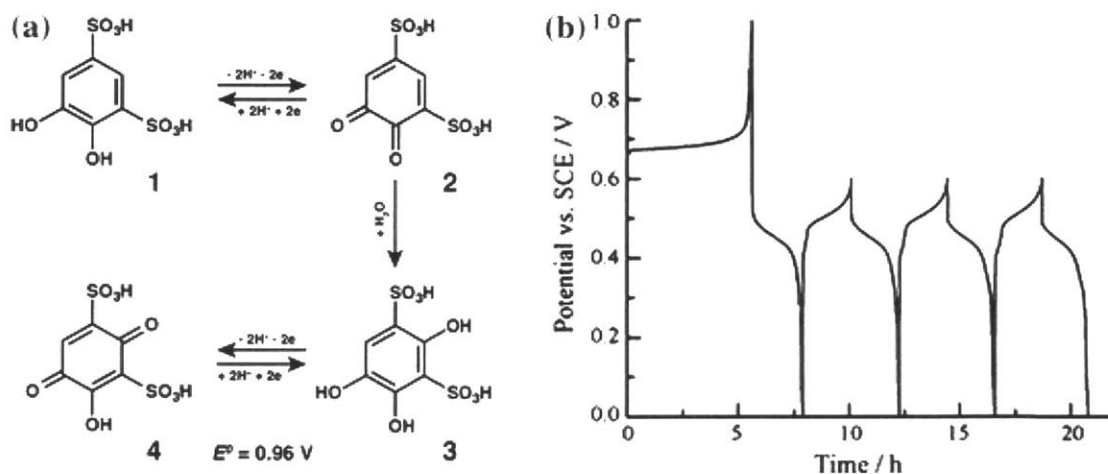
Figure 8: The mechanism of the redox reaction of 4,5-dihydroxybenzene-1,3-disulfonic acid (a). Electrolytic characterization of tiron in 3 M H_2SO_4 at 298 K with a lead counter electrode (b)[91]. Reproduced with permission. Copyright 2010 Electrochimica Acta

Combining Tiron and AQDS as the high potential and low potential redox active compounds, respectively, Yang et al. reported an all organic, aqueous redox flow cell with an open circuit voltage (OCV) of ~0.75 V [100 % state-of-charge (SOC)][92]. A demonstration cell was operated using 0.2 M Tiron (posolyte), 0.2 M AQDS (negolyte), and 1 M H_2SO_4 (electrolyte) at a

current density of 8 mA/cm^2 and a flow rate of 1000 mL/min, and displayed high current efficiency and acceptable capacity retention. In this paper, the authors also pointed out that the strong interaction between the ionized quinonoid species (R-SO$_3^-$) and water results in the low diffusion coefficient of the quinone-based redox active molecules. Corroborating this statement, computational analysis of the I-V relationship revealed that lowering mass transfer resistance is critical to achieving a high operating current density in this type of redox flow cell.

2.3   Metal-Centered Coordination Complexes in Nonaqueous Electrolytes

As a natural extension of the studies conducted on transition metals for aqueous RFBs, metal-centered coordination complexes have been investigated for use in nonaqueous systems. The structure of a metal-centered coordination complex can be expressed as [ML$_n$]$^{z+}$ where M is a transition metal center (i.e., ruthenium, iron, vanadium, chromium, manganese, nickel, etc.), L is a ligand (i.e., acetylacetonate (acac$^-$), 2,2'-bipyridine (bpy), phenanthroline (phen), etc.), n is the number of ligands (typically n = 3 for bidentate ligands), and z is the total charge that combines the valence of the metal center and the charge of the ligands. Because an entire compound must be neutral, a counter ion is necessary if z is not zero. Using [Ru(bpy)$_3$], [Ru(acac)$_3$], and [Ru(phen)$_3$] as examples, Figure 9 depict the bonding environment of the ruthenium metal center as well as 2-D structures of 2,2'-bipyridine, acetylacetonate, and phenanthroline. While the metal center provides the electrochemical activity of [ML$_n$], the coordinating ligands play a pivotal role in determining a number of key parameters of the complex, such as the solubility, diffusivity, reversibility, and redox potential of each electron transfer event. Moreover, non-innocent (redox active) ligands may store additional charge thus increasing the intrinsic capacity of the complex[93]. A multi-step redox process with a sufficient potential difference enables the use of the same redox

75

active compound as both the high potential and the low potential compound, which alleviates the concern of cross contamination. To date, most systems employ ACN and a non-coordinating salt (e.g., tetraethylammonium tetrafluoroborate (TEABF$_4$)) as the solvent and the supporting salt, respectively, with an anion exchange membrane (AEM) to separate the positive and negative electrolytes. Table 7 summarizes several reported metal-centered coordination complexes and the cell voltages of the proposed nonaqueous redox chemistries.
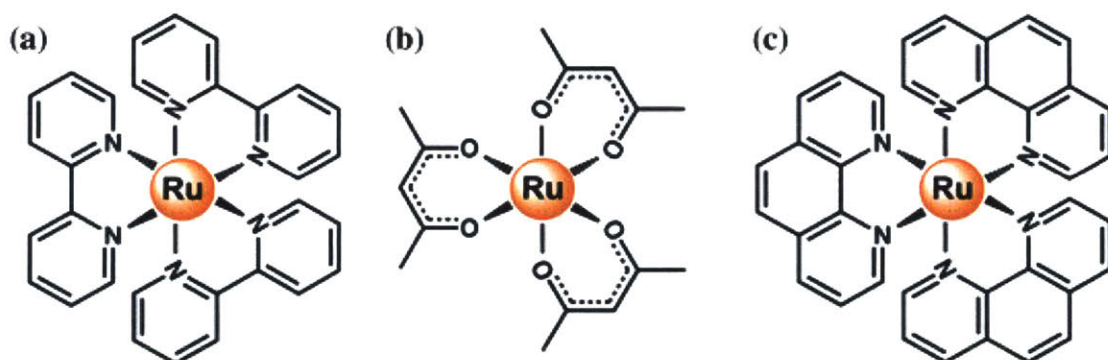
Figure 9: The molecular structures of (a) [Ru(bpy)$_3$], (b) [Ru(acac)$_3$], and (c) [Ru(phen)$_3$]

Table 7: Nonaqueous redox flow batteries based on metal-centered coordination complexes

Reactions	Electrolyte	Cell voltage (V)	Reference
[Mn(IV)(acac)$_3$]$^+$ + e$^-$ $\rightleftharpoons$ Mn(III)(acac)$_3$ Mn(III)(acac)$_3$ + e$^-$ $\rightleftharpoons$ [Mn(II)(acac)$_3$]$^-$	0.5 M TEABF$_4$ Acetonitrile	1.1	94
[Ru(IV)(acac)$_3$]$^+$ + e$^-$ $\rightleftharpoons$ Ru(III)(acac)$_3$ Ru(III)(acac)$_3$ + e$^-$ $\rightleftharpoons$ [Ru(II)(acac)$_3$]$^-$	0.05 M TEABF$_4$ Acetonitrile	1.77	95
[Co(III)(acacen)]$^+$ + e$^-$ $\rightleftharpoons$ Co(II)(acacen) Co(II)(acacen) + e$^-$ $\rightleftharpoons$ [Co(I)(acacen)]$^-$	0.1 M TEABF$_4$ Acetonitrile	2.0	96
[V(IV)(acac)$_3$]$^+$ + e$^-$ $\rightleftharpoons$ V(III)(acac)$_3$ V(III)(acac)$_3$ + e$^-$ $\rightleftharpoons$ [V(II)(acac)$_3$]$^-$	0.1 M TEABF$_4$ Acetonitrile	2.2	97
[Fe(III)(bpy)$_3$]$^{3+}$ + e$^-$ $\rightleftharpoons$ [Fe(II)(bpy)$_3$]$^{2+}$ [Ni(II)(bpy)$_3$]$^{2+}$ + 2e$^-$ $\rightleftharpoons$ Ni(0)(bpy)$_3$	0.05 M TEABF$_4$ Propylene carbonate	2.3	98
[Ru(III)(bpy)$_3$]$^{3+}$ + e$^-$ $\rightleftharpoons$ [Ru(II)(bpy)$_3$]$^{2+}$ [Ru(II)(bpy)$_3$]$^{2+}$ + e$^-$ $\rightleftharpoons$ [Ru(I)(bpy)$_3$]$^+$	0.1 M TEABF$_4$ Acetonitrile	2.6	99

In 1988, Matsuda et al. demonstrated the first nonaqueous redox flow cell using $[Ru(bpy)_3]^{2+}/[Ru(bpy)_3]^{3+}$ and $[Ru(bpy)_3]^{+}/[Ru(bpy)_3]^{2+}$ as the high potential and low potential couples, respectively, with an OCV of 2.6 V[99]. A static H-cell polarization experiment identified the efficiency/performance limiting reaction as $[Ru(bpy)_3]^{+}/[Ru(bpy)_3]^{2+}$, which might be due to a side reaction and/or the low stability of $[Ru(bpy)_3]^{+}$. A flow cell cycling experiment demonstrated the charge-discharge capability of the cell with a 1.2 V discharge voltage, a 40 % coulombic efficiency and a 47 % utilization efficiency at 5 mA/cm^2. Although the performance metrics of this cell were far from practical, this seminal work initiated the application of metal-centered coordination complexes to nonaqueous redox flow cells and triggered ensuing research interest in this area. More recently, Chakrabarti et al. investigated ruthenium acetylacetonate (Ru(acac)$_3$) that displayed two 1-electron transfer processes with ~1.77 V separation according to the cyclic voltammetry[95]. The charge/discharge performance of Ru(acac)$_3$ was studied in the H-cell configuration containing 40 mL of 0.1 M Ru(acac)$_3$, 1 M TEABF$_4$, and ACN in each compartment. At the charge and discharge rate of 1 mA and 0.5 mA, respectively, the first cycle gave an energy efficiency of 74 % and the second cycle gave an energy efficiency of 57 %. Based on this work, a redox flow cell using Ru(acac)$_3$ as the active materials with two 2.5-L storage tanks and 5 cm × 5 cm active area was demonstrated[100]. For 0.02 M Ru(acac)$_3$, the optimum power output was determined to be 35 mW at the discharge current density of 2.1 mA/cm^2 and the voltage efficiency is 52.1 % (at 100 % SOC). Increasing the concentration of Ru(acac)$_3$ to 0.1 M increased the current density and power output by a factor of 5 (at the same velocity) due to the improved mass transfer of the active species.

Thompson et al. investigated a series of metal acetylacetonates [M(acac)$_3$] (where M = V[101], Cr[102], and Mn[94]) for their potential application in nonaqueous redox flow batteries. Amongst

these beta-diketonate candidates, [V(acac)$_3$] has been systematically studied to optimize the cell performance with respect to the electrode surface, the impurity concentration, and the electrolyte. Specifically, the influence of the electrode surface (glassy carbon, platinum, and gold) on the electrochemistry of [V(III)(acac)$_3$]^0/[V(IV)(acac)$_3$]$^+$ (posolyte) and [V(II)(acac)$_3$]$^-$/[V(III)(acac)$_3$]^0 (negolyte) was examined[103]. The positive electrode reaction exhibits fast and reversible kinetics on all electrode surfaces. In contrast, the negative electrode reaction is surface-selective and the kinetic constant of [V(II)(acac)$_3$]$^-$/[V(III)(acac)$_3$]^0 on a gold electrode is about 6.5× higher than that on a glassy carbon electrode. As the main source of impurities, oxygen and water deteriorate the performance of [V(acac)$_3$]-based, nonaqueous redox flow cells[97]. Oxygen may degrade the electrolyte and block the reduction reaction on the negative electrode while water can not only impede the kinetics on the negative electrode but also hinder the positive electrode reaction by forming vanadyl acetylacetonate [VO(acac)$_2$]. In addition, a range of solvents (ACN, dimethylformamide, hexane, tetrahydrofuran, dimethylcarbonate) and salts [tetraethylammonium tetrafluoroborate, tetrabutylammonium tetrafluoroborate, tetrabutylammonium hexafluorophosphate,(1-butyl, 3-methyl)imidazolium bis(trifluoromethanesulfonyl)imide] were screened aiming at improving the conductivity of the electrolyte and the solubility of [V(acac)$_3$][104]. According to their results, ACN and TEABF$_4$ is still the optimal combination for [V(acac)$_3$]. However, even under carefully controlled conditions, the charge/discharge performance of [V(acac)$_3$] (in a stirred H-cell) was still not desirable with coulombic and energy efficiencies of 70 % and 35 %, respectively at 50 % SOC and a discharge current of 0.014 mA/cm^2.

Vanadium-centered coordination complexes using the non-innocent redox active ligand—maleonitriledithiolate [(mnt)$^{2-}$] were investigated for their potential application in nonaqueous RFBs[93]. It has also been demonstrated that the reduction of [V(mnt)$_3$]$^{2-}$ adds one electron to the

vanadium (IV) center and the oxidation of $[V(mnt)_3]^{2-}$ removes one electron from the $(mnt)^{2-}$ ligand. Therefore, non-innocent ligands may store additional electrochemical energy beyond what can be accessed from the metal center. Additionally, improved complex stability can be expected when electron transfer takes place on the ligand rather than involving metal-ligand bonding. The redox potential of V(III)/V(IV) is tunable by the selection of cation in the supporting electrolyte, which might be attributed to the decreased relative electrostatic stabilization of $[V(mnt)_3]^{2-}$ and the increased steric shielding of the cationic charge. The cycling performance using 0.02 M $TEA_2[V(mnt)_3]$ in 0.1 M tetrabutylammonium hexafluorophosphate ($TBAPF_6$) in ACN as both the positive and the negative electrolyte with a battery separator (Tonen) demonstrated the rechargeability of the nonaqueous redox flow cell with ~90 % coulombic efficiency and good capacity retention, although the energy efficiency is <45 %.

Promising results were reported by Mun et al. using [Fe(bpy)3] and [Ni(bpy)3] as the high potential and low potential compounds, respectively[98]. The 1-electron transfer $[Fe(II)(bpy)_3]^{2+}/[Fe(III)(bpy)_3]^{3+}$ takes place at +0.65 V vs. Ag/Ag^+ and the 2-electron transfer $[Ni(bpy)_3]^0/[Ni(II)(bpy)_3]^{2+}$ takes place at −1.66 V vs. Ag/Ag^+, which results in the nominal cell voltage of 2.31 V. The redox stability of both reactions in 0.05 M $TEABF_4$ in PC was verified by 100 cycles of cyclic voltammetry on a glassy carbon electrode. The advantageous electrochemical properties of the redox active compounds were further validated by the constant current (0.8 mA/cm^2) cycling in a flow cell containing 0.4 M $[Fe(bpy)_3](BF_4)_2$ and 0.2 M $[Ni(bpy)_3](BF_4)_2$ in 0.5 M $TEABF_4$ in PC, and an AEM. The OCV of the cell was 2.2 V and the coulombic and energy efficiencies of the cell were maintained at 90.4 % and 81.8 %, respectively, throughout the cycling. The utilization efficiency (based on the first charging phase) was 92.8 % of the theoretical capacity. However, the capacity of the cell decayed over time, which might be due to the crossover

of redox active species. An improved capacity retention was observed by replacing [Ni(bpy)₃] with [V(acac)₃] in a non-flowing cell[105]. Besides the nonaqueous chemistries discussed above, several other combinations such as [Ni(phen)₃]-[Fe(phen)₃], [Co(bpy)₃]-[Fe(bpy)₃], [Co(phen)₃]-[Fe(phendione)₃]₃ have been evaluated as well, and their performances were similar to that of the [Fe(bpy)₃]-[Ni(bpy)₃] cell[105].

Ferrocene is a well-known redox model compound for its superior electrochemical reversibility and stability in nonaqueous electrolytes, and has been widely adopted as an internal standard for electrochemical measurements[106]. However, ferrocene's low solubility (e.g., <0.1 M in carbonate-based solvent) restricts its use in RFBs for grid energy storage. Wei et al. described a structural modification strategy to greatly enhance the solubility of ferrocene[107]. Figure 10a shows the structure of the ferrocene derivative (Fc1N112-TFSI). As evidenced experimentally and computationally by nuclear magnetic resonance (NMR) and DFT, respectively, the quaternary ammonium cation accentuates the interaction between the ionic pendant and the polarizable oxygen atoms on the carbonate solvent molecules. As a result, the as-prepared ionic-derivatized ferrocene compound can be dissolved in a carbonate based electrolyte (1.2 M LiTFSI in the mixture of ethylene carbonate (EC)/propylene carbonate (PC)/ethyl methyl carbonate (EMC) (4:1:5 by weight)) up to 0.85 M—more than 20× higher than the solubility of pristine ferrocene in the same electrolyte. Besides advancing the solvation chemistry, the quaternary ammonium cation also induces the electron withdrawing effect on the ferrocene moiety, which increases the redox potential of the ferrocene derivative by 0.23 V as compared to pristine ferrocene. Stable half-cell cycling performance of 0.1 M Fc1N112-TFSI with a lithium foil negative electrode is shown in Figure 10b and c, further validating the electrochemistry of the compound. Furthermore, using a hybrid lithium-graphite negative electrode and appropriate additive (15 wt % fluoroethylene

carbonate) in the electrolyte, the cycling performance of 0.8 M Fc1N112-TFSI was demonstrated at 1.5 mA/cm^2, resulting in 90 % coulombic efficiency, 76 % energy efficiency, 0.93 %/cycle degradation of discharge capacity.
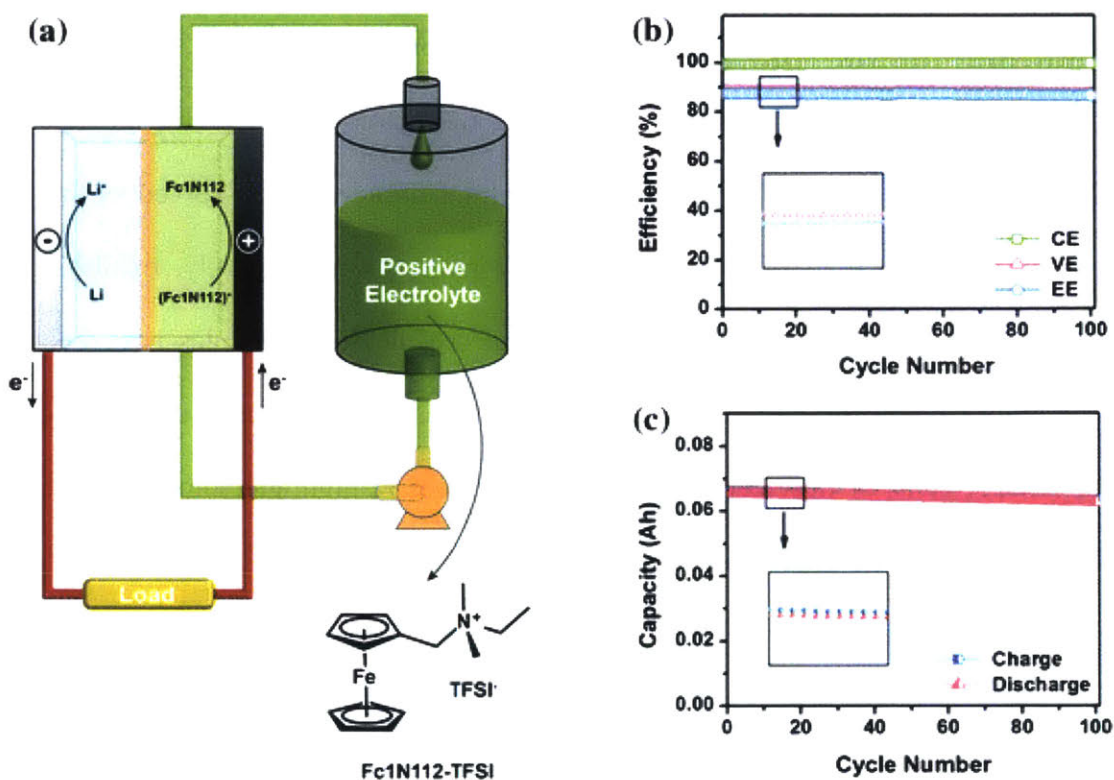
Figure 10: Cell schematic (discharge mode) and the molecular structure of Fc1N112-TFSI (a). Coulombic (CE), voltage (VE), and energy (EE) efficiencies (b) and capacities of the half-cell test (c) using 0.1 M Fc1N112-TFSI in 1.0 M LiTFSI in EC/PC/EMC with 5 wt% FEC at a current rate of 3.5 mA/cm2 and a flow rate of 40 mL/min[107]. Reproduced with permission. Copyright 2014 Advanced Energy Materials.

2.4   Organic Redox Active Molecules in Nonaqueous Electrolytes

Nonaqueous flow batteries employing redox active organic molecules are an emerging energy storage concept. Recent developments in all-organic nonaqueous chemistries with a focus on tailoring organic molecules for improved physical and electrochemical properties are summarized. Key opportunities and challenges in the science and engineering of these devices are presented with a goal of meeting the stringent grid cost targets.

81

2.4.1 All-Organic Nonaqueous Redox Flow Battery Redox Couples

Though first conceived in the 1980s, early reports of NAqRFBs were limited, and redox chemistries were based on metal or metal-ligand coordination complexes (e.g., Ru(bpy)$_3$[BF$_4$]$_2$)[33]. In 2011, Li et al. reported the first NAqRFB employing all-organic active materials, where 2,2,6,6-tetramethyl-1-piperidinyloxy (TEMPO) and N-methylphthalimide (NMP) served as the positive (high potential) and negative (low potential) active materials, respectively, exhibiting a cell potential of 1.6 V[108]. After that initial report, several organic redox couples have been paired together as proof-of-concept energy storage systems in demonstration cells utilizing coin cells, Swagelok cells, H-cells, or flow cells. Figure 11 and Figure 12 highlight some prominent redox chemistries, illustrating the active species pairs, supporting salts, and the cell performance.
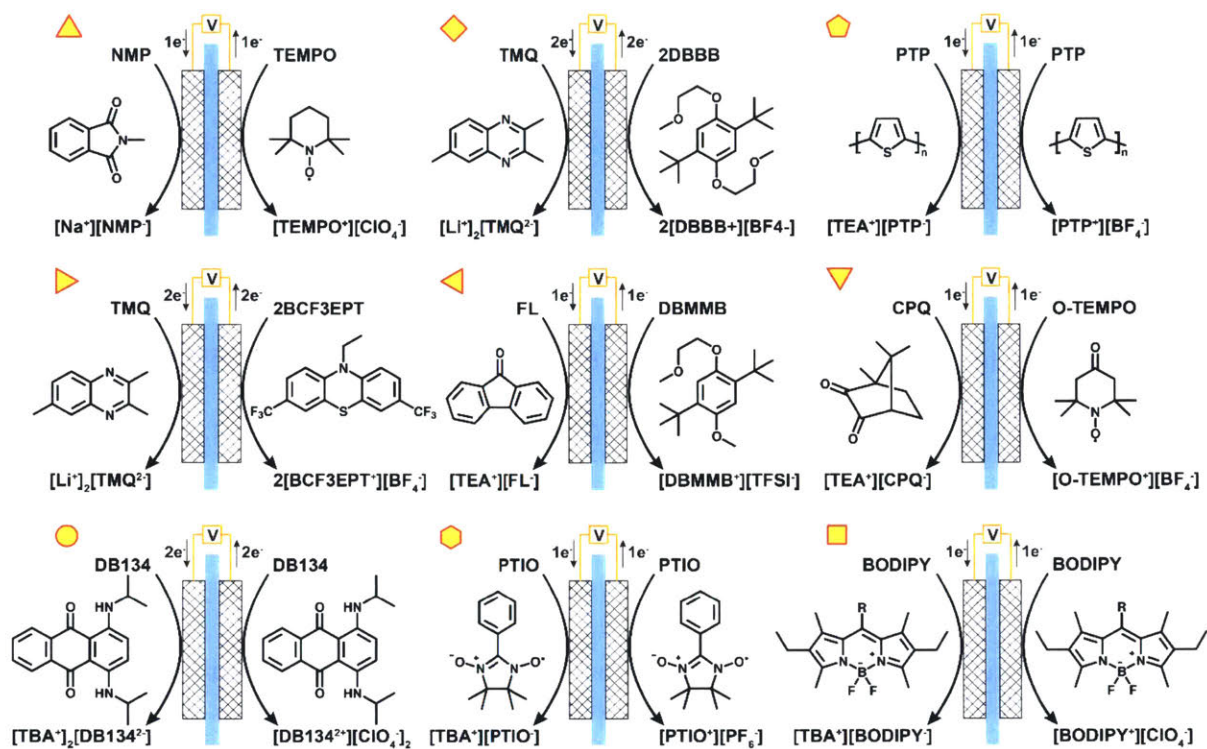
Figure 11: Summary of organic NAq chemistries demonstrated in coin cell, Swagelok® cell, H-cell, or flow cell configurations[108–116]
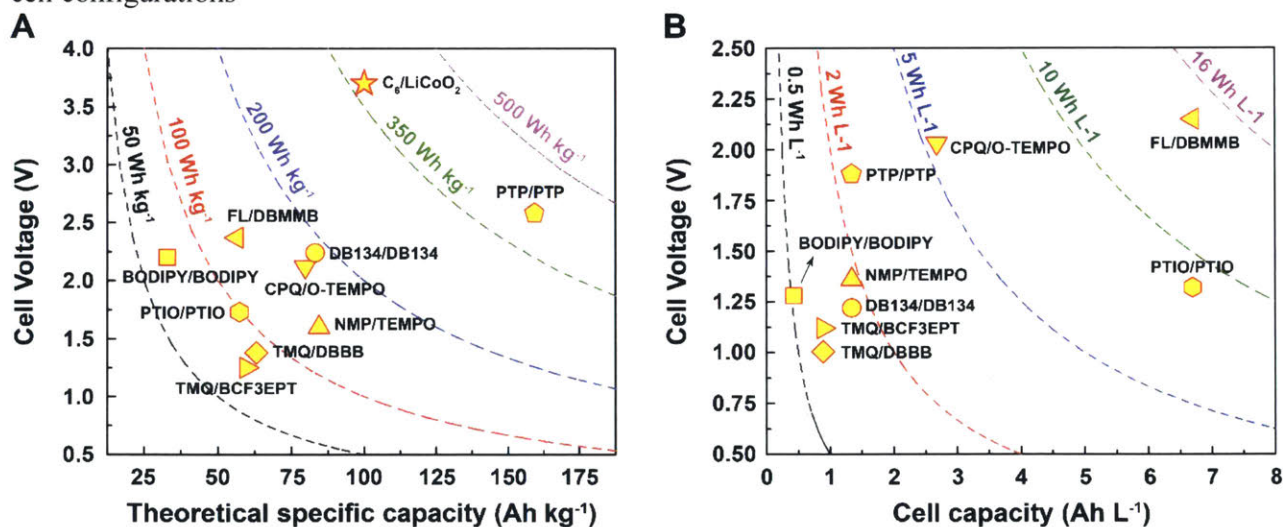
Figure 12: The theoretical capacity vs. the cell voltage for the NAqRFB chemistries shown in Figure 11. (a) The theoretical specific capacities are calculated based on the molecular weight of the active species, which provide the limiting capacity of the proposed chemistries. The cell voltages are calculated based on the experimentally determined half-wave potentials using cyclic voltammetry for each. The broken line for each color represents the relationship between capacity and voltage at the corresponding specific energy. (b) The cell capacities are calculated based on the active species concentration used in the corresponding reference. The cell voltages are the experimentally determined average cell discharge voltage. The broken line for each color represents the relationship between capacity and voltage at the corresponding energy density.

For high potential materials, many of the initial demonstrations employ active compounds that were originally designed as redox shuttles for overcharge protection in lithium-ion batteries (e.g., dialkoxybenzenes, phenothiazines, nitroxides)[117]. Although the desirable molecular properties differ for RFB applications, overcharge protection materials have proven performance and durability in relatively harsh electrochemical environments and thus are a reasonable starting point for RFBs. A few key examples are TEMPO[108], 4-Oxo-TEMPO (O-TEMPO)[110], 2,5-di-tert-butyl-1,4-bis(2-methoxyethoxy)benzene (DBBB)[109], 2,5-di-tertbutyl-1-methoxy-4-[2'-methoxyethoxy]benzene (DBMMB)[111], and 3,7-bis(trifluoromethyl)-N-ethylphenothiazine (BCF3EPT)[112].

For low potential materials, active compounds have been more difficult to identify due to the lack of research for other applications, leading to the exploration of new redox active organic molecules such as 2,3,6-trimethylquinoxaline (TMQ)[109,112], 9-fluorenone (FL)[111], and (1S)-(+)-camphoroquinone (CPQ)[110]. In two instances, symmetric organic NAqRFB prototypes utilized the same parent organic molecule as both the high and low potential active materials. These demonstration chemistries are 2-phenyl-4,4,5,5-tetramethylimidazoline-1-oxyl-3-oxide (PTIO)[113] and 1,4-bis(isopropylamino)anthraquinone (Disperse Blue 134, DB134)[114]. Such symmetric organic chemistries are especially attractive because the fully discharged cell contains the same molecule, in the same oxidation state, on both sides of the battery, unlike other symmetric flow batteries (e.g. all-vanadium) that access different redox states[114]. Discharging to a single parent species helps alleviate deleterious RFB cycling effects such as irreversible crossover and electrolyte imbalance[114,118]. Of the published set of symmetric demonstration chemistries, DB134 is particularly notable because this molecule has five accessible redox states and can engage in two electron transfer events on both the high and low potential sides of the battery[114]. In addition,

several studies have proposed other families of small redox active organic molecules, notably rubrene[95], cyanoazacarbons[119], biphenyl[120], and octafluoronaphthalene[120], for implementation in NAqRFBs, but, at the time of this review, none of these classes of molecules have been demonstrated in a prototype cell of any kind.

Recently, redox active organic macromolecules, such as polymers, have been investigated, beginning with an insoluble suspension of polythiophene (PTP) in a symmetric cell[115]. This concept not only illustrated polymers as active materials for flow batteries but also suggests that the organic species must not necessarily be soluble in the electrolyte. The first soluble organic redox active polymer (RAP) proposed for use in an RFB was poly(vinylbenzyl ethyl viologens) in 2014[121], and the first implementation of a full NAq cell based on soluble organic polymers arrived two years later in the form of poly(boron-dipyrromethane) (BODIPY) in a symmetric configuration[116]. Soluble RAPs show promise for enabling low-cost size exclusion separators, in place of more expensive charge-selective membranes, but currently suffer from high solution viscosities, which lead to additional pumping and reactor design challenges[121].

While these initial studies focus on proof-of-concept demonstrations of energy storage, the proposed redox chemistries are unlikely to supplant state-of-the-art AqRFBs, because the redox couples are generally between 1.5 and 2.5 V, on par with aqueous zinc–bromine and lead-acid systems, and therefore, do not leverage the full range of the electrochemical stability window enabled by NAq electrolytes. Additionally, while the possibility of high active species concentration is discussed in a few reports, most demonstration cells operate at concentrations from 0.02 to 0.5 M, which, in combination with the moderate voltage, leads to a relatively low cell energy density (0.5–15 Wh/L). Lastly, the reported cycle lifetimes are typically less than 100 cycles, often with noticeable capacity decay. With the exception of TEMPO, which has been

proven to be highly stable under certain electrolyte conditions[122,123], the lifetimes are about an order of magnitude too short.

Some of these challenges are exacerbated by limitations in prototype cell engineering, which hinder high concentration and high current density cycling of organic active materials. To date, the highest current densities and concentrations displayed were 20 mA/cm^2 and 0.5 M, respectively, by Duan et al.[113], which are both insufficient to compete with state-of-the-art AqRFBs[114]. Efforts have thus shifted toward tailoring redox active organic molecules to realize desired properties for NAqRFBs.

2.4.2   Molecular Engineering of Active Materials

Molecular engineering is the process of functionalizing a redox active moiety to obtain desired properties in line with performance and cost targets. The ideal redox active organic molecule would have a redox potential near the upper or lower edge of the electrolyte stability window, high solubility and long term stability through all states-of-charge in relevant electrolyte solutions, as well as a low molecular weight to maximize charge storage capacity and minimize chemical costs. Increasing active species solubility raises the maximum feasible active species concentration, which can decrease solvent costs, increase energy density, and lower kinetic and mass transfer resistances[28]. Additionally, decreasing molecular weight improves the active species gravimetric capacity, decreasing active species cost per unit charge stored. Further, highly stable active species can improve device lifetime, and extreme redox potentials can enable greater cell potentials, yielding higher energy and power densities. Optimizing these factors within the available design space of organic NAqRFBs could lead to a long lasting, energy dense, and low cost system[2]. Here

we review several initial molecular engineering campaigns with a focus on designing to one or more of the aforementioned traits.

As previously mentioned, redox shuttles for overcharge protection materials in lithium-ion batteries serve as a good starting point for new high-potential organic active materials because they exhibit many desirable electrochemical and physical properties, including high solubility, facile kinetics, good stability, and a high redox potential. DBBB has served as a platform for several design efforts involving substituted dialkoxybenzenes (Figure 13) because of its success as a redox shuttle and early demonstration in all-organic NAqRFBs[109]. Huang et al. targeted increased solubility and reduced molecular weight through the development of DBBB derivatives with an asymmetric structure[124]. Modification of the relative lengths of the ether chains led to a series of liquid-phase active materials. The asymmetry in the structures causes the molecule to have a larger overall dipole, which leads to a more polar molecule and therefore increases the solubility in polar solvents. In a parallel study, Huang and Su et al. targeted reduced stable structures through a subtractive engineering approach, which sought to remove or replace bulky functional groups on DBBB that did not contribute to charge storage[125]. As shown in Figure 13, without modifying the electrochemically active center (bold, red) of DBBB, the substitution of *t*-butyl groups by methyl groups and the shortening of the methoxyethyl groups significantly decrease the molecular weight and thereby improve the intrinsic capacity of the methoxybenzene-based redox active species[125]. The 2,5-dimethyl-1,4-dimethoxybenzene showed similar behavior to the parent DBBB compound. This indicates that the methyl groups were still sufficient to provide enough steric hindrance to protect the radical once the material is charged, and the shortened ether chain still provided enough electron delocalization to stabilize the radical cation.
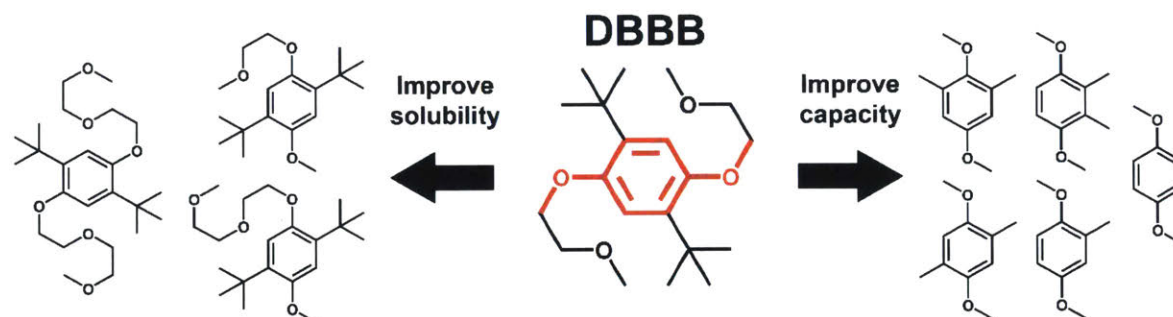
Figure 13: Modification to the core structure of DBBB for improved properties

Similarly, phenothiazine derivatives, also originally examined for overcharge protection[126,127], are now under investigation for NAqRFB applications with early efforts focused on increasing the redox potential through the addition of electron withdrawing groups. When electron withdrawing groups (e.g. a halide, a nitro-group, or a cyanide group) are added to a redox moiety, the valence electrons are more tightly bound to the core structure. Therefore, more energy is necessary to remove an electron, and the redox potential, which is related to the ionization energy, is increased. Kaur et al. targeted a higher redox potential by adding trifluoromethyl groups to phenothiazine, boosting the redox potential by 320 mV[112].

Turning toward the negative electrolyte, quinoxaline[109,128], pyridine[129], and anthraquinone[130] derivatives have been the most well-studied materials. Quinoxaline has been the focus of low potential compounds since its initial appearance in the TMQ/DBBB all-organic NAqRFB[109]. In this seminal study, structure-activity relationships were identified by investigating the effect of the number and position of the substituents (methyl groups and phenyl groups) on the benzene and pyrazine rings. To enable the high-throughput selection of a quinoxaline-based negative compound, Assary et al. calculated the reduction potential of 40 quinoxaline derivatives using quantum chemical methods[128]. Moreover, it has been recently discovered that Lewis acids such as BF₃, can promote the electrochemical activity of this category of compound by forming a

BF$_3$ — complex with the lone pair on nitrogen atoms[131,132]. This has shown to be a valuable tool in the development of other negative compounds for NAqRFBs[129].

Using pyridine as the starting material, Sevov et al. described an iterative workflow of molecular engineering for the development of low potential compounds[129]. The work first examined the decomposition pathways for pyridine derivatives and then modified the derivatives further to block degradation pathways selectively. The final product, N-methyl 4-acetylpyridinium tetrafluoroborate, shows high solubility (1.6 M in acetonitrile), low molecular weight (222 g/mol), two reversible electron transfer processes on the cyclic voltammetry timescale (in the presence of LiBF$_4$), and decent store stability (2 months) of both charged and discharged states. Of course, further characterization of this compound in battery cycling experiments is necessary to validate its promise as a negative compound in NAqRFBs.

Anthraquinone derivatives showed recent promise as a low potential compound in aqueous RFBs[86]. Modifications by Wang et al. have adapted the base anthraquinone molecule for NAq electrolytes by adding ether chains to increase solubility[130]. Two ether chains were added to the anthraquinone base molecule in the 1 and 5 positions. The flexible ether chains add to the overall polarity of the molecule and increase the disorder when the molecule dissolves. Both of these properties contribute to increasing the solubility in polar solvents.

The compounds discussed here represent just a few of the available starting materials for molecular engineering in the broad design space of organic redox active compounds. The same molecular engineering techniques and criteria can apply to other classes of organic compounds proposed for energy storage applications[133–136].

2.5 Conclusions and Future Directions

Electrochemical energy storage systems will play a pivotal role in the widespread integration of renewable, non-dispatchable energy sources and in the improvement of the energy efficiency of the electric power sector. RFBs are particularly attractive for these applications due to their favorable combination of performance, cost, and safety. However, present storage technologies are not yet cost-competitive, which drives research and development efforts toward new redox chemistries, electrolyte formulations, and cell designs. NAqRFBs utilizing redox active organic materials are a nascent but emerging storage concept with the potential for achieving the low costs needed for economic viability. In 2014, Darling et al. highlighted performance metrics required to realize a \$100/kWh NAqRFB, indicating that while such a battery was feasible, significant improvements are required over the current demonstrations[2]. These benchmarks present an opportunity for target-guided fundamental research of novel NAq redox chemistries including:

- Identifying electrochemical couples that, when paired together, enable a 3 V cell potential or higher. Multi-electron transfer couples would increase charge storage capacity and alleviate concentration requirements.

- Enhancing the stability of organic molecules, particularly the charged radicals, in NAq electrolytes to enable 1000s of cycles with minimal capacity fade. Electrolyte selection has already been shown to impact the stability of redox species and therefore contributes to a delicate balance between achieving required concentrations and reversibility[111,132].

- Increasing the solubility of organic molecules in NAq electrolytes at all states-of-charge. The high concentration regime, where solvent and solute molecules are of the same order

of magnitude, is relatively unexplored, and may require the development of new analytical methods to quantify solution structure and electrochemical performance.

Given the interconnected nature of these requirements, coupled with the multi-dimensional design space afforded by organic molecules, high throughput computational tools, in combination with targeted experimental work are a powerful strategy for driving discovery and development[129,137,138]. In concert with these molecular efforts, advances in the engineering science of NAqRFBs are needed:

- Tailoring rheological and electrochemical properties of redox electrolytes to minimize pumping costs and maximize charge transfer rates.

- Quantifying selectivity of porous electrode materials, particularly at potentials near the electrochemical stability window, to minimize electrolyte decomposition.

- Designing stable, selective, and conductive membranes to prevent species crossover.

- Constructing research prototypes, inspired by more mature electrochemical technologies (e.g., fuel cells), that enable high current densities and high active species concentrations.

- Predicting the chemical costs of newly developed organic molecules in a more rigorous fashion.

Opportunities exist for significant improvements through engineering of organic molecules for NAqRFBs. This multidisciplinary challenge requires expertise and collaboration across multiple fields including electrochemical science, molecular modeling and synthesis, reactor engineering, and techno-economic assessment. Together with an evolving regulatory environment, these R&D activities are expected to lead to the deployment of a range of new cost-effective flowable energy storage systems.

2.6 Thesis Outline

The overall goal of my thesis is to begin to develop and understand structure-function relationships for organic active materials for nonaqueous redox flow batteries using electrochemistry, spectroscopy, and flow cell testing. To this end, I have examined the electrochemical performance of multiple redox moieties and examined the impact of different functionalizations. This work started as single property modifications to small molecules, and once the material was stabilized; simultaneously multi-property optimization was examined. If a modified organic was determined to be unstable, it was used either to probe accepted stability techniques (e.g., bulk electrolysis) in order to standardize testing procedures or as a model decay compound to develop widely accessible, efficient testing protocols.

The second section of this thesis, Chapters 3 and 4, highlights some of my work on the dialkoxybenzene class of molecules. Even though these small organic molecules were not stable enough to perform an in depth multi-property functionalization study, they still provided general trends for molecular modifications and were able to be used as materials to validate decay techniques and standardize testing procedures. Using 2,5-di-tert-butyl-1,4-bis(2-methoxyethoxy)benzene (DBBB) as a starting material, subtractive engineering was first employed to determine which parts of the DBBB structure were necessary for its stability. By reducing the structure, the materials intrinsic capacity increases, and therefore the overall storage cost should decrease. Different reduced structures were examined by cyclic voltammetry and bulk electrolysis cycling, and it was found that reducing the length of the ether chains on DBBB and exchanging the *t*-butyl groups for methyl groups had a minimal impact on the stability but nearly doubled the intrinsic capacity. Using the reduced structure, the impact of halidization was examined. By adding electron withdrawing groups to the core structure, the redox potential

increases because it now takes more energy to remove an electron. A higher redox potential leads to larger cell voltages and therefore, a more energy dense system. The electrochemical performance of the halogenated compounds was again probed by cyclic voltammetry and bulk electrolysis. This molecular modification reduced the stability of the organic active materials by more than an order of magnitude.

The next section of this thesis, Chapters 5, 6, and 7, examines a more promising redox active core, N-ethylphenothiazine (EPT) and the multiple modifications that were made. Independently, we increased the solubility of all states of charge and stabilized the second electron transfer. First, a glycol chain was added to the ethyl group in order to increase the asymmetry and the polarity of the molecule. This functionalization, increased the solubility of the oxidized species by a factor of five without impacting the overall stability determined by low concentration cyclic voltammetry and bulk electrolysis. Because the material could be dissolved in electrolyte to high concentrations, symmetric cell cycling at 0.5 M was possible. Over the 100 cycle (80 h) experiment, negligible capacity fade was observed. In a parallel study, to increase the intrinsic capacity, methoxy groups were added *para-* to nitrogen, which stabilized the second electron transfer. The material cycled at low concentrations accessing both electron transfer events for 50 cycles (150 h) with minimal capacity fade. However, it was not soluble enough to test at high concentrations. Therefore, the methoxy groups were extended with glycol chains to further increase the solubility. This molecular modification allowed for greater than 1 M electron concertation in solution. Additionally, symmetric cell cycling was performed for 140 cycles (460 h) with minimal material decomposition.

Stability testing and techniques are examined in the next section, Chapters 8 and 9, in an effort to standardize testing procedures and develop widely applicable decay measurement

methods. It is clear that one of the major challenges of organic molecules is their stability, which is especially evident in nonaqueous systems because a radical is typically formed. Additionally, testing redox active organics for flow battery applications is relatively new, and therefore a standardized testing procedure does not currently exist. The cycling rate and accessed state of charge can be changed to impact the perceived stability (cycling number). Therefore, different bulk electrolysis conditions were examined for DBBB. The charging rate was varied from 0.125C to 1C, and two different states-of-charge were accessed (0 % - 100 % and 0 % - 50 %). It was determined that cycling time is a more consistent measure of the stability than cycle number. Additionally, a new technique using a microelectrode was developed to probe the stability of active materials. This technique uses the steady-state nature of microelectrodes to gain information about both the charged and discharged species simultaneously by taking cyclic voltammograms of a solution over time.

Finally, the last Chapter of this thesis, Chapter 10, discusses the major conclusions of my thesis work and provides an outlook for nonaqueous, organic active materials. In particular, molecular engineering of organic molecules is beginning to be used to alleviate some of the other challenges of organic flow batteries. In particular, oligomers are beginning to be examined to use nanoporous separators (e.g., polymers of intrinsic microporosity), which can significantly lower the system cost compared to using ion-exchange membranes. Lastly, there are some R&D efforts on electrolytes to couple an electrolyte to a given active material. By working on electrolytes and active materials simultaneously, flow battery operating conditions can be further optimized.

3 Subtractive Engineering of Dialkoxybenzenes

The development of new high capacity redox active materials is key to realizing the potential of nonaqueous redox flow batteries (RFBs). In this work, a series of substituted 1,4-dimethoxybenzene based redox active molecules have been developed via a subtractive design approach. Five molecules have been proposed and developed by removing or reducing the bulky substituent groups of DBBB (2,5-di-tert-butyl-1,4-bis(2-methoxyethoxy)benzene), a successful overcharge protection material for lithium-ion batteries. Of these derivatives, 2,3-dimethyl-1,4-dimethoxybenzene (23DDB) and 2,5-dimethyl-1,4-dimethoxybenzene (25DDB) are particularly promising as they demonstrate favorable electrochemical characteristics at gravimetric capacities (161 mA h/g) that approach the stability limit of chemically reversible dimethoxybenzene based structures. Diffusivity, solubility, and galvanostatic cycling results indicate that both 23DDB and 25DDB molecules have promise for nonaqueous RFBs. This chapter is partially reprinted from "A subtractive approach to molecular engineering of dimethoxybenzene-based redox materials for nonaqueous flow batteries" by Jinhua Huang, Liang Su, **Jeffrey A. Kowalski**, John L. Barton, Magali Ferrandon, Anthony K. Burrell, Fikile R. Brushett, and Lu Zhang from The Journal of Materials Chemistry A (2015, 3, 14971-14976).

3.1 Introduction

First proposed in the 1980s, small electroactive molecules have been employed as redox shuttles to improve lithium (Li)-ion cell safety, specifically overcharge protection. Through advances in molecular engineering and electrolyte formulation, a number of redox-active organic molecules have demonstrated stable performance for 100s of overcharge cycles with various Li-

ion cell chemistries. Many of the materials developed and knowledge gained in this field over the past 30 years can be directly leveraged to guide the design of high performance active materials for nonaqueous RFBs. However, differences in the material requirements between overcharge protection molecules in Li-ion batteries and redox compounds in nonaqueous RFBs lead to several new challenges. First, in flow batteries, the organic molecules serve as energy-bearing species requiring high charge carrier concentrations to enable high energy storage. Second, in flow batteries, the active species must be stable in their charged state for hours to days. In comparison, overcharge protection materials function as electrolyte additives and thus have lower solubility requirements. Also, they remain charged for the time period required to traverse the separator ($\sim$25–50 μm thickness) within an enclosed cell (generally, on the order of seconds).

Here, we aim to re-engineer a successful overcharge protection material, 2,5-di-tert-butyl-1,4-bis(2-methoxyethoxy)benzene (DBBB, Figure 14), for nonaqueous RFB applications[109,139]. In particular, we modify the substituent groups around the 1,4-alkoxybenzene redox center with the overarching goal of increasing molecular capacity and imparting other favorable properties (e.g., increased solubility). Based on DBBB, we have previously developed a series of room-temperature liquid redox active compounds by modifying the polyethylene oxide (PEO) side chains of the dimethoxy-di-tert-butyl-benzene based redox structure[111,124,140,141]. However, the storage capacities of these compounds are lower than desired ($\leq$100 mA h/g). In this contribution, we report on the electrochemical characterization of two promising dimethoxybenzene derivatives, 2,3-dimethyl-1,4-dimethoxybenzene (23DDB) and 2,5-dimethyl-1,4-dimethoxybenzene (25DDB), as high-potential redox active molecules for nonaqueous RFBs. As compared to DBBB, these compounds demonstrated increased gravimetric capacity and solubility without sacrificing

electrochemical performance. Furthermore, high gravimetric capacity may enable additive molecular design strategies to be employed to enhance stability.

DBBB   DB   MDB   26DDB   23DDB   25DBB
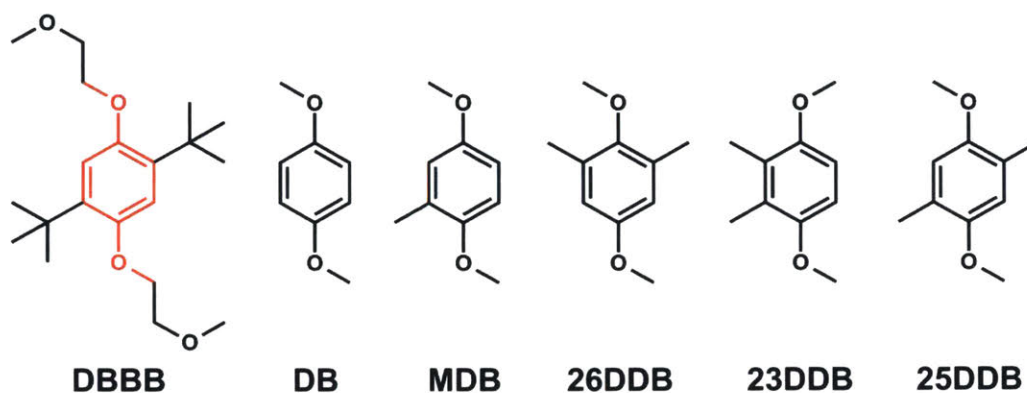
Figure 14: Molecular structures of 2,5-di-*tert*-butyl-1,4-bis(2-methoxyethoxy)benzene (DBBB), 1,4-dimethoxybenzene (DB), 2-methyl-1,4-dimethoxybenzene (MDB), 2,6-dimethyl-1,4-dimethoxybenzene (26DDB), 2,3-dimethyl-1,4-dimethoxybenzene (23DDB), and 2,5-dimethyl-1,4-dimethoxybenzene (25DBB).

Motivated by the favorable electrochemical properties but low gravimetric capacity of DBBB (79 mA h/g), we seek to develop higher capacity derivatives of DBBB by removing or minimizing substituent groups. The remarkable performance and durability of DBBB stems from its elegant chemical structure and can be attributed to: (1) the aromaticity of the dimethoxybenzene platform (Hückel's rule) which helps stabilize the radical cation[117]; (2) the bulky *tert*-butyl groups that provide both electron donating and steric protection effects to further stabilize the radical cation[142]; (3) the symmetry of the di-*tert*-butyl-dimethoxybenzene redox core[139,143]. To reduce the molecular weight without sacrificing electrochemical performance, two modifications are contemplated. First, given that the two *tert*-butyl groups contribute ~34% of DBBB's molecular mass, replacing these bulky groups will lead to the immediate reduction in molecular weight. As the smallest electron donating group that still provides some measure of steric protection, methyl groups appear to be a good choice. Second, the long ether chains on the DBBB molecule facilitate solubilization into polar solvents but are bulky (37% of the molecular weight) and do not influence the electrochemical performance. However, with the removal of the non-polar *tert*-butyl groups,

these ether chains may not be necessary for acceptable solubility. Thus, based on these design considerations, a family of dimethoxybenzene derived molecules including 2-methyl-1,4-dimethoxybenzene (MDB), 23DDB, 25DDB, and 2,6-dimethyl-1,4-dimethoxybenzene (26DDB), has been proposed. As 1,4-dimethoxybenzene (DB) is known to undergo irreversible electro-oxidation[144], methyl groups were gradually introduced onto the benzene ring to provide additional stabilization effects in order to construct electrochemical reversible systems.

3.2 Experimental

DB (99%), MDB (99%), and ferrocene (98%) were purchased from Aldrich without further purification. DBBB (99.9%, battery grade) was provided by the Materials Engineering Research Facility at Argonne National Laboratory. 23DDB, 25DDB, and 26DDB were synthesized based on the following procedures. 23DDB synthesis: NaH (880 mg, 60% dispersion in oil, 0.022 mol, Sigma-Aldrich) was added in small portions to a solution of 2,3-dimethylhydroquinone (1.36 g, 0.010 mol, 97%, Ark Pharm or Sigma-Aldrich) in anhydrous DMF (25 mL) under a nitrogen atmosphere. After the gas evolution had ceased, the resulting mixture was stirred at room temperature for 30 min. Iodomethane (2.49 mL, 0.040 mol, 99.5%, Sigma Aldrich) was added dropwise, and the reaction mixture was stirred at 40 °C for 2 h. Saturated NaCl solution was added slowly to quench the reaction, and the resulting mixture was extracted with EtOAc. The combined organic layers were washed with water and dried over Na_2SO_4. After the solvent removal in vacuo, the residue was purified by flash column chromatography (silica gel, eluted with ethyl acetate/hexanes = 1/15) to yield 23DDB (1.58 g, 95%) as a white solid. ^1H NMR (500 MHz, CDCl3) δ 6.67 (s, 2H), 3.78 (s, 6H), 2.17 (s, 6H); ^{13}C NMR (125 MHz, CDCl3) δ 151.9, 126.7, 107.9, 56.1, 12.0.

25DDB synthesis: NaBH$_4$ (1.13 g, 0.030 mol, 98+%, Acros Organics) was added in small portions to a solution of 2,5-dimethyl-1,4-benzoquinone (2.04 g, 0.015 mol, 99%, SigmaAldrich) in the mixture of ethanol (15 mL) and water (15 mL) under a nitrogen atmosphere. The reaction was stirred at room temperature for 30 min. A solution of KOH (6 mL, 10 M, 0.060 mol) was added, and the resulting mixture was stirred for another 30 min. Then it was heated to reflux, and dimethyl sulfate (5.70 mL, 0.060 mol, ≥ 99.8%, Sigma-Aldrich) was added drop wise. The resulting mixture was stirred at reflux for 12 h before it was cooled to room temperature and extracted with EtOAc. The combined organic layers were washed with water and dried over Na$_2$SO$_4$. After concentration in vacuo, the residue was purified by flash column chromatography (silica gel, eluted with ethyl acetate/hexanes=1/10) to provide 25DDB (2.11 g, 85%) as a white solid. ^{1}H NMR (500 MHz, CDCl3) δ 6.68 (s, 2H), 3.80 (s, 6H), 2.23 (s, 6H); ^{13}C NMR (125 MHz, CDCl3) δ 151.4, 124.3, 113.7, 56.1, 16.1.

26DDB synthesis: NaBH$_4$ (378 mg, 0.010 mol) was added in small portions to a solution of 2,6-dimethylbenzoquinone (0.68g, 0.005 mol, 99%, Sigma-Aldrich) in ethanol (5 mL) and water (5 mL) under a nitrogen atmosphere. The reaction was stirred at room temperature for 30 min. A solution of KOH (2 mL, 10 M, 0.020 mol) was added, and the resulting mixture was stirred for another 30 min. Then it was heated to reflux, and dimethyl sulfate (1.89 mL, 0.020 mol) was added drop wise. The resulting mixture was stirred at reflux for 12 h before it was cooled to room temperature and extracted with EtOAc. The combined organic layers were washed with water and dried over Na$_2$SO$_4$. After concentration in vacuo, the residue was purified by flash column chromatography (silica gel, eluted with ethyl acetate/hexanes=1/15) to provide 26DDB (0.73 g, 88%) as a colorless liquid. ^{1}H NMR (500 MHz, CDCl3) δ 6.55 (s, 2H), 3.75 (s, 6H), 3.68 (s, 3H), 2.27 (s, 3H); ^{13}C NMR (125 MHz, CDCl3) δ 155.3, 150.8, 131.7, 113.7, 59.9, 55.4, 16.3.

All electrochemical experiments were performed in an argon-filled glovebox (MBraun Labmaster) at 25 °C. All electrochemical data were collected on a VMP3 potentiostat/galvanostat (Bio-Logic). All potential values were referenced to Li/Li$^+$. Two different electrode combinations were used in this report. The electrochemical cell consisting of a 3 mm diameter glassy carbon (GC) working electrode (CH Instruments, Inc.), a gold coil counter electrode (CH Instruments, Inc.), and a lithium metal (Alfa Aesar) reference electrode was used for collecting the data displayed for MBD and 26DDB. For all other CV experiments, the electrochemical cell consisted of a 3 mm diameter glassy carbon working electrode (CH Instruments, Inc.), a lithium metal (Alfa Aesar) counter electrode, and a lithium metal reference electrode in a Vycor® fritted glass tube containing 0.5 M bis(trifluoromethane)sulfonimide lithium salt (LiTFSI, 99.95%, BASF) / propylene carbonate (PC, anhydrous, 99.7%, Sigma-Aldrich). All electrolyte solutions were dried for several days with 3 Å molecular sieves (Sigma-Aldrich). The measured water content in the electrolytes was less than 10 ppm. The glassy carbon electrode was consecutively polished on a MicroClothTM pad with 1 µm and 0.05 µm alumina powders (Buehler), and thoroughly rinsed with deionized water after being polished with each powder. The electrode was then sonicated for 1 min in deionized water (EMD Millipore) and dried under argon before moving into the glovebox. Cell resistances were measured prior to electrochemical experiments and were ca. 250 Ω for all electrolyte solutions. As peak currents range from 0.01 to 0.1 mA depending on scan rate, additional iR contributions of ca. 2.5 to 25 mV were automatically corrected for all CV measurements using the potentiostat software.

Diffusion coefficients of the neutral and charged species were estimated by applying the Randles-Sevcik equation for reversible systems to the baseline corrected peak currents of the anodic and cathodic sweeps of the cyclic voltammograms, respectively:

$$\left| i_p \right| = 0.4463 nFAC \left(\frac{nFD}{RT} v \right)^{1/2} \qquad (1)$$

where i_p is the baseline-corrected peak current of the anodic sweep (neutral to charged) or cathodic sweep (charged to neutral) of the cyclic voltammogram (A), n is the number of electrons transferred, F is the Faraday constant (96,485 C/mol), A is the electrode area (cm^2), D is the diffusion coefficient of neutral species (D_{red}) or the oxidized species (D_{ox}) (cm^2/s), v is the scan rate (V/s), C is the concentration of the neutral or the oxidized redox active compound (mol/cm^3), R is the universal gas constant (8.314 J/mol/K), and T is the temperature (K). It is important to note that the peak currents are not measured using the x-axis as a baseline. Rather, a background current baseline must first be extrapolated out to the peak potential. Then, the peak current is measured (vertically) from the peak down to the extrapolated baseline. Accordingly, the baseline corrections of the original data were performed in MATLAB®. Galvanostatic cycling of different compounds was studied in 0.5 M LiTFSI in PC using a three-electrode bulk electrolysis cell (BASi) with a high surface area reticulated vitreous carbon (RVC) working electrode, a lithium metal counter electrode in a ceramic fritted chamber with 2 mL electrolyte, and a lithium metal reference electrode in a Vycor® fritted glass tube with 0.2 mL electrolyte. The cell resistance is ca. 10 Ω as measured by the current interrupt technique. The concentration of the redox active compound was 0.001 M and the total volume in the working electrolyte chamber was 30 mL. Stirring at 900 rpm in the working electrolyte chamber was maintained throughout cycling experiments. The charge / discharge current was 0.402 mA corresponding to a 0.5 C rate (full charge or discharge in 2 h). For 23DDB, the charge and discharge time was set for 1 h (50% state of charge) and the high cut-off voltage (charging) was set at 4.15 V and the low cut-off voltage (discharging) was set at 3.85 V, whichever was reached first. For 25DDB and DBBB, the charge

and discharge time was set at 1 h (50% state of charge) and the high cut-off voltage (charging) was set at 4.10 V and the low cut-off voltage (discharging) was set at 3.80 V, whichever was reached first. The cut-off voltages were selected according to the corresponding cyclic voltammogram with ca. 0.15 V overpotential based on the average potential of the oxidation and the reduction peak (E^0) where for 23DDB, $E^0 \approx 4.00$ V, and for DBBB and 25DDB, $E^0 \approx 3.95$ V.

The solubility was investigated using a Dynamic Light Scattering Analyzer equipped with an optical camera and a temperature controller (0 to 70°C, DynaPro Plate Reader II, Wyatt Technologies Co.) also located in a nitrogen-filled glovebox. The assessment was performed using the produced images of each well as a function of temperature starting from 55°C down to 0°C in 2.5°C increments.

3.3   Cyclic Voltammetry

While all of the derivative molecules are significantly smaller than DBBB (>50% lower molecular weight) and of similar molecular structure, their electrochemical performances are quite different. As the smallest molecule in this study, MDB displayed poor chemical reversibility, likely due to the insufficient stabilization effect of the single methyl group (Figure 15a). For the dual methyl substituted compounds, the electrochemical behavior is strongly associated with the methyl group locations on the benzene ring. For example, regardless of the presence of two methyl groups on the benzene ring, 26DDB still exhibits an irreversible behavior based on the cyclic voltammetry results (Figure 15b).
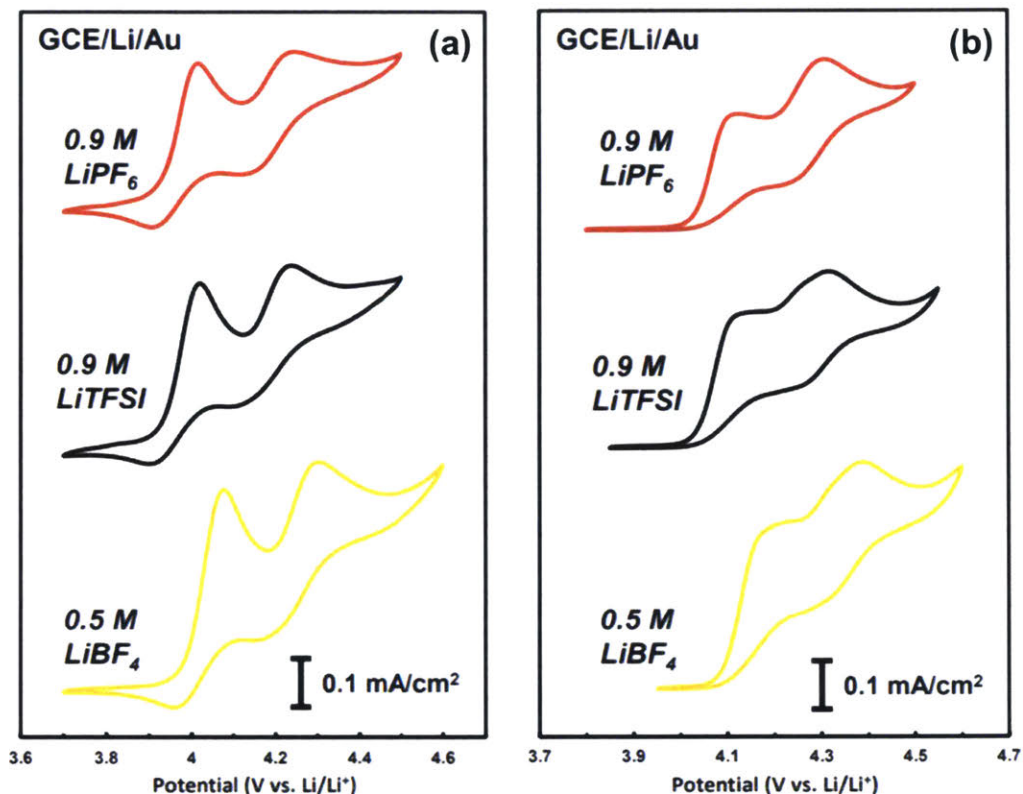
Figure 15: (a) Cyclic voltammograms of (a) MDB (0.010 M) and (b) 26DDB in PC containing different lithium salts. The working, reference, and counter electrodes are glassy carbon electrode, unfritted lithium metal, and gold coil, respectively. The scan rate is 5 mV/s.

When the two methyl groups were introduced on 2,3- or 2,5-positions, the cyclic voltammograms of the 23DDB and 25DDB molecules show well defined symmetric reduction and oxidation features comparable to DBBB (Figure 16). Furthermore, the location of the methyl groups appears to have a minor impact on the redox potential as the redox potential of 25DDB is similar to that of DBBB, a slight, positive shift was observed for 23DDB. Cyclic voltammetry results indicate that the modifications on the bulky moieties of DBBB, such as removing ether chains and replacing the *tert*-butyl groups with methyl groups, do present a possible pathway to construct chemically reversible molecules with reduced molecular weight but comparable electrochemical response. The gravimetric capacity of 23DDB and 25DDB (161 mA h/g) is more than twice that of DBBB (79 mA h/g) due to the

103

decreased molecular weight (166 g/mol *vs.* 338 g/mol). These materials appear to approach the minimal substitution requirements necessary to stabilize 1,4-dimethoxybenzene based structures and thus represent the upper capacity limit for this family of single electron transfer molecules.
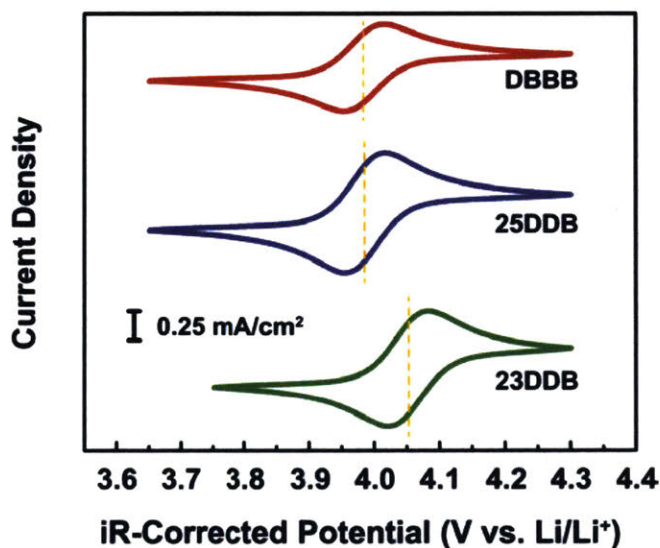
Figure 16: Cyclic voltammograms of 2,5-di-*tert*-butyl-1,4-bis(2-methoxyethoxy)benzene (DBBB), 2,5-dimethyl-1,4-dimethoxybenzene (25DDB), 2,3-dimethyl-1,4-dimethoxybenzene (23DBB). All electrolytes consisted of 0.010 M active species in 0.5 M LiTFSI in PC. The working, reference, and counter electrodes are glassy carbon electrode, fritted lithium metal, and unfritted lithium metal, respectively. The scan rate is 20 mV/s.

Quantitative analysis of cyclic voltammograms over a range of scan rates are used to determine electrochemical and mass transfer parameters for DBBB, 23DDB, and 25DDB. The cyclic voltammograms and corresponding Randles–Sevick plots are shown in Figure 17. The results of these analyses are summarized in Table 8. For comparison, the characteristics of ferrocene, a well-studied standard reference compound for nonaqueous systems[106], are reported in the same electrolyte. As described above, the half-wave potentials ($E_{1/2} = (E_{pa} + E_{pc})/2$, also known as the redox potential) for DBBB and 25DDB are practically identical whereas 23DDB is about 50 mV more positive. All molecules demonstrated similar redox reversibility with peak separations ($\Delta E = E_{pa} - E_{pc}$) near the theoretical 0.059 V (at 25 °C) associated with a Nernstian, one-electron transfer couple. The peak separation for all four compounds showed a slight dependence on scan

104

rate (from 5 to 100 mV/s). The diffusion coefficients of DBBB, 23DDB, and 25DDB are estimated as 1.24×10^{-6}, 2.24×10^{-6}, 2.43×10^{-6} cm^2/s, respectively. The diffusion coefficients of 23DDB and 25DDB are roughly twice that of DBBB, as predicted by the Stokes–Einstein relationship[145], highlighting an advantage of smaller redox active compounds. Chemical reversibility is determined by studying the cathodic discharge/anodic charge (Q_{red}/Q_{ox}) ratios. All three compounds show minor non-idealities in chemical reversibility given the time scale of a CV experiment, but no scan rate dependence was observed. While the primary source of this deviation is likely the instability of the oxidized radical ions, irreversible electrolyte oxidation, especially at high electrode potentials, may also contribute to the charge imbalance. By comparison, ferrocene showed near complete charge retention (0.999 ± 0.001) though it is important to note this occurs at a lower voltage well within the electrolyte stability window.

Table 8: A summary of electrochemical properties obtained from cyclic voltammetry of DBBB, 25DDB, 23DDB, and ferrocene. The experimental conditions are identical as those in Figure 16. $E_{1/2}$ is the half-wave potential. $E_{pa} - E_{pc}$ is the peak separation. D_{red} and D_{ox} are diffusion coefficients of the reduced and oxidized species, respectively. Q_{red}/Q_{ox} is the charge ratio of the reduction process to the oxidation process. All experiments were performed in triplicate

	$E_{1/2}$ (V vs. Li/Li$^+$)	$E_{pa} - E_{pc}$ (V)	D_{red} ($\times 10^{-6}$ cm^2/s)	D_{ox} ($\times 10^{-6}$ cm^2/s)	Q_{red}/Q_{ox}
DBBB	3.985 ± 0.001	0.062 ± 0.001	1.241 ± 0.040	1.202 ± 0.037	0.977 ± 0.007
25DDB	3.983 ± 0.001	0.061 ± 0.001	2.427 ± 0.170	2.385 ± 0.170	0.975 ± 0.008
23DDB	4.039 ± 0.007	0.062 ± 0.001	2.243 ± 0.033	2.156 ± 0.005	0.964 ± 0.014
Ferrocene	3.299 ± 0.001	0.060 ± 0.001	2.283 ± 0.030	2.291 ± 0.029	0.999 ± 0.001
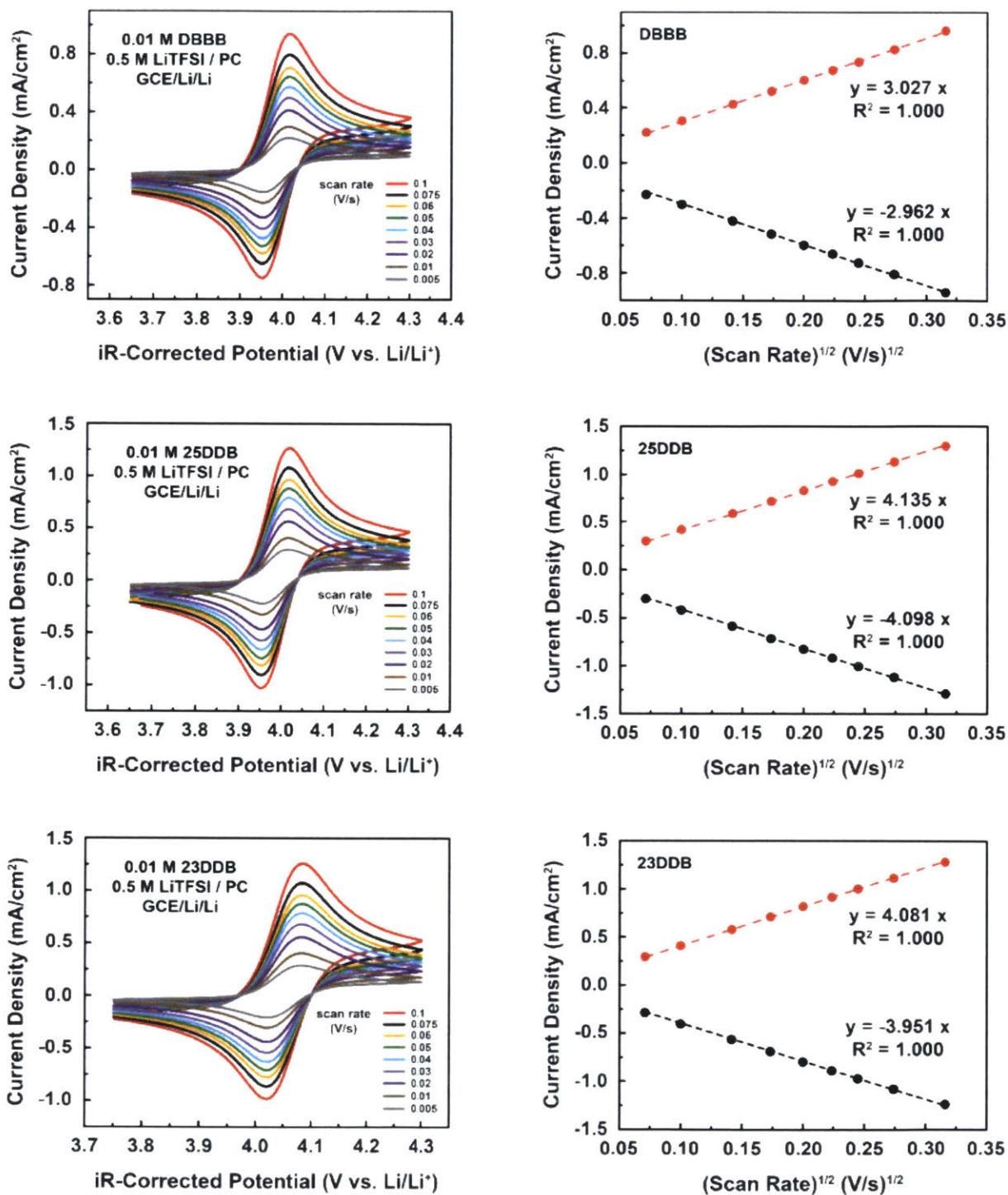
Figure 17: Cyclic voltammograms and the corresponding Randles – Sevcik plot of DBBB, 25DDB, and 23DDB. All electrolytes consist of 0.010 M active species in 0.5 M LiTFSI in PC. The working, reference, and counter electrodes are glassy carbon electrode, fritted lithium metal, and unfritted lithium metal, respectively.

106

In addition to increased gravimetric capacity and diffusivity, 23DDB and 25DDB demonstrate higher solubility than DBBB. The room temperature solubility of DBBB in 0.5 M LiTFSI in PC is ca. 0.3 M[137], while in the same electrolyte the solubility of 23DDB and 25DDB are 2.0 M and 0.6 M, respectively. As discussed earlier, this enhanced solubility can be partially attributed to the absence of bulky non-polar *tert*-butyl groups. However, the dramatic increase in 23DDB's solubility may be due to its asymmetric structure which increases the intramolecular dipole moments resulting in greater intermolecular interactions between the active species and the polar solvent (PC). We note that the solubility of the redox molecules in their charged state is equally important for successful flow battery operation. Detailed quantification of solubility as a function of state-of-charge and various electrolyte solutions will be the subject of future work.

3.4 Bulk Electrolysis

Building on the CV results, 23DDB, 25DDB, and DBBB are further evaluated by galvanostatically cycling in a bulk electrolysis cell which enables characterization of redox species' stability over multiple charge and discharge cycles. An electrolyte comprised on 0.001 M active species in 0.5 M LiTFSI in PC was cycled at a charge/discharge current of 0.402 mA (0.5 C rate) between 0 and 50% SOC for 100 cycles. Note that the theoretical capacity of DBBB, 23DDB, and 25DDB are 79.2 mA h/g, 161.4 mA h/g and 161.4 mA h/g, thus 50% SOC for each are 39.6 mA h/g, 80.7 mA h/g, and 80.7 mA h/g (Figure 18). The upper and lower cut-off voltages were set at ca. 150 mV above and below the redox potential established by cyclic voltammetry. Representative voltage profiles for all three compounds for the first 10 cycles and the last 10 cycles are shown in Figure 19. Due to the low currents and high stirring rate, iR contributions were minimal leading to high voltage efficiencies (~99%) for all three compounds. In the first 10 cycles,

the charge/discharge behavior of all compounds is similar although the voltage profiles of 23DDB start to evolve (steeper slopes) from the 8th cycle. All compounds reach the 50% SOC before the upper cut-off voltages. For the last 10 cycles, the voltage profiles have significantly changed with all compounds reaching the upper and lower cut-off voltages. Furthermore, while the behavior of DBBB and 25DDB are similar, significant resistance (ca. 0.1 V) appeared in 23DDB voltage profiles resulting in shortened charge/discharge curves (Figure 19f).
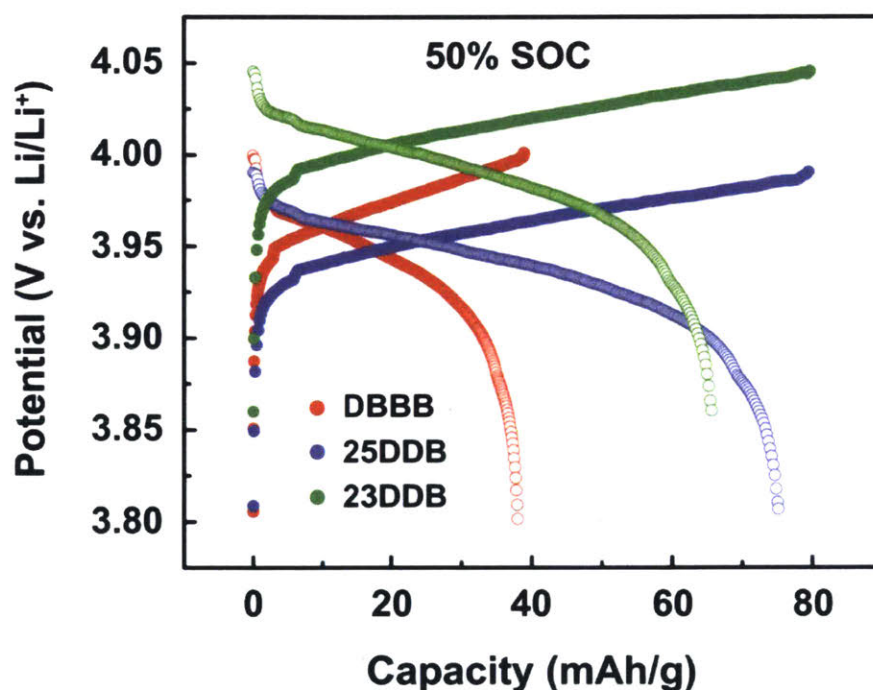
Figure 18: Representative charge (solid circle)/discharge (open circle) cycles of DBBB (red), 25DDB (blue), and 23DDB (green) at 0.5 C from 0 to 50% state of charge in a bulk electrolysis cell. All electrolytes consisted of 0.001 M active species in 0.5 M LiTFSI in PC and a total solution volume of 30 mL.
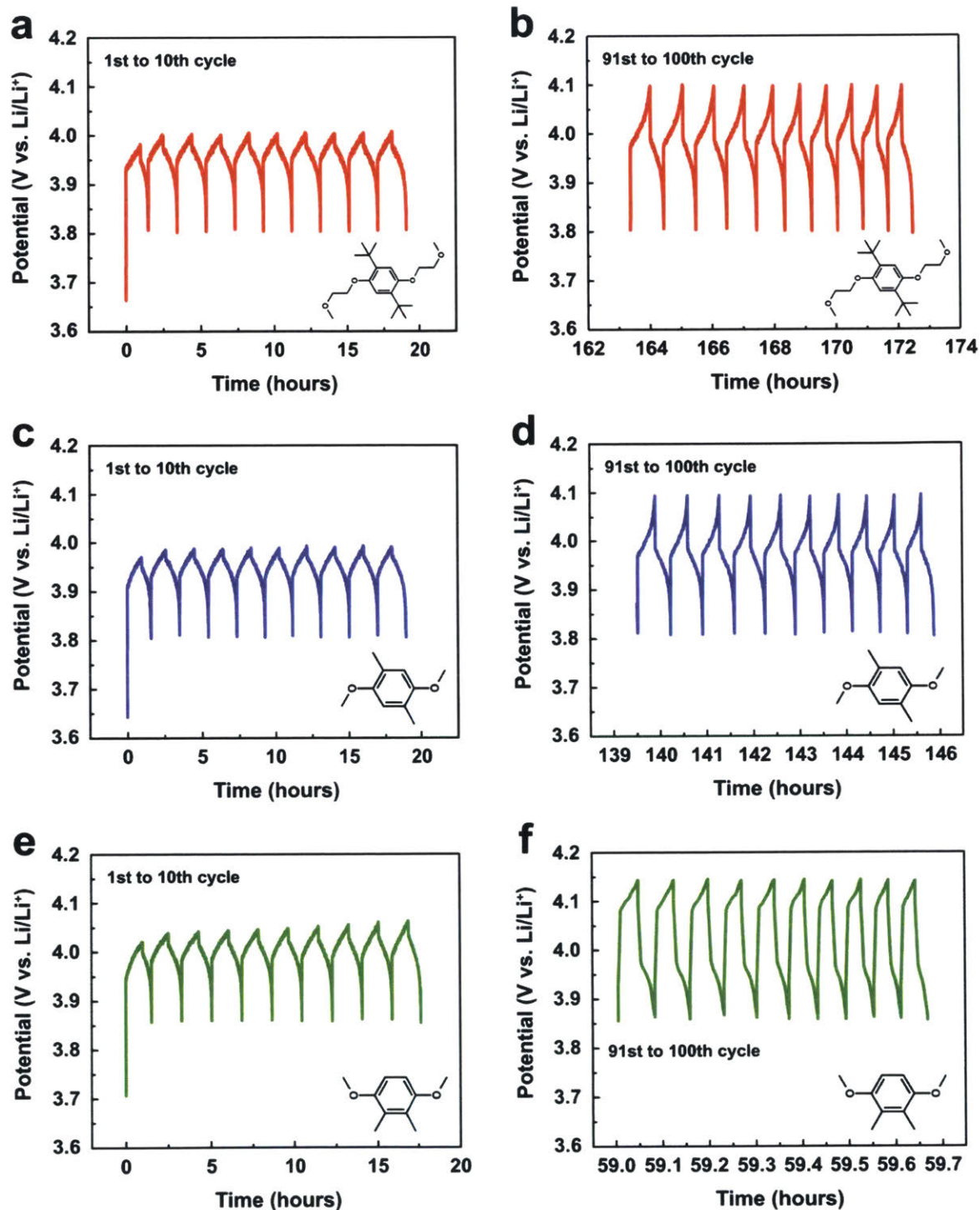
Figure 19: Cycling profiles of DBBB (red), 25DDB (blue), and 23DDB (green) at 0.5 C from 0–50% state of charge for 1st to 10th cycle (a, c, e) and 91st to 100th cycle (b, d, f) in a bulk electrolysis cell. All electrolytes consisted of 0.001 M active species in 0.5 M LiTFSI in PC and a total solution volume of 30 mL.

The charge/discharge capacities and the corresponding coulombic efficiency plots for DBBB, 23DDB, and 25DDB are shown in Figure 20a and b, respectively. Figure 20a shows the charge and discharge capacity of each compound over 100 cycles. The capacity decay from the theoretical 50% SOC over time reflects the degradation of radical intermediates. Specifically, under these experimental conditions, 50% DBBB was converted to non-rechargeable species after 75 ± 4 cycles whereas it took 48 ± 4 and 15 ± 1 cycles to irreversibly consume 50% 25DDB and 23DBB, respectively. DBBB shows the best capacity retention, which can be explained by the finely-tuned molecular structure (discussed above). Compared to DBBB, the 25DDB does not show as stable performance but still outperforms its asymmetric isomer 23DDB. This observation is consistent with previous studies, which showed the symmetric molecular structures tend to exhibit higher electrochemical stability as compared to their asymmetric counterparts[109,139,143]. The less stable performance of 23DDB is consistent with the abnormal voltage profiles observed in Figure 19f, and it is believed that the significant resistance is related to the decomposition of 23DDB during cycling. However, a more rigorous evaluation of the stability of 23DDB is required for conclusive assessments. Detailed studies of the stability of a series of substituted alkoxybenzene-based redox active compounds and the corresponding degradation pathways via coupled electrochemical and electron paramagnetic resonance (EPR) methods is on-going and will be reported in due course.
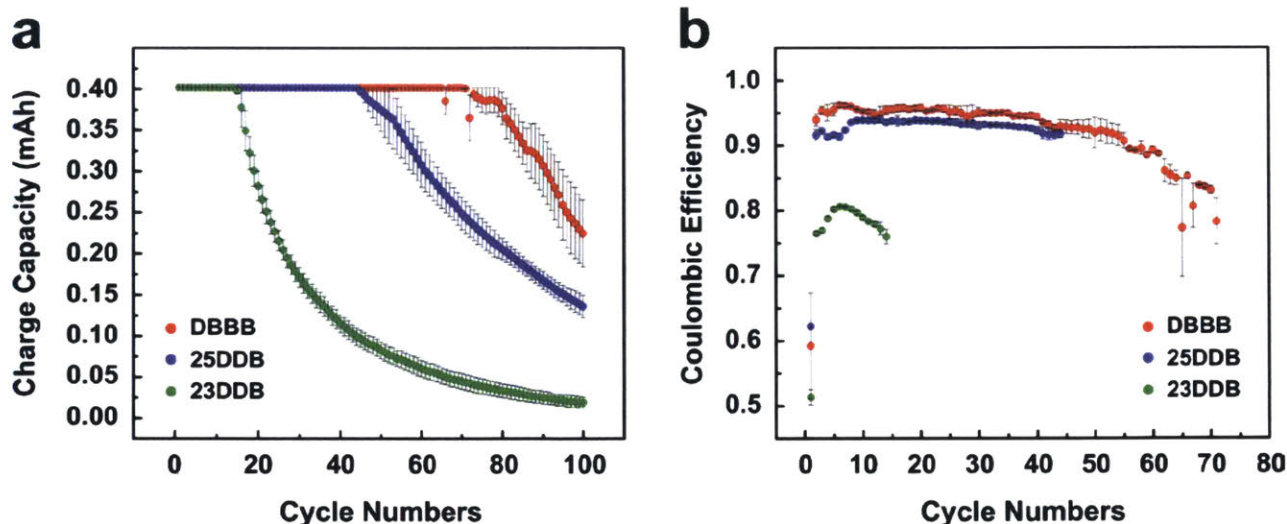
Figure 20: (a) Charge capacity profiles for DBBB (red), 25DDB (blue), and 23DDB (green) with respect to the cycle number based on the data from Figure 19. (b) Coulombic efficiencies of the plateaued region on the corresponding capacity profile. Data shown represents the average of two independent experiments for each compound.

Figure 20b shows the coulombic efficiencies (CE) of DBBB, 23DDB and 25DDB prior to the start of charge capacity decay. Note that the first cycle efficiency of all three compounds is significantly lower than subsequent cycles. This is likely due to the initial interfacial reactions that are typical to thermodynamically unstable systems and are comparable to the solid-electrolyte interphase (SEI) formation in Li-ion batteries [58,124]. Note that the frit separating the lithium metal counter electrode chamber and the working electrode chamber is not ion-selective thus some species crossover is expected. However, this is expected to have a similar impact on all of the compounds tested. After the first cycle, the average CEs of DBBB and 25DDB are >90% with DBBB being slightly higher, whereas the 23DDB is significantly lower at ca. 75–80%. These observations are in line with the capacity retention curves as well as with the CV data shown in Table 8.

3.5   Conclusions

In summary, we report on the development and electrochemical performance of a series of substituted 1,4-dimethoxybenzene derivatives. In particular, our goal was to improve the gravimetric capacities of the redox active molecules without sacrificing performance while imparting other favorable properties. Two promising derivatives, 25DDB and 23DDB, have been developed by reducing the substituent groups of DBBB, such as the *tert*-butyl groups and ether chains. As a result both molecules not only demonstrated desirable electrochemical and physical characteristics, but achieve these at about half the molecular weight of the parent compound, resulting in a marked enhancement in gravimetric capacity (161 mA h/g). Further, given the small size of these molecules, additive strategies may be employed to enhance the long-term cycle stability while maintaining high capacities. Consequently, both 23DDB and 25DDB are promising materials for nonaqueous RFBs. Future studies will focus on translating these tailored molecules into high concentration redox electrolytes and evaluating the performance and durability of nonaqueous flow cells based on these chemistries.

4 Halidization of Dialkoxybenzenes

Functionalized organic molecules are emerging as charge storage materials in electrochemical technologies as the breadth and diversity of the organic design space offers the possibility of purpose-built materials with property sets optimized for a particular application. First developed as overcharge protection materials in lithium-ion batteries, substituted dialkoxybenzenes represent a potentially promising molecular platform for advancing soluble charge storage materials. Here, we systematically substitute a series of halide groups at the 2- and 5-positions of the 1,4-dimethoxybenzene core, investigate the impact the halide groups have on molecular properties using electrochemical and spectroscopy methods, and compare these results to those of 2,5-dimethyl-1,4-dimethoxybenzene (25DDB), a previously reported derivative. In general, we observe that introduction of heavy halogen atoms leads to decreased gravimetric capacity as compared to 25DDB, but concomitantly improves solubility and redox potentials. As the halide functional group increases in size, the active material becomes less stable in its oxidized state as evinced by both cyclic voltammetry and bulk electrolysis cycling. None of the halogenated species are as stable as 25DDB indicating that these materials may be better suited for applications with more rapid cycling conditions (e.g., redox shuttling). More broadly, these results may serve as a useful data set for computational methods for materials discovery and optimization. This chapter is partially reprinted from "An investigation on the impact of halidization on substituted dimethoxybenzenes" by **Jeffrey A. Kowalski**, Thomas J. Carney, Jinhua Huang, Lu Zhang, and Fikile R. Brushett, which has been submitted to Electrochimica Acta.

4.1   Introduction

While a number of molecular families have been examined including nitroxides[122,123,146],

phenothiazines[147–152], cyclopropeniums[153–155], and isonicotinates[129,156], substituted

dialkoxybenzenes are amongst the most well studied for electrochemical

applications[109,111,124,125,139,157–161]. One particular dialkoxybenzene, 2,5-di-*tert*-butyl-1,4-bis(2-

methoxyethoxy)benzene (DBBB), has been used and modified for several different applications

including overcharge protection for lithium-ion batteries[139] and a redox active molecule for flow

batteries[109]. Originally designed for overcharge protection due to its high redox potential and

stability in nonaqueous electrochemical environments, DBBB has provided a promising platform

for molecular engineering. To this end, efforts have been made to increase the solubility and to

decrease the overall molecular weight. Huang *et al.* adjusted the length and symmetry of the ether

chains on the 1- and 4-positions depressing the melting temperature such that several derivatives

were liquid a room temperature, drastically increasing the solubility/miscibility in common

nonaqueous electrolytes[124]. More recently, Huang *et al.* sought to identify a stable minimal

structure, using DBBB as a starting materials, to increase atom economy and potentially reduce

the active material cost by decreasing the number of synthesis steps[125]. That work lead to the

development of 2,5-dimethyl-1,4-dimethoxybenzene (25DDB) where the *tert*-butyl groups, which

provide steric protection for radical cation formed during oxidation, were replaced to methyl

groups and the polyethylene glycol chains, which enable solubilization in polar electrolytes, were

shortened to a single methoxy group. 25DDB showed similar stability and solubility to DBBB

while doubling the gravimetric capacity.

Here, we seek to increase the redox potential of 25DDB to approach the upper stability

limit of nonaqueous electrolytes, thus maximizing the available electrochemical window.

114

Specifically, we substitute a series of halide groups (fluorine, chlorine, bromine, and iodine) onto the 25DDB structure on the 2- and 5-positions, in place of the methyl groups, and evaluate the effect on the physical and electrochemical properties of the molecule. Figure 21 shows the five molecules examined in this study: 25DDB, 2,5-difluoro-1,4-dimethoxybenzene (25FDB), 2,5-dichloro-1,4-dimethoxybenzene (25ClDB), 2,5-dibromo-1,4-dimethoxybenzene (25BrDB), and 2,5-diiodo-1,4-dimethoxybenzene (25IDB). While this work focuses on adjusting a single property (i.e., redox potential) with a goal of developing structure-property correlations for halides as functional groups on dialkoxybenzenes that may ultimately serve as inputs for future computational discovery tools[156], it also highlights some of the challenges in tuning specific property of a redox molecule without adversely impacting other properties.
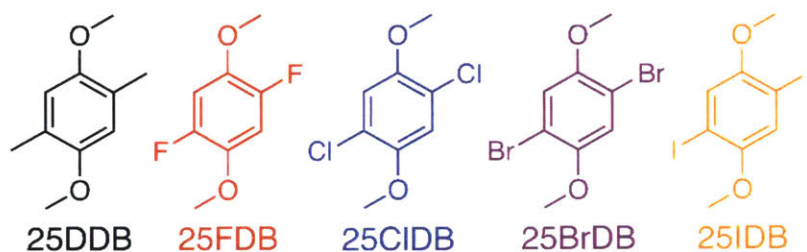
Figure 21: Chemical structures of 2,5-dimethyl-1,4-dimethoxybenzene (25DDB, black), 2,5-difluoro-1,4-dimethoxybenzene (25FDB, red), 2,5-dichloro-1,4-dimethoxybenzene (25ClDB, blue), 2,5-dibromo-1,4-dimethoxybenzene (25BrDB, purple), and 2,5-diiodo-1,4-dimethoxybenzene (25IDB, orange).

4.2 Experimental

Materials and Synthesis. Propylene carbonate (PC, anhydrous, 99.7%), ethylene carbonate (EC, anhydrous, 99%), dimethyl carbonate (DMC, anhydrous, $\geq$ 99%) and 1,2-dimethoxyethane (DME, anhydrous 99.5%) were purchased from Sigma Aldrich. Bis(trifluoromethane) sulfonimide lithium salt (LiTFSI, 99.9%) was purchased from BASF Corporation (Florham Park, NJ). All materials were stored in an argon-filled glovebox (MBraun Labmaster, O_2 < 1 ppm, H_2O < 5 ppm). Prior to use, all solvents were dried over activated molecular sieves (3 Å beads, Fluka) for at least 24 h.

115

2,5-dimethyl-1,4-dimethyoxybenzene (25DDB) was synthesized in house at Argonne National Laboratory following a modified procedure previously reported[125]. In brief, sodium borohydride (NaBH$_4$, 7.57 g, 0.200 mol, Sigma-Aldrich, $\geq$ 96%) was added dropwise to a solution of 2,5-dimethyl-1,4-benzoquinone (13.62 g, 0.100 mol, Sigma-Aldrich, $\geq$ 98.0%) in ethanol (100 mL, ACROS, 99.5%) and water (100 mL) under nitrogen. The reaction was stirred for 30 min at room temperature. A solution of potassium hydroxide (40 mL, 10 M, 0.400 mol, Sigma-Aldrich, $\geq$ 85%) was then added, and the resulting mixture was stirred for another 30 min and was heated under reflux. Dimethyl sulfate (37.85 mL, 0.400 mol, Sigma-Aldrich, $\geq$ 99.8%) was added dropwise. The resulting mixture was stirred under reflux for 12 h before being cooled to room temperature and extracted with ethyl acetate (Sigma-Aldrich, 99.8%). The combined organic layers were washed with water and dried over Na$_2$SO$_4$ (Sigma-Aldrich, $\geq$ 99.0%). After being concentrated in vacuo, the residue was purified by flash column chromatography (silica gel, eluted with ethyl acetate / hexanes, (Sigma-Aldrich, $\geq$ 98.5%) = 1/10) to yield the product (14.57 g, 88%) as a white solid. ^{1}H NMR (500 MHz, CDCl$_3$) δ 6.68 (s, 2H), 3.80 (s, 6H), 2.23 (s, 6H); ^{13}C NMR (125 MHz, CDCl$_3$) δ 151.4, 124.3, 113.7, 56.1, 16.1. 2,5-difluoro-1,4-dimethyoxybenzene (25FDB, Sigma-Aldrich, 99%), 2,5-dichloro-1,4-dimethyoxybenzene (25ClDB, Sigma-Aldrich, $\geq$ 98.0%), 2,5-dibromo-1,4-dimethyoxybenzene (25BrDB, Sigma-Aldrich, 97%), 2,5-diiodo-1,4-dimethyoxybenzene (25IDB, Oakwood Chemical, 95%) were used as received.

Electrolyte preparation and viscosity measurements. All electrolyte formulations and subsequent experiments were performed in an argon-filled glove box at ca. 29 °C. All electrolytes were prepared in volumetric flasks to account for the volume change associated with the high concentration of supporting salt and active material. Electrolyte viscosity was measured using a

vibrational viscometer probe (Viscolite V-700, ± 0.1 cP accuracy) and electrolyte density was determined using an analytical balance (Metler-Toledo XP105, ± 0.1 mg accuracy) and a known electrolyte volume.

Voltammetry. Cyclic voltammetry (CV) was performed in a three-electrode electrochemical cell with a 3 mm diameter glassy carbon disk electrode (CH Instruments) or an 11 ± 2 μm diameter carbon fiber microelectrode (UME, CH Instruments) as the working electrode, a gold coil counter electrode (CH Instruments), and fritted lithium foil (99.9%, Alfa Aesar) as the reference electrode. Before each measurement, the working electrodes were polished on a MicroCloth pad with 0.05 μm alumina powder (Buehler Ltd.), rinsed with deionized water (Millipore), and wiped dry with lens paper (VWR). Before being placed in the fritted tube with a 1 M LiTFSI in PC fill solution, the lithium reference electrode was scraped with polypropylene to clean the metal surface. For the disk electrode experiments, all data was collected using a Bio-Logic VSP-300 potentiostat, applying 100% automated iR compensation. The resistance measured for each experiment was about 100 Ω, which corresponds to a correction of ca. 10 mV at the highest currents. The scan rates used were 10, 20, 30, 40, 50, 75, and 100 mV/s.

The disk electrode experiments were used to calculate the redox potential, peak separation (reversibility), and diffusion coefficient. The redox potential was calculated by taking the average of the anodic and cathodic peak potentials while peak separation was determined by taking the difference between these two peak potentials. The diffusion coefficient for the neutral species was estimated using the Randles-Sevcik equation:

$$i_p = 0.4463nFAC \left(\frac{nFD}{RT}v\right)^{0.5} \tag{1}$$

where i_p is the peak current (A), n is the number of electrons transferred (n = 1), F is the Faraday constant (96485 C/mol e⁻), A is the electrode area (0.0707 cm²), C is the bulk concentration (1 × 10⁻⁵ mol/cm³), R is the universal gas constant (8.314 J/mol-K), T is the absolute temperature (302.15 K), D is the diffusion coefficient (cm²/s), and v is the scan rate (V/s). The peak current was obtained by using the peak current from the cyclic voltammogram and subtracting an extrapolated background current[125].

All data using the UME was collected with a 630E potentiostat (CH Instruments, Inc.) at a scan rate of 10 mV/s. The steady-state currents were obtained from the UME voltammetry to estimate the active species concentration in solution:

$$i_{ss} = 4nFrDC \tag{2}$$

Where i_{ss} is the steady state current obtained at high overpotentials (A), n is the number of electrons transferred (n = 1), F is the Faraday constant (96485 C/mol e⁻), r is the UME radius (5.5 × 10⁻⁴ cm), C is the bulk concentration (mol/cm³), and D is the diffusion coefficient (cm²/s).

Bulk electrolysis. Extending cycling experiments were performed in a commercial bulk electrolysis cell (BASi) controlled by the VSP-300 potentiostat (Bio-Logic). The working, counter, and reference electrodes were reticulated vitreous carbon (BASi), lithium foil (Alfa Aesar), and fritted lithium foil (Alfa Aesar), respectively. All extended cycling experiments used 30 mL of 1 M LiTFSI in a 1:1 by weight mixture of EC:DMC with 0.001 M active species and were stirred at a rate of 900 rpm. The current for the galvanostatic cycling was set to 0.402 mA (equivalent to a 0.5 C rate) and the solutions were charged between 0 and 50% state of charge (SOC). Each solution was charged and discharged for 1 h each or until a predetermined potential cutoff was reached

(150 mV above and below the corresponding peak potentials obtained from CV), whichever occurred first. The potential cutoff was set in order to avoid accessing additional irreversible faradaic reactions involving either the active material or the supporting electrolyte.

Decay analysis of the 25FDB was performed at higher active species concentration and thus a custom H-cell with a higher surface area-to-volume ratio for electrolysis experiments was used. A similar configuration has been described in previous reports[147,156,162]. The cell consisted of two electrolyte chambers (3.5 mL), separated by an ultra-fine glass frit (P5, Adams and Chittenden) to minimize crossover. In these experiments, 3.5 mL of 0.01 M active species in 1 M LiTFSI was loaded into each side of the cell. Both chambers were stirred continuously during cycling experiments (1400 rpm). Two reticulated vitreous carbon electrodes (ERG Aerospace Corp.), one in each chamber, were used as the working and counter electrodes with a fritted lithium foil (Alfa Aesar) reference electrode housed in the working electrode chamber. These experiments sought to access the full SOC range (0 – 100%) thus potential cutoffs were set 0.25 V above and below the redox potential to charge and discharge the working solution. The current was set to 0.938 mA such that the theoretical charging and discharging times were 1 h each (equivalent to a 1 C rate). CV was performed before cycling and after each cycle using a 3 mm glassy carbon electrode inserted into the bulk electrolysis working electrode chamber. Reticulated vitreous carbon and fritted lithium foil served as the counter electrode and the reference electrode, respectively. Liquid phase nuclear magnetic resonance (NMR) experiments were conducted at room temperature using a Bruker Avance-400 NMR Spectrometer. Prior to NMR analysis, all solutions were mixed in a 1:1 ratio with deuterated dimethyl sulfoxide (99.9 atom % D, anhydrous, Aldrich).

Solvated Diameter. The Stokes-Einstein equation was used to experimentally estimate the solvated diameter of the active species:

$$D = \frac{kT}{6\pi\mu r} \tag{3}$$

Where D is the diffusion coefficient (m²/s), k is the Boltzmann constant (1.38×10^{-23} J/K), T is the absolute temperature (K), μ is the dynamic viscosity (kg/m-s), and r is the Stokes radius (m). The diffusion coefficient was previous determined using the Randles-Sevcik analysis (Equation 1). The viscosity of the supporting electrolyte (solvent and 1 M supporting salt) was used as it was assumed that a 0.010 M concentration of active species would have a negligible contribution on the solution viscosity.

Computation. The molecular diameter was calculated using Chem3D Pro. The optimal structure was calculated using MM2 energy minimization. The distance between the centers of the atoms was then calculated using the Cartesian coordinates provided by the Chem3D Pro. For each of the structures, the Van der Waals diameter[163] (for hydrogen, fluorine, chlorine, bromine, and iodine) was added to the calculated distance in order to account for the additional radius of each of the molecules. Density functional theory (DFT) was used to calculate the wave functions and bond lengths for each active material using B3LYP with a basis of 6-31+G(d) in a polarizable continuum model of water. The iodine-substituted species could not be computed accurately because of the large number of electrons.

4.3   Results and Discussion

The electrochemical properties and cycle stability of a series of halide substituted 1,4-dimethoxybenzenes (25FDB, 25ClDB, 25BrDB, and 25IDB) are measured using voltammetric and electrolytic techniques in combination with density functional theory (DFT) analysis and

nuclear magnetic resonance spectroscopy (NMR). The characteristics of these molecules are compared to each other as well as to 25DDB to correlate trends in performance-relevant properties with molecular structure.

Voltammetric analysis

Cyclic voltammetry (CV) measurements were performed to determine the redox potential, reversibility (chemical and electrochemical), and diffusion coefficient of each compound. In all experiments, the active species were dissolved in a supporting electrolyte consisting of 1 M lithium bis(trifluoromethane)sulfonimide (LiTFSI) in either propylene carbonate (PC) or 1,2-dimethoxyethane (DME). PC was initially selected as a solvent due to its wide electrochemical stability window and low volatility; however, as 25IDB was found to be insoluble in the PC-based electrolyte, DME was also used as a solvent. Figure 22 shows cyclic voltammograms of all compounds in 1 M LiTFSI in DME (solid lines) and 1 M LiTFSI in PC (dashed lines).
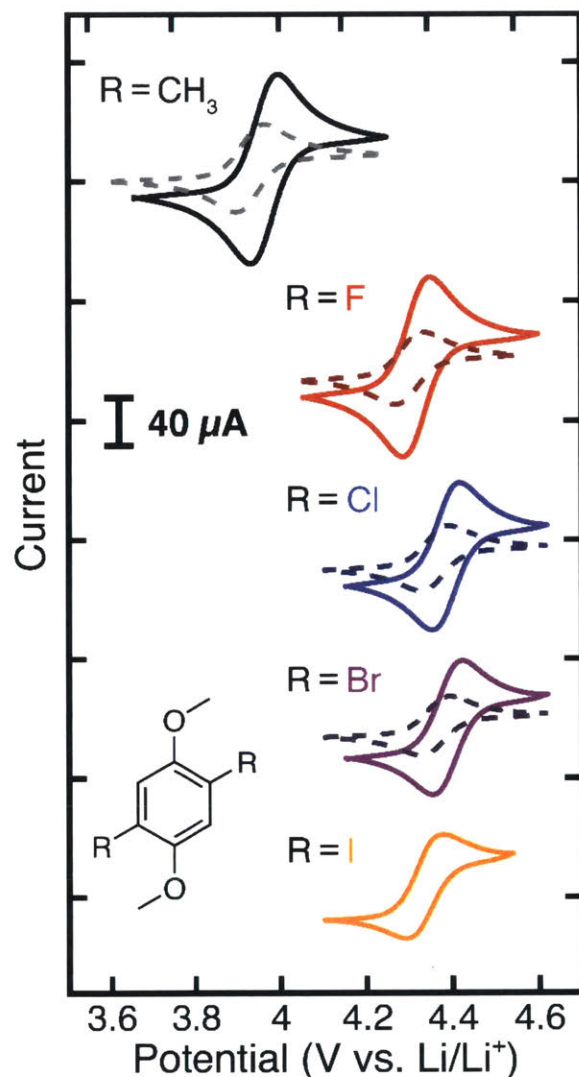
Figure 22: Cyclic voltammograms from top to bottom of 25DDB (black, gray), 25FDB (red), 25ClDB (blue), 25BrDB (purple), and 25IDB (orange). The solid and dashed lines correspond to supporting electrolytes of 1 M LiTFSI in DME and 1 M LiTFSI in PC, respectively. All data was collected with a scan rate of 20 mV/s with 0.010 M active species. The working, counter, and reference electrodes used were a 3 mm glassy carbon disk, a gold coil, and a fritted lithium foil.

Based on the analysis of the CVs, electrochemical and transport properties can be extracted (Table 9). As expected, each of the halide derivatives has a redox potential 300 – 400 mV more positive than that of 25DDB as the more electron-withdrawing halides lower the electron density around the aromatic core, resulting in a greater ionization potential (calculated by DFT, Table 9) and, consequently, an increased oxidation potential. As weak electron-withdrawing substituents, halides impart both induction and resonance effects which manifest as electron-withdrawing and

electron-donating behaviors, respectively. Therefore, though fluorine is the most electronegative substituent, due to its strong resonance effect, 25FDB does not afford the highest potential, but rather the lowest of the halide-substituted molecules. 25BrDB demonstrates the highest redox potential in both electrolytes, followed by 25ClDB, 25IDB, and then 25FDB in agreement with the Hammett sigma constants for the substituent groups [164,165]. We note the slight offset (15 – 30 mV) in redox potential across all tested species in the two electrolytes, which we attribute to a combination of different junction potentials between the electrolyte solution and the reference electrode as well as different interactions between the electrolyte solution and the solubilized redox molecules.

Table 9: A summary of electrochemical and transport properties of 25DDB, 25FDB, 25ClDB, 25BrDB, and 25IDB as determined from CV experiments performed in 1.0 M LiTFSI in PC (top) and 1.0 M LiTFSI in DME (*bottom*), and the ionization potential determined by DFT. All electrochemical experiments were performed in triplicate.

	25DDB	25FDB	25ClDB	25BrDB	25IDB
Redox Potential (V vs. Li/Li$^+$)	3.930 ± 0.001 *3.964 ± 0.001*	4.301 ± 0.001 *4.318 ± 0.001*	4.359 ± 0.001 *4.386 ± 0.001*	4.361 ± 0.001 *4.388 ± 0.001*	— *4.332 ± 0.001*
Ionization Potential (eV)	5.447	5.643	5.663	5.654	—
Peak Separation (mV)	60.3 ± 0.7 *62.2 ± 0.3*	61.0 ± 0.6 *60.3 ± 0.3*	61 ± 1 *62.7 ± 0.9*	61.7 ± 0.9 *65 ± 2*	— *80 ± 5*
Peak Current Ratio (I$_{p,o}$/ I$_{p,r}$)	1.003 ± 0.002 *1.01 ± 0.01*	1.03 ± 0.01 *1.01 ± 0.01*	1.04 ± 0.02 *1.05 ± 0.01*	1.08 ± 0.03 *1.06 ± 0.03*	— *1.17 ± 0.05*
Diffusivity (× 10^{-6} cm^2/s)	2.4 ± 0.1 *12.0 ± 0.4*	1.6 ± 0.1 *8.6 ± 0.9*	1.4 ± 0.1 *7.6 ± 0.2*	1.3 ± 0.1 *7.1 ± 0.1*	— *5.5 ± 0.2*

Analyses of the oxidative and reductive peaks of the CV, as a function of scan rate and electrolyte composition, provide insight into the stability of the charged species, as well as the kinetic and transport characteristics of the redox species. Of the halide-substituted molecules, 25FDB has the smallest peak separation of 61.0 ± 0.6 mV at a scan rate of 10 mV/s, with peak

123

separation increasing with increasing halide size (Table 9). Over all of the scan rates tested, the peak separation for each molecule only increases by about 2 mV from scan rates of 10 to 100 mV/s after 100% iR compensation; the slight increase in the peak separation indicates that the electrochemical reactions are quasi-reversible, but still have relatively large kinetic rate constants, that could not be resolved by the techniques used in this work. Further, as the halide becomes larger, the peak current ratio increasingly deviates from unity, signifying that either the oxidized species is less stable for the larger halogenated species or oxidative electrolyte decomposition is convoluting the electrochemistry at these high potentials. As all of the halogenated species have a similar redox potential and the electrolyte does not show a significant current at these potentials, it appears more likely that the derivatives with the large halide groups are reacting with the electrolyte, reducing the oxidative stability. As expected the diffusion coefficient, as determined by Randles-Sevcik analysis, decreases as the substituted halide size, and thus Stokes radius, increase (Table 9).

Upon examining the effective solvated diameter via the Stokes-Einstein relationship (solution viscosities: 8.5 cP in 1 M LiTFSI in PC and 1.3 cP in 1 M LiTFSI in DME), the solvated diameters for the halide-substituted compounds appear larger than expected suggesting complexation between the active species and electrolyte (Table 10). The lone electron pairs on the halides can be incorporated into conjugation, resulting in enhanced electron density, which, in turn, can complex with Li cations in the supporting salt, increasing the effective solvated diameter[166]. Weaker intermolecular interactions are anticipated for methylated compounds leading to a smaller solvation diameter[167]. This becomes particularly evident when comparing the ratio of the effective solvated diameter to the molecular diameter, as calculated from the energy minimization of the structure, across the series in both supporting electrolytes. Larger solvated diameters are observed

in the DME-based electrolyte as compared to the PC-based electrolyte which we hypothesize is due to differences in the solvent structure. Specifically, DME has many freely rotating bonds whereas PC has a more rigid ring structure, thus DME can more easily coordinate with the redox active species and itself[166].

Table 10: A summary of physical properties of 25DDB, 25FDB, 25ClDB, 25BrDB, and 25IDB in 1 M LiTFSI in PC (top) and 1 M LiTFSI in DME (*bottom*).

	25DDB	25FDB	25ClDB	25BrDB	25IDB
Molecular Diameter (Å)	9.1	8.4	9.7	10.2	11.0
Effective Solvated Diameter (Å)	21 ± 1 *28 ± 1*	32 ± 1 *40 ± 4*	36 ± 2 *44 ± 1*	41 ± 2 *48 ± 1*	— *62 ± 2*
Solubility (mol/L)	0.10 *0.35*	0.19 *0.42*	0.10 *0.27*	0.05 *0.18*	Insol. *0.03*

The active species solubility of both the oxidized and neutral species is another important property for achieving high-capacity charge-storage solutions. Unfortunately, each oxidized species could not be isolated, and therefore the solubility could not be measured. UV-Vis did not yield a linear signal for the neutral halogenated structures at low concentrations (0.0001 M – 0.030 M), as would be expected from Beer's Law. Therefore, solubility was estimated using a combination of electrochemical techniques. First, a saturated solution of the active material was made by adding an excess of active material to 3 mL of electrolyte and allowing the solution to equilibrate for 48 h. The supernatant was then probed via microelectrode voltammetry where the measured steady-state current was used to estimate a saturation concentration (Figure 23). Note that this calculation requires knowledge of the active species diffusion coefficient which can vary as a function of concentration[145,168,169]. For the initial measurement, we assume that the diffusion coefficient measured under dilute conditions (see Table 9) is a sufficient representation. To

validate this assumption, the saturated solution was diluted by a known amount, based on the previously estimated concentration, and Randles-Sevcik analysis was employed to provide a second estimate of the saturation concentration. In greater detail, the saturated solutions are diluted to a concentration between 0.005 and 0.010 M, and CV measurements are performed, over a range of scan rates to generate a Randles-Sevcik plot, from which an "actual" concentration can be determined, again based on the knowledge of the diffusion coefficient which was previously determined in a similar concentration regime. By multiplying this "actual" concentration by the dilution factor, a more accurate estimate of saturation concentration can be obtained (Table 10). We note that all of the refined estimates were within 5% of the initial estimate from the microelectrode, which is consistent as the overall solubilities of the compounds were not high enough to significantly impact the solution viscosity or the intermolecular interactions. When the increase in supporting salt concentration is accounted for, the determined solubility of 25DDB is in agreement with prior literature in PC[125].
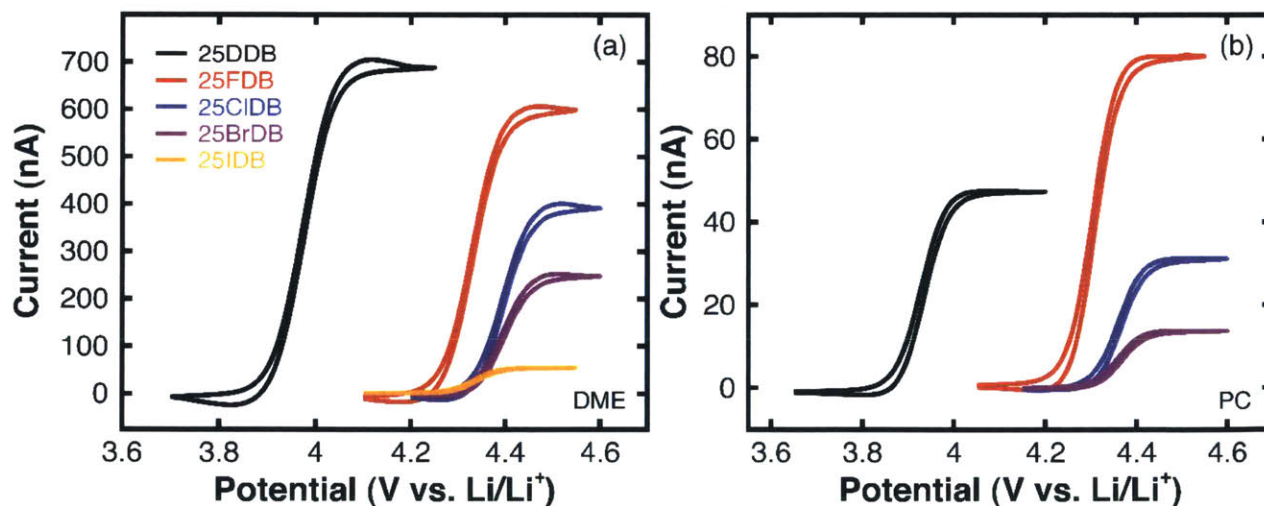
Figure 23: Cyclic voltammograms using a microelectrode of saturated solutions of 25DDB (black), 25FDB (red), 25ClDB (blue), 25BrDB (purple), and 25IDB (orange) in 1 M LiTFSI in DME (a) and 1 M LiTFSI in PC (b). The working, counter, and reference electrodes are a carbon fiber, lithium foil, and fritted lithium foil, respectively.

In agreement with prior reports, the solubility of all of the species is greater in the DME-based electrolytes than in the PC-based electrolytes[137,170]. In general, as the halide substituent becomes larger, the solubility decreases in both electrolytes as larger local dipoles exist with smaller halides, due to increased electronegativity, which increases the solubility in polar solvents. The polarity of the C-F, C-Cl, C-Br, and C-I bonds are 1.43, 0.61, 0.41, and 0.11, respectively[163]. Additionally, the solubility of 25FDB is greater than that of 25DDB due to its smaller size and the greater electronegativity of the substituent groups[171].

Electrolytic analysis

Bulk electrolysis cycling was performed to investigate the cyclability of the halogenated compounds over longer time periods (~ 1 day). For these experiments, the electrolyte composition was changed to 1 M LiTFSI in a binary solvent mixture of ethylene carbonate (EC) and dimethyl carbonate (DMC) in a 1:1 weight ratio. This electrolyte was selected in an attempt to reduce the presence of asymmetric background processes that convolute analyses of the charge storage efficiency and species decomposition, which are present, to a greater extent, in both PC and DME. All redox species exhibit similar voltammetric and solubility behavior in the mixed carbonate electrolyte as compared to in the PC electrolyte, including the insolubility of 25IDB. Therefore, all active materials except 25IDB were tested at 0.001 M in 30 mL of solution with a current of 0.402 mA (0.5 C) and charged to 50% SOC. Figure 24 shows the voltage profiles for cycles 2 to 6 for each compound tested.
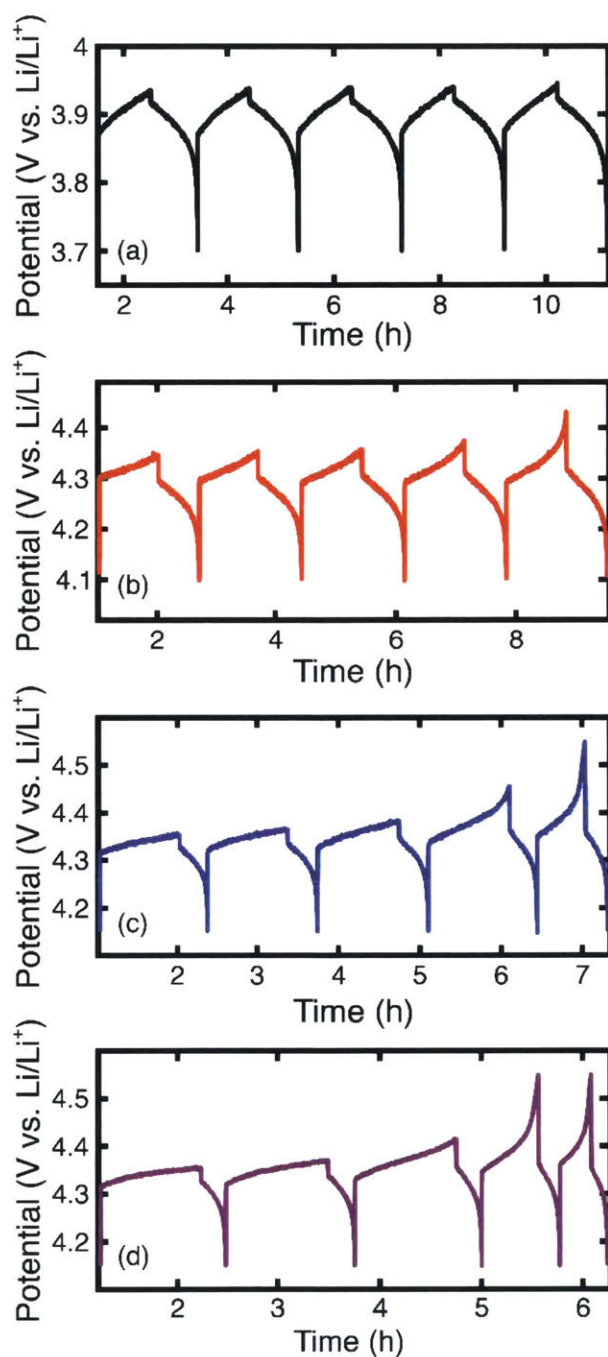
Figure 24: Bulk electrolysis voltage profiles for the second through sixth cycles of 0.001 M 25DDB (a), 25FDB (b), 25ClDB (c), and 25BrDB (d) each in 1 M LiTFSI in 1:1 weight ratio of EC:DMC. The concentration of active species was 0.001 M and the charge/discharge current was 0.402 mA (0.5 C). 25IDB was not insoluble in this electrolyte solution.

From the 2nd to 6th cycles, a trend of the stability can be inferred because the potential cutoff

for all halogenated compounds is reached whereas the 25DDB molecule always reaches the time

cutoff. This trend is confirmed by examining the charging capacity as a function of cycle number (Figure 25) because as the halide substituent becomes larger, the faster the capacity fades. The coulombic efficiency of the cycles that reach the time cutoff further support the decomposition trend (Figure 26). The average coulombic efficiency of 25FDB, 25ClDB, and 25BrDB is 65%, 33%, and 26%, respectively. When compared to the coulombic efficiency of the 25DDB (96%), it is consistent that the halide substituted species are much less stable than 25DDB, and as the substituted halide becomes larger, the charged species becomes less stable. Because the coulombic efficiencies are so low and the cycling lifetime is short, it is likely that the charged active material decays to a new species which is not redox active in the potential window used in these experiments. Note that the first bulk electrolysis cycle is not shown here as it does not display representative charging/discharging behavior. This is an artifact of cycling between 0 and 50% state-of-charge, a range that was chosen to enable comparison with prior work on substituted dialkoxybenzenes[124,125]. Specifically, the first cycle represents a preconditioning of the solution and electrodes. This generally leads to a full charging cycle and a very limited discharging cycle, and thus, a poor coulombic efficiency.
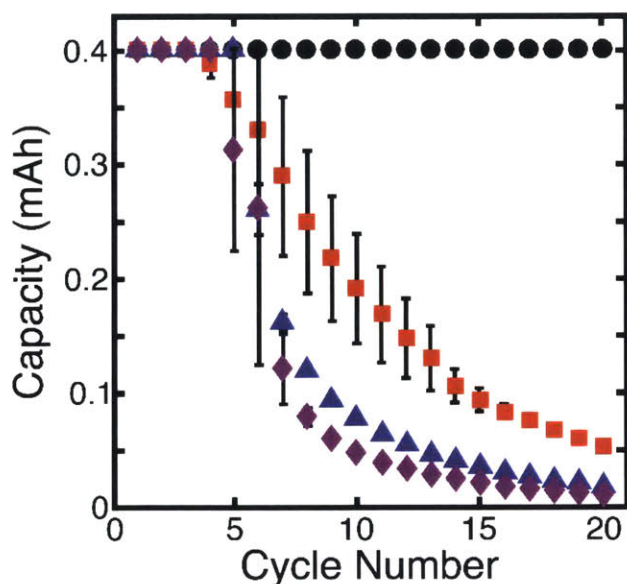
Figure 25: Bulk electrolysis charging capacity of 0.001 M of 25DDB (black, circles), 25FDB (red, squares), 25ClDB (blue, triangles), and 25BrDB (purple, diamonds) each in 1 M LiTFSI in 1:1 EC:DMC. All experiments were conducted in duplicate. 25IDB was not insoluble in this electrolyte solution.
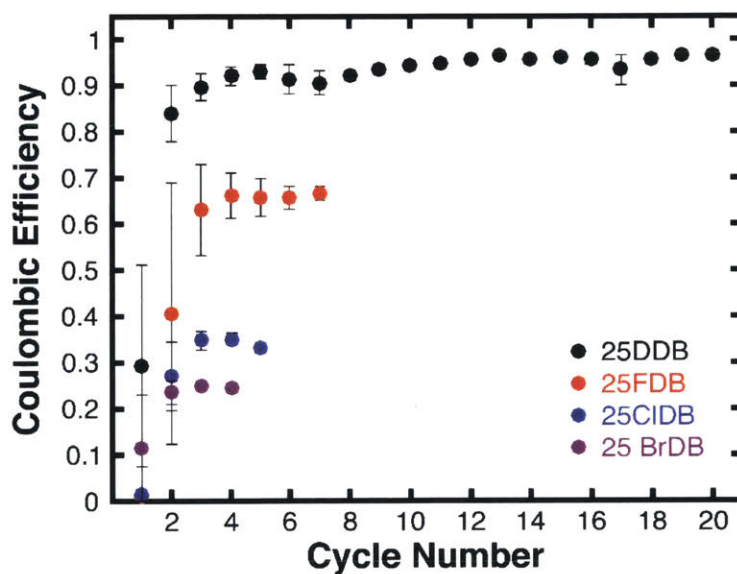
Figure 26: Coulombic efficiency as a fuction of cycle number for each of the materials cycled for bulk electrolysis. All experiments were performed in duplicate.

Decay Characterization

To better understand the decay behavior observed in Figure 25, particularly the halide dependence, DFT calculations were performed on 25DDB, 25FDB, 25ClDB, and 25BrDB. The

130

highest occupied molecular orbital (HOMO) was examined for both the neutral and oxidized species (Figure 27). As expected, as the halide size and therefore the overall number of associated electrons increases, the electron density around the halide increases for both the neutral and oxidized species, making it a better leaving group. Thus, we hypothesize that the increased capacity fade with larger halide size is due to the halide breaking off from the charged redox species through solvent attack[172,173].
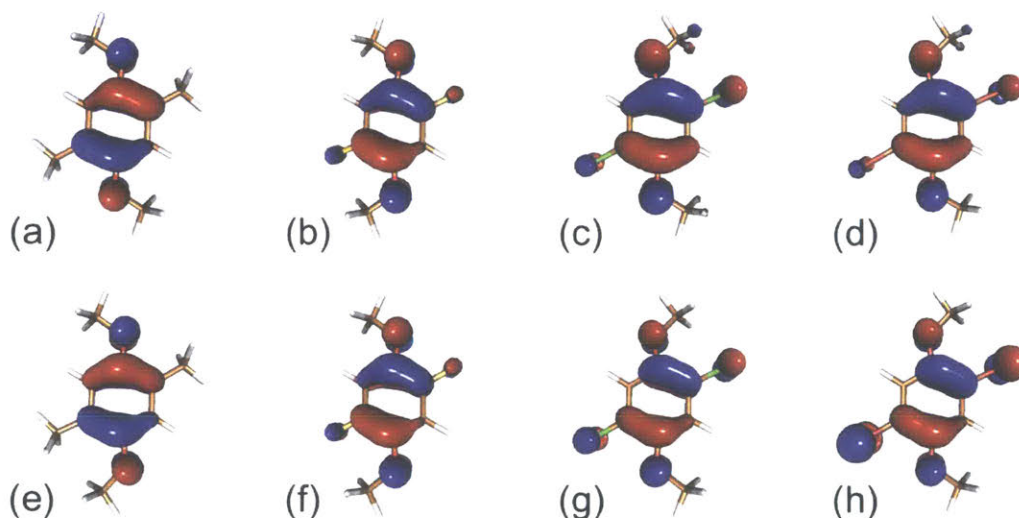
Figure 27: Calculated HOMO by DFT of 25DDB (a), 25DDB⁺ (e), 25FDB (b), 25FDB⁺ (f), 25ClDB (c), 25ClDB⁺ (g), 25BrDB (d), and 25BrDB⁺ (h).

Both ^{1}H NMR and ^{19}F NMR were performed on 25FDB before cycling and after the capacity faded below 1% of the initial capacity (20 cycles) with major peak locations summarized in Table 11. Here, to improve the NMR signal, the active species concentration was increased to 0.010 M. Additionally, the solvent was switched to PC from the mixed carbonate solvent in order to reduce the number of compounds in solution. In this case, because 25FDB has the lowest redox potential of the substituted halides, the higher potential electrolyte was also not as necessary. During cycling in the PC based electrolyte, a similar decay rate was observed for 25FDB as in the mixed carbonate system. In the ^{19}F NMR, the only peaks present before cycling corresponded to

the 25FDB parent molecule (Figure 28a) and the TFSI⁻ anion in the supporting salt (LiTFSI). After

cycling, the only peaks that remain are from the TFSI⁻ anion (Figure 28a). Consistent with the ^{19}F

NMR, the ^{1}H NMR data (Figure 28b) showed decay of the 25FDB species but also provides a

clear indication of the decay mechanism complexity. Quantitative analysis of these emergent

features is beyond the scope of the present work, especially considering critical fine details are

likely to be masked by the strong PC solvent signal. Note that Figure 28 only highlights where

non-solvent peaks appeared or disappeared over the full range.

Table 11: Summary of the major NMR peaks before and after cycling. Note that the solvent and supporting salt peaks are omitted from this table

	^{1}H NMR	^{19}F NMR
Before cycling	3.55 (s), 7.06 (dd) J = 10.5	-138.7 (t) J = 10.1
After cycling	3.19 (s), 3.47 (s), 4.48 (s), 5.93 (s)	None
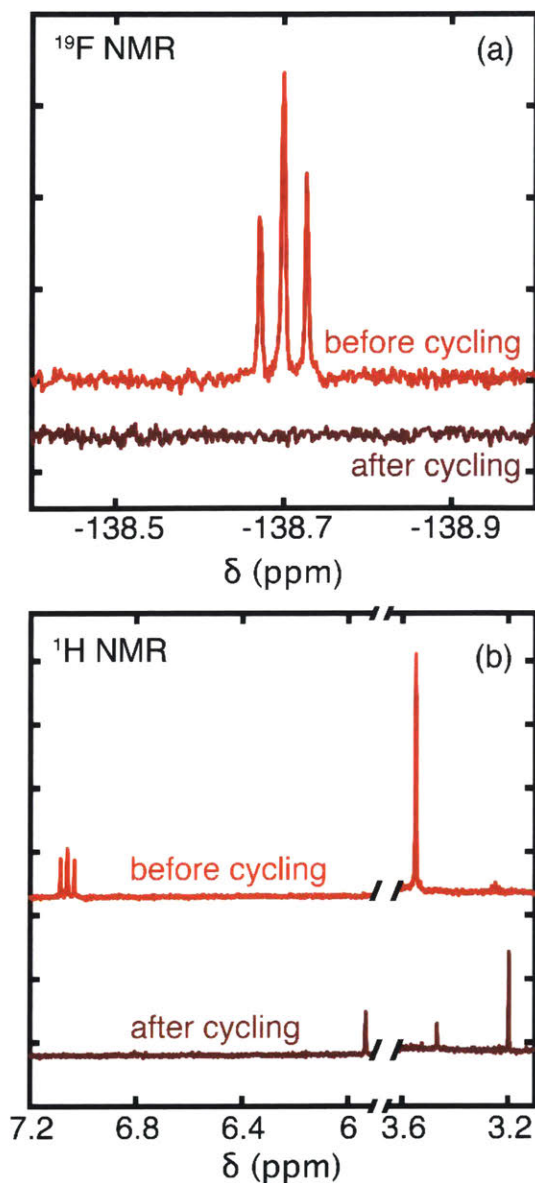
Figure 28: The ^{19}F NMR (a) and ^{1}H NMR (b) both before cycling (red) and after cycling (dark red) for 0.010 M 25FDB in 1 M LiTFSI in PC.

Taken together, these NMR spectra suggest that the decomposition process involves the halide leaving the molecule due to the disappearance of the fluorine peaks in ^{19}F NMR and the triplet corresponding to the benzene in ^{1}H NMR. As no additional fluorine peaks are observed by NMR we hypothesize that any free fluoride anions rapidly complex with excess lithium cations, present in the supporting electrolyte, and precipitate as lithium fluoride (LiF). However, LiF was

not isolated from the electrolyte due to the low active material concentration, and the low solubility of LiF in PC[174].

In an effort to better understand the decay processes, bulk electrolysis was combined with voltammetry to evaluate the evolution in the CV profile of 25FDB as a function of charge/discharge cycling. Overall, 25FDB was cycled to 100% state-of-charge for a total of 10 cycles (Figure 29a). The charging capacity (Figure 29b) was monitored and CV scans from 1.5 to 4.55 V vs. Li/Li$^+$, were taken before testing and then after every charge/discharge cycle for 10 cycles (Figure 30). Finally, the solution was allowed to rest for 10 h, with all of the electrodes removed from the solution, after which a final CV was performed to determine if chemical processes continue in the absence of electrochemical stimulus (Figure 29c).
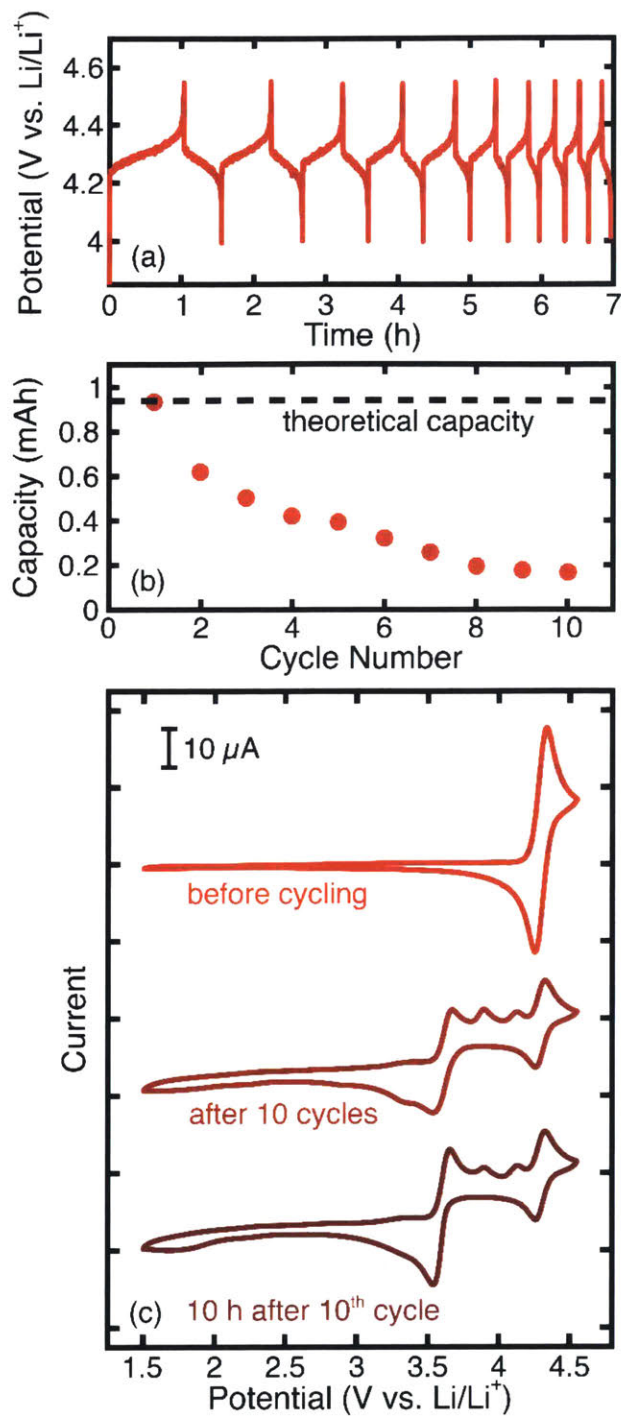
Figure 29: The voltage profiles of the first 10 cycles of 25FDB (a), and the corresponding capacity vs. cycle number profile (b). Cyclic voltammograms before cycling (top), immediately after 10 cycles (middle), and 10 h after 10 cycles (bottom) for 25FDB using a scan rate of 20 mV/s (c). The initial electrolyte composition was 0.010 M 25FDB in 1 M LiTFSI in PC. The working electrode, reference electrode, and counter electrode used were a 3 mm glassy carbon disk, a fritted lithium foil, and a RVC, respectively. The applied current was 0.938 mA (1C) for both charge and discharge.

With every cycle, the peak current ratio associated with the redox potential of 25FDB remained constant, but the overall magnitude of the oxidative and reductive peak heights decreased indicating that the charged species decays, but does not negatively interact with the neutral species. Additionally, the decrease in the oxidative peak height of 25FDB generally tracks with the charging capacity accessed during cycling. As 25FDB is cycled, the voltammetry response evolves and becomes more complicated suggesting intricate decomposition processes and the formation of multiple electroactive decay intermediates and products. As expected, the magnitude of these newly formed peaks increased with cycle number indicating that, with further cycling, the decomposition continued. From the full set of voltammograms Figure 30), a reduction peak at 3.379 V vs. Li/Li^+ appeared after the first cycle. After 25FDB is cycled further, 3 new oxidation peaks of similar magnitudes appeared at 3.653 V vs. Li/Li^+, 3.897 V vs. Li/Li^+, and 4.135 V vs. Li/Li^+. After cycle 5, a new reduction peak begins to form at 3.539 V vs. Li/Li^+, and the reduction peak at 3.379 V vs. Li/Li^+ starts to decrease in magnitude. The changes in the voltammogram profile and the current magnitudes as a function of cycle number indicate that 25FDB initially decays, but as the solution continues to cycle, these intermediates start to decay themselves, signifying a tiered mechanism. This is further evinced by comparing the voltammograms after 10 cycles and 10 h after completion of cycling. Even with no electrochemical stimulus applied to the solution, the voltammogram evolves, showing that the decomposition products are not stable on their own. As such, unambiguous identification of decay products is challenging due to the complexity of the electrochemical signal and NMR data. Thus, decomposition products could not be identified nor could a decomposition mechanism be confirmed. Previous work on substituted dialkoxybenzenes suggest that quinone and dimer formation are likely decay products[157,158,161]. Expanding upon these efforts, future work on halogenated species should aim to correlate possible

decomposition products with the corresponding electrochemical and spectroscopy responses to confirm their presence. Once the decomposition products and the decay pathways are determined, the next generation of derivatives can be designed to be resilient to these failure modes but still enable increased redox potential[129,156,159].
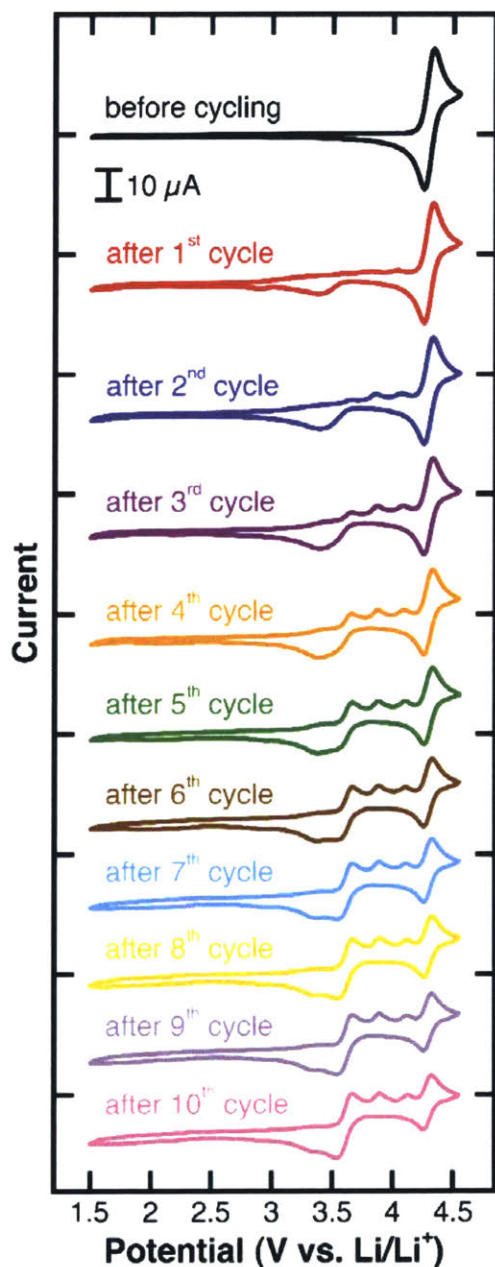
Figure 30: Cyclic voltammograms of 25FDB after each bulk electrolysis cycle for 10 cycles in 1 M LiTFSI in PC. The working, counter, and reference electrodes used were glassy carbon, reticulated vitreous carbon, and fritted lithium foil, respectively. The active species concentration was 0.005 M.

4.4 Conclusions

This work investigates the effect of halidization on the dimethoxybenzene core using electrochemical techniques, NMR spectroscopy, and DFT calculations. Halidization is an effective method to increase the redox potential so that the oxidation occurs at or near the upper limit of the electrolyte stability window, potentially allowing for higher energy applications. Cyclic voltammetry was used to determine the redox potential, electrochemical reversibility, chemical reversibility, and the diffusion coefficient. With the exception of the iodide derivative, the increase in redox potential does not significantly affect the chemical reversibility at low concentrations on the CV timescale (~100 s).

Of the halide substitutions made, the fluorine derivative has many desirable properties as compared to the parent methyl compound. The fluorine groups increased the redox potential by about 360 mV, but only increased the molecular weight by 8 a.m.u compared to 25DDB. The fluorine groups also increased the solubility in the electrolytes used due to the additional polarity. However, the cyclability of this and other halide-substituted materials, is hampered by the limited charged state stability as the radical cation, which appears to decompose through immolation of the carbon-halide bonds. While initial decay pathways were probed, the full decomposition mechanism could not be determined but appears complex and tiered. Further investigation of these mechanisms may inform molecular engineering of more robust derivatives which retain the high redox potentials of this initial set. While these halogen-substituted materials do not appear suitable for use as energy storage materials (e.g., active materials for redox flow batteries) as their limited charge state stability hampers cyclability, they may find use as part of a computational training set to guide the design of substituted dialkoxybenzenes with improved stability[156] or as redox mediators in electrochemical technologies including as overcharge protection additives in Li-ion

batteries[117], as well as charge shuttles in dye-sensitized solar cells[175] and in flow batteries with solid materials in the tanks[176,177].

5   Increasing the Solubility of N-Ethylphenothiazine

Nonaqueous redox flow batteries (NAqRFBs) employing redox-active organic molecules show promise to meet requirements for grid energy storage. Here, we combine the rational design of organic molecules with flow cell engineering to boost NAqRFB performance. We synthesize two highly soluble phenothiazine derivatives, N-(2-methoxyethyl)phenothiazine (MEPT) and N-[2-(2-methoxyethoxy)ethyl]phenothiazine (MEEPT), via a one-step synthesis from inexpensive precursors. Synthesis and isolation of the radical-cation salts permit UV-vis decay studies that illustrate the high stability of these open-shell species. Cyclic voltammetry and bulk electrolysis experiments reveal the promising electrochemical properties of MEPT and MEEPT under dilute conditions. A high performance nonaqueous flow cell, employing interdigitated flow fields and carbon paper electrodes, is engineered and demonstrated; polarization and impedance studies quantify the cell's low area-specific resistance ($3.2-3.3$ Ω cm^2). We combine the most soluble derivative, MEEPT, and its tetrafluoroborate radical-cation salt in the flow cell for symmetric cycling, evincing a current density of 100 mA/cm^2 with undetectable capacity fade over 100 cycles. This coincident high current density and capacity retention is unprecedented in NAqRFB literature. This chapter is partially reprinted from "High current density, long duration cycling of soluble organic active species for non-aqueous redox flow batteries" by Jarrod D. Milshtein, Aman, P. Kaur, Matthew D. Casselman, **Jeffrey A. Kowalski**, Subrahmanyam Modekrutti, Peter L. Zhang, N. Harsha Attanayake, Corrine F. Elliott, Sean R. Parkin, Chad Risko, Fikile R. Brushett, and Susan A. Odom from Energy and Environmental Science (2016, 99 3531-3543)[147].

5.1   Introduction

Most reports of new active materials for nonaqueous flow batteries (NAqRFBs) have focused on

molecular discovery and electrochemical characterization under dilute conditions[125,129], with only

a few attempts to engineer performance systems with highly soluble active species [112,113,122,124] or

advanced flow-cell designs[123,178]. Simultaneous engineering at the molecular and cell levels is a

challenging task because NAqRFB failure might arise from active species degradation (e.g.,

charged species decay) or from inadequate flow cell design (e.g., high resistance, membrane

fouling, crossover). Advancing the field will require demonstrating cycling of an organic molecule

with a long lifetime at a high current density.

Many classes of redox-active organic molecules have been proposed for use in NAqRFBs,

such as anthraquinones[130] and dialkoxybenzenes[109,111,122,124]. Of the proposed redox-active organic

molecules, nearly all, with the exception of N-oxidanyl amines (e.g., TEMPO)[108,122,179], suffer from

rapid capacity fade or poor solubility[107,111]. N-Ethylphenothiazine (EPT, Figure 31a) is a

commercially available and stable electron-donating organic molecule that oxidizes at ~0.3

V *vs.* ferrocene/ferrocenium (Fc/Fc$^+$) in carbonate electrolytes. The long lifetime of this molecule

as an overcharge protection material in lithium-ion batteries highlights its remarkable

stability[126,127,180,181]. Our studies have further demonstrated the stability of EPT in aprotic, organic

solvents, both in the neutral and singly oxidized (radical-cation) states[182]. This stability suggests

that EPT could serve as a one-electron-donating material in NAqRFB electrolytes, but the

solubility of EPT in carbonate- or nitrile-based solvents (~0.1 M) is too low for practical

implementation[2]. By comparison, we reported previously that 3,7-bis(trifluoromethyl)-N-

ethylphenothiazine (BCF3EPT)[112,127], an EPT derivative, dissolves at concentrations up to 2 M in

nonaqueous electrolytes and is even more stable than EPT[127]. The synthesis of BCF3EPT,

however, requires multiple steps, the last of which entails a low-yielding trifluoromethylation reaction[127]. Ideally, organic active materials for NAqRFBs will be easily synthesized from cheap precursors, leading to active-material costs ≤$5/kg. Additionally, active materials should be highly soluble (>1 M) to ensure that electrolytes are sufficiently energy-dense and low-cost to be economically viable[2].

EPT
(a)
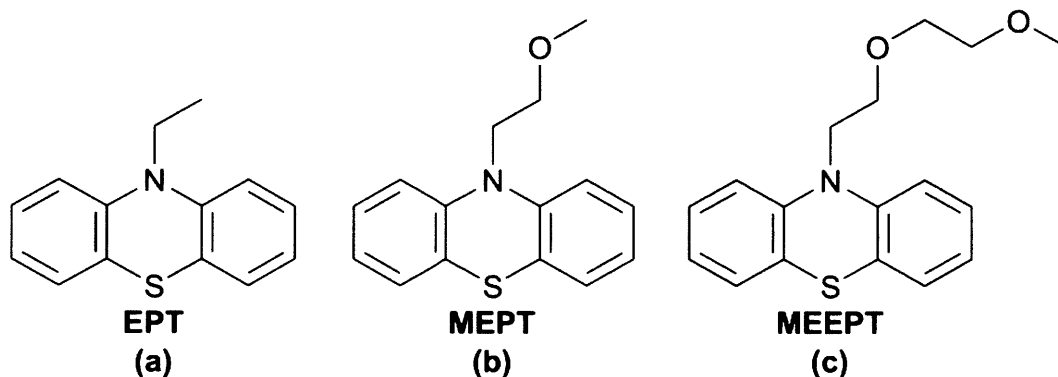
MEPT
(b)

MEEPT
(c)

Figure 31: Chemical structures of (a) N-ethylphenothiazine (EPT), (b) N-(2-methoxyethyl)phenothiazine (MEPT), and (c) N-(2-(2-methoxyethoxy)ethyl)phenothiazine (MEEPT).

Furthermore, NAqRFB design has failed to incorporate advanced flow-cell architectures developed for aqueous RFBs over the past few years[183,184]. Organic-based aqueous RFBs have demonstrated vast reductions in area-specific resistance (ASR) by transitioning from initial prototypes[86] to advanced cell designs[185,186] inspired by all-vanadium RFB literature. Many NAqRFBs implement thick (>1 mm) flow through electrodes, leading to large ohmic and mass-transfer resistances, subsequently forcing cell operation at low current densities only[162,187]. Prior work on vanadium RFBs suggests that zero-gap[183,184], interdigitated flow fields (IDFFs) with thin (<500 μm) carbon-paper electrodes will offer the best balance of ASR and pressure drop for at-scale RFBs[45,188]. The IDFF requires that all electrolyte flows through a short path of porous electrode, enabling high current densities, but not developing an unacceptably large pressure drop[45,188]. Thin carbon-paper electrodes offer a balance of high surface area, good mass transport,

143

and low ohmic resistance[184]. We previously reported a flow cell with IDFFs and carbon-paper electrodes designed for compatibility with nonaqueous electrolytes[123], but no demonstration of cycling of an organic active species in such a flow cell has been reported.

In this work, we engage in molecular and cell-level engineering to afford high-rate, long-duration cycling of soluble EPT derivatives. We first describe the synthesis and solubility of two new phenothiazine derivatives, N-(2-methoxyethyl)phenothiazine (MEPT, Figure 31b) and N-[2-(2-methyoxyethoxy)ethyl]phenothiazine (MEEPT, Figure 31c), as well as the stability of their tetrafluoroborate radical-cation salts. These compounds are synthesized in a single step from an inexpensive, commercially available precursor. Both neutral species have significantly lower melting points and higher solubilities in nonaqueous electrolytes than EPT. MEEPT, in fact, is a liquid at room temperature. We investigate the fundamental electrochemical properties of these new phenothiazine derivatives using cyclic voltammetry (CV) to determine redox potentials, chemical reversibility, and diffusion coefficients, and use bulk electrolysis to examine cycling behavior under dilute conditions. Next, we employ the most soluble derivative (MEEPT) at a moderate concentration (0.5 M active species) in a high-performance flow cell (Figure 32) incorporating IDFFs and carbon-paper electrodes. This flow cell exhibits the lowest reported cell ASR for NAqRFBs (3.2–3.3 Ω cm^2), allowing the stable MEEPT molecule to cycle at an aggressive current density of 100 mA/cm^2 with negligible capacity fade over 100 cycles. The molecular and cell engineering principles outlined in this paper, aimed at high concentration, high stability, and high current densities, apply to other emerging redox chemistries and provide a framework for advancing NAqRFBs towards a technology-readiness level competitive with aqueous RFBs.
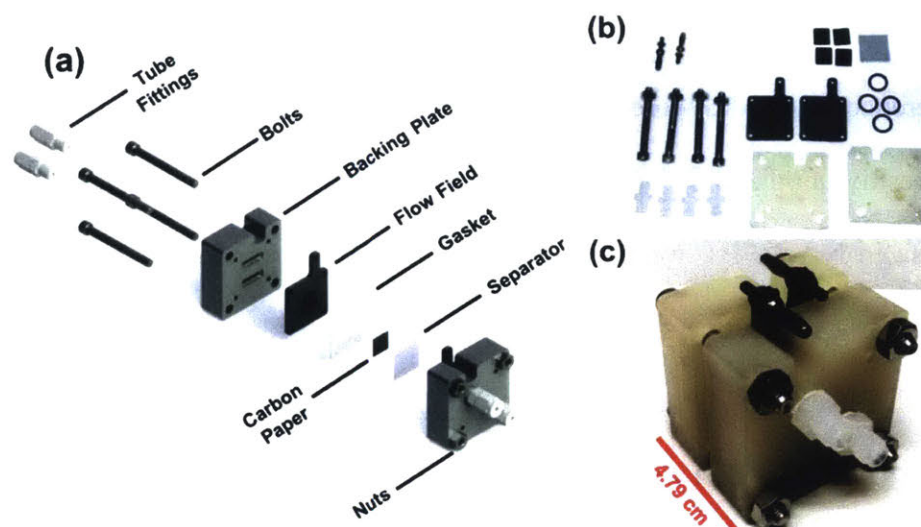
Figure 32: (a) Schematic of the nonaqueous-compatible flow cell employed in this work, exhibiting IDFFs and carbon paper electrodes. (b) Photograph of the flow cell components. (c) Photograph of the assembled flow cell.

5.2   Experimental

Phenothiazine (99%), 1-bromo-2-(2-methoxyethoxy)ethane (90%), and sodium hydride (60% dispersion in mineral oil) were purchased from Acros Organics. 2-Chloroethyl methyl ether (98%) and NOBF₄ (98%) were purchased from Alfa Aesar. NOBF₄ was stored and weighed in an argon filled glovebox (MBraun, $O_2 < 0.1$ ppm, $H_2O < 0.6$ ppm), and removed in a capped vial only immediately prior to use. Other reagents and chromatography solvents were purchased from VWR. Silica gel (65 × 250 mesh) was purchased from Sorbent Technologies.

All electrochemical measurements were performed in argon-filled gloveboxes ($O_2 < 0.7$ ppm, $H_2O < 0.6$ ppm) from MBraun or Innovative Technologies. Propylene carbonate (PC, 99.99%) and tetraethylammonium tetrafluoroborate (TEABF₄, 99.9%) were purchased from BASF and used as received, while anhydrous acetonitrile (ACN) (99.9%) was purchased from Acros Organics. Kryptofix® 222 (cryptand, 4,7,13,16,21,24-hexaoxa-1,10-diazabicyclo[8.8.8]-hexacosane, Acros Organics, 98%) and silver tetrafluoroborate (AgBF₄, Sigma Aldrich, 98%)

145

were used as received. Silver wire was purchased from Alfa Aesar. Silver–silver chloride (Ag/AgCl) reference electrodes were purchased from CH Instruments, removed from their glass housing, and freshly anodized before use. Due to the lack of stable and conductive separators available for use in NAqRFBs, we implemented a Daramic separator to minimize interactions between the separator and active species, as well as eliminate separator decay as a performance degradation mechanism[162]. In particular, a Daramic 175 separator (thickness = 175 μm, porosity = 58%, mean pore size = 100 nm) was used as received and employed as the separator material in flow cell experiments.

^{1}H and ^{13}C nuclear magnetic resonance (NMR) spectra were obtained on Varian spectrometers in deuterated chloroform from Cambridge Isotope Laboratories. J values are reported in Hz. Mass spectra were obtained on an Agilent 5973 Network mass selective detector attached to an Agilent 6890N Network GC system. Elemental analyses were performed by Atlantic Microlab Inc. Electron paramagnetic resonance (EPR) spectra were acquired on a Bruker EMXplus spectrometer with a PremiumX bridge containing an ER 4119HS-W1 high sensitivity cavity. To prepare the sample, 5 mg of EPT-BF$_4$, MEPT-BF$_4$, or MEEPT-BF$_4$ was dissolved in 20 mL of DCM and transferred to a 4 mm Wilmad-Labglass quartz EPR tube. The spectrum was acquired immediately thereafter at room temperature.

Synthesis of neutral species

N-Ethylphenothiazine (EPT) was synthesized according to a prior report[182]. For small-scale synthesis of MEPT and MEEPT, phenothiazine (1.99 g, 0.0100 mol) was dissolved in anhydrous N,N-dimethylformamide (DMF, 20 mL) under nitrogen atmosphere. A 60% dispersion

of sodium hydride (NaH) in mineral oil (0.48 g, 0.012 mol) was added, and the reaction mixture was heated to 60 °C for 30 min. Then, 2-chloroethyl methyl ether (1.10 mL, 0.012 mol, for MEPT) or 1-bromo-2-(2-methoxyethoxy)ethane (1.62 mL, 0.012 mol, for MEEPT) was added, and the reaction mixture was stirred at 60 °C for 12 h. The reaction was quenched by pouring the contents into ice water, after which the organic components were extracted with ethyl acetate three times, and the combined extracts were washed with brine. The organic extracts were dried over magnesium sulfate ($MgSO_4$), filtered to remove solids, and concentrated by rotary evaporation. The crude product was purified by column chromatography using a gradient of 0 to 10% ethyl acetate in hexanes to afford the desired products after concentration by rotary evaporation.

N-(2-Methoxyethyl)phenothiazine (MEPT). Yield: 2.16 g (84%). White crystalline solid (m.p. 47 °C). ^{1}H NMR (400 MHz, $CDCl_3$) δ1.57 (H_2O), 3.40 (s, 3H), 3.76 (t, 2H, J = 6.4 Hz), 4.09 (t, 2H, J = 6.4 Hz), 6.89–6.94 (m, 4H), 7.12–7.17 (m, 4H). ^{13}C NMR (100 MHz, $CDCl_3$) δ 47.5, 59.2, 69.9, 115.3, 122.7, 124.8, 127.5, 127.6, 145.1. EI-MS: *m/z* 257 (54%), 212 (100%), 198 (20%), 180 (61%). Anal. calcd for $C_{15}H_{15}NOS$ C, 70.01; H, 5.88; N, 5.44. Found C, 69.99; H, 5.91; N, 5.39.

N-[2-(2-Methoxyethoxy)ethyl]phenothiazine (MEEPT). Yield: 2.22 g (74%). pale yellow oil. ^{1}H NMR (400 MHz, $CDCl_3$, Me_4Si) δ 1.55 (H_2O), 3.38 (s, 3H), 3.53–3.56 (m, 2H), 3.64–3.66 (m, 2H), 3.85 (t, 2H, J = 6.5 Hz), 4.12 (t, 2H, J = 6.5 Hz), 6.90–6.93 (m, 4H), 7.11–7.16 (m, 4H). ^{13}C NMR (100 MHz, $CDCl_3$, Me_4Si) δ 47.5, 59.2, 68.5, 70.8, 72.1, 115.4, 122.8, 124.8, 127.5, 127.6, 145.1. EI-MS: *m/z* 301 (48%), 212 (100%), 198 (22%), 180 (46%). Anal. calcd for $C_{17}H_{19}NO_2S$ C, 67.75; H, 6.35; N, 4.65. Found C, 67.48; H, 6.41; N, 4.88.

For a large-scale synthesis of MEEPT, phenothiazine (10.00 g, 0.05025 mol) was dissolved in anhydrous DMF (120 mL) under nitrogen atmosphere in an oven-dried, three-neck round-

bottomed flask equipped with a reflux condenser. A 60% dispersion of NaH in mineral oil (2.90 g, 0.0725 mol) was added, and the reaction mixture was stirred for 15 min. Then, 1-bromo-2-(2-methoxyethoxy)ethane (8.10 mL, 0.0602 mol) was added, and the reaction mixture was heated and stirred at 60 °C for 16 h. The reaction was quenched by pouring the reaction mixture into ice water, after which the organic components were extracted with diethyl ether, and the organic layer was washed with brine. The organic extracts were dried over $MgSO_4$, filtered to remove solids, and concentrated by rotary evaporation. The crude product was purified by column chromatography using a gradient of 0 to 10% ethyl acetate in hexanes to afford the desired products after concentration by rotary evaporation. Yield: 13.40 g (88%). ^{1}H NMR and mass spectra matched those observed for the small-scale syntheses.

Synthesis of radical-cation salts

The neutral compound (0.001 mol) and anhydrous DCM (10 mL) were added to an oven-dried, round-bottomed flask cooled under nitrogen atmosphere. The resulting solution was purged with nitrogen for 20 min. $NOBF_4$ (0.122 g, 0.00105 mol) was added to the solution, which immediately turned dark orange. The reaction vessel was capped with a rubber septum and the reaction mixture was stirred under nitrogen for 1 h, after which diethyl ether (20 mL) was added gradually with continued stirring, producing a dark precipitate. The precipitate was filtered, then dissolved in DCM (10 mL) and re-precipitated with a second addition of diethyl ether (20 mL). This process was repeated once more to ensure removal of any unreacted starting material. The final precipitate was dried under vacuum and stored in an argon filled glovebox.

N-Ethylphenothiazine tetrafluoroborate salt (EPT-BF₄). EPT (5.04 g, 0.0222 mol) and NOBF₄ (2.54 g, 0.0233 mol) were reacted according to the general procedure to yield EPT-BF₄ (4.53 g, 65%). Crystals for X-ray diffraction (XRD) were grown in DCM and toluene. A saturated solution of salt in DCM was placed in a NMR tube. Toluene was run down the side of the tube using a syringe to form a discrete layer. The NMR tube was capped and placed in the freezer, and crystals formed at the interface of the solvent layers.

N-(2-Methoxyethyl)phenothiazine tetrafluoroborate salt (MEPT-BF₄). MEPT (3.00 g, 0.0116 mol) and NOBF₄ (1.43 g, 0.0122 mol) were reacted according to the general procedure to yield MEPT-BF₄ (2.51 g, 61%). Crystals for XRD were grown by dissolving the salt in DCM and placing this vial inside of another vial containing pentane. The outer vial was capped and was placed in a freezer, and crystals formed through vapor diffusion.

N-(2-(2-Methoxyethoxy)ethyl)phenothiazine tetrafluoroborate salt (MEEPT-BF₄). MEEPT (16.1 g, 0.0534 mol) and NOBF₄ (6.55 g, 0.0561 mol) were reacted according to the general procedure to yield MEEPT-BF₄ (12.5 g, 60%). Crystals for XRD were grown in DCM and toluene. A saturated solution of salt in DCM was placed in a NMR tube. Toluene was run down the side of the tube using a syringe to form a discrete layer. The NMR tube was capped and placed in a freezer, and crystals formed at the interface of the solvent layers.

An Agilent diode-array spectrometer was used to collect UV-vis absorption spectra using ACN or PC as the solvent. Radical-cation salts were dissolved at 0.00015 M in the appropriate solvent and pipetted into optical glass cuvettes (Starna) with a 1 cm path length. Solutions were added to the cuvettes inside an argon filled glovebox and then sealed with a Teflon screw cap. The sealed cuvette was then removed from the glovebox for spectral analysis. Spectra were collected at 0, 1, 3, 5, and 24 h after dissolution.

The solubility limits of the neutral molecules (EPT, MEPT, and MEEPT) and the radical-cation salts (EPT-BF$_4$, MEPT-BF$_4$, and MEEPT-BF$_4$) in pure ACN and an electrolyte comprised of ~0.5 M TEABF$_4$ in ACN were estimated by a shake-flask method. Active material was added in excess to either pure ACN or the electrolyte. Then, the solution was diluted slowly, stirring between additions, with either pure ACN or the electrolyte. The dilution process continued until the active species was dissolved, as determined by visual inspection.

CV experiments were performed using a custom three-electrode cell comprised of a 3 mm diameter glassy-carbon working electrode (CH Instruments), platinum wire counter electrode (CH Instruments), and freshly anodized, un-fritted Ag/AgCl wire reference electrode. Electrochemical data was collected on a CH Instruments 650E potentiostat. No solution resistance compensation (iR correction) was applied. Electrolytes were comprised of 0.001 M neutral active material (EPT, MEPT, or MEEPT), 0.1 M TEABF$_4$, and either ACN or PC as the solvent. In some experiments, ~0.0007 M ferrocene was added as an internal reference. Redox (half-wave) potentials ($E_{1/2}$) were calculated as the mean potential between CV peaks from voltammograms recorded at 100 mV/s and are reported relative to the Fc/Fc$^+$ internal reference. Diffusion coefficients of the active species were determined using Randles–Sevcik analysis (Equation 1) and the peak currents of voltammograms, at the following scan rates: 25, 50, 75, 100, 200, 300, 400, and 500 mV/s. In Equation 1, i_p is the peak current (A), n is the number of electrons transferred (mol$_e$/mol), A is the electrode surface area (cm^2), C is the reactant concentration (mol/cm), s is the scan rate (V/s), R is the gas constant (J/mol/K), T is temperature (K), and D is the diffusion coefficient (cm^2/s).

$$i_p = 0.4463 nFAC \left(\frac{nFD}{RT} v \right)^{0.5} \tag{1}$$

Bulk electrolysis experiments were performed in custom H-cells, similar to those reported by Laramie et al.[162], which have two 3.5 mL electrolyte chambers separated by an ultra-fine porous glass frit (P5, Adams and Chittenden). The glass frit helped to minimize species crossover between the two compartments. In one chamber, a piece of reticulated vitreous carbon (45 PPI, Duocell) served as the working electrode, and a fritted $Ag/Ag(cryptand)^+$ reference electrode contained saturated cryptand, 0.010 M $AgBF_4$, and 0.5 M $TEABF_4$ in PC[189]. In the second chamber, another piece of reticulated vitreous carbon served as the counter electrode. Both the working and counter electrode chambers were continuously stirred during bulk electrolysis cycling. A Biologic VMP3 potentiostat applied a constant current of 0.469 mA, equivalent to a C-rate of 1C, for 10 cycles (7 h). Potential cut-offs of ~0.1 and 0.5 V $vs.$ Fc/Fc^+ were imposed on the working electrode to avoid accessing undesired redox couples or electrolyte decomposition. A 3 mm glassy-carbon working electrode (CH Instruments) was used to record CVs of the electrolyte in the working electrode chamber before and after cycling. Electrolytes comprised of 0.005 M neutral active species (EPT, MEPT, or MEEPT), 1 M $TEABF_4$, and ACN were added to the working electrode chamber, while the counter-electrode chamber contained electrolytes of 0.005 M radical-cation active species (EPT-BF_4, MEPT-BF_4, or MEEPT-BF_4), 1 M $TEABF_4$, and ACN.

Small volume custom flow cells with interdigitated flow fields, as previously described by Milshtein et al., were used in this work (Figure 32)[123]. Flow cell backing plates were machined from polypropylene, which was selected due to its chemical compatibility with ACN. Flow fields were machined from 3.18 mm thick impregnated graphite (G347B, MWI, Inc.). Electrodes were cut from 190 ± 30 µm thick carbon paper (25 AA, SGL group) and used as received without any pre-treatments. Two pieces of carbon paper were layered together to serve as electrodes for both sides of the flow cell and were compressed by ~20%. A single layer of Daramic 175 served as the

151

battery separator material. The electrodes and separator were sealed into the cell using gaskets cut from flexible polytetrafluoroethylene gasket tape (Gore). The assembled cells had geometric active areas of 2.55 cm^2. Flow cells were assembled outside of the glovebox and then dried for at least 1 h under vacuum (−91 kPa$_g$) before beginning electrochemical testing. All flow cell cycling, impedance, and polarization measurements were performed inside an argon filled glovebox.

Sealed jars (10 mL, Savillex), made from perfluoroalkoxy alkane (PFA), housed the electrolyte. A peristaltic pump (Masterflex L/S Series) carried the electrolyte into the flow cell at 10 mL/min. Norprene tubing (Masterflex) was used inside the pump head, while PFA tubing (Swagelok) connected the pump head, reservoir, and flow cell together. All tubing had an inner diameter of 1.6 mm. All tubing connections were coupled together with PFA or stainless steel compression fittings (Swagelok). The fully assembled and filled cell is shown in Figure 33.
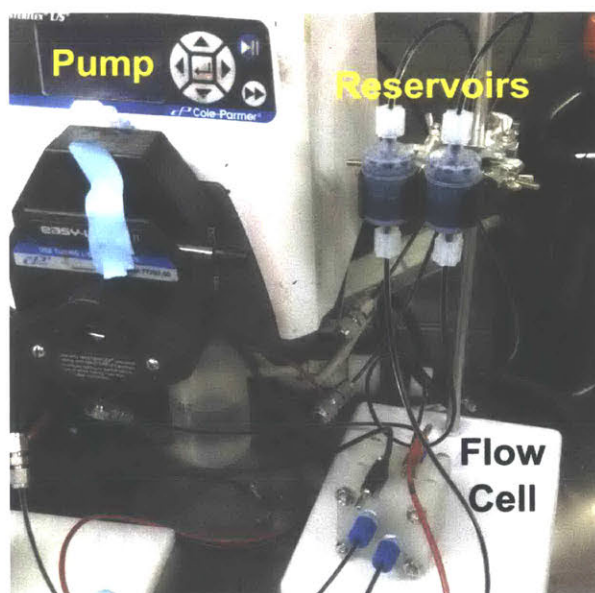
Figure 33: Photograph of the assembled flow cell, connected to the pump and reservoirs.

Starting electrolytes for flow cell experiments were comprised of 0.25 M MEEPT/0.25 M MEEPT-BF$_4$ in 0.5 M TEABF$_4$ in ACN, so that the battery was at 50% SOC. This initial configuration allowed impedance and polarization measurements to be collected at 50% SOC prior

to beginning cycling experiments. Each reservoir contained 0.5 M total active species in 10 mL of electrolyte, enabling a theoretical capacity of 13.4 Ah/L (134 mAh). Impedance measurements were recorded about the cell open-circuit voltage (OCV) at 50% SOC, with an amplitude of 10 mV, over a frequency range of 200 kHz to 5 mHz. Polarization measurements were collected by initiating potentiostatic holds for 1 min in alternating ±50 mV steps, allowing for data collection over the range of −0.4 to 0.4 V without significantly changing electrolyte SOC. Data points were recorded every 0.1 s, and the mean current and potential values of the final 50% of data points were used in the I–V curves.

Before beginning symmetric flow cell cycling experiments, a constant current pre-discharge was performed to bring the cell to its fully charged state. Then, cycling experiments were performed by applying a constant current density, calculated from the geometric electrode area (2.55 cm^2). Two total flow cell experiments were performed. In the first experiment, the current density was varied from 50 to 125 mA/cm^2, in increments of 25 mA/cm^2, for 5 cycles at each current density, and potential cut-offs of ±0.45 V were imposed. The cell was then returned to the initial current density of 50 mA/cm^2 for 5 additional cycles. This rate study was completed in 31.8 h. In the second experiment, the flow cell underwent constant current cycling for 100 cycles (80.6 h) at a current density of 100 mA/cm^2, with potential cut-offs of ±0.45 V.

5.3 Results and Discussion

Deprotonation of phenothiazine and a subsequent S$_N$2 reaction with the corresponding alkyl halide produces EPT, MEPT, or MEEPT in good yields (Figure 34). MEPT is a white, crystalline solid with a melting point (47 °C) significantly lower than that of EPT (103–104 °C). MEEPT is a pale yellow

liquid at room temperature. NMR, mass spectrometry, and elemental analysis confirm product structure

and purity.
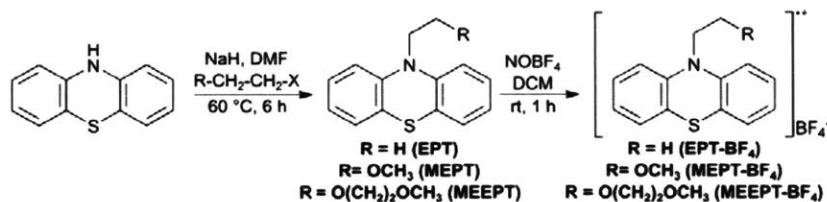
Figure 34: Synthesis of EPT, MEPT, and MEEPT via the alkylation of phenothiazine and subsequent preparation of the radical-cation salts via chemical oxidation.

While phenothiazines have been extensively studied for applications in lithium-ion battery

overcharge protection [126,180–182], the design constraints for RFB active materials are fundamentally

different than those for overcharge protection. Redox-active materials for RFBs must achieve

higher concentrations and have a lower cost per unit mass. We have previously investigated a

highly soluble phenothiazine derivative for RFB applications[127], but the low yielding, multi-step

synthesis currently renders the material infeasible for low-cost NAqRFBs. Hence, the simple one

step synthesis from cheap precursors outlined in Figure 34 represents a new approach towards

achieving a low-cost, soluble active species for NAqRFBs.

Isolation of a neutral redox-active molecule does not ensure the stability of the radical-

cation form, which is typically the more reactive state of a redox-active organic couple. To enable

stability studies of the radical cation itself, we synthesized tetrafluoroborate radical-cation

salts via chemical oxidation of the neutral molecules with nitrosonium tetrafluoroborate (NOBF4)

(Figure 34). We employed single crystal XRD to identify the structures of the radical-cation salts

and confirm their chemical compositions (Figure 35), and EPR (Figure 36) of solutions containing

these salts in dichloromethane (DCM) to confirm the presence of a radical species. The EPR

spectra are consistent with our previous reports of the hexachloroantimonate radical-cation salt of

EPT[182], an expected result due to the similar electronic structure of these *N*-alkylated phenothiazine species.

EPT-BF₄
(a)

MEPT-BF₄
(b)
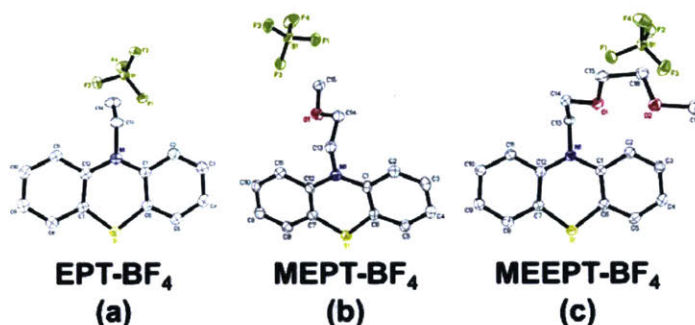
MEEPT-BF₄
(c)

Figure 35: Thermalellipsoid plots of the crystal structures of (a) *N*-ethylphenothiazine tetrafluoroborate (EPT-BF₄), (b) *N*-(2-methoxyethyl)phenothiazine tetrafluoroborate (MEPT-BF₄), and (c) *N*-(2-(2-methoxyethoxy)ethyl)phenothiazine tetrafluoroborate (MEEPT-BF₄).
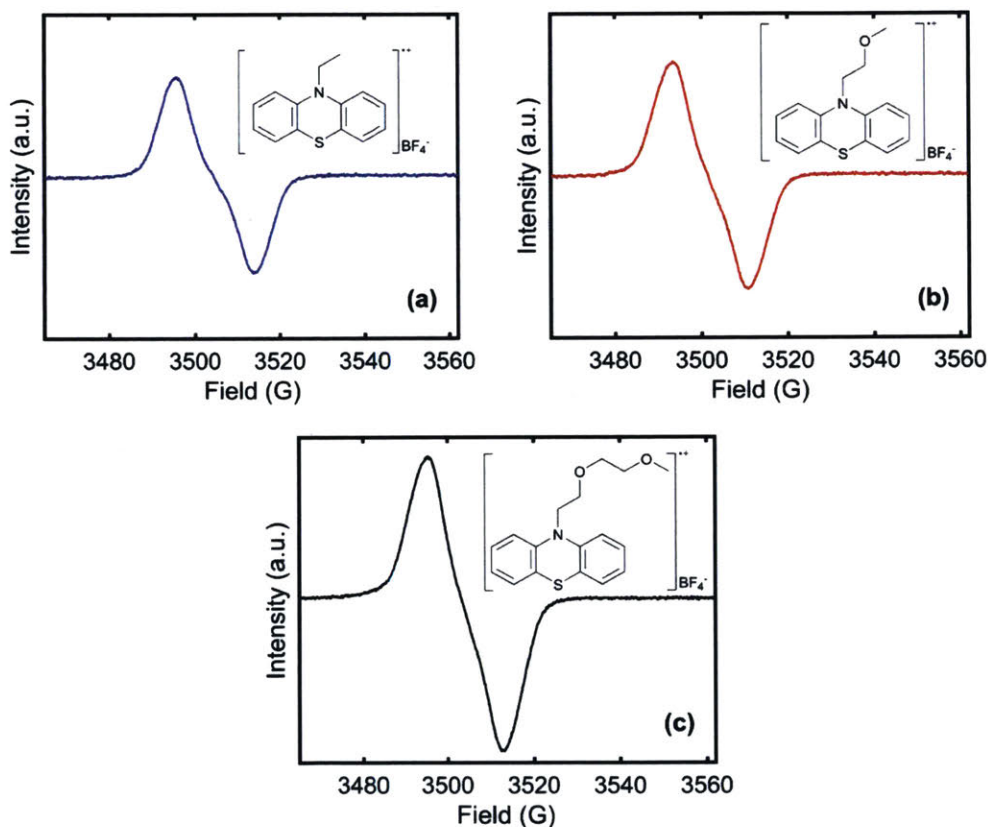
Figure 36: EPR spectra of **(a)** EPT-BF₄, **(b)** MEPT-BF₄, and **(c)** MEEPT-BF₄ salts in dichloromethane.

UV-vis absorption spectroscopy can monitor the lifetimes of radical cations that absorb visible light; this technique has been used to evaluate redox shuttle candidates for overcharge protection of lithium-ion batteries [126,181]. Herein, we employed UV-vis to compare the stability of

dilute solutions of EPT-BF$_4$, MEPT-BF$_4$, or MEEPT-BF$_4$ radical-cation salts in acetonitrile (ACN) and propylene carbonate (PC). Figure 37 depicts the absorption spectra of the three radical-cation salts at 0, 1, 3, 5, and 24 h after dissolution in ACN. The spectra are nearly identical for EPT-BF$_4$, MEPT-BF$_4$, and MEEPT-BF$_4$, exhibiting characteristic peaks at the following wavelengths: 316, 445, 514, 760, and 847 nm. Also, the major peak for all species at 514 nm decays by less than 5% over 24 h in ACN. Due to the low concentration of the active species (0.00015 M) employed in UV-vis measurements, trace impurities in the solvent may contribute to the observed decay, which may not manifest at higher concentrations. For example, the EPT-BF$_4$, MEPT-BF$_4$, and MEEPT-BF$_4$ radical-cation salts undergo a chemical reaction in the presence of nucleophiles such as water, and the neutral molecules undergo a slow chemical decay in the presence of oxygen. As such, this study moves towards investigating the solubility, stability, and performance of EPT, MEPT, and MEEPT in environments relevant to their implementation in a flow battery, employing ACN.
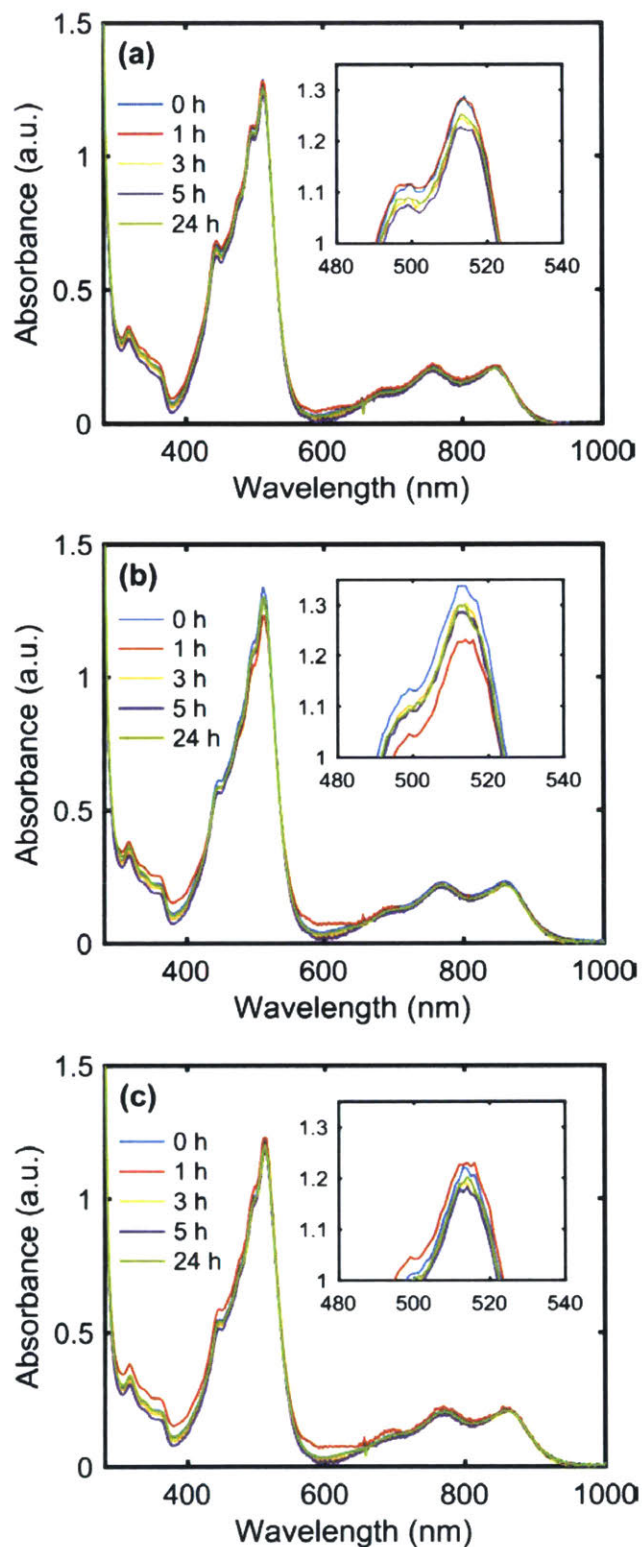
Figure 37: UV-vis spectra of (a) EPT-BF4, (b) MEPT-BF4, and (c) MEEPT-BF4 at 0.00015 M in ACN, recorded at 0, 1, 3, 5, and 24 h after dissolution. Insets: Expansion of the most intensely absorbing peak in the visible region.

157

Knowledge of the active species solubility is of paramount importance when selecting flow battery operating conditions, because a stable battery can only support an active species concentration as high as the solubility of the least soluble oxidation state. The solubilities of MEPT and MEEPT are significantly higher in organic solvents compared to EPT (ca. 0.1 M), perhaps due to the greater polarity of the oligo(glycol) chains relative to the small alkyl group in EPT, as well as the increased disorder arising from the more flexible side-chains (Table 12). MEPT is soluble to >2 M and MEEPT is miscible with both ACN and our electrolyte of interest, 0.5 M tetraethylammonium tetrafluoroborate (TEABF$_4$) in ACN. A later flow cell experiment employs this supporting electrolyte composition.

Table 12: Solubilities of the neutral molecules and their radical-cation salts in pure solvent (ACN) and in supporting electrolyte (0.5 M TEABF$_4$ in ACN). Solubilities are reported in molarity (M)

Solvent	EPT, EPT-BF4	MEPT, MEPT-BF4	MEEPT, MEEPT-BF4
ACN	0.25, 0.2	>2.0, 0.2	Miscible, 0.6
0.5 M TEABF$_4$ in ACN	0.1, 0.1	>2.0, 0.1	Miscible, 0.5

Although MEPT and MEEPT are highly soluble in pure ACN, flow batteries require that the active species remain soluble across all states-of-charge (SOCs) in an electrolyte containing supporting salt, the presence of which can suppress the solubility of redox-active materials[104,162,190]. As such, we investigated the solubilities (Table 12) of the radical-cation salts (EPT-BF$_4$, MEPT-BF$_4$, MEEPT-BF$_4$) in pure ACN solvent and in 0.5 M TEABF$_4$ in ACN. We found that MEEPT-BF$_4$ is 3× to 5× more soluble than the smaller MEPT-BF$_4$, and that, unlike the neutral compounds, MEPT-BF$_4$ solubility does not improve over EPT-BF$_4$. Additionally, the solubilities of all species decrease in the presence of the supporting salt, agreeing with prior studies[104,162,190]. The MEEPT/MEEPT-BF$_4$ couple appears to be the best candidate for flow cell

implementation, pending validation of its electrochemical performance, because that couple maintains the highest solubility in both the neutral and oxidized states.

Economically viable NAqRFBs will require high active-species concentrations (>1 M)[2]. Several prior studies have investigated redox-active organic molecules that exhibit >1 M solubility in pure solvent, in the fully discharged state[113,122,124,125,129]. All of these studies fail, however, to report active species solubility in an electrolyte, containing supporting salt, or the solubility in the fully charged state. Some studies on metal-centered complexes have considered how dual solutes impact solubility[104,162], but still do not mention solubility of the charged species. Arguably, charged species solubilities have been ignored in recent literature due to the difficulty in isolating the charged states of active materials. In the present work, the drastic decreases in MEPT and MEEPT solubilities from the neutral to radical-cation states illustrate an additional molecular design challenge for redox-active organic molecules. The solubilities of the radical-cation salts thereby limit the maximum feasible operating concentrations for MEPT and MEEPT to 0.1 M and 0.5 M, respectively, in a supporting electrolyte of 0.5 M TEABF$_4$ in ACN. These values are less than required concentrations for economic viability, and addressing the challenge of improving the radical-cation salt solubility is a key step to enabling even higher feasible concentrations for future NAqRFB active materials.

CV offers a method of investigating the redox potential, chemical reversibility, kinetics, and diffusion coefficients associated with EPT, MEPT, and MEEPT. Figure 38 presents cyclic voltammograms of the active species in an electrolyte containing 0.1 M TEABF$_4$ in ACN. Like EPT, the first oxidations of MEPT and MEEPT are chemically reversible in CV experiments, with MEPT and MEEPT exhibiting slightly higher oxidation potentials than EPT (Figure 38 and Table 13). This trend in oxidation potential is consistent with the increasing adiabatic ionization

159

potentials (IPs, Table 13) from EPT to MEPT/MEEPT, determined at the B3LYP/6-311G(d,p) level of theory [191–193]. These calculations were performed with the self-consistent reaction field (SCRF) polarizable continuum method[194], implemented in Gaussian09 (revision A.02), employed to model the acetonitrile ($\varepsilon = 35.7$) environment. The variations in IP arise, as expected, from the stronger electron-withdrawing character of the alkylether substituents relative to the ethyl group.
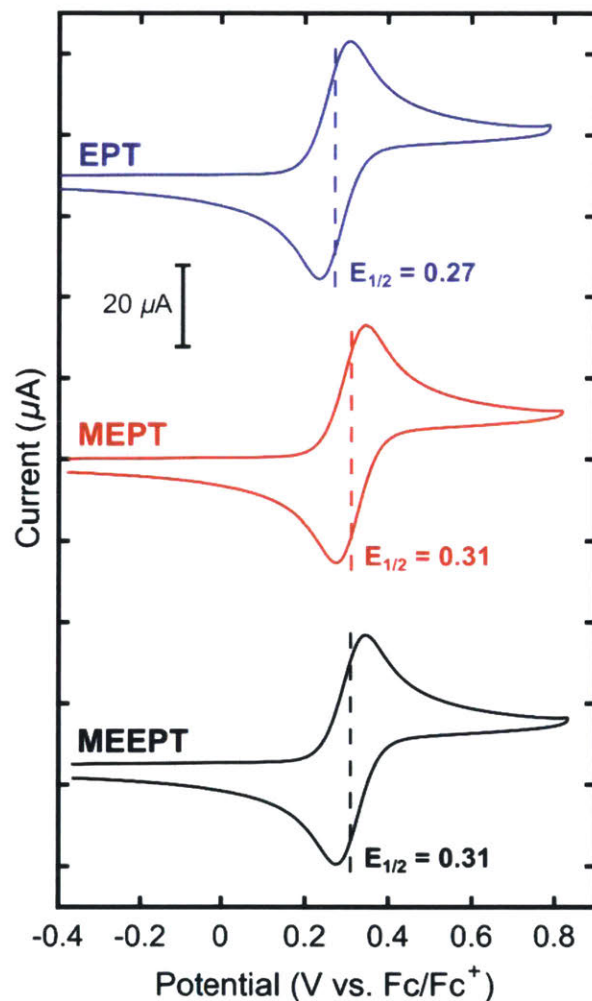
Figure 38: Cyclic voltammograms (cycle 1) of EPT (blue, top), MEPT (red, middle), and MEEPT (black, bottom) at 0.001 M in 0.1 M TEABF$_4$ in ACN. Dashed lines denote the half-wave (redox) potentials ($E_{1/2}$).

Table 13: Calculated adiabatic ionization potentials (IPs), half-wave (redox) potentials (E1/2), and diffusion coefficients for EPT, MEPT, and MEEPT. In all cases, TEABF4 is dissolved at 0.1 M in ACN and the active species concentration was 0.001 M.

Compound	Adiabatic IP (ev)	$E^{0/+}_{1/2}$ (V vs. Fc/Fc$^+$)	Diffusion coefficient ($\times 10^{-5}$ cm^2/s)
EPT	5.08	0.27	1.26
MEPT	5.12	0.31	1.23
MEEPT	5.13	0.31	1.16

A scan rate-dependent CV study (Figure 39) allows for estimation of diffusion coefficients for each active species (Table 13) using Randles–Sevcik analysis (Equation 1). The diffusion coefficients decrease slightly as the size of the active species increases due to increasing solvated radii with increasing molecule size. The CV scan rate study also indicates the electrochemical reversibility of EPT, MEPT, and MEEPT, as the peak separations (~60 mV), peak potentials, and peak current ratios (~1) are invariant with scan rate.
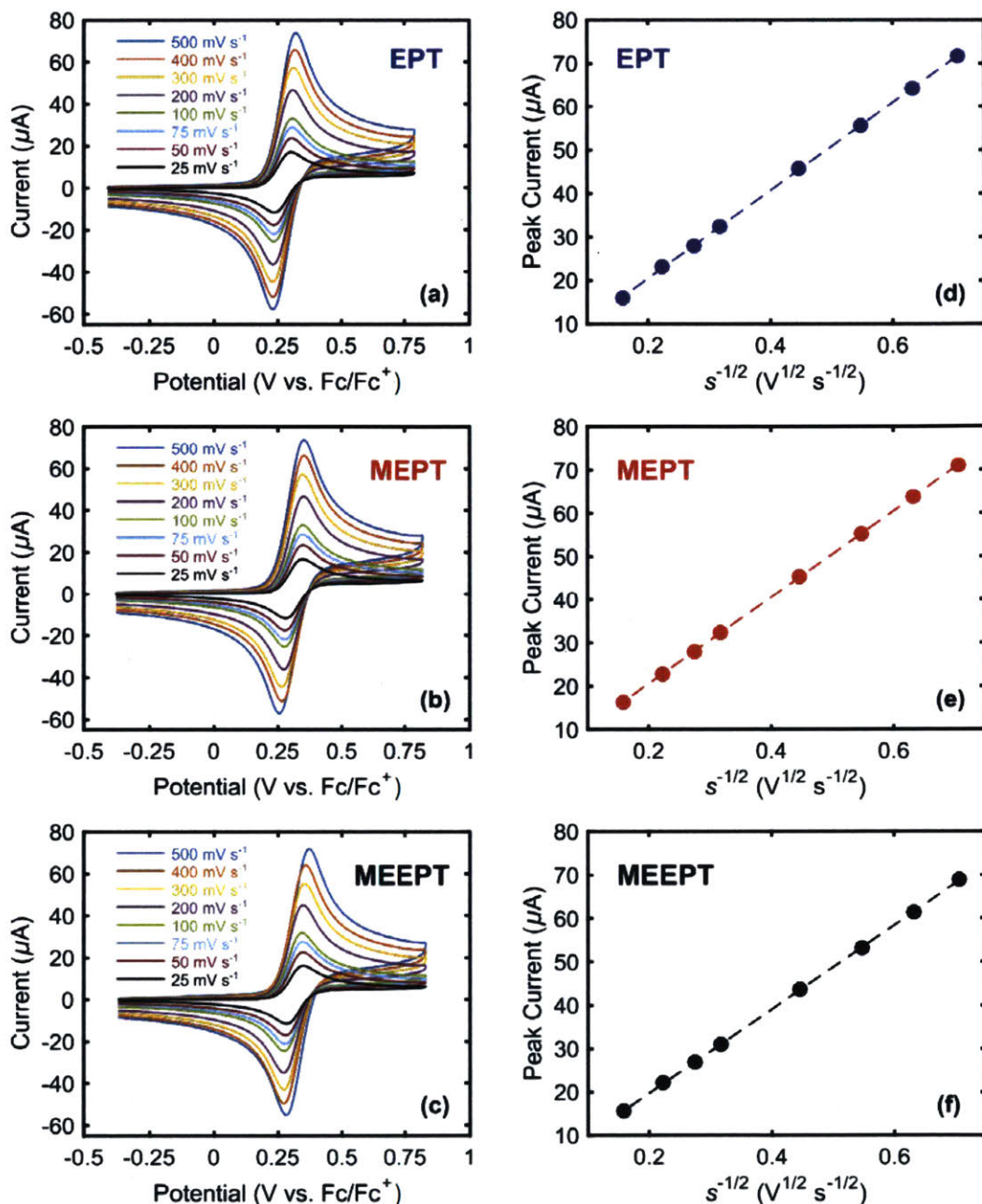
Figure 39: CV scan-rate dependence study for (a) EPT, (b) MEPT, and (c) MEEPT, and Randles-Sevcik construction (peak current vs. square root of scan rate) for the oxidative (anodic) waves of (d) EPT, (e) MEPT, and (f) MEEPT.

Bulk electrolysis experiments allow for further characterization of the electrochemical performance of EPT, MEPT, and MEEPT by assessing the capacity retention of the active species while cycling under dilute conditions for hour time scales. Bulk electrolysis cannot cycle high

concentrations of active material due to mass transfer limitations of the stirred electrolyte, and

contaminant crossover from the counter electrode can poison the working electrode environment,

convoluting capacity-retention data later in the experiment. Nonetheless, bulk electrolysis (Figure

40) can confirm the ability of the active species to charge and discharge at dilute levels.
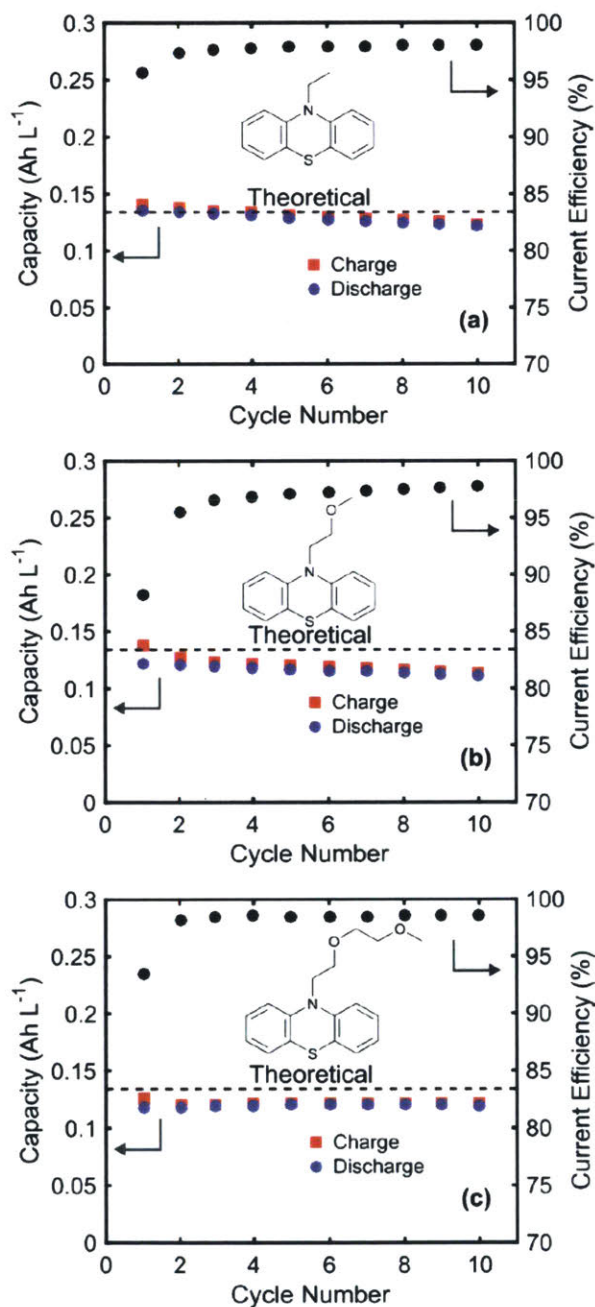
Figure 40: Capacities and current efficiencies from bulk electrolysis cycling experiments of (a) EPT, (b) MEPT, and (c) MEEPT. Theoretical capacities are 0.134 Ah/L (0.469 mAh) for each experiment, and 10 cycles completed in 7 h.

All three active species display reasonable capacity retentions of 87.7%, 82.5%, and 96.8% for EPT, MEPT, and MEEPT, respectively. The capacity fades observed in bulk electrolysis likely arise from crossover through the porous glass frit and deleterious interactions with side product species generated in the counter electrode's chamber or on the counter electrode itself. Mean current efficiencies for EPT, MEPT, and MEEPT in bulk electrolysis were 97.6%, 96.1%, and 98.0%, respectively. Losses in current efficiency likely relate to crossover or side reactions amounting to the corresponding capacity fade. The capacity *vs.* potential cycling curves (Figure 41) validate charging and discharging of the anticipated one electron process for each active species at the redox potentials measured via CV. Further, the measured charge capacities are extremely close to the theoretical capacities, indicating that all of the active material contributes one electron's worth of storage to the available capacity under dilute conditions. Finally, CVs of the active species were collected and analyzed before and after cycling (Table 14), confirming that the electrochemical behavior (e.g., redox potentials, peak heights, peak height ratios) of all active species remains the same. This brief bulk electrolysis study indicates that the active species warrant longer duration cycling experiments in a flow cell, where the counter electrode and poor mass transfer do not confound the results.

Table 14: Quantitative CV characteristics of EPT, MEPT, and MEEPT before and after bulk electrolysis.

	Compound	$E_{1/2}{}^{0/+}$ (V vs. Fc/Fc$^+$)	Peak Separation (mV)	Peak Current Ratio	Peak Oxidative Current (μA)
Before Bulk Electrolysis	EPT	0.284	65	1.050	34.7
	MEPT	0.327	63	1.072	33.9
	MEEPT	0.327	63	0.991	28.7
After Bulk Electrolysis	EPT	0.261	78	0.964	36.8
	MEPT	0.327	70	1.005	33.2
	MEEPT	0.324	76	1.004	30.5
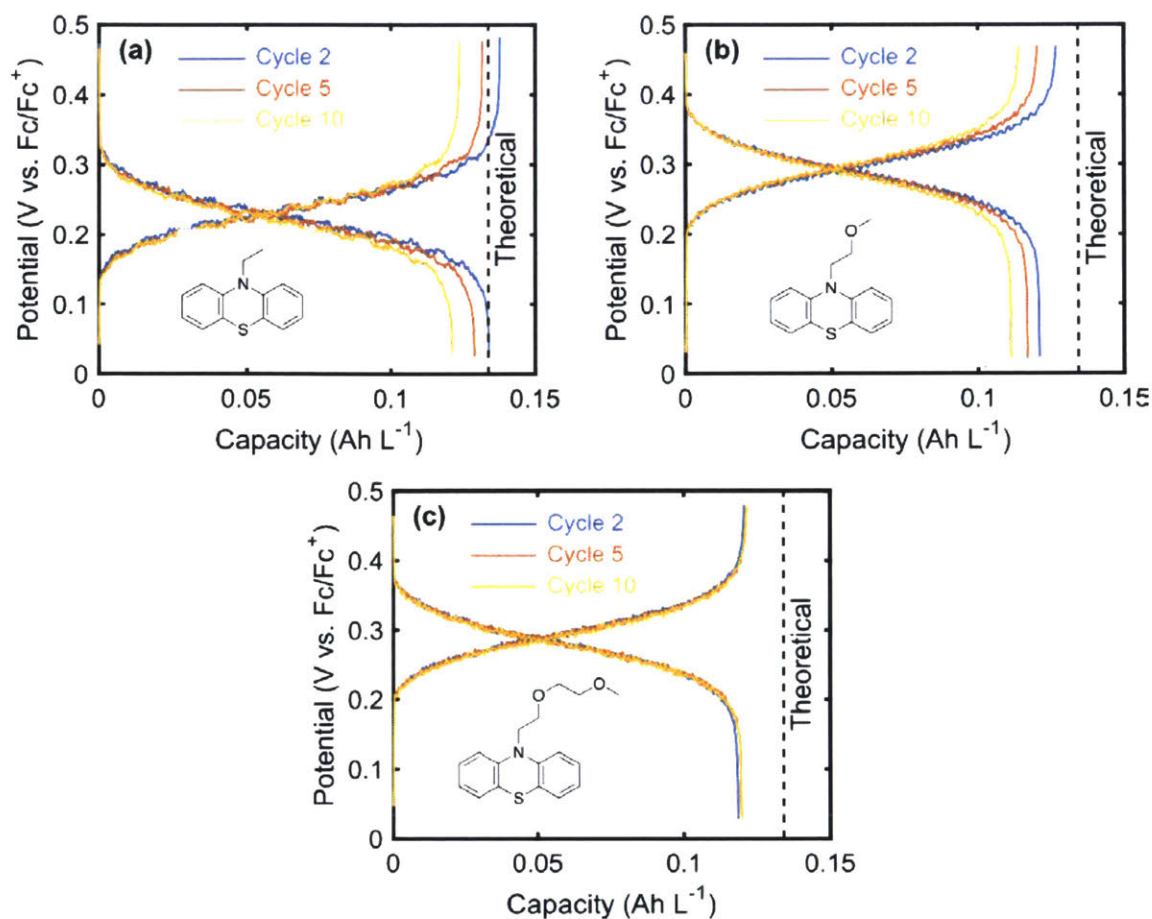
Figure 41: Potential vs. capacity curves from bulk-electrolysis experiments showing cycles 2, 5, and 10 for each of (a) EPT, (b) MEPT, and (c) MEEPT at 0.005 M in 1 M TEABF4 in ACN. Theoretical capacities are 0.134 Ah/L (0.469 mAh) for each experiment, and 10 cycles completed in 7 h.

Given that EPT, MEPT, and MEEPT perform very similarly in radical-cation stability, CV, and bulk electrolysis experiments, we use solubility to determine which derivative to use in flow-cell cycling experiments, choosing the most soluble active species, MEEPT. The stability and solubility of the MEEPT-BF4 radical-cation salt allows for symmetric flow cell cycling, a technique recently introduced[123]. The symmetric flow cell technique offers several advantages when investigating the capacity retention of a single active species. First, this technique allows for simultaneous cycling of both the neutral and oxidized species in the MEEPT redox pair to determine MEEPT stability under flow cell conditions in the absence of any other species. Second,

unlike bulk electrolysis, symmetric flow cell cycling removes the need for a counter electrode of a dissimilar material, eliminating the possibility of side products crossing from the counter electrode chamber and contaminating the working electrode. Thus, the symmetric flow cell technique offers a more controlled electrolyte environment as compared to bulk electrolysis. Third, the flowing electrolyte improves mass transfer of active species to the electrode surface, enabling higher concentration and high current density studies. Finally, the symmetric flow cell investigates capacity retention using porous carbon electrodes relevant to flow-battery applications (e.g., carbon paper) instead of reticulated vitreous- or glassy-carbon[123].

Figure 42a shows a schematic of the symmetric flow cell, where MEEPT is the starting positive electrolyte (posolyte) active species, and MEEPT-BF$_4$ is the initial negative electrolyte (negolyte) active species. Accordingly, a tetrafluoroborate anion must migrate across the separator, and the active species on either side of the cell oscillates between MEEPT and MEEPT-BF$_4$. For all flow cell experiments in this work, both reservoirs initially contain electrolyte pre-mixed at 50% SOC to allow for polarization (Figure 42b) and impedance measurements (Figure 42c) prior to cycling. Polarization measurements illustrate the high rate capability of the flow cell employed in this work, achieving current densities as great as $\sim$110 mA/cm^2 at $\pm$0.4 V. These high current densities are possible due to a low cell ASR, as indicated by the impedance spectrum in Figure 42c. The low-frequency intercept denotes the total direct current (DC) contribution (R_{DC}) to the cell impedance (3.2 Ω cm^2), and closely matches the slope of the polarization curve (3.3 Ω cm^2) for cell potential magnitudes under 0.15 V, indicating that the Nyquist plot low frequency intercept is a good measure of the cell ASR for small overpotentials.
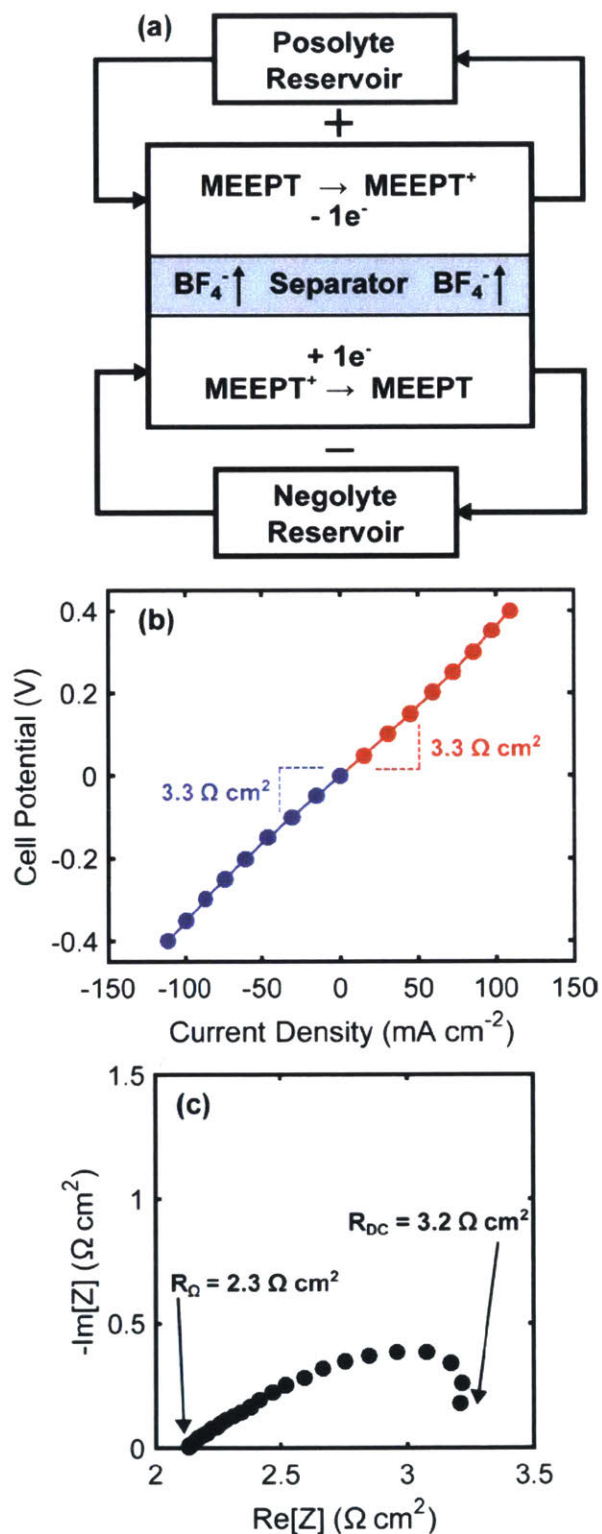
Figure 42: (a) Schematic of the MEEPT symmetric flow cell during charging. (b) Polarization curve and (c) Nyquist plot of the flow cell at 50% SOC before cycling.

The ohmic contribution (R_Ω = 2.3 Ω cm^2) to the cell ASR is similar to that of a prior NAqRFB study employing a Daramic separator and similar supporting electrolyte[178]. Further, the linearity of the polarization curve at low overpotentials (<0.15 V) suggests that the charge transfer (kinetic) resistance contribution to the total ASR is small and unchanging. Impedance analysis confirms the small charge transfer resistance due to the absence of a distinct charge transfer impedance feature. Redox-active organic molecules in nonaqueous electrolytes typically exhibit fast kinetic rate constants (i.e., greater than 10^{-3} cm/s)[2], as confirmed for MEEPT in the CV scan rate study, which leads to negligibly small charge transfer losses[123]. At higher cell potentials (>0.15 V), the polarization curve begins to deviate from linearity slightly due to the increasing mass-transfer limitation; at even higher overpotentials, the cell would approach limiting current. Overall, the cell ASR in this work is low in comparison to recent NAqRFB cycling literature[111,113,195], outperforming the lowest reported ASR to date by a factor of two[178]. The ASR reported here is on par with recommended values for enabling cost competitive NAqRFBs (2.3–5.0 Ω cm^2)[2,118].

The low cell ASR facilitates high rate cycling of MEEPT at high current densities not previously achieved by nonaqueous flow cells. The first flow cell cycling experiment engages a rate study to understand variations in accessed capacity with increasing current density and to select optimized parameters for a long duration cycling experiment. Figure 43 shows capacity vs. potential curves, as well as the accessed charge and discharge capacities. For constant current cycling at 50, 75, 100, and 125 mA/cm^2, the accessed capacities are 97.3%, 86.3%, 66.7%, and 35.0% of the theoretical (13.4 Ah/L), respectively. As anticipated, the accessed capacity decreases with increasing current density due to larger cell polarization. The rate study also

demonstrates the stability of MEEPT and the resiliency of this system's capacity after undergoing

high rate cycling; the capacity in cycle 25 rebounded to 99.8% of the accessed capacity in cycle 5.
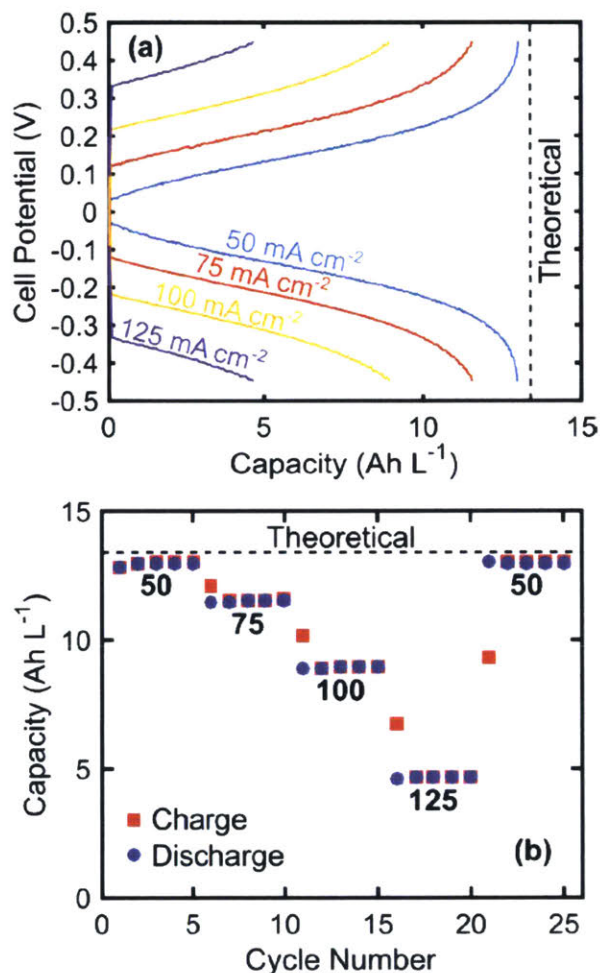
Figure 43: Rate study of MEEPT cycling in a symmetric flow cell, showing (a) capacity *vs.* potential for various current densities. Potential curves are from the 5th cycle at each current density. (b) Cycle number *vs.* capacity for various current densities. Numbers underneath each capacity segment represent current densities with units of mA/cm^2. Potential cut-offs imposed during the flow cell experiment were ±0.45 V. The theoretical capacity (dashed line) is 13.4 Ah/L (134 mAh), and the experiment runtime was 31.8 h.

From the rate study, we chose a current density of 100 mA/cm^2 to demonstrate long

duration cycling of MEEPT. Figure 44a shows select capacity *vs.* potential curves over 100 cycles;

each curve is nearly identical, indicating that no new electrochemical processes arise during

cycling and highlighting again the robust stability of MEEPT. Also, Figure 44b displays the charge

169

and discharge capacities as a function of cycle number, as well as the current efficiencies. The capacity rises slightly in the first ca. 15 cycles because the cell is assembled at 50% SOC, after which the capacity and current efficiencies stabilize. The mean capacity accessed is 76.9% (10.3 Ah/L) of the theoretical value (13.4 Ah/L), and after cycle 1, all cycles access were between 74.8 and 77.6% of the theoretical capacity. These charge depths are close to a recommended value of 80% for economically viable cycling of RFBs[2]. Capacity fade is undetectable over the 100 cycles of the symmetric flow cell experiment, solidifying MEEPT as a highly stable redox-active molecule, especially considering the total runtime (80.6 h) of the experiment. The mean current efficiency for this cell is 99.5%, and given the high capacity retention, current inefficiencies are most likely due to crossover through the porous Daramic separator. After the cycling experiment completed, the flow cell did not show signs of degradation to any of the components, including the Daramic separator, Gore gaskets, carbon paper electrodes, graphite flow fields, tube fittings, tubing, reservoirs, or polypropylene backing plates. As a whole, the long duration flow-cell cycling experiment combines a robust active material with an advanced cell design, permitting stable, deep charge, and high rate cycling of a NAqRFB active material in an unprecedented manner.
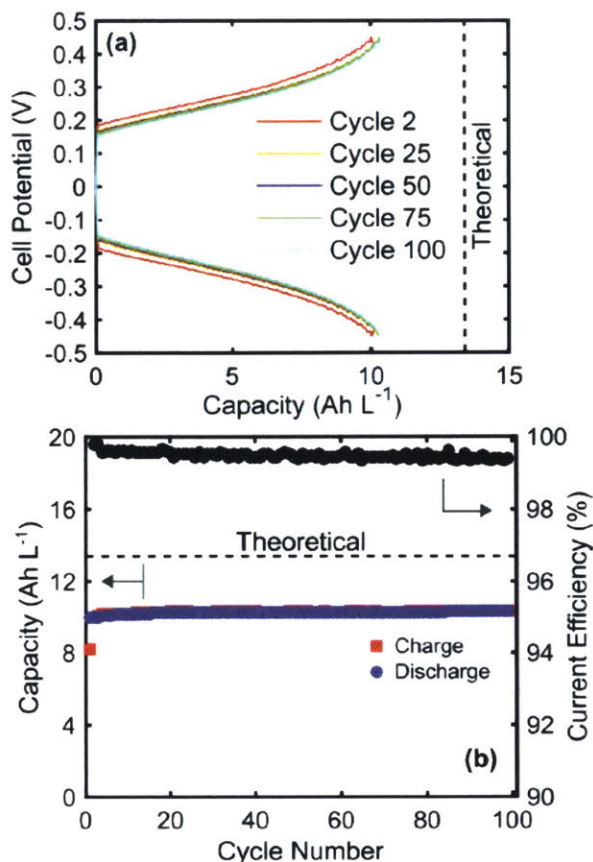
Figure 44: Constant current cycling of MEEPT in a symmetric flow cell at 100 mA/cm^2: (a) capacity *vs.* potential; (b) charge (red ■) and discharge capacities (blue ●), as well as current efficiencies (black ●), as a function of cycle number. Potential cut-offs imposed during the flow cell experiment were ±0.45 V. The theoretical capacity (dashed line) is 13.4 Ah/L (134 mAh), and the experiment runtime was 80.6 h.

5.4   Conclusions

In this work, we demonstrated stable, soluble redox-active organic molecules and a low ASR flow cell for NAqRFBs. By molecular modification of a stable but low solubility parent molecule (EPT), we synthesized two new molecules, MEPT and MEEPT, in a single step each. The inexpensive phenothiazine precursor and straightforward synthesis may enable low-cost scale-up of the new derivatives, which are miscible in ACN and an electrolyte comprised of 0.5 M TEABF$_4$ in ACN. Although both the neutral MEPT and MEEPT exhibit high solubilities, the MEEPT-BF$_4$ radical-cation salt exhibited superior solubility over MEPT-BF$_4$. The solubility of

both radical-cation salts needs to be improved for practical application, presenting a new challenge for rational molecular design. A decay study of the EPT-BF$_4$, MEPT-BF$_4$, and MEEPT-BF$_4$ radical-cation salts under dilute conditions indicates that all three radical species exhibit essentially identical stability. CV shows that all of the molecules considered exhibit electrochemically reversible behavior. The functionalized derivatives (MEPT and MEEPT) have a redox potential of 0.31 V vs. Fc/Fc$^+$, a value slightly higher than that of EPT and in agreement with the calculated IPs. Bulk electrolysis illustrates that all three active species cycle similarly under dilute conditions. Further, we designed a high performance flow cell, with IDFFs and thin carbon paper electrodes, that demonstrates the lowest ASR for a NAqRFB to date (3.2–3.3 Ω cm^2), permitting current densities >100 mA/cm^2. Combining the most soluble compound investigated, MEEPT, with the high performance flow cell, we first engaged a rate study, illustrating the durability of MEEPT and the flow cell's achievable high current densities. Finally, extended cycling of MEEPT at a constant current density of 100 mA/cm^2, with undetectable capacity fade after 100 cycles of deep charging, highlights the unprecedented performance realized through the combination of a robust active material and high performance flow cell.

The molecular and cell engineering principles outlined in this work can be extended to other electrolyte systems proposed for NAqRFBs. Molecular modification of EPT represents a logical pathway towards stable and soluble molecules via facile synthesis, and towards low-cost NAqRFBs with long cycle lifetimes, inexpensive electrolytes, and small mass-transfer losses. The flow cell implements prior advances in aqueous RFB architecture to improve the ohmic and mass-transfer resistances over other nonaqueous flow cell designs. Future molecular engineering will aim to enhance the solubility of the radical-cation species by introducing asymmetry to the active species and varying the counter-anion type[196]. Future cell engineering will focus on scale-up and

further ASR reduction by minimizing separator thickness, increasing operating concentration, and

lowering contact resistances.

6 Stabilizing the Second Electron Transfer of Phenothiazines

Stable electron-donating organic compounds are of interest for numerous applications that require reversible electron-transfer reactions. Although many organic compounds are stable one-electron donors, removing a second electron from a small molecule to form its dication usually leads to rapid decomposition. For cost-effective electrochemical energy storage utilizing organic charge-storage species, the creation of high-capacity materials requires stabilizing more charge whilst keeping molecular weights low. Here we report the simple modification of N-ethylphenothiazine, which is only stable as a radical cation (not as a dication), and demonstrate that introducing electron-donating methoxy groups *para* to nitrogen leads to dramatically improved stability of the doubly oxidized (dication) state. Our results reveal that this derivative is more stable than an analogous compound with substituents that do not allow for further charge delocalization, rendering it a promising scaffold for developing atom-efficient, two-electron donors. This chapter is partially reprinted from "Engineering Stable Two-Electron-Donating Electro-active Organic Materials" by **Jeffrey A. Kowalski**, Matthew D. Casselman, Aman P. Kaur, Jarrod D. Milshtein, Subrahmanyam Modekrutti, Naijao Zhang, N. Harsha Attanayake, Sean R. Parkin, Chad Risko, Fikile R. Brushett, and Susan A. Odom from The Journal of Materials Chemistry A (2017, 5, 24371-24379)[148].

6.1 Introduction

Phenothiazines provide a promising and scalable platform for the development of electron-donating materials. Indeed, derivatization of phenothiazine has afforded numerous products in the pharmaceutical industry (e.g., methylene blue, promethazine, and chlorpromazine)[197–199]. The general stability of phenothiazine derivatives in the radical-cation form has enabled their

incorporation as one-electron donors in a variety of electronic and electrochemical devices including photo-redox catalysts in atom-transfer radical polymerizations[200,201], active materials in electrochromic displays[202,203], semiconductors in organic field-effect transistors[149], and redox shuttles in dye-sensitized solar cells[204]. In the field of electrochemical energy storage, phenothiazines have been reported as redox shuttles to protect against cell overcharge and subsequent thermal runaway in Li-ion batteries. Notably, Dahn and co-workers demonstrated extensive overcharge protection of Li-ion cells using N-alkylated phenothiazines as redox shuttles[150,151]. More recently, we have reported effective overcharge mitigation at higher voltages, enabled by molecular functionalization of the phenothiazine core[127,147,180]. Given these properties, phenothiazines hold considerable promise for RFB applications. N-(2-Methoxyethyl)phenothiazine (MEPT) and N-(2-(2-methoxyethoxy)ethyl)phenothiazine (MEEPT) are highly miscible in nonaqueous electrolytes, and their radical cations are sufficiently stable to permit their isolation as crystalline salts[147]. Their stability is further demonstrated by cycling symmetric flow cells containing 0.5 M active material. At constant current densities as high as 100 mA/cm^2, capacity fade was undetectable after 100 deep charge/discharge cycles (experimental runtime of over 80 h)[147].

Although the radical cations of MEPT and MEEPT are stable in a variety of nonaqueous electrolytes, their dication states are subject to rapid decomposition, limiting their capacity to one redox event per molecule. To increase the capacity of phenothiazines for use as active materials in RFBs, we explored derivatization at positions on the periphery of the conjugated ring system, specifically targeting the reactive positions *para* to nitrogen (3 and 7). A variety of derivatives containing substituents at the 3 and 7 positions undergo an irreversible second oxidation event, as determined by cyclic voltammetry (CV) experiments. However, substituents that are both electron-

donating and conjugated could result in extended charge delocalization that may stabilize the dication state. Here, we report the synthesis and characterization of a phenothiazine derivative containing conjugated electron-donating substituents, *N*-ethyl-3,7-dimethoxyphenothiazine (DMeOEPT, Figure 45). For comparison, we examined the performance of parent compound *N*-ethylphenothiazine (EPT, Figure 45) and a derivative containing electron-donating methyl substituents at the 3 and 7 positions (DMeEPT, Figure 45) in which charge delocalization is expected to be less extensive compared to DMeOEPT.
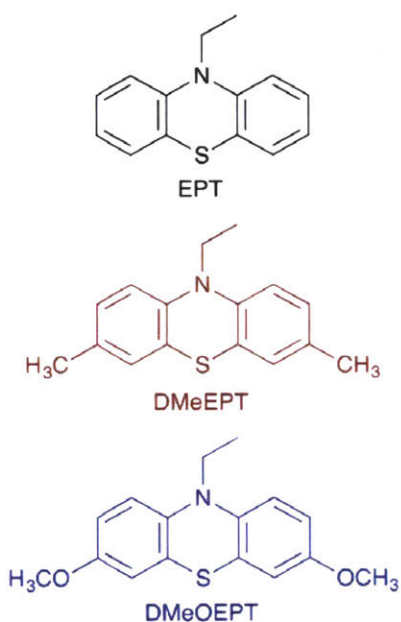
Figure 45: Representations of the chemical structures of N-ethylphenothiazine (EPT, black, top), N-ethyl-3,7-dimethylphenothiazine (DMeEPT, red, middle), and N-ethyl-3,7-dimethoxyphenothiazine (DMeOEPT, blue, bottom).

6.2 Experimental

Synthesis of N-ethyl-3,7-dimethoxyphenothiazine (DMeOEPT). In a 25 mL round-bottomed flask immersed in an ice-water bath, a 5 M solution of sodium methoxide was prepared by dissolving sodium (0.25 g, 0.0096 mol) in methanol (2 mL) under nitrogen atmosphere. To the resultant solution, CuI (0.763 g, 0.00401 mol), 3,7-dibromo-*N*-ethyl-

177

phenothiazine (0.383 g, 0.00100 mol), and anhydrous pyridine (5 mL) were added. The reaction mixture was sparged with nitrogen for 15 min. A reflux condenser was attached and the reaction was heated at 120 °C for 12 h. Upon completion of the reaction, the reaction mixture was diluted with diethyl ether and washed with brine. The organic extracts were dried over magnesium sulfate, filtered to remove solids, and concentrated by rotary evaporation. The organic residue was purified by silica-gel chromatography using 0-10% ethyl acetate in hexanes as eluent to afford the product as a white crystalline solid (0.264 g, 91%). ^{1}H NMR (DMSO-d_6, 400 MHz, ppm) δ 6.88-6.90 (m, 2H), 6.75-6.77 (m, 4H), 3.79 (q, J = 6.8 Hz, 2H), 3.69 (s, 6H), 3.33 (s, H_2O), 1.24 (t, J = 6.8 Hz, 3H). ^{13}C NMR (DMSO-d_6, 100 MHz, ppm) δ 154.5, 138.4, 124.3, 115.9, 112.9, 112.4, 55.4, 41.1, 12.8. GCMS: m/z 287 (41%), 258 (100%), 215 (18%). Anal. calcd. for $C_{16}H_{17}NO_2S$ C, 66.87; H, 5.96; N, 4.87. Found C, 66.70; H, 5.94; N, 4.95. Melting point: 115-116 °C. Crystals for X-ray diffraction were grown in a solution of methanol and water.

Synthesis of N-ethyl-3,7-dimethoxyphenothiazine tetrafluoroborate (DMeEPT-BF$_4$). 3,7-DMeEPT (0.12 g, 0.00047 mol) was dissolved in anhydrous dichloromethane (10 mL) in an oven-dried 50 mL round-bottomed flask fitted with a rubber septum and cooled under nitrogen. The resulting solution was purged with nitrogen for 10 min. Nitrosonium tetrafluoroborate (0.061 g, 0.00052 mol) was added to the solution, which immediately turned dark pink. The reaction vessel was capped and the reaction mixture stirred under nitrogen for 30 min, after which diethyl ether (20 mL) was added gradually with continued stirring, producing a dark precipitate. The precipitate was filtered, then dissolved in DCM (10 mL) and re-precipitated with diethyl ether (20 mL). This process was repeated once more to ensure removal of any unreacted starting material. The final precipitate was dried under vacuum (0.07 g, 44%) and stored in an argon-filled glovebox.

Synthesis of N-ethyl-3,7-dimethoxyphenothiazine tetrafluoroborate (DMeOEPT-BF$_4$). 3,7-DMeOEPT (2.12 g, 0.00739 mol) was dissolved in anhydrous acetonitrile (100 mL) in a 250 mL round-bottomed flask fitted with a rubber septum under nitrogen atmosphere. Nitrosonium tetrafluoroborate (NOBF$_4$, 0.798 g, 0.00700 mol) was added in a single portion, and the reaction was stirred at room temperature for 30 min. Upon completion, the reaction was concentrated under reduced pressure, producing a red solid. This solid was dissolved in dry acetone (ca. 40 mL) and cooled to 0 °C. Hexanes (200 mL) was added to precipitate the radical-cation salt, which was filtered and isolated. The precipitation and isolation procedure was repeated twice. The red solid was then dried under vacuum overnight to remove residual solvent, affording 1.47 g (56%) of product.

X-ray diffraction data were collected at 90.0(2) K on a Nonius kappaCCD diffractometer using MoK(α) X-rays. Raw data were integrated, scaled, merged, and corrected for Lorentz-polarization effects using the HKL-SMN package[205]. Corrections for absorption were applied using SADABS[206]. The structure was solved by direct methods[207], and refinement was carried out against F^{2}by weighted full-matrix least-squares[207]. Hydrogen atoms were found in difference maps but subsequently placed at calculated positions and refined using a riding model. Non-hydrogen atoms were refined with anisotropic displacement parameters. Atomic scattering factors were taken from the International Tables for Crystallography.

All DFT calculations were performed using the Gaussian09 (Revision A.02b) software suite. Geometry optimizations of the neutral, radical-cation, and dication states were carried out with the B3LYP functional and 6-311G(d,p) basis set. Frequency analyses of all (fully relaxed) optimized geometries were performed to ensure that the geometries were energetic minima. Molecular orbitals were generated using an isovalue of 0.04.

Measurements on solutions containing 0.000375 M analyte (EPT, DMeEPT, or DMeOEPT) in 0.1 M LiTFSI in PC were performed using a spectroelectrochemical cell kit from Pine Research Instrumentation. The sample solution (1 mL) was placed in the quartz cuvette equipped with a Pt honeycomb electrode card, used as the working and counter electrodes, and a freshly anodized Ag/AgCl electrode used as the reference electrode. UV-vis spectra were obtained on an Agilent 8453 diode array spectrometer and electrochemical analysis was performed using a CH Instruments 650E potentiostat. First a UV-vis spectrum and a cyclic voltammogram were recorded on the sample. Bulk electrolysis (with coulometry) was then performed for 1 min at 0.1 V increments from 0 to 2.0 V vs. Ag/AgCl (-0.18 to 1.82 V vs. $Cp_2Fe^{+/0}$) for EPT and DMeEPT, or from 0 to 1.5 V vs. Ag/AgCl (-0.18 to 1.32 V vs. $Cp_2Fe^{+/0}$) for DMeOEPT, and then back to 0 V vs. Ag/AgCl for all, followed by a UV-vis measurement at each of those potentials. The chosen potential window was obtained from the cyclic voltammetry measurement.

All electrochemical experiments for molecules evaluated in this study were performed in 1 M LiTFSI in PC. This solvent was chosen because of its wide electrochemical stability window, low volatility, moderate ionic conductivity, and compatibility with lithium salts. Cyclic voltammetry (CV) was performed to determine the chemical and electrochemical reversibility of each oxidation event and the diffusion coefficients of the neutral and radical-cation species. All CV experiments were performed at 0.001 M with 100% IR correction. The resistance measured for each experiment was ca. 200 Ω, which leads to a correction of less than 0.5 mV for the largest measured currents.

All electrochemical measurements were performed in an argon-filled glovebox (MBraun Labmaster) with water <5 ppm and oxygen <1 ppm at 29 °C (ambient box temperature) using a VSP-300 potentiostat (Bio-Logic). All CV experiments were performed in a three-electrode cell

with a 3 mm diameter glassy carbon disc working electrode (CH Instruments, Inc.), a gold coil counter electrode (CH Instruments, Inc.), and a fritted Li foil reference (Alfa Aesar). Before each measurement, the glassy carbon electrode was polished on a MicroCloth pad with 0.05 μm alumina powder (Buehler Ltd.). The electrode was then rinsed with deionized water (Millipore) and wiped with lens paper (VWR). To reference to $Cp_2Fe^{+/0}$, before each electrochemical measurement, an additional CV was performed on an electrolyte solution containing 0.005 M ferrocene; the adjustment in potential of the ferrocene redox couple was applied to electrolyte solutions containing EPT, DMeEPT, and DMeOEPT to calibrate potentials to $Cp_2Fe^{+/0}$ at 0 V, similar to previous examples[208]. Diffusion coefficients for each of the charged and uncharged species were estimated using the Randles–Sevcik equation.

$$i_p = 0.4463nFAC\left(\frac{nFD}{RT}v\right)^{0.5}$$ (1)

In the Randles–Sevcik equation i_p is the peak current (A), n is the number of electrons transferred (here, $n = 1$), F is the Faraday constant (96 485 C/(mol e$^-$)), A is the electrode area (0.0707 cm^2), C is the bulk concentration (0.001 M), R is the universal gas constant (8.314 J/mol/K), T is the temperature in Kelvin (302.15 K), D is the diffusion coefficient (cm^2/s), and v is the scan rate (V/s). The scan rates used to estimate the diffusion coefficients were 20, 30, 40, 50, 60, and 100 mV/s.

Extended-cycling (50-cycle) experiments were performed in a commercially available bulk electrolysis cell from BASi (MF-1056) [14]. All long-term cycling experiments used 30 mL of electrolyte solution with 0.001 M active species and were stirred at 1400 rpm. The working electrode, counter electrode, and reference electrode were reticulated vitreous carbon (BASi),

lithium foil (Alfa Aesar), and fritted lithium foil (Alfa Aesar), respectively. The current for the galvanostatic cycling was set to 0.804 mA, such that the theoretical charging and discharging times were 1 h per electron transfer, based on the concentration and volume of the active material. This rate was selected to enable reasonable experimental runtimes, minimize species crossover, and facilitate high accessed capacity. Each solution was charged and discharged until a predetermined potential cut-off was reached, which was set to completely encompass the redox event. For the two-cycle experiment, a previously reported H-cell with a P5 ceramic frit (Adams & Chittenden Scientific Glass) was used starting with 3.5 mL of electrolyte solution with 0.005 M active species on each side of the frit[129,147]. Reticulated vitreous carbon (45 ppi, ERG Aerospace Corp.) acted as both the working and counter electrodes, while fritted lithium foil (Alfa Aesar) was used as the reference electrode. Again, galvanostatic cycling was used with potential cut-offs set to completely charge and discharge the working solution. The current for the galvanostatic cycling was set to 0.469 mA, such that the theoretical charging and discharging times were 1 h per electron transfer, based on the concentration and volume of the active material. This rate was selected to enable reasonable experimental runtimes, minimize species crossover, and facilitate high accessed capacity. Each solution was charged and discharged until a predetermined potential cut-off was reached, which was set to completely encompass the redox event.

6.3   Results and Discussion

EPT[182] and DMeEPT[180] were synthesized as previously reported. The synthesis of DMeOEPT was accomplished in two high-yielding steps from EPT. Bromination of EPT with *N*-bromosuccinimide gave previously reported 3,7-dibromo-*N*-ethylphenothiazine (DBrEPT)[180]. Subsequent methoxylation was accomplished using sodium methoxide/copper(I)

iodide. In addition to analysis by nuclear magnetic resonance spectroscopy and mass spectrometry, X-ray analysis of single crystals grown in methanol/water confirmed the structure of the product. Atom economy is an important factor for charge storage[2]. At 287 g/mol, the molecular weight of DMeOEPT is 60 g/mol greater than EPT (227 g/mol), constituting an approximate 26% increase in molecular weight. However, if DMeOEPT's doubly oxidized form is stable, an increase of 58% in overall molecular gravimetric capacity could be achieved as compared to parent EPT, which can reversibly donate only one electron.

Cyclic voltammograms of EPT, DMeEPT, and DMeOEPT in propylene carbonate (PC) containing 1 M lithium bis(trifluoromethane)sulfonimide (LiTFSI) are shown in Figure 46. The voltammograms depict electrochemically reversible first oxidation events and the formation of stable radical cations, as evidenced by peak-potential separations of 60–62 mV and peak-current ratios near 1, with all values independent of scan rate (Figure 47). The first oxidation event proceeds most readily for DMeOEPT (0.068 V $vs.$ ferrocenium/ferrocene ($Cp_2Fe^{+/0}$)), followed by DMeEPT (0.174 V $vs.$ $Cp_2Fe^{+/0}$), and then EPT (0.289 V $vs.Cp_2Fe^{+/0}$). This trend is consistent with the Hammett constants of the substituents: methoxy (−0.27) donates more strongly than methyl (−0.17), which, in turn, donates more strongly than hydrogen (0.0)[165]. With EPT and DMeEPT, the second oxidation event is less reversible, as shown by peak separations significantly larger than 60 mV and peak-current ratios greater than 1. While these characteristics suggest the formation of unstable dications in both cases, the peak symmetries are consistent with DMeEPT having a more stable dication than EPT. By contrast, the second oxidation event of DMeOEPT is reversible, with a peak separation of 60 mV and a peak-current ratio of 1.02 ± 0.03, again independent of the scan rate, demonstrating that the DMeOEPT dication is stable on the cyclic voltammetry experimental timescale (ca. 12–120 s). DMeOEPT exhibits similar behavior in 1 M $LiBF_4$ in PC and 1 M

TBAPF$_6$ in acetonitrile, indicating that the second electron transfer is stable in both electrolytes. While the oxidation potentials of DMeOEPT are lower by about 200–300 mV compared to EPT, the ability to access both electron transfer events increases the net potential of this donor. The average potential of the two redox events for DMeOEPT, at ca. 0.350 V $vs.$ Cp$_2$Fe$^{+/0}$, which is about 60 mV higher than the first oxidation potential of EPT at 0.289 V $vs.$ Cp$_2$Fe$^{+/0}$. In general, this tradeoff highlights a key challenge in molecular engineering of active species; specifically, attempting to enhance one property (e.g. molecular charge capacity) can often have unintended negative effects on other desirable properties (e.g. redox potential). Understanding and controlling these tradeoffs is necessary for designing active species with property sets that align with a desired application.
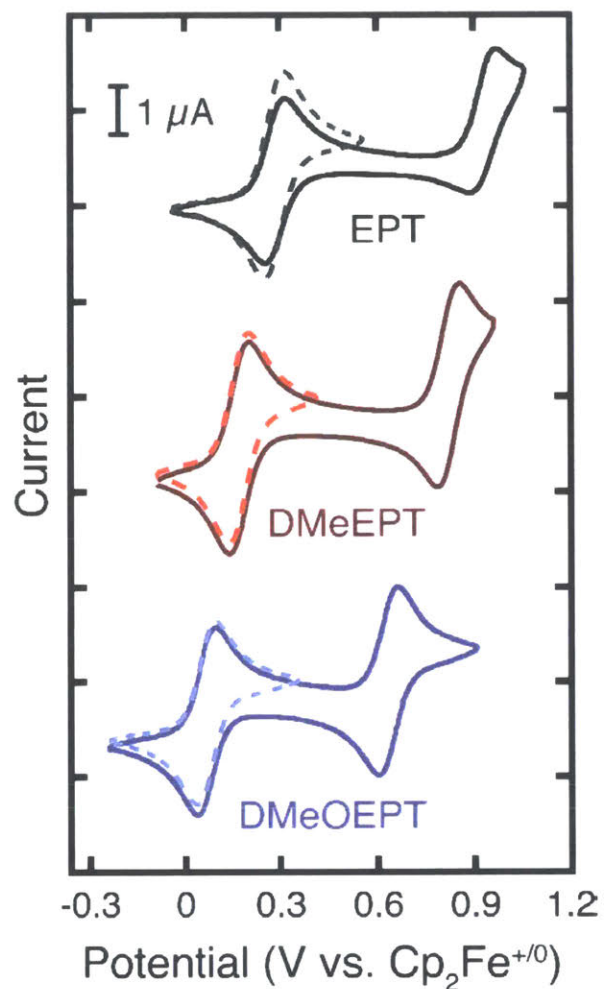
Figure 46: Cyclic voltammograms of the first and second oxidations of 0.001 M EPT (black, top), DMeEPT (red, middle), and DMeOEPT (blue, bottom) in 1 M LiTFSI in PC at a scan rate of 10 mV/s. Solid lines depict CVs accessing both oxidation reactions, while dashed lines depict CVs accessing the first oxidation alone.
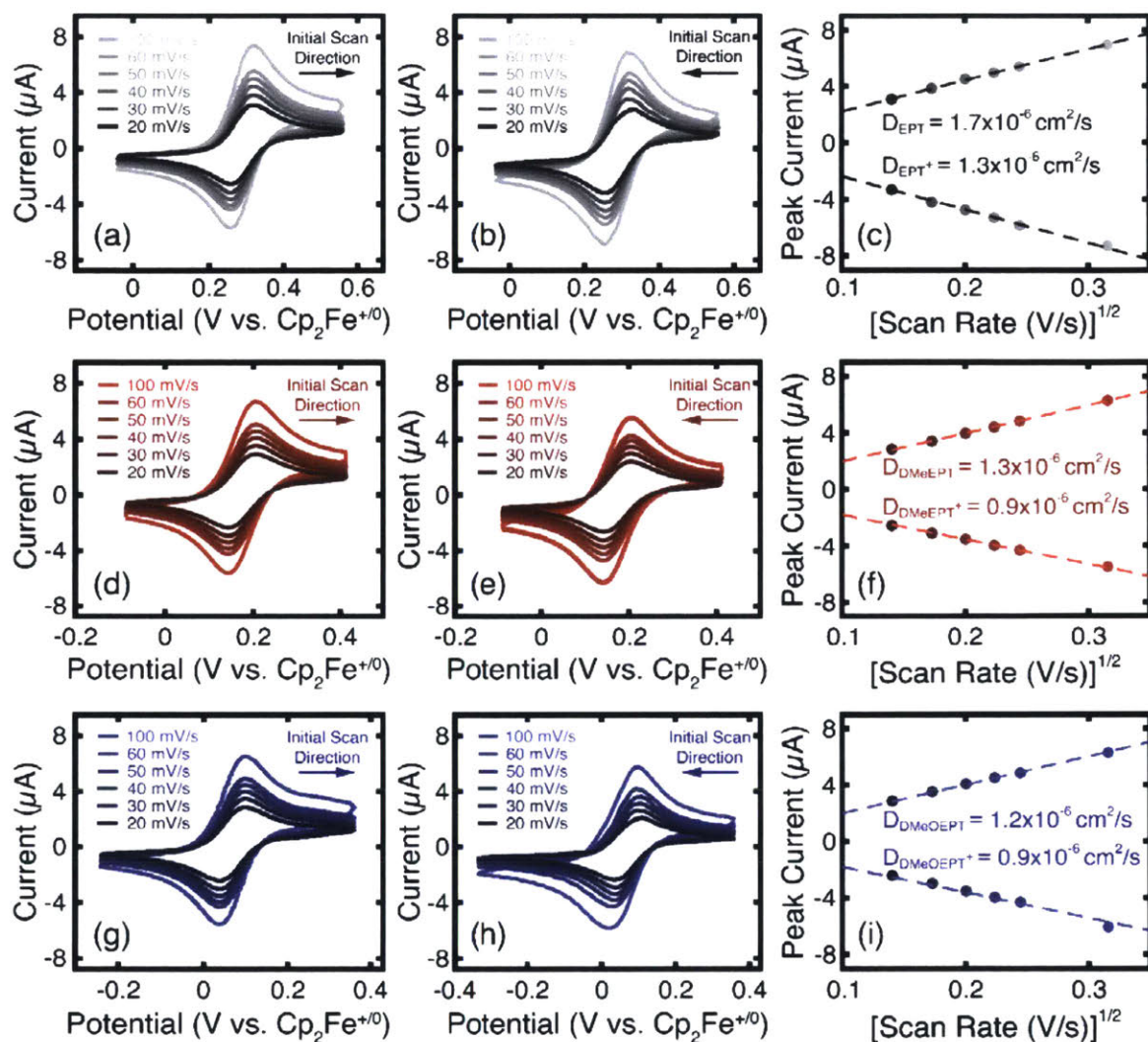
Figure 47: Cyclic voltammograms as a function of scan rate for EPT (a), EPT⁺ (b), DMeEPT (d), DMeEPT⁺ (e), DMeOEPT (g), DMeOEPT⁺ (h), and the corresponding Randles-Sevcik peak-current analysis for EPT/EPT⁺ (c), DMeEPT/DMeEPT⁺ (f), and DMeOEPT/DMeOEPT⁺ (i). All experiments were conducted with 0.001 M active material in 1 M LiTFSI in PC.

Diffusion coefficients were estimated by applying the Randles–Sevcik equation to the positive sweep of the CV for the neutral species and the negative sweep of the CV for the radical-cation salts at various scan rates (Figure 47). As expected, the diffusion coefficient decreases with increasing molecular size. Additionally, the diffusion coefficient for the radical cation of each species is lower than that of the corresponding neutral species, likely due to interactions with counter-ions in solution, which contribute to a larger effective radius. Finally, the relative

186

solubilities of EPT, DMeEPT, and DMeOEPT were measured in the electrolyte. DMeOEPT in

LiTFSI in PC has the lowest solubility of the three compounds examined. For all three compounds,

the radical cation is more soluble than the neutral species, likely due to the polarity of the

electrolyte that results from the high concentration of LiTFSI. All results discussed above are

summarized in Table 15.

Table 15: Measured half-wave potentials, peak separations, and peak-current ratios for the first and second oxidations, diffusion coefficients, and solubilities of EPT, DMeEPT, and DMeOEPT, their tetrafluoroborate radical-cation salts, and their tetrafluoroborate dication salts in 1 M LiTFSI in PC. For clarity, the radical-cation values are italicized and the dication is bolded. All cyclic voltammetry was performed at 0.001 M active material concentration. The peak separations and peak-current ratios were calculated at a scan rate of 10 mV/s.

Compound	First Oxidation			Second Oxidation			Diffusion Coefficient— neutral, *radical cation* ($\times 10^{-6}$ cm^2/s)	Compound Solubility neutral, *radical cation*, **dication** (M)
	Potential (V vs. Cp$_2$Fe$^{+/0}$)	Peak Separation (mV)	Peak Current Ratio ($i_{p,ox}/i_{p,red}$)	Potential (V vs. Cp$_2$Fe$^{+/0}$)	Peak Separation (mV)	Peak Current Ratio ($i_{p,ox}/i_{p,red}$)		
EPT	0.289 ± 0.001	60 ± 1	1.007 ± 0.001	0.928 ± 0.001	73 ± 1	14 ± 5	1.7 ± 0.3 *1.3 ± 0.1*	0.10 ± 0.01 *0.42 ± 0.01*
DMeEPT	0.174 ± 0.001	62 ± 1	1.05 ± 0.01	0.824 ± 0.001	71 ± 2	1.31 ± 0.03	1.3 ± 0.1 *0.9 ± 0.1*	0.07 ± 0.01 *0.12 ± 0.01*
DMeOEPT	0.068 ± 0.001	60 ± 1	1.01 ± 0.01	0.632 ± 0.001	60 ± 1	1.02 ± 0.03	1.2 ± 0.1 *0.9 ± 0.1*	0.05 ± 0.01 *0.15 ± 0.01* **0.10 ± 0.01**

Spectroelectrochemistry was employed to further investigate the redox processes of EPT,

DMeEPT, and DMeOEPT. Dilute solutions of each neutral phenothiazine derivative were prepared

in 0.1 M LiTFSI in PC and placed in a spectroelectrochemical cell, which was used to charge the

solution. Spectra of each species are shown in Figure 48. The absorption spectra of the neutral

species exhibit absorption onsets and lowest-energy maxima at similar values (EPT at 311 nm,

DMeEPT at 314 nm, DMeOEPT at 315 nm). Upon charging, however, significant variations arise.

While the lower-energy features are similar for the radical cations of EPT and DMeEPT, with each

maximum absorbance at 510–550 nm, the radical cation of DMeOEPT exhibits a more intense,

red-shifted absorption feature at 616 nm. The differences among the dication absorption spectra

are even more distinctive. The dication of DMeOEPT displays a characteristic maximum that is blue-shifted by about 20 nm relative to its radical-cation form. This feature is significantly more intense than any feature observed in the UV-visible region for either of the EPT or DMeEPT dications. These results demonstrate that the radical cation and dication of DMeOEPT differ in character from the corresponding forms of EPT and DMeEPT, likely due to greater electronic delocalization onto the methoxy groups compared to the hydrogen atoms in EPT or the methyl groups in DMeEPT.
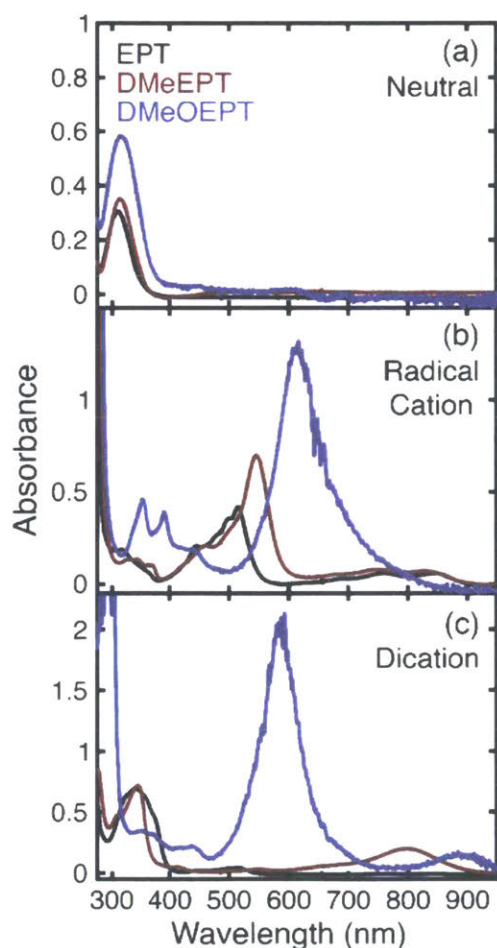
Figure 48: UV-vis spectra of the neutral (a), radical cation (b), and dication (c) of EPT (black), DMeEPT (red), and DMeOEPT (blue) in 0.1 M LiTFSI in PC. The radical cation and dication were generated by bulk electrolysis of solutions consisting of 0.000375 M active material in 0.1 M LiTFSI in PC.

Density functional theory (DFT) calculations were employed to confirm this hypothesis and, in particular, to evaluate whether the methoxy groups would lead to a larger degree of charge delocalization in the dication state of DMeOEPT, thereby impacting its oxidation potentials and overall chemical stability when compared to EPT and DMeEPT[209,210]. The frontier molecular orbitals for the dication states (highest occupied molecular orbital, HOMO; note that this is the HOMO-1 of the neutral species), determined at the UB3LYP/6-311G(d,p) level of theory, exhibit a greater degree of wavefunction delocalization for DMeOEPT as compared to EPT and DMeEPT (Figure 49). Specifically, the π-based wavefunctions extend onto the methoxy oxygens in DMeOEPT. Mulliken charges were used to provide a numerical representation of the charge delocalization in each system (Figure 49). In DMeOEPT, the methoxy groups hold a greater positive charge in the dication state than do the hydrogen atoms in EPT or methyl groups in DMeEPT, occupying the same positions (per *para* substituent: methoxy +0.30, methyl +0.20, hydrogen +0.20) (Figure 49). The molecular length of DMeOEPT (13.8 Å in dication form) is larger than EPT (9.4 Å) and DMeEPT (11.4 Å), allowing for electron density of the DMeOEPT dication to be delocalized over a larger volume and over more atoms (Table 16).
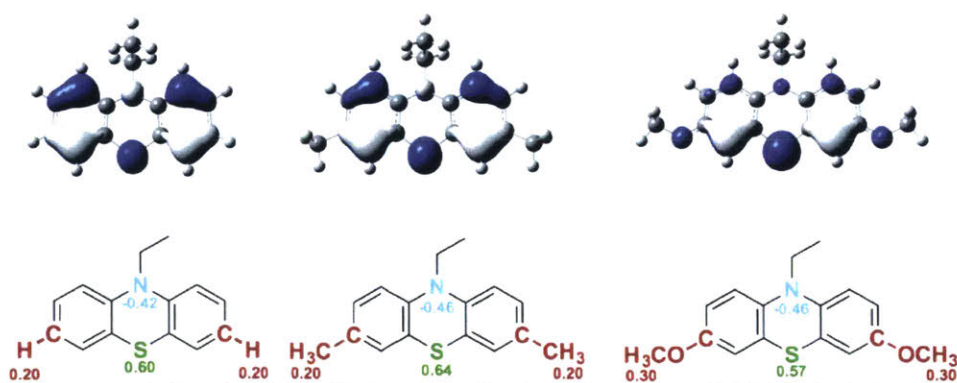
Figure 49: Highest occupied molecular orbitals of the dications (top row) of EPT (left), DMeEPT (middle), and DMeOEPT (right), and select Mulliken charges for the dications of each of the molecules (bottom). All of the calculations were performed by DFT at the B3LYP/6-311G(d,p) level of theory.

Table 16: Molecular lengths (Å) in the neutral, radical-cation, and dication forms of EPT and 3,7-disubstituted derivatives, measured between outermost H atoms (H-H distance) or between outermost C atoms via the internal N atom (C-N-C distance).

| Molecule | Molecular Length (Å) | | | | | |
| | H-H Distance | | | C-N-C Distance | | |
	Neutral	Radical Cation	Dication	Neutral	Radical Cation	Dication
EPT	9.13	9.46	9.44	8.47	8.46	8.44
DMeEPT	11.08	11.54	11.43	11.53	11.52	11.47
DMeOEPT	13.18	13.83	13.83	12.95	12.94	12.96

Bulk electrolysis was used to determine the long-term stability of EPT, DMeEPT, and DMeOEPT. Figure 50 shows the cycling profiles for each of the bulk electrolysis experiments. Figure 51 compiles the charging capacities across all cycling. First, to validate the technique, EPT was cycled through its first oxidation event, which was shown to be reversible on the CV timescale. Charging to 0.6 V vs. $Cp_2Fe^{+/0}$ is sufficient to access the first oxidation event without accessing the second, irreversible event. The coulombic efficiency in this cycling experiment ranged from 99 to 100%, with an overall capacity retention of 96% after 50 charge/discharge cycles at an applied current of 0.804 mA, which should afford a complete charge in 1 hour (Figure 51). The slight capacity fade observed is likely due, at least in part, to species crossover through the porous frit that separates the counter-electrode chamber from the working-electrode chamber of the bulk electrolysis cell. Note that ca. 80% of the theoretical capacity of the electrolyte solution was accessed because the cell must operate at ca. 25% of its limiting current, determined at 0% state of charge, in order to maintain the applied current. Cyclic voltammograms of the solution before and after cycling exhibit similar features (Figure 52), confirming that EPT is stable for the first electron transfer and validating the bulk electrolysis experiment. These results demonstrate the stability of EPT in its neutral and radical-cation forms in the chosen electrochemical environment, consistent with previously reported studies on the stability of EPT[147].

190
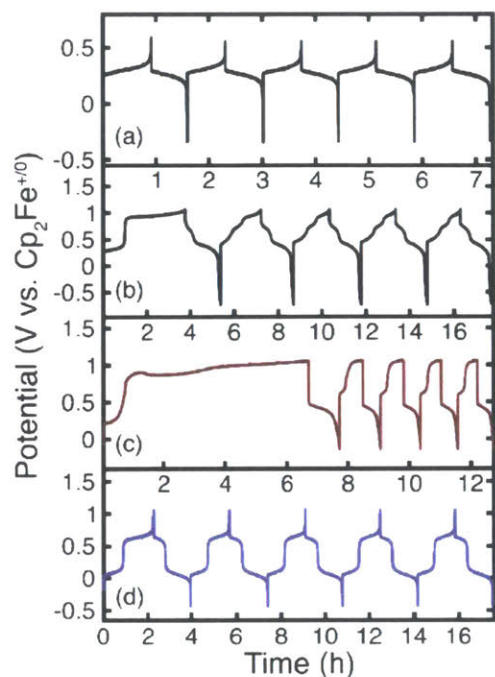
Figure 50: Potential profiles for the first 5 cycles of bulk electrolysis charge/discharge experiments that access the first oxidation reaction of EPT (a). Potential profiles for the first 5 cycles of bulk electrolysis charge/discharge experiments that access the first and second oxidation reactions of EPT (b), DMeEPT (c), and DMeOEPT (d). All cycling was performed at 0.001 M active material in 1 M LiTFSI in PC at a constant applied current of 0.804 mA.
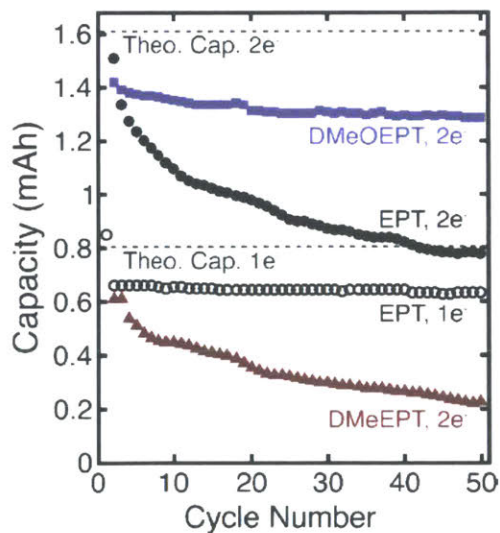
Figure 51: Charging capacity *vs.* cycle number for bulk electrolysis charge/discharge experiments that access the first oxidation reaction of EPT (hollow, black circles), or both oxidation reactions for EPT (filled, black circles), DMeEPT (filled, red triangles), or DMeOEPT (filled, blue squares). All experiments were performed at 0.001 M active species in 1 M LiTFSI in PC at a constant applied current of 0.804 mA. Note, in an attempt to represent the capacity more clearly, the first cycle for charging each material to two electrons is not shown because the accessed capacity for EPT and DMeEPT is much greater than the theoretical capacity.
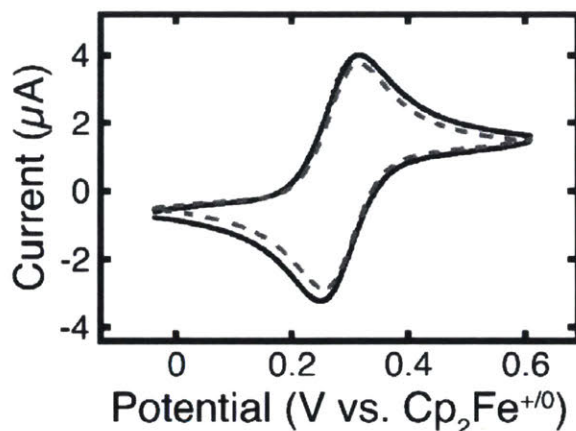
Figure 52: Cyclic voltammograms of 0.001 M EPT in 1 M LiTFSI in PC before (solid line) and after (dashed line) 50 cycles of bulk electrolysis accessing only the first oxidation of EPT. Voltammograms were recorded at a scan rate of 20 mV/s.

Bulk electrolysis was then extended to access the second oxidation of EPT using a fresh solution, which we expected would demonstrate the poor stability of EPT's dication. A cut-off potential of 1.05 V *vs.* $Cp_2Fe^{+/0}$ is sufficient to access the second oxidation event while minimizing electrolyte decomposition. After the first charge/discharge cycle, a new redox plateau appeared between the first and second oxidation potentials, suggesting the presence of a new redox species (Figure 50b). This hypothesis is further supported by the initial charging half-cycle, which was nearly twice as long as expected (4 h rather than 2 h), suggesting an interplay between electrochemical oxidation and chemical reduction processes due to the instability of the dication form. All subsequent cycles exhibited three charging plateaus and two discharging plateaus. Over the course of the experiment, the cell capacity decreased by 50% (Figure 51). The coulombic efficiency (Figure 53) ranged between 88 to 95% for the first 10 cycles, during which EPT decayed at a higher rate, accounting for roughly 65% of the total decay. After this initial period, the coulombic efficiency stabilized between 96 and 97%, and the EPT decay rate slowed. Cyclic voltammetry recorded before and after bulk electrolysis showed significant decay, as evidenced by the disappearance of well-defined redox waves (Figure 54).
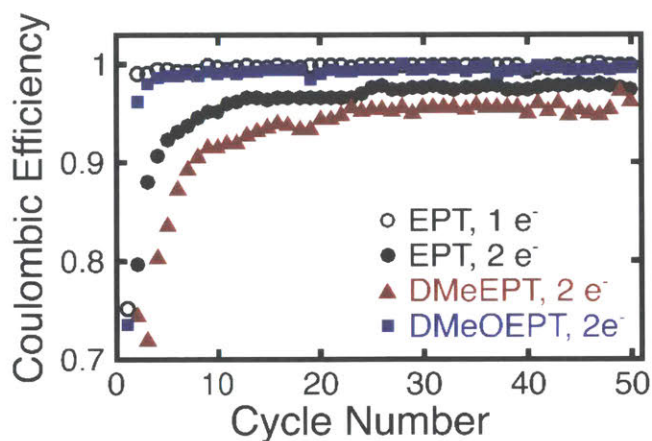
Figure 53: Coulombic efficiency vs. cycle number for bulk electrolysis charge/discharge experiments accessing the first oxidation of EPT (black, hollow circles), or both oxidations of EPT (black, filled circles), DMeEPT (red, filled triangles), or DMeOEPT (blue, filled square). For all experiments, the active species concentration was 0.001 M in 1 M LiTFSI in PC (30 mL of solution), and the charge/discharge current was 0.804 mA.
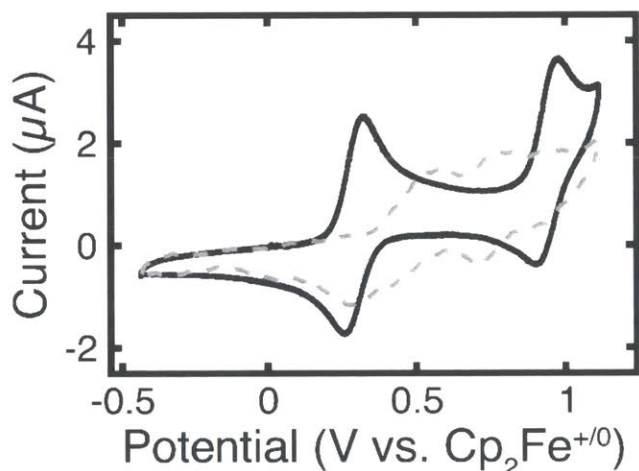
Figure 54: Cyclic voltammograms of 0.001 M EPT in 1 M LiTFSI in PC before (solid line) and after (dashed line) 50 cycles of bulk electrolysis accessing both the first and second oxidations of EPT. Voltammograms were recorded at a scan rate of 20 mV/s.

Satisfied that the radical cations of DMeEPT and DMeOEPT are stable, we next explored the degree to which the disparate *para*-substituents stabilized the dications of these compounds. In bulk electrolysis experiments, the potential cut-off was set to 1.05 V *vs.* $Cp_2Fe^{+/0}$, allowing the second electron transfer event to be accessed while attempting to minimize electrolyte decomposition. The initial charging half cycle lasted three times longer than expected (6 h rather than 2 h), suggesting reductive decomposition of the DMeEPT dication into one or more unknown

electroactive species, indicating the instability of the dication (Figure 50c). The originally observed first-oxidation charging potential plateau was absent in subsequent cycles, and a new redox event around 0.6 V *vs.* $Cp_2Fe^{+/0}$ dominated further charging cycles (Figure 51). Over the 50-cycle experiment, the capacity dropped to 13% of the theoretical value with the most-rapid decay occurring during the first 10 cycles. Cyclic voltammograms recorded before and after the 50-cycle experiment showed significant changes, including the appearance of a new ill-defined reduction wave around 0.4 V *vs.* $Cp_2Fe^{+/0}$, the same potential as the discharge plateau observed in bulk electrolysis (Figure 55). These observations indicate that methyl substituents *para-* to nitrogen are insufficient to stabilize the dication in this environment.
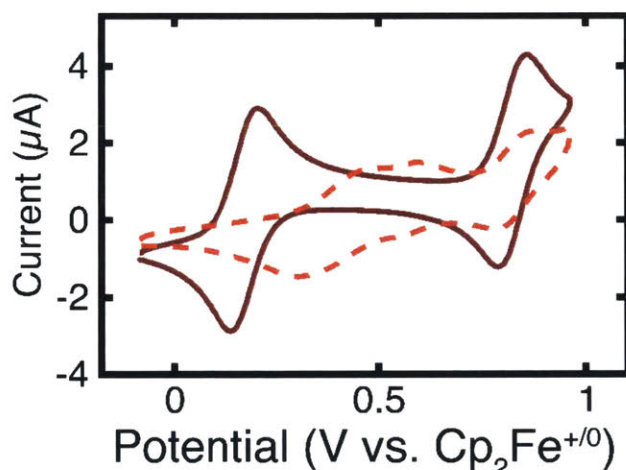
Figure 55: Cyclic voltammograms of 0.001 M DMeEPT in 1 M LiTFSI in PC before (solid line) and after (dashed line) 50 cycles of bulk electrolysis accessing both the first and second oxidations of DMeEPT. Voltammograms were recorded at a scan rate of 20 mV/s.

Finally, we examined the stability of the DMeOEPT dication using bulk electrolysis experiments, again charging to 1.05 V *vs.*$Cp_2Fe^{+/0}$ (Figure 50d). Here the cycling efficiency ranged from 98 to 100%, with an overall capacity retention of 93% after 50 cycles (Figure 51). Because the features in the original charge/discharge cycles remained consistent over the course of the 163 h experiment, we concluded that this fade is due to active-species crossover from the working-electrode chamber to the counter-electrode chamber rather than active-species decomposition. As

before, we note that the theoretical capacity was not achieved (ca. 80%) in this experiment due to the applied current selected. The robustness of the dication is further supported by cyclic voltammograms recorded before and after cycling, which show nearly identical features. Only a slight decrease in peak height was observed, consistent with the capacity fade that occurs during cycling (Figure 56). From the results of these experiments, we concluded that the incorporation of methoxy groups *para*- to the nitrogen atom effectively stabilized the DMeOEPT dication.
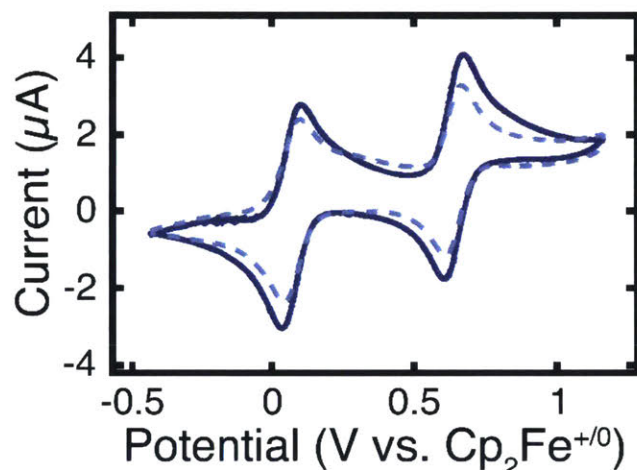
Figure 56: Cyclic voltammograms of 0.001 M DMeOEPT in 1 M LiTFSI in PC before (solid line) and after (dashed line) 50 cycles of bulk electrolysis accessing both the first and second oxidations of DMeOEPT. Voltammograms were recorded at a scan rate of 20 mV/s.

6.4   Conclusions

Compared to the unstable EPT dication, incorporating delocalizing, electron-donating methoxy groups at the positions *para* to nitrogen is more effective at stabilization than the electron-donating (but not delocalizing) methyl groups at the same positions. While the molecular weight of the new compound, DMeOEPT, is 26% larger than the parent compound, EPT, the stabilization of a second oxidation increases the overall molecular gravimetric capacity by 58%, leading to a charge storage capacity of 187 Ah/kg. This work provides an example of the successful design of a stable two-electron-donating organic species using simple modifications that extend the delocalization of

195

charge in this small molecule. While the solubility of the species investigated here is too low for direct application in flow batteries, future efforts will focus on incorporating a more soluble version of DMeOEPT into nonaqueous flow cells. The use of soluble two-electron-transfer molecules with disparate redox events will introduce new challenges in cell polarization and battery efficiency that could offset some of the advantages associated with multi-electron transfer in RFBs. Understanding these cell-level tradeoffs will allow for the identification of design principles to improve molecular engineering efforts. More broadly, the experimental approach used in this work can be applied to advance the design of new redox-active organic molecules for use in emerging electrochemical energy storage systems.

7 Multi-property Modifications of Phenothiazines

This study aims to advance our understanding of the physical and electrochemical behavior of nonaqueous redox electrolytes at elevated concentrations and to develop experimentally informed structure-property relationships that may ultimately enable deterministic design of soluble multi-electron organic redox couples for use in redox flow batteries (RFBs). To this end, we functionalized a phenothiazine core to simultaneously impart two desired properties: high solubility and multiple electron transfer. Specifically, we report the synthesis, solubility, and electrochemical analysis of two new phenothiazine derivatives, 3,7-dimethoxy-*N*-(2-(2-methoxyethoxy)ethyl)phenothiazine and *N*-ethyl-3,7-bis(2-(2-methoxyethoxy)ethoxy)phenothiazine, which are both two-electron donors that are miscible with non-aqueous solvents and electrolytes. The latter is soluble to 0.54 M in its least soluble state, enabling solutions of up to 1.08 M in electron storage capacity to be realized. This dual-property improvement allows for extended symmetric flow cell experiments for 460 h of cycling of a multi-electron transfer system at high concentrations that better approximate practical devices. This chapter is partially reprinted "Tailoring Two-Electron Donating Phenothiazines to Enable High Concentration Redox Electrolytes for Use in Nonaqueous Redox Flow Batteries" by N. Harsha Attanayake, **Jeffrey A. Kowalski**, Katharine Greco, Matthew D. Casselman, Jarrod D. Milshtein, Steven Chapman, Sean R. Parkin, Susan A. Odom, and Fikile R. Brushett which was submitted to Chemistry of Materials.

7.1 Introduction

In an effort to improve our understanding of the physical and electrochemical behavior of nonaqueous redox electrolytes at elevated concentrations and develop experimentally informed structure-property relationships that may ultimately enable deterministic design of high-performance organics for use in RFBs, specifically focusing on the performance of highly soluble multi-electron redox couples. As illustrated in Figure 57, we combined efforts previously utilized to impart greater molecular solubility as well as increase atom economy as a means of increasing volumetric charge-storage capacity of resultant electrolytes[147,148]. For example, we showed improvement of *N*-ethylphenothaizine (EPT, Figure 57) by increasing its solubility through incorporation of an oligoglycol chain at the *N* position, leading to N-(2-(2-methoxyethoxy)-ethyl)phenothiazine (MEEPT, Figure 57)[147]. This functionalization increased solubility of all of the states of charge such that the neutral species was a liquid that is miscible with the electrolyte, and further the charged species' solubility increased five-fold compared to that of the parent compound. More recently, in an attempt to increase the intrinsic capacity of the parent EPT, we reported that introducing methoxy groups at the *para-* (3 and 7) positions resulted in a marked improvement in stability of the dication of *N*-ethyl-3,7-dimethoxyphenothiazine (DMeOEPT, Figure 57)[148]. DMeOEPT was not soluble enough to run meaningful flow cell experiments (< 0.1 M in all states of charge), highlighting the need for further modification to operate a flow cell with this two-electron-donating core at high concentrations.
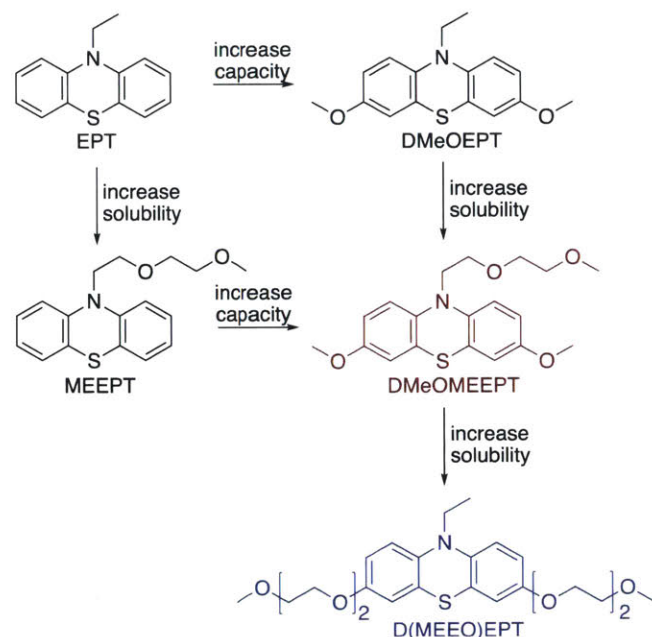
Figure 57: Representations of the chemical structures of *N*-ethylphenothiazine (EPT), *N*-(2-(2-methoxyethoxy)-ethyl)phenothiazine (MEEPT), *N*-ethyl-3,7-dimethoxyphenothiazine (DMeOEPT), *N*-(2-(2-methoxyethoxy)ethyl)-3,7-dimethoxyphenothiazine (DMeOMEEPT, red), and *N*-ethyl-3,7-di(2-(2-methoxyethoxy)ethoxy)phenothiazine (D(MEEO)EPT, blue). Vertically, the molecules are arranged to show an increase in the relative solubility from top to bottom. Horizontally, the molecules are arranged from left to right to show an increase in stability of the dication form.

Here we modified the phenothiazine core to impart two desired properties simultaneously: high solubility and multiple electron transfer. We report the synthesis, solubility, and electrochemical analysis of two new phenothiazine derivatives. The first, *N*-(2-(2-methoxyethoxy)ethyl)-3,7-dimethoxyphenothiazine (DMeOMEEPT, Figure 57, red), combines the results from our previous work by installing an oligoglycol chain on the *N* position of the DMeOEPT structure. The second extends the methoxy groups in the 3 and 7 positions with oligoglycol chains, yielding *N*-ethyl-3,7-di(2-(2-methoxyethoxy)ethoxy)phenothiazine (D(MEEO)EPT, Figure 57, blue). Compared to two-electron donating DMeOEPT, both derivatives exhibit greater solubility without compromising stability. This dual-property improvement allowed for extended symmetric flow cell cycling experiments of a multi-electron

transfer system at high concentrations, thus laying the foundation for studying multi-property, structure-function relationships in relevant RFB conditions.

7.2 *Experimental*

Phenothiazine, sodium hydride (60% dispersion in mineral oil) and copper iodide were purchased from Acros Organics. Diethylene glycol monomethyl ether and methyl formate were purchased from Tokyo Chemical Incorporated. Nitrosonium tetrafluoroborate (98%) was purchased from Alfa Aesar and was stored and weighed in an argon-filled glovebox (MBraun, O_2 < 0.1 ppm, H_2O < 0.5 ppm). Anhydrous pyridine (99.8%), *N*-bromosuccinimide (NBS), anhydrous methanol, and sodium were purchased from Sigma-Aldrich. Other solvents were purchased from VWR. Silica gel (65 x 250 mesh) was purchased from Sorbent Technologies. ^{1}H and ^{13}C NMR spectra were obtained on 400 MHz Varian spectrometers in DMSO-d_6 from Cambridge Isotope Laboratories. Mass spectra were obtained on an Agilent 5973 Network mass selective detector attached to Agilent 6890N Network GC system. Elemental analyses were performed by Atlantic Microlab, Inc. Solubility tests were performed in an argon-filled glove box.

N-ethylphenothiazine (EPT)[148], *N*-((2-methoxy)ethoxy)ethylphenothiazine (MEEPT)[147], *N*-ethyl-3,7-dibromophenothiazine (DBrEPT)[148], *N*-ethyl-3,7-dimethoxyphenothiazine (DMeOEPT)[148] and *N*-ethyl-3,7-dimethoxyphenothiazine tetrafluoroborate (DMeOEPT-BF₄)[148], were synthesized as previously reported.

3,7-Dimethoxy-*N*-((2-methoxy)ethoxy)ethylphenothiazine (DMeOMEEPT). Sodium methoxide (~3 mL ethanol) solution was prepared by dissolving sodium (0.50 g, 0.022 mol) in 7 mL methanol. To the methoxide solution, copper(I) iodide (1.65 g, 0.00868 mol), DBrMEEPT

(1.00 g, 0.00217 mol) and pyridine (10.8 mL) were added. The reaction mixture was purged with nitrogen for 15 min. A reflux condenser was attached and the reaction was refluxed for 12 h. Upon completion of the reaction, the reaction mixture was diluted with diethyl ether and washed with brine. The organic extracts were dried over magnesium sulfate, filtered and concentrated by rotary evaporation. The organic residue was purified by silica gel chromatography using 40% ethyl acetate in hexanes as the eluent to afford the product as a colorless oil (0.35 g, 45%). ^{1}H NMR (DMSO-d_6, 400 MHz, ppm) δ 6.95 – 6.90 (m, 2H), 6.78 – 6.72 (m, 4H), 3.92 (t, J = 5.9 Hz, 2H), 3.68 (s, 6H), 3.66 (d, J = 5.9 Hz, 2H), 3.54 – 3.48 (m, 2H), 3.43 – 3.37 (m, 2H), 3.20 (s, 3H). ^{13}C NMR (DMSO-d_6, 100 MHz, ppm) δ 154.7, 138.5, 124.6, 116.1, 112.9, 112.4, 71.3, 69.7, 67.5, 58.04, 55.4, 47.3. GCMS: m/z 361 (77%), 272 (100%), 258 (78%), 240 (60%), 215 (26%), 172 (12%). Anal. calcd. for $C_{19}H_{23}NO_4S$ C, 63.14; H, 6.41; N, 3.88. Found C, 63.16; H, 6.55; N, 3.90.

N-ethyl-3,7-di(2-(2-methoxyethoxy)ethoxy)phenothiazine (D(MEEO)EPT), Method 1. An oven-dried 1 L round-bottomed flask was transferred to an argon filled glove box, then diethylene glycol monomethyl ether (390 mL, 3.41 mol) was added into the round-bottomed flask, which was capped and removed from the glove box. Freshly cut sodium metal (9.56 g, 0.416 mol) was dissolved in diethylene glycol monomethyl ether under nitrogen atmosphere. Then, copper(I) iodide (31.65 g, 0.1682 mol), DBrEPT (16.00 g, 0.04155 mol) and anhydrous pyridine (320 mL) were added to the resulting solution. Afterward, the reaction mixture was sparged with nitrogen about 15 min while stirring. The round-bottomed flask was immersed in an oil bath and the reaction mixture was refluxed for overnight. Upon completion of the reaction, the reaction mixture was concentrated by rotary evaporation. Then reaction mixture was diluted with ethyl acetate and washed with 1 M aq. HCl, water and brine. The combined organic extracts were dried over magnesium sulfate and concentrated by using rotary evaporation. Finally, organic residue was

purified on a silica gel column using 20-50% ethyl acetate in hexanes. The silica gel was neutralized with trimethylamine (2 -3 mL) during packing the column. The product was yellow/light red viscous liquid (14.8 g, 77%). ^{1}H NMR (DMSO-d_6, 400 MHz, ppm) δ 6.90 – 6.85 (m, 2H), 6.79 – 6.75 (m, 4H), 4.05 – 3.98 (m, 4H), 3.79 (q, J = 6.9 Hz, 2H), 3.71 – 3.65 (m, 4H), 3.58 – 3.52 (m, 4H), 3.47 – 3.41 (m, 4H), 3.23 (s, 6H), 1.23 (t, J = 6.9 Hz, 3H). ^{13}C NMR (DMSO-d_6, 100 MHz, ppm) δ 153.9, 138.7, 124.5, 116.0, 113.8, 113.3, 71.5, 69.9, 69.1, 67.8, 58.3, 41.3, 12.9. GCMS: m/z 463 (100%), 434 (30%), 360 (11%), 230 (14%), 103(18%), 59(47%). Anal. calcd. for $C_{24}H_{33}NO_6S$ C, 62.18; H, 7.18; N, 3.02. Found C, 62.40; H, 7.22; N, 3.03.

The solubilities of the neutral molecules, their radical cation salts, and the dication salts of DMeOMEEPT and D(MEEO)EPT were determined in 0.5 M tetraethylammonium bis(trifluoromethane)sulfonamide (TEATFSI, IoliTec, > 99%) in acetonitrile (ACN, BASF, 99.98%). The tetrafluoroborate (BF_4) was the counter anion of the radical cation salts and the dication salts. All the tests were performed in an argon-filled glove box and each solubility test was completed within about 5 min. A known amount of active material was added to a glass vial. Then, the electrolyte solution was added slowly and stirred the solution between additions. The electrolyte addition was continued until the active species was completely dissolved (this was determined by visual inspection). This process was triplicated for each active species, then the average molar concentrations were calculated.

All cyclic voltammetry (CV) measurements were performed in an argon-filled glovebox (MBraun Labmaster, O_2 < 0.1 ppm, H_2O < 5 ppm) at 26 °C (ambient glovebox temperature) using a VSP-300 potentiostat (Bio-Logic). CV was performed in 0.5 M TEATFSI in ACN with one of two different types of working electrodes: a 3 mm diameter glassy carbon working electrode (CH Instruments, Inc.) or an 11 μm diameter carbon fiber working electrode (CH Instruments, Inc.).

Before each measurement, the working electrode was polished on a MicroCloth pad containing an aqueous slurry of 0.05 μm alumina powder (Buehler Ltd.) following which, the electrode was then rinsed with deionized water (Millipore) and wiped with lens paper. In all cases, the counter electrode was a gold coil (CH Instruments, Inc), and a fritted Ag/Ag^+ electrode was used as the reference. To reference to ferrocenium/ferrocene, before each measurement, an additional CV was taken in the electrolyte containing 0.005 M ferrocene.

For the macroelectrode voltammetry, A macroelectrode (3 mm glassy carbon) was used to determine the redox potential (average of anodic and cathodic peak potentials), chemical reversibility (peak height ratio), and electrochemical reversibility (peak separation) of each redox event. Additionally, the diffusion coefficient of the bulk species was obtained using Randles-Sevcik analysis. Active materials were studied at 0.001 M in the electrolyte, and 100% iR correction was applied. The resistance measured was about 50 Ω, which leads to a correction of less than 0.1 mV for the largest measured currents. The diffusion coefficients were analyzed using the Randles-Sevcik equation with background current corrections, according to prior literature procedure:

$$i_p = 0.4463nFAC \left(\frac{nFD}{RT} v \right)^{0.5} \tag{1}$$

Where i_p is the peak current (A), n is the number of electrons transferred (-), F is the Faraday constant (96485 C/mol), A is the electrode area (cm^2), c is the concentration (mol/cm^3), D is the diffusion coefficient (cm^2/s), R is the gas constant (8.314 J/mol/K), T is the temperature (K), and v is the scan rate (V/s). Data obtained from voltammograms at scan rates of 10, 20, 30, 40, 50, 75, and 100 mV/s were used for diffusion coefficient calculations.

For the microelectrode voltammetry, a microelectrode (11 μm diameter carbon fiber) was used to probe the solution before and after the symmetric flow cell cycling experiments. The CV with the microelectrode provides information about the dominant species (neutral, radical cation, dication) present by examining which current plateau is closest to zero. The magnitude of the current plateau for a microdisc electrode is given by:

$$i_{ss} = 4nFrDc \qquad (2)$$

Where i_{ss} is the plateau current (A), r is the radius of the electrode, and c is the bulk concentration (mol/cm^3). For all microelectrode experiments, the scan rate was 10 mV/s.

For all flow cells in this work, a small-volume flow cell with interdigitated flow fields, previously described by Milshtein et al.[123], was employed. The backing plates were machined from polypropylene, which was chosen for its chemical compatibility with all of the materials used in this study. The flow fields were machined in house from 3.18 mm thick impregnated graphite (product G347B, MWI Inc., Rochester, NY). The electrodes were cut to 1.7 cm x 1.5 cm dimensions from 190 ± 30 μm thick carbon paper (SGL 29 AA, SGL group, Wiesbaden, Germany) and used as received. On each side of the flow cell, two pieces of carbon paper were layered and compressed to ~20% during cell assembly. Daramic 175 was used as the separator (Daramic LLC, Charlotte, NC.) The cell was sealed using custom gaskets cut from polytetrafluoroethylene gasket tape (Goretex Tape, Gallagher Fluid Seals Inc., King of Prussia, PA). The geometric area of the cell was 2.55 cm^2. All flow cells were completely assembled outside of the glovebox and then brought immediately into an argon-filled glovebox (Innovative Technologies, O_2 < 10 ppm, H_2O < 0.1 ppm).

Perfluoroalkoxy alkane (PFA) jars (10 mL, Savillex) were used as electrolyte reservoirs during all flow cell operations. A peristaltic pump (Masterflex L/S Series) was used to flow the

electrolyte from the PFA jars to the flow cells at a rate of 10 mL/min. Norprene tubing (Masterflex) was used inside the pump head, and PFA tubing (Swagelok) connected the reservoirs to the flow cell. The Norprene tubing was attached with either PFA or stainless steel compression fittings (Swagelok). The inner diameter of all tubing used was 1.6 mm.

The electrolyte used in the flow cell study consisted of 0.3 M D(MEEO)EPT-BF$_4$ and 0.5 M TEATFSI in ACN. This electrolyte has a theoretical capacity of 16.1 Ah/L (161 mAh), assuming two electron transfer events and 10 mL of electrolyte per side (20 mL total). Prior to cycling the symmetric flow cell, a constant current pre-discharge was performed to bring the cell to its completely discharged state, wherein D(MEEO)EPT-BF$_4$ is oxidized to D(MEEO)EPT-(BF$_4$)$_2$ at the negative electrode and reduced to D(MEEO)EPT at the positive electrode. All cycling experiments were performed by applying a constant current density, which was determined from the geometric electrode area (2.55 cm^2). Data was collected using a VSP-300 potentiostat (BioLogic). Two types of flow cell studies were performed: (i) a rate study and (ii) a stability study. The rate study was performed to gain insight into the tradeoff between the current density, which relates to the power, and the accessed capacity. In this experiment, the current density was varied from 10 to 50 mA/cm^2, in increments of 10 mA/cm^2, for 5 cycles at each current density, and potential cutoffs of ± 0.775 V were imposed. The cell was then returned to its initial current density of 10 mA/cm^2 for 5 additional cycles. This rate study was completed in a total time of 145 h. For the stability study, which provides information about the species cyclability, the flow cell underwent constant current cycling for 140 cycles (460 h) at a current density of 25 mA/cm^2, with potential cutoffs of ± 0.775 V.

7.3   Results and Discussion

DMeOMEEPT and D(MEEO)EPT were both prepared in three steps from commercially available materials. To synthesize DMeOMEEPT, phenothiazine was alkylated at the N position to append the 2-(2-methoxyethoxy)ethyl group. The alkylated product, MEEPT, was then brominated at the 3 and 7 positions after which methoxy groups were introduced, replacing the bromine atoms. By accessing two electrons per molecule the gravimetric capacity increased from 89 mAh/g to 148 mAh/g compared to MEEPT. Similarly, to synthesize D(MEEO)EPT, an alkyl group (ethyl) was first installed at the N position of phenothiazine to yield EPT, which was brominated at the 3 and 7 positions, and then treated with the deprotonated oligoglycol to replace the bromine atoms with 2-(2-methoxyethoxy)ethoxy groups, which leads to a gravimetric capacity of 116 mAh/g assuming two electron transfer events. Detailed synthetic procedures, characterization, and the yield for each synthesis step can be found in the supporting information.

Materials Screening

Cyclic voltammetry (CV) was performed to analyze fundamental, short-term electrochemical behavior, including redox potentials, diffusion coefficients, and both the chemical (stability) and electrochemical (kinetic) reversibilities. Cyclic voltammograms in 0.5 M TEATFSI in ACN are shown in Figure 58, with values for peak potentials, peak separations, and peak-current ratios in Table 17. Based on the peak separation and peak-current ratios, the first oxidation events of both materials are chemically (peak-current ratio of 0.98 – 1.02) and electrochemically (peak separation of 60 – 61 mV) reversible on the CV timescale (~ minutes). However, only for D(MEEO)EPT is the second oxidation event both chemically and electrochemically reversible.
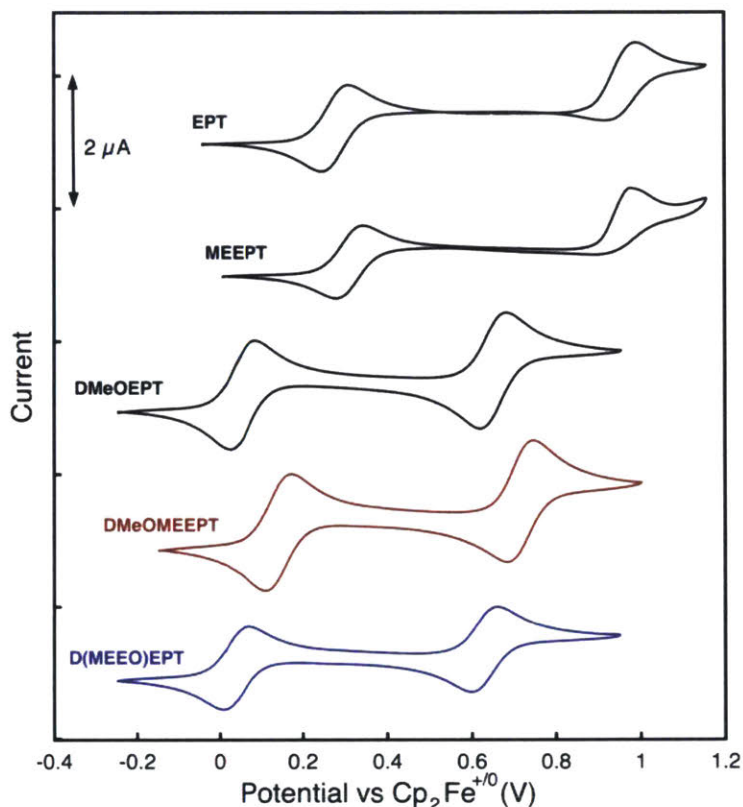
Figure 58: Cyclic voltammograms showing the first and second oxidation events of EPT, MEEPT, DMeOEPT, DMeOMEEPT, and D(MEEO)EPT at 0.001 M in 0.5 M TEATFSI in ACN at a scan rate of 10 mV/s, referenced to ferrocenium/ferrocene at 0 V.

Table 17: Measured half-wave potentials, peak separations, and peak-current ratios for the first and second oxidations, and diffusion coefficients of EPT, MEEPT, DMeOEPT, DMeOMEEPT, and D(MEEO)EPT. All cyclic voltammetry was performed at 0.001 M active concentration. The peak separations and peak-current ratios were calculated at a scan rate of 10 mV/s. All measurements were performed in triplicate.

| Compound | First Oxidation | | | Second Oxidation | | | Diffusion Coefficient ($\times 10^{-6}$ cm^2/s) |
	Potential (V vs. Cp$_2$Fe$^{+/0}$)	Peak Separation (mV)	Peak Current Ratio ($i_{p,ox}/i_{p,red}$)	Potential (V vs. Cp$_2$Fe$^{+/0}$)	Peak Separation (mV)	Peak Current Ratio ($i_{p,ox}/i_{p,red}$)	
EPT	0.278 ± 0.001	61 ± 1	1.00 ± 0.01	0.956 ± 0.002	68 ± 6	0.57 ± 0.09	2.3 ± 0.1
MEEPT	0.311 ± 0.001	61 ± 1	1.00 ± 0.01	0.937 ± 0.002	79 ± 2	0.26 ± 0.02	1.6 ± 0.1
DMeOEPT	0.056 ± 0.001	60 ± 1	0.99 ± 0.01	0.655 ± 0.001	60 ± 1	1.01 ± 0.01	1.8 ± 0.1
DMeOMEEPT	0.093 ± 0.001	60 ± 1	0.99 ± 0.02	0.666 ± 0.001	60 ± 1	0.90 ± 0.05	1.6 ± 0.1
D(MEEO)EPT	0.064 ± 0.001	61 ± 1	1.02 ± 0.04	0.654 ± 0.001	61 ± 1	1.01 ± 0.01	0.8 ± 0.1

The potentials of the first and second oxidation events are similar for both DMeOMEEPT (0.093, 0.666 V vs. $Cp_2Fe^{+/0}$) and D(MEEO)EPT (0.025, 0.625 V vs. $Cp_2Fe^{+/0}$), with DMeOMEEPT exhibiting slightly higher (more positive) potentials than D(MEEO)EPT due to the inductive effect of the oxygen atoms in the 2-(2-methoxyethoxy)ethoxy group at the N position in DMeOMEEPT, which is more electron-withdrawing than the ethyl group at the equivalent (N) position in D(MEEO)EPT. We previously observed the same trend with a difference of similar magnitude in the first oxidation potentials of EPT and MEEPT, which contain the same functional groups (ethyl and 2-(2-methoxyethoxy)ethoxy, respectively) at their N positions[147]. The oxidation potentials of DMeOMEEPT and D(MEEO)EPT are reduced by ca. 0.2 V compared to their N-alkylated equivalents MEEPT and EPT, respectively, due to the resonance contribution of the O atoms to the phenothiazine π system. A difference of similar magnitude was observed in EPT and DMeOEPT[148]. It is worth noting that while the first redox event occurs at a less positive potential than for derivatives without alkoxy groups at the 3 and 7 positions, given the ability to access the second redox event at higher potentials than the first oxidation potential of N-substituted phenothiazines, the average redox potential increases. Figure 59 contains the data for variable scan rate voltammograms.
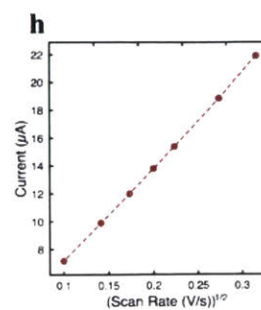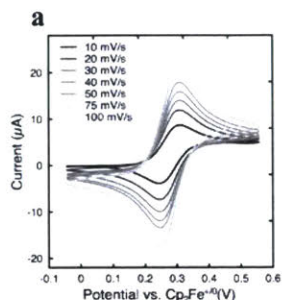
Figure 59: Cyclic voltammograms of EPT (a), MEEPT (c), DMeOEPT (e), DMeOMEEPT (g), and D(MEEO)EPT (i) at 0.001 M in 0.5 M TEATFSI in ACN at scan rates of 10, 20, 30, 40, 50, 75, and 100 mV/s. Additionally, the corresponding Randles-Sevcik plots are shown for EPT (b), MEEPT (d), DMeOEPT (f), DMeOMEEPT (h), and D(MEEO)EPT (j).

To determine the upper bounds for materials utilization in a flow cell, the solubility of each relevant state of charge (neutral, radical cation, and dication) must be known to identify the least soluble species. Thus, radical cation and dication salts of DMeOMEEPT and D(MEEO)EPT were prepared and isolated as solid products. Chemical oxidation with one or two equivalents of NOBF$_4$ results in electron transfer from the phenothiazine core to the nitrosonium (NO$^+$) cation, forming one or two equivalents of the neutral NO gas and either the mono-tetrafluoroborate salt of the radical cation or the bis(tetrafluoroborate) salt of the dication, respectively. UV-vis spectra of the

oxidized products verify that unique products form, as evidenced by the features that are distinctive both from each other and from the features of the starting material (Figure 60). Key features include a peak at 318 nm for the neutral compound; an intense peak at 629 nm and two sharp, less intense peaks at 354 and 394 nm for the radical cation; and peaks at 593 and 922 nm for the dication. These spectra are nearly identical to those of previously reported DMeOEPT[148]. This result is consistent with the similar electronic structure expected for these phenothiazines based on their alkoxy containing substituents *para* to the *N* position[148].
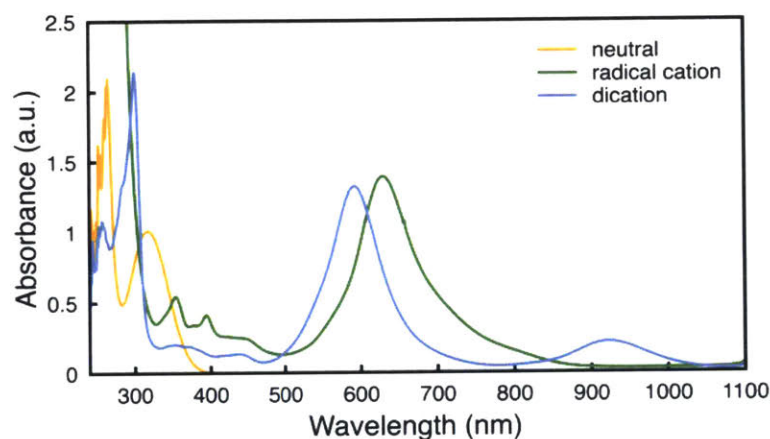
Figure 60: UV-vis absorption spectra of the neutral, radical cation, and dication forms of D(MEEO)EPT in ACN.

The solubility of the neutral, radical cation, and dication forms of DMeOMEEPT and D(MEEO)EPT were measured in 0.5 M TEATFSI in ACN, the same electrolyte used for electrochemical analysis. As expected based on the difference in solubilities of EPT vs MEEPT, compared to DMeOEPT – a solid – the new materials containing oligoglycol groups are both liquids that are miscible in nonaqueous electrolytes. The radical cation and dication salts of both compounds are solids, with lower solubilities than the miscible neutral forms. With two glycol chains, at 0.55 and 0.54 M, the radical cation and dication forms of D(MEEO)EPT were more soluble than DMeOMEEPT, with only one glycol chain, at 0.11 and 0.10 M (Table 18). Because

of the combination of its higher solubility in both oxidized forms and because of the more reversible nature of its second oxidation, we chose to utilize D(MEEO)EPT in flow cell experiments.

Table 18: Solubilities of the neutral molecules, their radical cation salts, and the dication salts of DMeOMEEPT and D(MEEO)EPT in 0.5 M TEATFSI in ACN. The radical cation salts and the dication salts had tetrafluoroborate (BF_4) as a counter ion. Solubility values are reported in molarity (M).

Compound	Neutral Species (M)	Radical Cation (M)	Dication (M)
EPT	0.10 ± 0.01	0.28 ± 0.01	–*
MEEPT	miscible	0.40 ± 0.01	–*
DMeOEPT	0.05 ± 0.01	0.06 ± 0.01	0.05 ± 0.01
DMeOMEEPT	miscible	0.11 ± 0.01	0.10 ± 0.01
D(MEEO)EPT	miscible	0.55 ± 0.01	0.54 ± 0.01

*Dication data is not included for EPT and MEEPT, given the instability of their dication forms.

Given that D(MEEO)EPT was the most soluble of the stable two-electron donors, it was necessary to scale up the synthesis of this material, in its radical cation form, as the starting point on both sides of the flow cell. Thus, we scaled up the synthesis of the tetrafluoroborate radical cation salt of D(MEEO)EPT, performing reactions in batches as large as 8 g (mass of isolated material), again using $NOBF_4$ as the chemical oxidant. To confirm the identity of the radical cation salt, we crystallized the expected product, D(MEEO)EPT-BF_4, and analyzed resultant crystals using X-ray diffraction. The thermal ellipsoid plot obtained from X-ray experiments is shown in Figure 61 . Notably, the isolation of this salt as X-ray quality single crystals provides proof of structural assignment and demonstrates the substantial stability of this material.
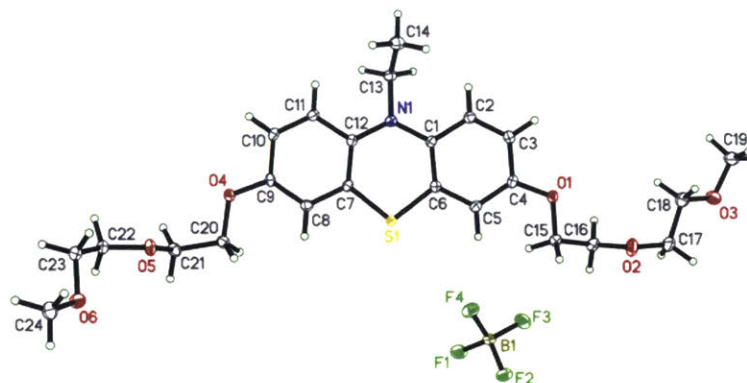
Figure 61: Thermal ellipsoid plot of D(MEEO)EPT-BF₄ obtained from single-crystal X-ray diffraction experiments.

Flow Cell Cycling

Symmetric cells offer many benefits when evaluating new active materials[123,147,211]. All relevant states-of-charge can be accessed, and cells can be cycled for long durations in relevant flow battery conditions. Additionally, the possibility of contamination from a counter electrode is removed, thus leading to a more controlled electrolyte environment. Furthermore, flowing the electrolyte increases mass transfer compared to stationary experiments, and therefore allows for higher concentrations of active materials to be cycled. Lastly, in flow cells, porous carbon felts and papers are used as electrodes, which provide more relevant surfaces for electrochemical reactions than glassy carbon electrodes typically used in CV experiments. Thus, to test the stability and performance of D(MEEO)EPT in a more realistic operating environment without convoluting our analysis by including a complementary active material, we chose to employ symmetric flow cells containing only the posolyte species[147,211].

In symmetric cells utilizing one-electron donors, two different states of charge are accessed in each chamber: the neutral species, P, and the radical cation, $P^{+\bullet}$. For symmetric cells containing two-electron donating active species, three different states-of-charge are present: in addition to the

neutral species and the radical cation, the dication, P^{++}, is also accessed (Figure 62a). In an ideal constant current cycling experiment, two unique potential plateaus occur at voltages opposite from one another, with each plateau corresponding to 50% of the total charge capacity (Figure 62b). Therefore, at 50% state-of-charge, a sharp increase (charging) or decrease (discharging) in the potential will occur. When charging begins, the P is oxidized to $P^{+\bullet}$ on one side of the cell, and P^{++} is reduced to $P^{+\bullet}$ on the other side, leading to the first voltage plateau. Once P and P^{++} are depleted, both tanks contain only $P^{+\bullet}$. At this point, $P^{+\bullet}$ is oxidized to P^{++} on one side of the cell and is reduced to P on the other. The presence of these reactions creates the second plateau. During discharge, the reverse reactions occur, again leading to two voltage plateaus.
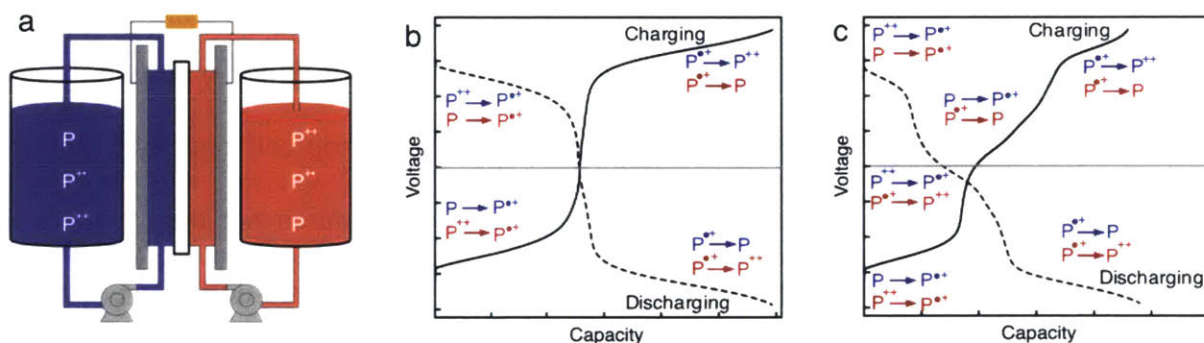
Figure 62: Schematic of a symmetric flow cell showing the states of charged accessed for a given molecule, P, (a), and the corresponding charging (dotted line) and discharging (solid line) potential profiles for constant current cycling labeled with the electrochemical reactions corresponding to each voltage plateau (b and c).

A misbalanced cell can result from a mismatch in total volume on each side of the cell (e.g. from crossover) and/or from a mismatch in concentration in respective active species concentrations. This phenomenon may be a result of cell polarization and species crossover which is exacerbated by the use of a non-selective separator. Specifically, as the current density increases, the cell will reach its voltage cutoff before all of the molecules have been completely oxidized or reduced. The

unreacted molecules will result in a mix of P/ $P^{+\bullet}$ and $P^{+\bullet}/P^{++}$. In that case, a new, third potential plateau will be present (Figure 62c). If the amount of P on one side of the cell is less than the amount of P^{++} the other side, upon complete oxidation of P to $P^{+\bullet}$, an excess of P^{++}will remain unreduced on the opposite side. An example of this, with neutral species as the limiting factor, is shown in the discharge curves in Figure 62c. If P^{++} is the limiting species, then an excess of P will be present upon complete reduction of P^{++} to $P^{+\bullet}$. An example of a voltage profile in this scenario is shown in Figure 62c during both charge and discharge. In both scenarios, the expected cell voltage is 0 V because the reaction is cycling against itself[123]. The capacity of this middle plateau is dependent on the amount of excess active material (whether P or P^{++}) present on one side of the cell. Note that a third plateau would also form if the reduction of P^{++} to $P^{+\bullet}$ was the limiting reaction. The formation of this new potential plateau emphasizes a challenge with two electron transfer molecules and the importance of preventing crossover during cell operation for two-electron transfer molecules because a mismatch in species concentration not only reduces the capacity that is accessed, but it will also alter the voltage profile observed during charging and discharging as the cell cycles.

Importantly, starting with a balanced cell is required. This can be done by (i) putting equal volumes of separate solutions P and P^{++} of the same molarity on each side of a flow cell, (ii) mixing P and P^{++} in a 1:1 ratio and dividing the resulting solution into two equivalent volumes for each side of the cell, then charging the cell to get to P only on one side and P^{++} on the other side as a pre-charging step, or (iii) making a solution of only $P^{+\bullet}$, then dividing the volume in two for each side of the cell, and then charge the cell to only have P on one side of the cell and only P^{++} on the other. In both the second and third cases, a pre-charging step is needed to fully reduce one side to P and fully oxidize to P^{++}. The second and third options are appealing because the preparation of

214

only one solution is needed; the third option is more appealing than the second because, in the third option, only one state of charge is used to make the solution. Thus, we chose to start our full cell cycling with 100% $P^{+\bullet}$ on each side of our flow cells.

Next, we determined which current density would be appropriate for running symmetric cell experiments to test the stability of D(MEEO)EPT. Thus, we first conducted a rate study, cycling D(MEEO)EPT for five cycles each at current densities of 10, 20, 30, 40, and 50 mA/cm^2, followed by five more cycles at 10 mA/cm^2, the last of which was performed to determine whether accessing the higher current densities affected the cell (e.g. electrode degradation) and/or active material. The voltage vs. capacity profiles for the fifth cycle at each current density are shown in Figure 63a, and the charging and discharging capacity with the coulombic efficiency are shown in Figure 63b. As expected, the accessed capacity decreases as current densities increase, which is due to the larger cell polarization present at high current densities. As evidenced by a comparison the 5th cycle in the first and last sets of 10 mA/cm^2 cycles, the capacity faded by about 8% over the course of the 145 h experiment. However, in the later cycles, the third plateau centered around 0 V starts to form, to which we tentatively attribute the capacity fade.
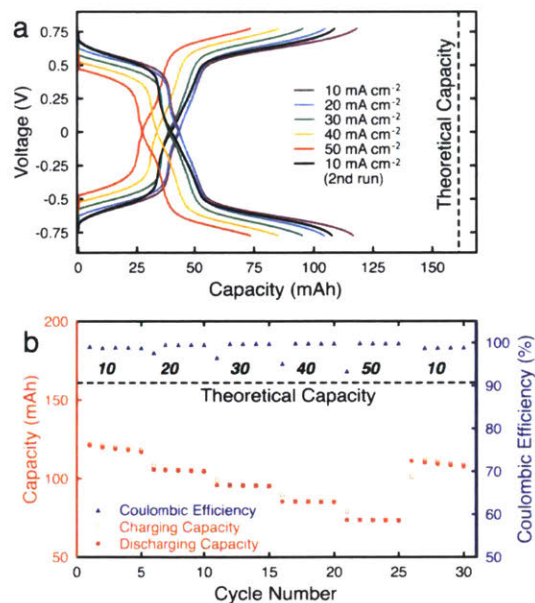
Figure 63: Rate study of D(MEEO)EPT cycling in a symmetric flow cell, showing the potential vs. capacity (a) and the capacity vs. cycling number (b) at various current densities. The numbers underneath each capacity segment represent the current densities in mA/cm². The potential cut-offs for each flow cell experiment were ± 0.775 V. The dashed black line is drawn to represent the theoretical capacity (16.1 Ah/L or 161 mAh). The total experimental run time was 145 h.

Table 19 highlights the additional tradeoff between the current density and the charging/discharing efficiency observed. The difference in accessed capacity of the two voltage plateaus observed in the voltage vs. capacity profiles in Figure 63a and Table 19 show the cell's deviation from the ideal behavior illustrated in Figure 62b. The percent of charging and discharging capacity accessed at each plateau is calculated by identifying the maximum (charging) or minimum (discharging) in the derivative of the voltage profile as each extreme represents the transition from one redox plateau to another[212]. For reference, in the ideal case, the capacity would be split evenly between the low and high voltage plateaus with no intermediate voltage plateaus.

Table 19: Percent of the charging and discharging capacity accessed on each potential plateau during charging and discharging and the corresponding accessed capacity and coulombic efficiency for each of the current densities examined, obtained from the variable-rate cycling data shown in Figure 63. The data corresponds to the average of each charge/discharge cycle.

Current Density (mA cm^{-2})	Charging			Discharging			Accessed Capacity (%)	Coulombic Efficiency (%)
	Lower Plateau (%)	Middle Plateau (%)	Upper Plateau (%)	Lower Plateau (%)	Middle Plateau (%)	Upper Plateau (%)		
10	33.3 ± 0.2	9.6 ± 0.2	57.1 ± 0.4	56.5 ± 0.2	9.4 ± 0.3	34.1 ± 0.1	73.5	98.8
20	37.5 ± 0.3	10.7 ± 0.3	51.8 ± 0.1	51.7 ± 0.1	10.6 ± 0.1	37.7 ± 0.1	65.1	99.5
30	37.8 ± 0.4	11.9 ± 0.1	50.3 ± 0.3	50.2 ± 0.1	11.8 ± 0.1	38.0 ± 0.1	59.2	99.8
40	36.9 ± 0.7	13.6 ± 0.1	49.5 ± 0.4	49.7 ± 0.1	13.1 ± 0.1	37.2 ± 0.1	52.9	99.9
50	35.5 ± 0.8	14.0 ± 0.4	51 ± 1	51.5 ± 0.2	14.9 ± 0.5	33.6 ± 0.6	45.6	99.9
10	30 ± 2	14.9 ± 0.4	55 ± 2	52.9 ± 0.2	14.6 ± 0.4	32.5 ± 0.1	67.6	98.9

Two interesting trends are observed in Table 19. First, as anticipated the lower current densities, thus longest cycles, have the lower coulombic efficiency, albeit only 1.0 to 1.1% lower than the shortest cycle. We attribute this minor inefficiency to in-cycle active species crossover and self-discharge through the non-selective separator. Second, in general, the active materials appear to spend more time in the extreme voltage plateaus, here, the upper plateau during charging and the lower plateau during discharging. A similar but simpler case (i.e., no convection) of this behavior would be voltage profiles associated with Sand's time measurements for different oxidation states of multiple electron transfer materials[212]. If translated to full redox flow cell operation (e.g., second redox couple at a disparate voltage), this observation suggests lower voltage efficiencies and consequently reduced energy efficiencies. Indeed, similar observations were made by Laramie et al. when studying two electron transfer molecules in a full cell[162]. We note that there does not appear to be a current density dependence of this trend over the relatively narrow range of current densities explored which is also in agreement with Sand's time analysis[212]. More broadly, this inefficiency is intrinsic to materials with multiple, independent electron transfer

events, suggesting that, in principle, greater volumetric capacities are achievable but with a concomitant penalty in voltaic efficiency.

To test the long-term stability of D(MEEO)EPT, constant current symmetric cell cycling was performed. Here, a symmetric cell was assembled with each half cell containing 10 mL of solution with 0.3 M D(MEEO)EPT (0.6 M faradaic concentration) in 0.5 M TEATFSI in ACN was cycled at 25 mA/cm². From the rate study, a current density of 25 mA/cm² was chosen to balance the experimental runtime (roughly 2 h for each half cycle), and fraction of the capacity accessed per cycle. Figure 64a shows the voltage vs. capacity profiles for the charge and discharge of selected cycles. The charge and discharge capacities and coulombic efficiencies for each cycle are shown in Figure 64b.
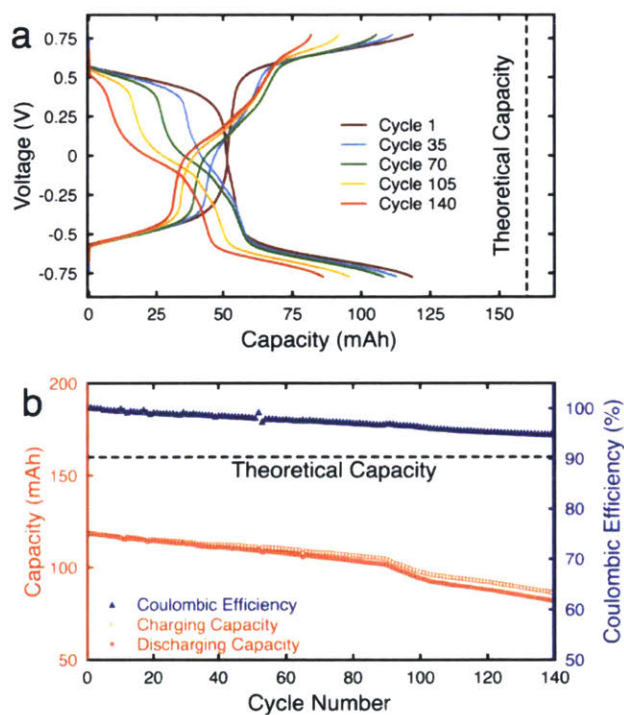
Figure 64: Constant current cycling of D(MEEO)EPT in a symmetric flow cell at 25 mA/cm² accessing both electron transfer events: capacity vs. potential (a), charging (red, square) and discharging (red, circle), as well as the coulombic efficiencies (blue, triangle) as a function of cycle number (b). The potential cut-offs imposed during the flow cell experiment were ± 0.775 V. The theoretical capacity (dashed black line) is 16.1 Ah/L (161 mAh) and the total experimental runtime was 460 h.

218

In this cycling experiment, about 80% of the theoretical capacity was accessed initially. Over the experiment (460 h), a 27% capacity fade was observed. We hypothesize that most of this fade may be due to a combination of polarizing the cell and crossover rather than material degradation because of the observation that the volume of the two electrolyte chambers were noticeably unequal after the stability study and the post cell analysis (Figure 65). Additionally, the new voltage plateau around 0 V appeared, deviating from ideal cycling behavior (Figure 62b). For the first 85 cycles (300 h), the capacity faded at a rate of ca. 0.1% per cycle, while for cycles 86-140 the average fade rate increased to ca. 0.4% per cycle. The new voltage plateau near 0 V increased upon further cycling; by cycle 140, the capacity accessed on this middle plateau was equal to that accessed on the lower plateau and larger than that of the upper potential plateau[162]. As the new plateau continued to increase, the accessed capacity decreased because more $D(MEEO)EPT^{+\bullet}$ remains either unoxidized or unreduced on one side of the cell.
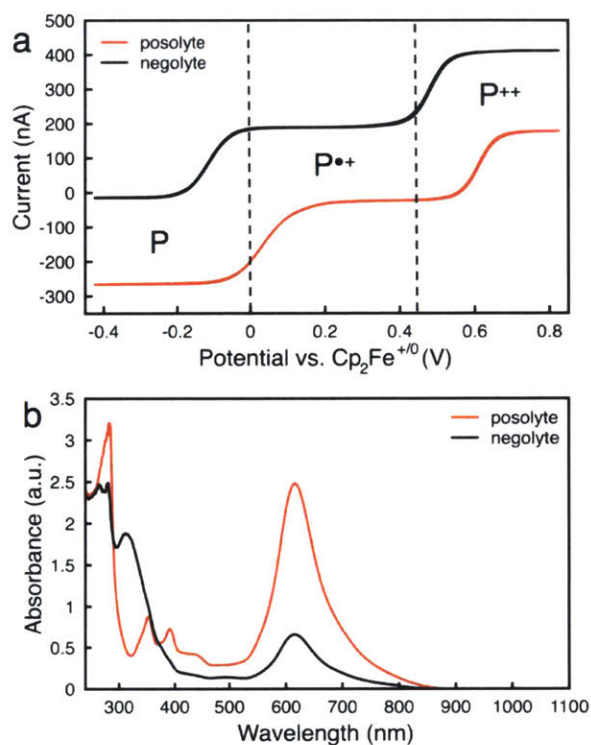
Figure 65: Carbon fiber microelectrode cyclic voltammetry scans (10 mV/s) of the posolyte (red) and negolyte (black) after symmetric cell cycling at 0.3 M in active material (a), and corresponding UV-vis absorption spectra (b). For UV-vis measurements, the working solutions were diluted 1000× to reach a concentration of 0.0003 M.

To determine whether the major loss of capacity was due to cell polarization and crossover or species decomposition, we analyzed the cycled posolyte and negolyte solutions using microelectrode voltammetry (Figure 65a) and UV-vis absorption spectroscopy (Figure 65b). A microelectrode was used because it is a steady-state voltammetry technique so the bulk concentration is probed rather than the diffusion layer. In the microelectrode voltammograms, the three current plateaus were observed. The lowest current plateau corresponds to the neutral form of D(MEEO)EPT, the middle plateau to the radical cation, and the highest current plateau to the dication. Note that the zero-current plateau represents the dominant species in solution (e.g. the species at the highest concentration).

Both the voltammogram and UV-vis spectra of the posolyte solution indicate that the radical cation is the dominant species. From the microelectrode (Figure 65a), the current is around 0 A for the middle current plateau, and from the UV-vis (Figure 65b), the signal only contains peaks consistent with the radical cation (353, 391, and 615 nm). The microelectrode data from the negolyte (Figure 65a) shows zero current around the lowest potential plateau indicating that the neutral species is the dominant species. The UV-vis spectra are consistent with this result, showing peaks that match the neutral compound (312 nm). However, the largest radical cation peak is still present (616 nm), but it is much smaller in magnitude, still suggesting that the neutral species is the dominant species (Figure 65b). In both the microelectrode voltammetry and UV-vis experiments, no evidence of the dication was observed in either the negolyte or posolyte.

Because the dication was not observed in either of the solutions, we suspected that the dication may have self-discharged to the radical cation form, due to the dication being too reducing for the electrolyte environment. To test this hypothesis, we monitored the stability of the radical cation and dication as dilute solutions in TEATFSI in ACN using UV-vis spectroscopy. As shown in Figure 66a, the absorption spectrum of the radical cation shows little change over 3 h in the flow cell electrolyte. By contrast, the absorption spectrum of the dication (Figure 66b) loses intensity and changes shape over the course of the experiment. Peaks consistent with the radical cation appear and become more intense over the first 2 h, stabilizing over the last hour. This result suggests that the dication does not persist in the electrolyte environment, but rather than undergoing decomposition via covalent bond cleavage/formation, the dication abstractions an electron from the electrolyte. This result is consistent with the hypothesis of why the lowest current density had the highest percent of charging at the high potential during the rate study.
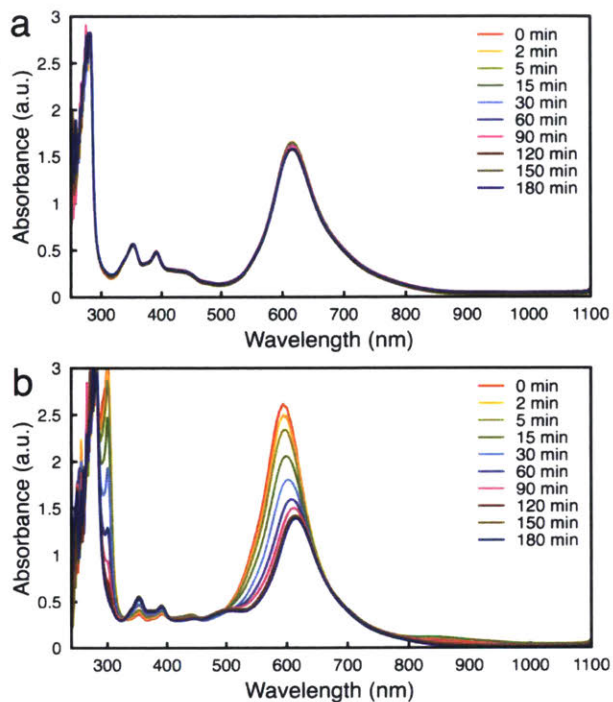
Figure 66: UV-vis absorption spectra of the D(MEEO)EPT radical cation (a) and dication (b) at 0.0001 M in 0.5 M TEATFSI in ACN for 0 to 3 h after dissolution.

7.4 Conclusions

In summary, we report two new two-electron-donating phenothiazine derivatives in which solubility of the neutral, radical cation, and dication forms in a nonaqueous electrolyte were increased significantly by introduction of one or two oligoglycol chains on the periphery of a less soluble core. Both derivatives are miscible with 0.5 M TEATFSI in ACN, and D(MEEO)EPT, the derivative with two oligoglycol chains, which only increased the molecular weight by a factor of ca. 1.5 compared to MEEPT, is sufficiently soluble in all three states of charge to allow for symmetric flow cell cycling experiments to be performed at concentrations of 0.3 M (0.6 M faradaic concentration). From the rate study, a new challenge associated with cycling two-electron transfer species was introduced. Due to cell polarization, additional inefficiencies exist using two

electron transfer materials because of the asymmetry of the two charging plateaus and discharging plateaus (i.e., more time charging in the upper potential plateau and more time discharging in the lower potential plateau). During long term symmetric cell cycling, D(MEEO)EPT cycled for 460 h with about 30% capacity fade. However, much of this fade is likely due to crossover during the long cycling time and polarizing the cell leading to a misbalanced concentration as evidenced by the appearance of a new potential plateau around 0 V. Microelectrode and UV-vis analysis of flow cell electrolytes post cycling indicate that the coulombic inefficiencies are mostly due to self-discharge of the dication form of D(MEEO)EPT through an electron-transfer reaction. Importantly, although capacity fade is observed, we did not find significant amounts of chemically decomposed materials, offering hope that the identification of a more appropriate electrolyte may lead to more extensive cycling of this posolyte candidate.

8 Impact of Cycling Conditions on Perceived Stability

New active materials are being examined in an attempt to reduce flow battery costs. The major challenge of these materials is their stability, which is most commonly evaluated by bulk electrolysis cycling. However, cycling parameters are not standardized, making it difficult to compare new species. In this work, we use a well-studied, substituted dialkoxybenzene as a model compound to examine the impact cycling conditions have on the perceived stability. We show that cycling time is a better measure of the stability than cycle number, and that accessing a fraction of the capacity increases the cycle time due to the lower concentrations of the charged species. This chapter is partially reprinted from "Bulk Electrolysis Protocols for New Active Species for Redox Flow Batteries" by **Jeffrey A. Kowalski** and Fikile R. Brushett, which is in preparation.

8.1 Introduction

In an effort to reduce total system costs, new charge storage materials are being examined. In particular, organic molecules are gaining traction because they consist of earth abundant elements, which can reduce active material costs, and have a highly tunable structure, which allows for property modification (*e.g.*, potential, solubility) through functionalization[61,213,214]. One of the major challenges of these new active materials is their stability; currently, their lifetime is much less than the multi-year operation times required for RFB viability[211,213]. While multiple methods are under development to explore stability, such as completely charging a solution and monitoring the active species concentration after a single charge by EPR[159,161,215], NMR[129,156], or UV-Vis[112,147], the most common method is bulk electrolysis cycling[124,148,156,162] or symmetric cell cycling[147,211]. During bulk electrolysis, a dilute solution of the active species is charged to a

predetermined state-of-charge (SOC) and then immediately discharged. This process is repeated until a certain capacity fade is reached as a function of cycle number. Currently, bulk electrolysis conditions are not standardized, and therefore, different charging methods (*e.g.* galvanostatic[125,156] and potentiostatic[211]), charging/discharging rates[147,148,156,160,216], SOCs accessed,[125,147,148,217] cell geometries,[148,156,162,217] and active species concentration[147,148,156,160,216] are used. These inconsistencies make it difficult to compare new species emerging in the literature because the cycling conditions can have a significant impact on the number of cycles and therefore the perceived stability. In this work, we examine the impact of different charging rates and SOCs accessed using a commercially available bulk electrolysis cell and a well-studied, moderately stable, substituted dialkoxybenzene, 2,5-di-tert-butyl-1,4-bis(2-methoxyethoxy)benzene (DBBB), in nonaqueous electrolytes.[125,139,158,168,217,218]

8.2   Experimental

All work was completed inside of an argon-filled glovebox (MBraun Labmaster) with the water < 5 ppm and oxygen < 1 ppm at 26 °C (ambient glovebox temperature). Solutions were prepared using volumetric flasks and then diluted to the desired active species concentration. The electrolyte was 1 M lithium bis(trifluoromethanesulfonyl)-imide (LiTFSI, BASF, > 99.9 % purity) in propylene carbonate (PC, BASF, > 99.9 % purity). The electrolyte was chosen due to its large electrochemical stability window, moderate ionic conductivity, and low volatility allowing for long experimental runtimes. The active species concentration was always diluted to 0.001 M DBBB.

Electrochemical data was collected using a VSP-300 potentiostat (Bio-Logic). Before all bulk electrolysis measurements, cyclic voltammetry was run on the solution to determine the higher and lower potential bounds for the cycling experiments, which were set to be about 0.3 V above and below the half wave potential. Cyclic voltammetry measurements were performed in a three electrode cell with a 3 mm glassy carbon working electrode (CH Instruments, Inc.), a lithium foil (Alfa Aesar) counter electrode, and a fritted lithium foil (Alfa Aesar, fill solution: 1 M LiTFSI in PC) reference electrode with a scan rate of 20 mV/s. Before each voltammogram, the glassy carbon working electrode was polished on a MicroCloth pad with a slurry of 0.05 μm alumina powder (Buehler Ltd.) in deionized water (Millipore). The electrode was then rinsed with deionized water and wiped with lens paper (VWR).

All cycling was performed in a commercially available bulk electrolysis cell (BASi, MF-1056) with 30 mL of solution containing electrolyte and active species. The working electrode, counter electrode, and reference electrode used were a high surface area reticulated vitreous carbon (BASi, MF-2077), lithium foil (Alfa Aesar) in a fritted glass chamber (BASi, MR-1196), and fritted lithium foil (Alfa Aesar, fill solution: 1 M LiTFSI in PC), respectively. During operation, the solution was stirred at a rate of 1400 rpm. Two different electrochemical techniques were used with this set up. The first determined the limiting current of the cell by polarization, and the second was long term cycling. For polarization, the potential was stepped from 3.6 V to 4.175 V vs. Li/Li^+ with potential steps of 0.025 V holding each step for 2 minutes, which was sufficient to reach a steady state current. Between each step, the voltage was reduced to 3.6 V vs. Li/Li^+ for 10 minutes to reduce any oxidized species and bring the solution back to 0 % SOC. Long term cycling was performed using galvanostatic methods, where the same current was used for both charging and discharging. The currents were 0.804 mA, 0.402 mA, 0.201 mA, and 0.1005 mA, which

correspond to 1 C, 0.5 C, 0.25 C, and 0.125 C, respectively. When accessing 100 % SOC, only potential limits were set as determined from the voltammograms. Whereas when accessing 50 % SOC, both a time cutoff and potential cutoffs were applied. The potential cutoffs were again about 0.3 V above and below the half wave potential; the time cutoff was reached once half of the initial theoretical capacity was reached (e.g., 1 hour for 0.5C). Whichever cutoff was reached first determined the end of the half cycle. Each independent charging/discharging rate and SOC accessed was performed in duplicate using two different cells with separately prepared materials.

8.3   Results and Discussion

Before any cycling, the limiting current of the cells was determined. The limiting current provides information about the meaningful charging rates that can be applied to the cell. For bulk electrolysis, the limiting current depends on the active species concentration and diffusivity, cell geometry, stir rate, and the electrochemical surface area[212]. In galvanostatic cycling, as higher currents are used, the cell polarizes more leading to larger overpotentials and less accessed capacity. Figure 67 shows the polarization curve of one of the cells used. Note that the limiting current was similar for the two cells used in this study and was ca. 3 mA when using 30 mL of solution, 0.001 M DBBB, and a stir rate of 1400 rpm. This current corresponds to a C-rate of ca. 3.7C. In order to ensure that mass transfer was not limiting the cycling data significantly, the largest currents chosen were around 25% of the limiting current.
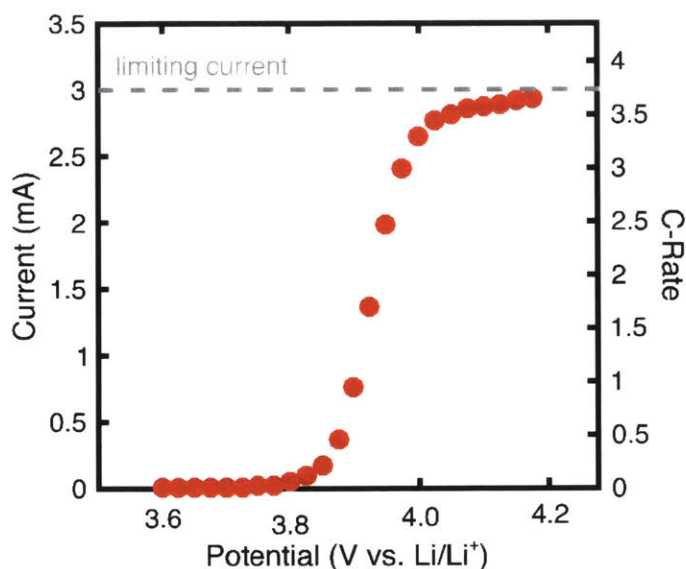
Figure 67: Polarization curve for the bulk electrolysis cell using 0.001 M DBBB at 0% SOC in 1 M LiTFSI in PC showing the limiting current of about 3 mA. The C-rate on the right axis corresponds to the experimental set up of 0.001 M active material in 30 mL of solution.

For all of the currents used, the charging capacity fade is comparable for both cells across all cycling conditions, Figure 68 and Figure 69. As expected, as the current increases, the capacity accessed deceased due to the larger cell polarization (Figure 68c compared to Figure 69)[147]. In all cycling experiments, the coulombic efficiency of the first cycle was lower than that of the other cycles. For 1C, 0.5C, 0.25C, and 0.125C, the coulombic efficiency of the first cycle was about 59%, 71%, 70%, and 64%, respectively, while all of the other cycles had a coulombic efficiency around 98%, 93%, 86%, and 71%, respectively. The low coulombic efficiencies of the first cycle are consistent with previous studies and are believe to be due to cell conditioning such as solid electrolyte interphase (SEI) formation on the lithium counter electrode. Overall, the coulombic inefficiency is much greater than the capacity fade observed, indicating that multiple processes (e.g. crossover to the counter electrode[118], numerous decay pathways[157]) are involved, which is further supported by the decreasing coulombic efficiency as the cycling rate decreases (increasing time per cycle).
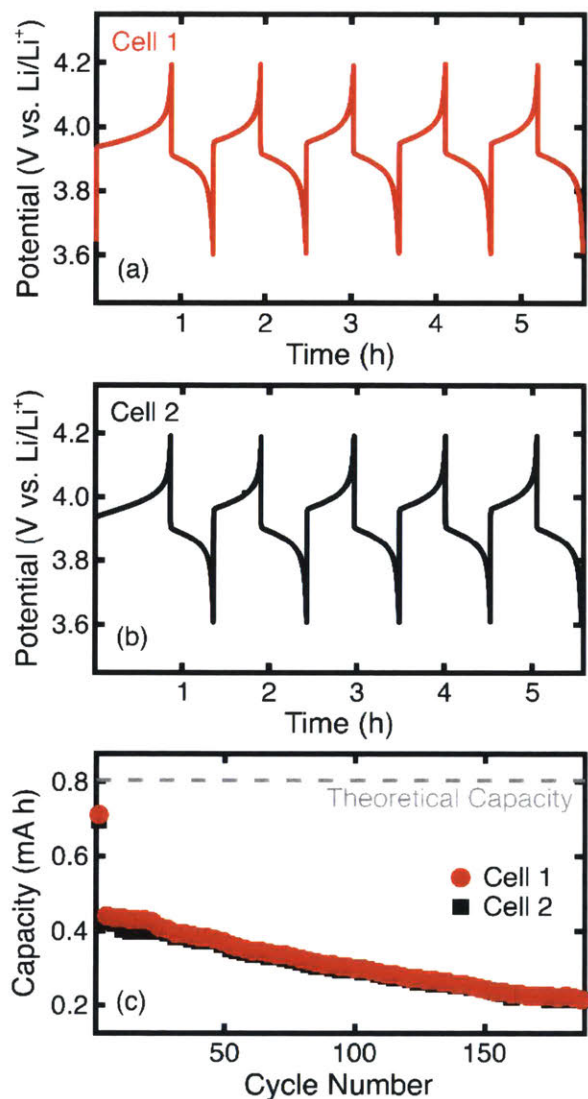
Figure 68: First 5 cycles of bulk electrolysis of 0.001 M DBBB in 1 M LiTFSI in PC in cell 1 (a) and cell 2 (b) and the corresponding charging capacity as a function of cycle number for each of the cells (c). The charging/discharging rate of 1C (0.804 mA) was used accessing 100% SOC.
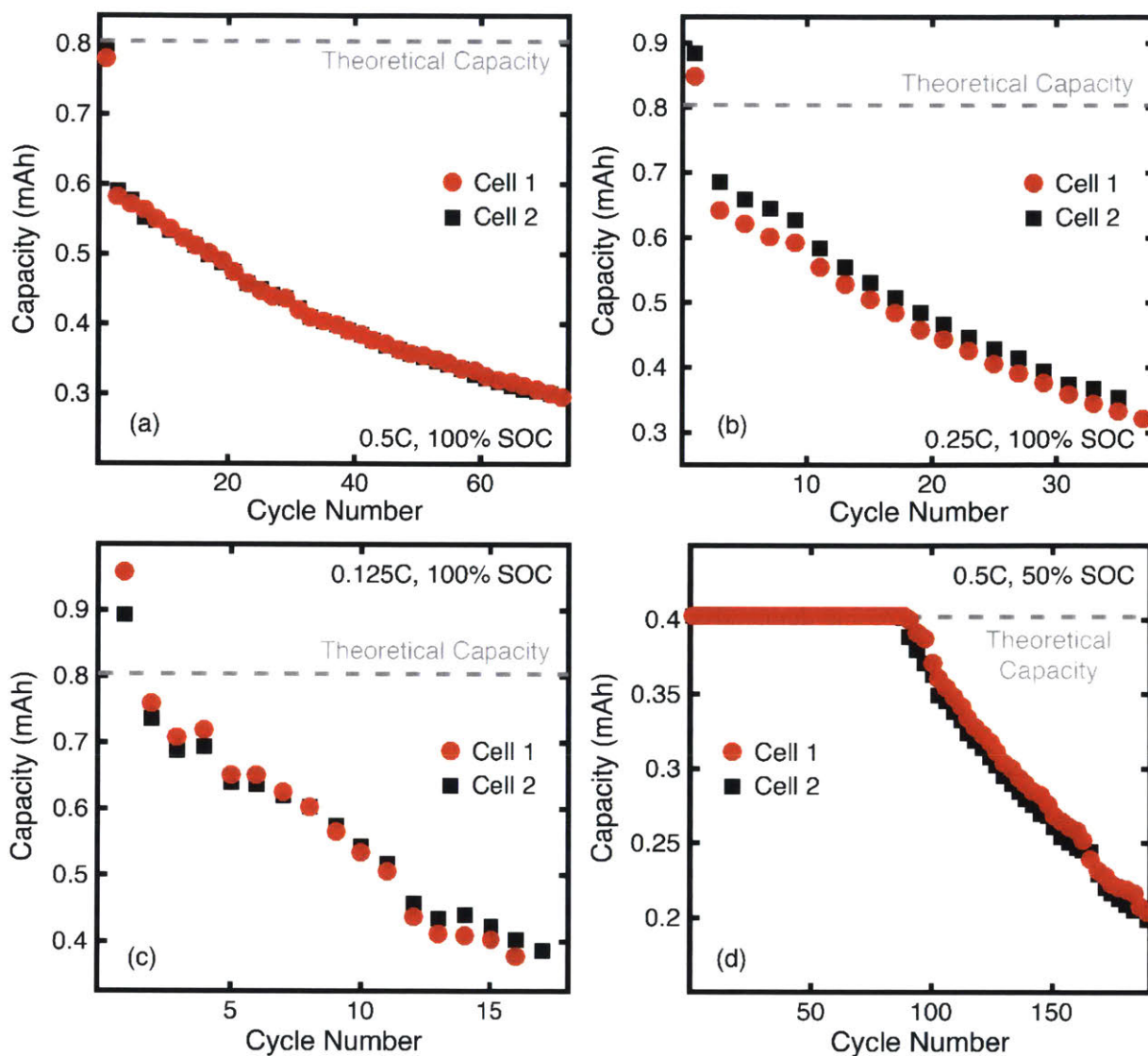
Figure 69: Charging capacity as a function of cycle number using two different BASi bulk electrolysis cells with an electrolyte composition of 0.001 M DBBB in LiTFSI in PC with a charging rate of 0.5 C (0.402 mA) accessing 100% SOC (a), 0.25 C (0.402 mA) accessing 100% SOC (b), 0.125 C (0.1005 mA) accessing 100% SOC (c), and 0.5 C (0.402 mA) accessing 50% SOC (d).

In order to determine the impact of charging rate, the capacity fade was observed using both the cycle number, Figure 70a (cell 1) and Figure 71a (cell 2), and cycle time, Figure 70b (cell 1) and Figure 71b (cell 2). The charging capacity is normalized to the second cycle in order to compare the capacity fade more easily by excluding the cell conditioning (first cycle) and minimizing the differences in capacity accessed due to the different currents used.
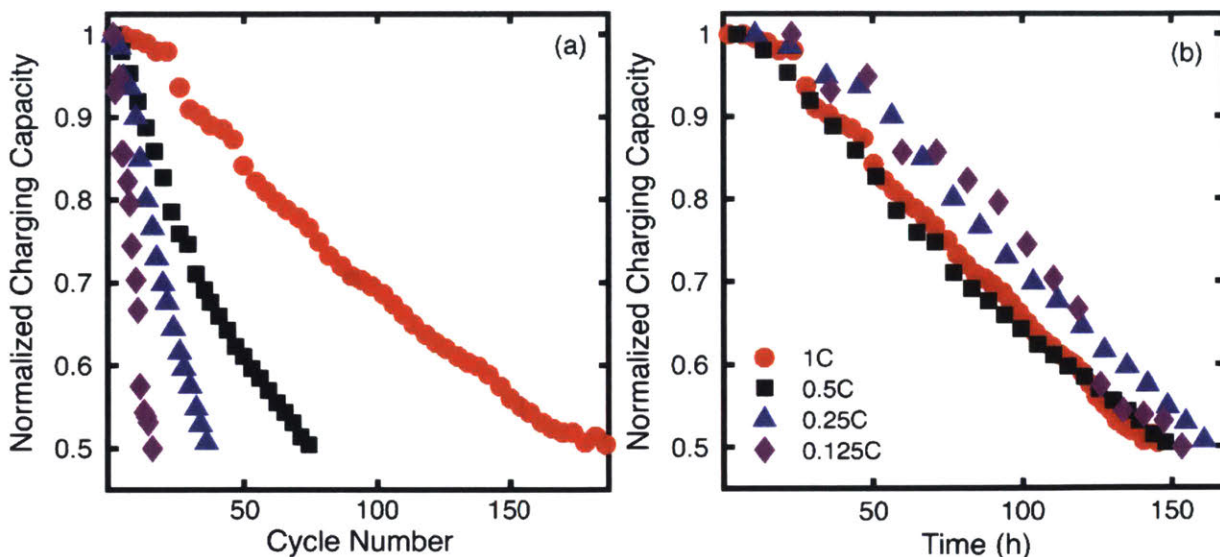
Figure 70: Normalized charging capacity as a function of cycle number (a) and time (b) accessing 100% SOC for 1C (0.804 mA, red circles), 0.5C (0.402 mA, black squares), 0.25C (0.201 mA, blue triangles), and 0.125C (0.1005 mA, purple diamonds) for cell 1. The electrolyte used was 0.001 M DBBB in 1 M LiTFSI in PC. The charging capacity is normalized to the second charging cycle.
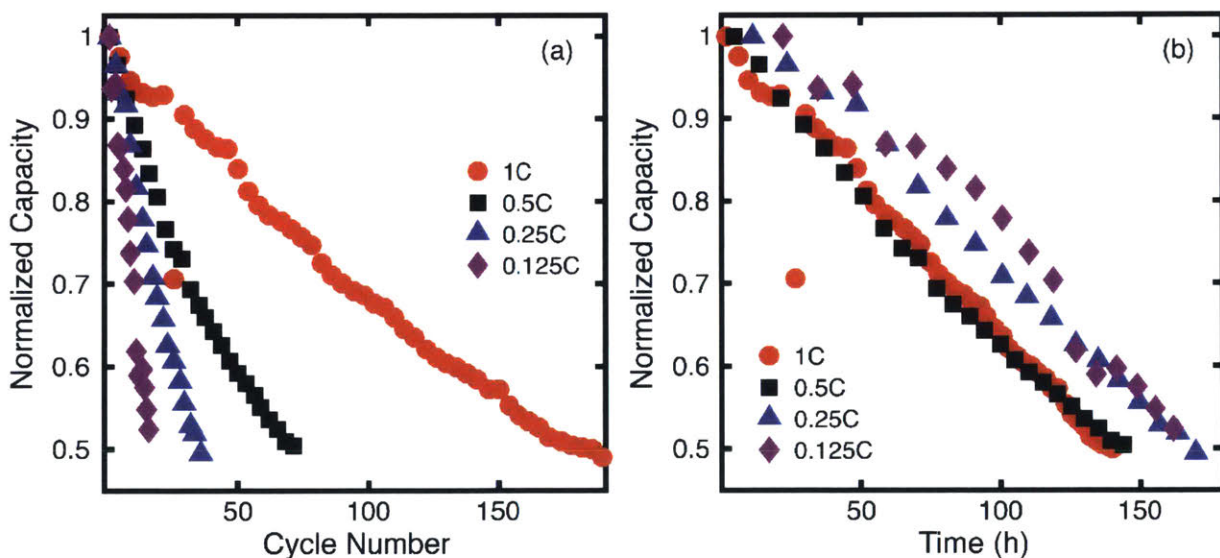
Figure 71: Normalized charging capacity as a function of cycle number (a) and time (b) accessing 100% SOC for 1C (0.804 mA, red circles), 0.5C (0.402 mA, black squares), 0.25C (0.201 mA, blue triangles), and 0.125C (0.1005 mA, purple diamonds) for cell 2. The electrolyte used was 0.001 M DBBB in 1 M LiTFSI in PC. Note, the charging capacity is normalize to the second charging cycle.

Currently, the most widely used metric to measure the stability is cycle number (Figure 70a, Figure 71a) [124,125,147,148,156,160,162,211]. However, cycle number is drastically impacted by the

charging rate. For example at 1C, DBBB cycled for 186 cycles before the capacity dropped to 50% of the second cycle, while for 0.125C, the capacity dropped by 50% after 16 cycles. Even though it is the same material, the perceived stability of DBBB is very different especially when comparing the capacity fade per cycle. The fade rate according to cycle number increases as 0.3% per cycle, 0.7% per cycle, 1.5% per cycle, and 3.7% per cycle from 1C to 0.125C. Therefore, cycle number is not a consistent way to measure the cyclability. A better measure of the stability would be looking at the cycle time (Figure 70b, Figure 71b) because it more accurately represents how long the charged/unstable state exists in solution. From Figure 70b, the cycle fade rate as a function of time is consistent across all of the charging rates used, about 0.4% per hour.

Another common inconsistency is the SOC accessed. Typically, a material is either cycled from 0% to 100% SOC[130,148,157] or from 0% to 50% SOC[124,125]. Therefore, the impact on the perceived stability of these two SOC ranges are shown in Figure 72 and Figure 73 using a C-rate of 0.5C (0.402 mA). Again, both the charging capacity fade as a function of cycle number (Figure 72a, Figure 73a) and cycling time (Figure 72b, Figure 73b) are shown.
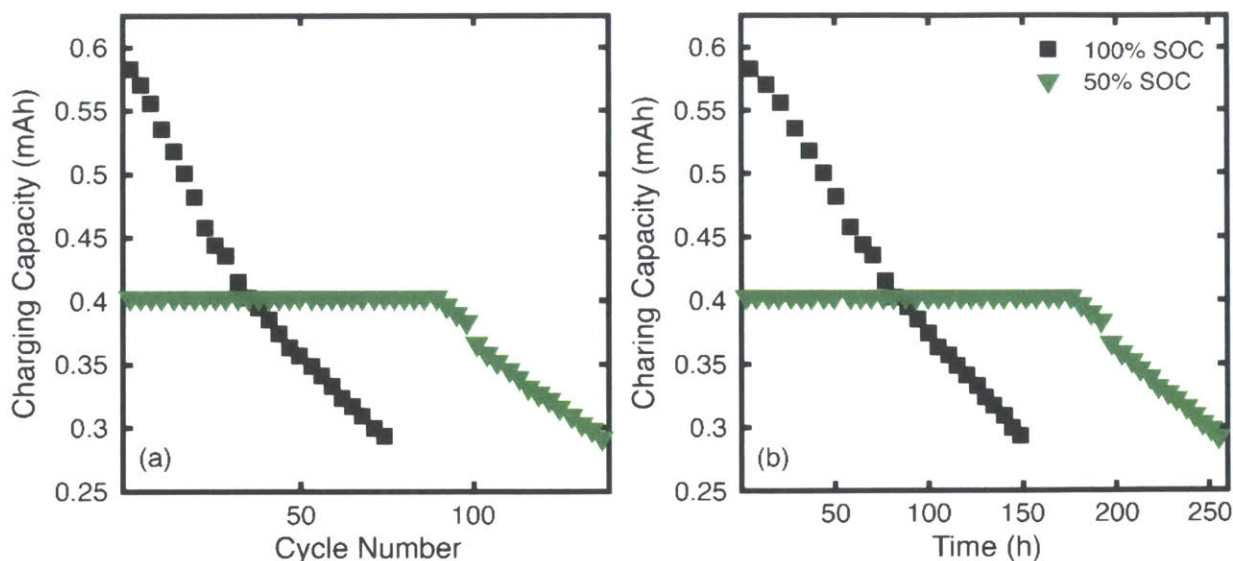
Figure 72: Charging capacity as a function of cycle number (a) and time (b) accessing 100% SOC (black squares) and 50% SOC (green triangles) with a charging rate of 0.5C (0.402 mA) for cell 1. The electrolyte used was 0.001 M DBBB in 1 M LiTFSI in PC.
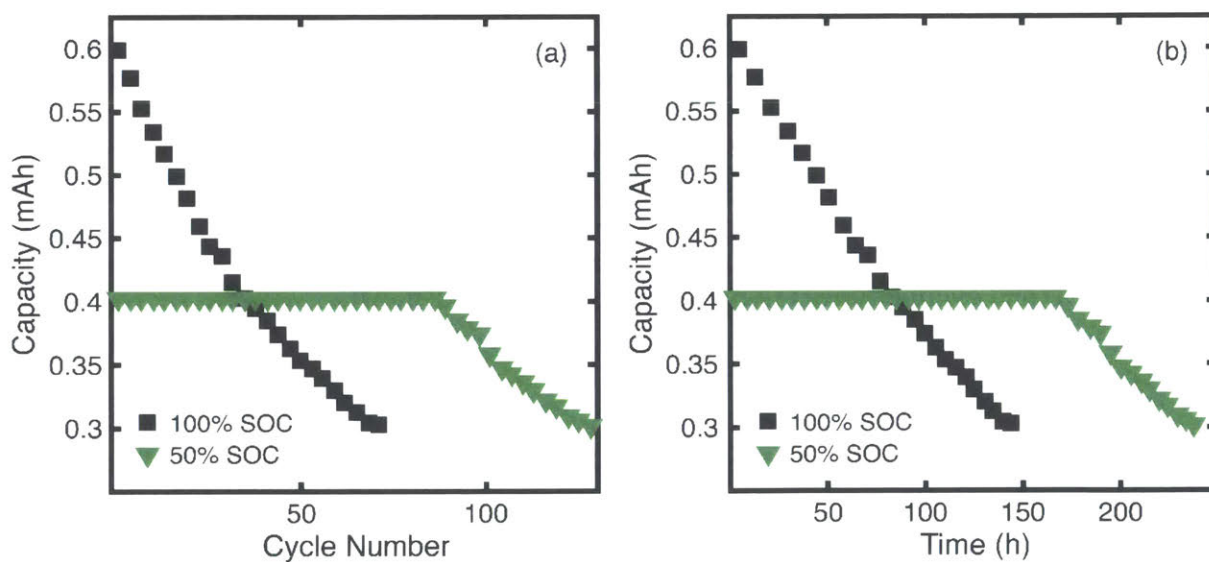
Figure 73: Charging capacity as a function of cycle number (a) and time (b) accessing 100% SOC (black squares) and 50% SOC (green triangles) with a charging rate of 0.5C (0.402 mA) for cell 2. The electrolyte used was 0.001 M DBBB in 1 M LiTFSI in PC.

When comparing the cycle number and the cycle time, the data looks very similar because it is the same charging rate. However, comparing different charging rates and different SOCs accessed would yield larger differences between the analyses. In general, when accessing a fraction

of the SOC, cycling is longer because for each cycle, the active material is in the charged/unstable state for less time and at lower concentrations; therefore, when only accessing a fraction of the SOC, cycling takes longer, which is directly related to the fraction of the SOC accessed. In this experiment accessing 50% SOC, the cycling time and cycling number are only about 1.8 times larger to achieve the same capacity fade (instead of 2). This is a result of the capacity accessed on the second cycle. When accessing 100% SOC only 0.59 mAh, 73% of the theoretical capacity, was accessed; while at 50% SOC, 0.40 mAh were accessed, which is half of the theoretical capacity. Because slightly more than half of the capacity was accessed at 50% SOC compared to 100% SOC, the cycling time and number are slightly less than twice that of 100% SOC.

8.4 Conclusions

Bulk electrolysis cycling is one of the most common methods to probe the initial long-term stability of new active materials at low concentrations. However, there are currently many different operating conditions which have an impact on the perceived stability, which is determined by the number of cycles until a capacity fade is reached. The most common operating inconsistencies are accessing different states-of-charge and using different charging/discharging rates. It was determined that the cycling time rather than cycle number is a better representation of an active species stability because it better expresses how long the active species is in the charged/unstable state[157,211]. Similarly, when only accessing a fraction of the capacity on each cycle, both the cycling time and cycle number are increased due to the decreased concentration of the charged species and deceased time in the charged state per cycle for a given charging rate. Therefore, the important parameters for bulk electrolysis cycling are how long the unstable species is in solution and how concentrated the unstable species is in solution.   Other factors to be aware of in bulk

electrolysis cycling are the cell limitations due to the cell geometry, supplied convection, and charging method. This includes how long the cell can be operated until crossover interferes with the results (especially for symmetric cell cycling), knowing the limiting current of your cell, and using a charging/discharging rate that is appropriate for your application.

9 Measuring Decay Using a Microelectrode

As longer lifetimes of soluble redox active materials become more prevalent, more efficient methods to measure their stability are needed. The current methods include cycling the material until the capacity fades, NMR, EPR, and UV-Vis. Each of these techniques has their own limitations such as accessibility and ability to test materials in relevant flow battery conditions. Here, we propose the use of a microelectrode as a probe for analyzing decay rates of active materials. Utilizing a microelectrode allows for the identification of a charged material decay rate (reversible material loss) and a total material decay rate (irreversible material loss), simultaneously, which is much more difficult with the current methods. In addition to validating this technique with ferrocene, different sources of error were examined, such as the impact of unequal diffusion coefficients of the oxidized and reduced species; the maximum error was found to be < 5 %. Finally, the technique was demonstrated with a well-studied, moderately stable, substituted dialkoxybenzene [2,5-di-*tert*-butyl-1,4-bis(2-methoxyethoxy)benzene]. This chapter is partially reprinted from "Decay determination of redox active materials using a microelectrode" by **Jeffrey A. Kowalski** and Fikile R. Brushett, which is in preparation.

9.1 Introduction

As the need for cost effective energy storage on many scales increases, many storage technologies are being further developed and commercialized[2,55]. These technologies require new materials and utilize conditions that are relatively unexplored (e.g. high concentrations and long lifetimes).[2,55,168] As these materials are tested more closely to the operating conditions, new challenges begin to surface[168]. Therefore, there is a need to advance the testing protocols to align

with the new applications[211]. Of the newly explored materials, highly soluble organic redox active molecules are gaining traction[1,61,146,151,213]. However, the major challenge associated with these organics is their stability in the charged state[129,157,211,213,215,217]. The poor stability can lead to both single cycle inefficiencies from self-discharge and overall storage capacity fading due to active species decomposition. Determining the active species lifetime at relevant concentrations is of particular interest[168] because all of the currently utilized methods have drawbacks associated with them.

The classic method to measure the lifetime of an active material is electrochemical cycling to exhaustion, which involves charging and discharging the active material in solution[125,147,148,154,156,160,162,211,217]. Once the charging capacity drops below a certain amount, the corresponding cycle is considered the cycling lifetime. This process can take a very long time, and as the material becomes more stable, the longer the process will take to determine the cycling lifetime. Additionally, there is not a standardized method to cycle materials, and therefore many different cycling conditions such as charging methods (*e.g.* galvanostatic[125,156] and potentiostatic[211]), charging/discharging rates[147,148,156,160,216], SOCs accessed,[125,147,148,217] cell geometries,[148,156,162,217] and active species concentration[147,148,156,160,216] are utilized for cycling. These inconsistencies make it very difficult to compare stability data across different experiments. Therefore, a much quicker and more consistent method to measure material lifetime needs to be established at relevant concentrations.

Different spectroscopy methods are beginning to be used with electrochemical techniques to measure the decay rates such as electron paramagnetic resonance for radical cation decay determination (EPR)[159,161,215], nuclear magnetic resonance when a radical cation is absent (NMR),[129,156] and UV-Vis spectroscopy.[112,147] All of these methods measure a decay rate rather

than a cycling lifetime and therefore lead to a more consistent comparison. They typically start with the isolated active material, either charged or discharged, and then measure the change in the signal response over time. However, each of these techniques is limited by the concentration used and the expense/availability of the machines to take the measurements. Additionally, the presence of salt in the electrolyte can further mask the signal in all of these techniques, adding a level of complexity to the analysis. Another drawback of each of these techniques is it is possible to obtain the decay rate of the initial material relatively easily, but it is much more difficult to determine different types of decomposition (charged state to neutral state vs. charged state to a different decomposed material).

One underutilized method to identify decay pathways is to probe the solution electrochemically with a microelectrode (electrode diameter ~ μm). Microelectrode operation is identical to classic cyclic voltammetry at a macroelectrode (electrode diameter ~ mm). However, because the microelectrode diameter is much smaller, the magnitude of currents obtained, and therefore the ohmic drop due to the solution resistance is significantly reduced[212,219] Additionally, the electrode diameter is on the same order of magnitude as the diffusion boundary layer leading to nonplanar (steady state) diffusion[212,219]. These unique aspects of microelectrodes led them to mainly be used for electroanalytical chemistry to determine electrochemical properties (e.g. diffusion coefficient, kinetic rate constant) for both low and high concentration solutions[137,212], probing solutions to determine the presence of an electroactive species at low concentrations[220–223], and electrochemical synthesis[224,225]. However, microelectrodes are not typically used to probe the concentration over time to determine how a material decays. By monitoring the change in the current response over time, it is possible to extract decay rates of electrochemically active

materials. Microelectrodes offer an accessible, inexpensive way to determine and compare the decay rates of electroactive materials at relevant concentrations in the operating conditions.

In this work, we present a decay determination technique using a microelectrode to measure the charged species decay and the total species decay simultaneously. We begin by discussing microelectrode theory and how it pertains to determining species decay. The different sources of error, including the measurement changing the bulk concentration, unequal diffusion coefficients, electrode fouling, and temperature variations from charging the solution, are then examined using ferrocene as a model, stable compound. Finally, the microelectrode technique was applied to a model decay compound, 2,5-di-tert-butyl-1,4-bis(2-methoxyethoxy)benzene (DBBB)[137,139,158,217], to observe the different types of decay (charged species and total species).

9.2 Experimental

All work was performed in an argon-filled glovebox (MBraun Labmaster, H_2O < 5 ppm, O_2 < 1) with an ambient temperature of 26 °C. All experiments were conducted with the same electrolyte, 1 M bis(trifluoromethane)sulfonamide lithium salt (LiTFSI, BASF) in propylene carbonate (PC, BASF), which were both stored in the glovebox. This electrolyte was chosen due to its large electrochemical stability and low volatility. The active species used were ferrocene (Sigma Aldrich), ferrocenium (Sigma Aldrich), and 2,5-di-tert-butyl-1,4-bis(2-methoxyethoxy)benzene (DBBB). All solutions were made the day before electrochemical testing to ensure that the active material and salt were completely dissolved.

Solutions were charged electrochemically using a VSP-300 potentiostat (Bio-Logic); charging occurred in a commercially available three electrode bulk electrolysis cell (BASi) using

30 mL of solution (solvent, supporting salt, and active species) and a stir rate of 1600 rpm. The working electrode, counter electrode, and reference electrode were reticulated vitreous carbon (BASi), lithium foil (Alfa Aesar), and fritted lithium foil (Alfa Aesar) with 1 M LiTFSI in PC as the fill solution, respectively. A potentiostatic method was used to charge the solution; the set potential was 300 mV above the equilibrium potential of the redox couple. A coulombic cutoff at 100% state-of-charge was used to determine when the material was fully charged. For the low concentrations tested (0.001 M, 0.003 M, 0.005 M), this process took about an hour, whereas charging the 0.025 M solution took ca. 3 h. Once the coulombic cutoff was reached, the solution was immediately transferred into two 20 mL scintillation vials (VWR) to minimize additional contamination from the counter electrode chamber generated during charging. The solution temperature was measured directly after electrolysis and again after all decay measurements were completed. The electrolyte viscosity was then measured separately at the determined temperatures using a Viscolite 700 laboratory viscometer (Vindum Engineering).

After each charging procedure, either square wave voltammetry (SWV) (working electrode: 3 mm diameter glassy carbon electrode [CH Instruments, Inc.]) or cyclic voltammetry (working electrode: platinum disc microelectrode [CH Instruments, Inc.]) measurements were taken for 14 h. The SWV measurements were collected every hour on a VSP-300 potentiostat (Bio-Logic) to avoid significantly affecting the bulk solution properties, while the microelectrode measurements were collected every 15 min with a CHI-630E (CH Instruments, Inc.). The counter and reference electrodes for both types of data collection were a platinum coil (BASi), and a fritted $Ag/Ag^+_{cryptand}$ reference electrode with a fill solution of 0.1 M $AgBF_4$ (Sigma-Aldrich), 0.04 M kryptofix (Acros Organics), and 1 M LiTFSI in PC[189], respectively. Before the first measurement of each data set, the electrodes were polished on a MicroCloth pad with 0.05 µm alumina powder

(Buehler Ltd.). The electrodes were then rinsed with deionized water (Millipore) and wiped with lens paper. Between each measurement (either 15 min or 1 h), the working, counter, and reference electrodes were left in the solution. Therefore, the working electrodes were not polished between each step to avoid changing the surface area or position relative to the other electrodes. All measurements were performed in triplicate.

9.3   Microelectrode Decay Theory

For a microelectrode, a steady state current leading to a diffusion-limited current plateau occurs at high overpotentials, either much greater or less than the equilibrium potential. For a microdisc geometry, the steady state current is given by:

$$i_{ss} = 4nFcrD \tag{1}$$

where, i_{ss} is the steady state/plateau current at large overpotentials (A), n is the number of electrons transferred (here, n =1), F is the Faraday constant (96485 C/mol e⁻), c is the concentration (mol/cm³), r is the radius of the microelectrode (0.00055 cm), and D is the diffusion coefficient (cm²/s)[212,219]. Using the steady state current (Equation 1), a relative concentration of the charged species and the total species can be obtained. Figure 74 shows the raw voltammetry data at the initial scan and a scan at a later time to highlight the relevant steady state currents.
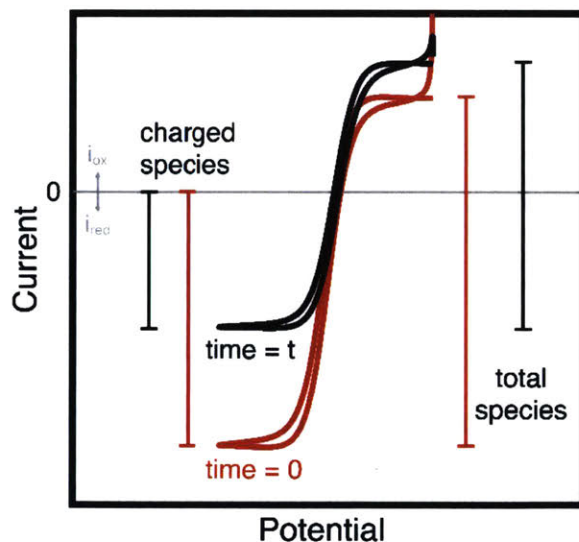
Figure 74: Raw voltammetry data from the microelectrode experiments at time 0 (red) and some later time, t, (black) showing how to obtain the charged species and total species relative concentrations for an oxidized species.

Taking the ratio of the steady state current from the charged species at any time to the initial steady state current (left side of Figure 74) will give the concentration ratio because the concentration should be the only changing value in Equation 1. This information provides how the charged species concentration is changing over time. Looking at the magnitude of the difference in the current from the oxidative steady state current to the reductive steady state current (right side of Figure 74) gives information about the total species concentration (sum of the oxidized and reduced species' concentrations). If the diffusion coefficient of the oxidized and reduced species are equal, a reasonable initial assumption[212], the ratio of steady state currents is equal to the ratio of the total species concentration. For both the charged species and total species, the decay behavior and even a decay rate could be obtained. The advantage of using the microelectrode as a probing technique allows you to observe the decay of the charged material and the total material. By collecting both of these concentration profiles simultaneously, it is possible to differentiate the decay into recoverable vs. irrecoverable losses.

243

9.4   Types of Error

Aspects of this measurement that can lead to error, which can convolute the decay signal and lead to an artificial decay rather than a true decay. The sources of artificial decay come from the measurement, rather than the active species instability in either the charged or discharged state. False decay can occur due to the current significantly affecting the bulk concentration, unequal diffusion coefficients between the oxidized and reduced species, electrode fouling, or significant temperature changes from the experimental setup.

Conversion per Cycle

In order to ensure that the conversion per cycle is not significant compared to the bulk concentration, the number of coulombs converted per cycle and the total number of coulombs accessible in the solution must be compared. The total number of accessible coulombs in the solution is given by:

$$Q_{sol} = nFcV \qquad (2)$$

where Q_{sol} is the total accessible coulombs in solution (C) and V is the solution volume (cm^3). For simplicity, a maximum number of coulombs accessed per cycle can be approximated as if the steady state current were accessed for the entire cycle as seen in Equation 3.

$$Q_{cyc} = i_{ss}t_{cyc} \qquad (3)$$

Where Q_{cyc} is the maximum number of coulombs accessed by a measurement (C) and t_{cyc} is the time for one cycle (s). Taking the ratio of Equation 3 to Equation 2, and combining Equation 1

with Equation 3, yields the fraction of material accessed, F_{acc}, per measurement, shown in Equation 4.

$$F_{acc} = \frac{4rDt_{cyc}}{V} \tag{4}$$

Using the upper limit of values determined by experiment for r (1×10^{-3} cm), D (1×10^{-4} cm^2/s), t_{cyc} (100 s), and V (15 cm^3) gives an upper estimate for the fractional conversion per cycle: 3×10^{-6}. With the fractional conversion of 3×10^{-6}, it would take 3333 cycles before accessing 1% of the total bulk concentration, which corresponds to 34 days taking a measurement every 15 min. Thus, as only 14 h of measurements are taken, the bulk concentration is not significantly changed by the measurement.

Unequal Diffusion Coefficients

To determine the validity of the assumption that the diffusion coefficients of the oxidized and reduced species are equal, the error for equal diffusion coefficients compared to unequal diffusion coefficients for the oxidized and reduced species was calculated. First, the ratio of the total concentration at any time and the total, initial concentration can be calculated, R_c, as shown in Equation 5.

$$R_c = \frac{c_r + c_o}{C_{r,i} + C_{o,i}} \tag{5}$$

In Equation 5, c_r is the concentration of the reduced species, c_o is the concentration of the oxidized species, $C_{r,i}$ is the initial concentration of the reduced species, and $C_{o,i}$ is the initial concentration of the oxidized species. Substituting Equation 1 into Equation 5 and simplifying yields:

$$R_c = \frac{i_{ss,r}\gamma + i_{ss,o}}{I_{ss,r}\gamma + I_{ss,o}} \tag{6}$$

245

where, $i_{ss,r}$ is the steady state current of the reduced species at any time, $i_{ss,o}$ is the steady state current of the oxidized species at any time, $I_{ss,r}$ is the initial steady state current of the reduced species, $I_{ss,o}$ is the initial steady state current of the oxidized current, and γ is the ratio of the diffusion coefficient of the reduced species to the diffusion coefficient of the oxidized species (D_r/D_o). When the diffusion coefficients are equal, γ is unity. The percent error, ε, for the case of unequal diffusion coefficients can be described as:

$$\varepsilon = \frac{\dfrac{i_{ss,r} + i_{ss,o}}{I_{ss,r} + I_{ss,o}} - \dfrac{i_{ss,r}\gamma + i_{ss,o}}{I_{ss,r}\gamma + I_{ss,o}}}{\dfrac{i_{ss,r}\gamma + i_{ss,o}}{I_{ss,r}\gamma + I_{ss,o}}} \tag{7}$$

Simplifying Equation 7 and substituting in α for the ratio of $i_{ss,r}$ to $i_{ss,o}$ and β for $I_{ss,r}$ to $I_{ss,o}$ yields:

$$\varepsilon = \frac{(\alpha - \beta)(1 - \gamma)}{(\gamma\alpha + 1)(\beta + 1)} \tag{8}$$

Note, that from Equation 8, if γ is one, the error is zero. Figure 75 plots the error for different γ values for reasonable values of α and β determined from the experiment.
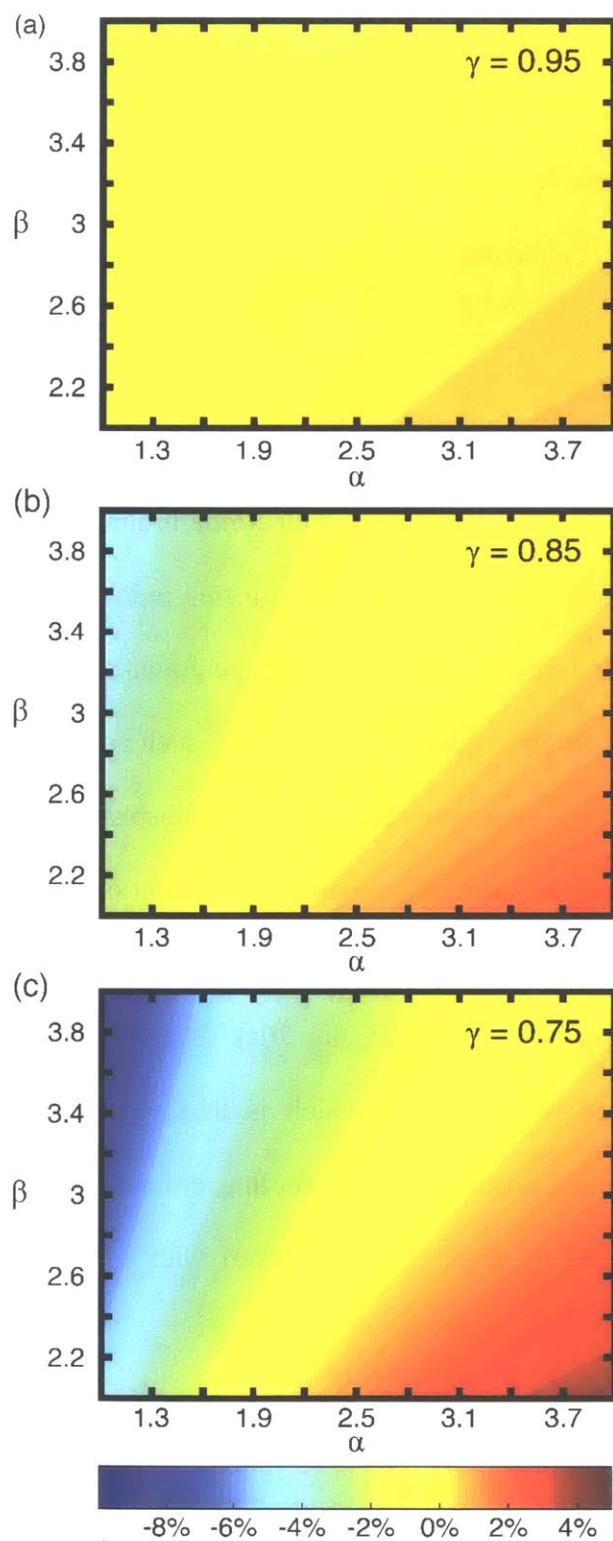
Figure 75: Plots of the error analysis for the total species concentration for γ (Dr/Do) = 0.95 (a), γ = 0.85 (b), and γ = 0.75 (c). Both α (ratio of the instantaneous reduced current to the instantaneous oxidized current) and β (ratio of the initial reduced current to the initial oxidized current) represent the range of values observed in the experiments for this work.

For all of the ratios of steady state currents obtained in this work, the error is never greater than 5% for the total species concentration, which is reasonable over the course of the experiment. However, as seen from Figure 75 and Equation 8, as the diffusion coefficients begin to differ more, the error in the total species concentration increases.

Electrode Fouling

To determine if decay occurs because of electrode fouling or temperature variations, the ferrocene/ferrocenium couple was examined because this redox couple has been shown to be extremely stable and has even been used as a reference potential in nonaqueous electrolytes[106]. First, to avoid any possible complications from charging such as counter electrode impurities or temperature variations, 0.005 M ferrocenium hexafluorophosphate was used directly. At first, a carbon fiber microelectrode was used, but a significant amount of decay was observed due to the electrode fouling. Therefore, a platinum microelectrode was used, and minimal artificial decay was observed over the 14 h experiment (Figure 76a). Over the course of the experiment, the ferrocenium signal decayed by ca. 0.5%, which is thus representative of the measurement resolution. Therefore, to ensure that electrode fouling did not occur in future tests, after all measurements, an additional measurement was taken with a freshly polished electrode and compared to the last scan.

Temperature Variations

Second, to investigate if the charging method played a role in observed decay, 0.005 M ferrocene was used and charged electrochemically, and then monitored with the platinum microelectrode (Figure 76b). Unexpectedly, within the first 2.5 h of monitoring, the concentration

dropped about 10% and then stabilized. We attribute this "decay" to solution cooling, which in turn impacts the diffusivity and therefore the limiting current via temperature and viscosity as can be seen from the Stokes-Einstein relationship (Equation 9).

$$D = \frac{k_b T}{6\pi\mu a}$$ (9)

Where k_b is the Boltzmann constant (1.38×10^{-23} J/K), T is the temperature (K), μ is the solution dynamic viscosity (Pa s), and a is the hydrodynamic radius of the material in solution (m). When the temperature and viscosity were measured just after charging the solution, the values were 30 °C and 8.0 cP, respectively. By the end of the measurement, the temperature dropped to 26 °C and the viscosity rose to 8.7 cP. The temperature increase is most likely a result of mechanical stirring and joule heating from charging the solution. With this change in temperature and viscosity, the diffusion coefficient and therefore the steady state current should change by about 10%, which is in agreement with the 10% drop seen in the first 2.5 h. Therefore, if the first time point used is 2.75 h after charging, about 1% decay is noticed over the 11 h of experiment (Figure 76c).
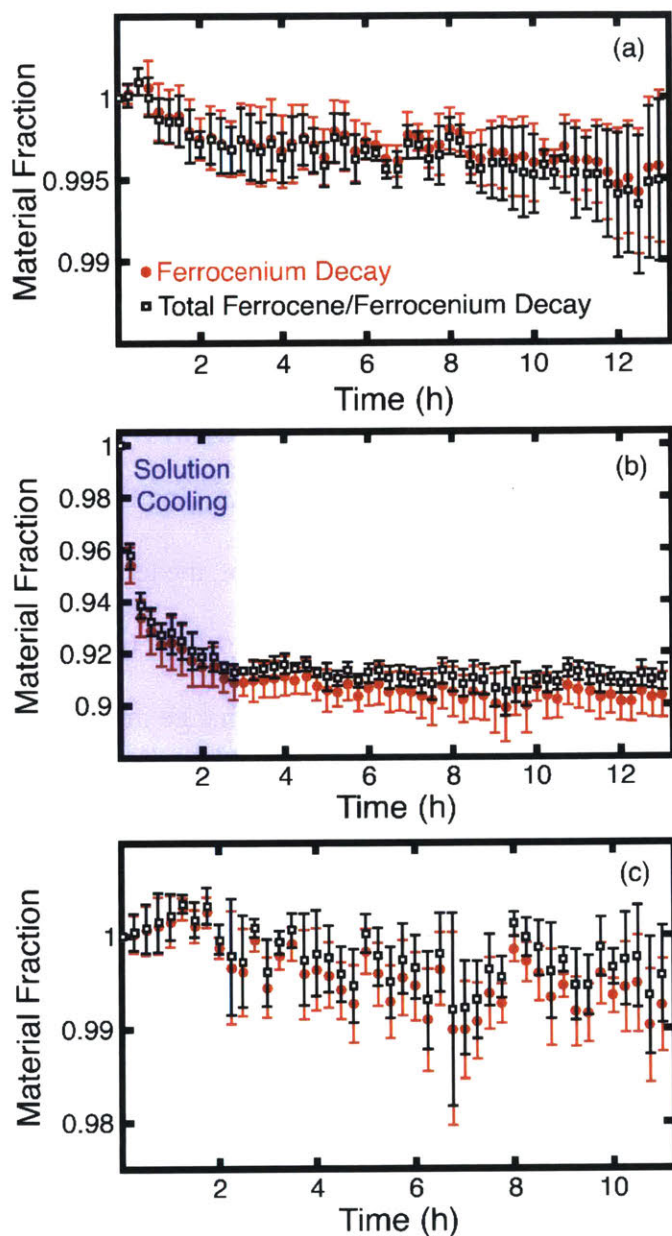
Figure 76: Relative concentration as a function of time for the ferrocene/ferroceneium redox couple for an initial solution of 0.005 M ferrocenium (a), an initial solution of 0.005 M ferrocene charged by bulk electrolysis (b), and the same data from (b) using the 2.75 h time point as the initial fraction of material in order to give the temperature of the solution time to equilibrate (c). For all plots the relative concentration of the ferrocenium (red circles) and the relative total concentration of redox active material (black squares) are shown, and the electrolyte used was 1 M LiTFSI in PC. All data was collected in triplicate.

Once the technique was validated to the point where artificial decay was not observable, DBBB

was used to examine the technique when there is decay expected[158]. For the first test, 0.005 M of

DBBB was used, the same concentration as the ferrocene experiments (Figure 77). At 0.005 M,

the charged species decays to about 60% of the initial value, but the total species is only decays

about 5%. This means that most of the charged DBBB material decays into the neutral species.
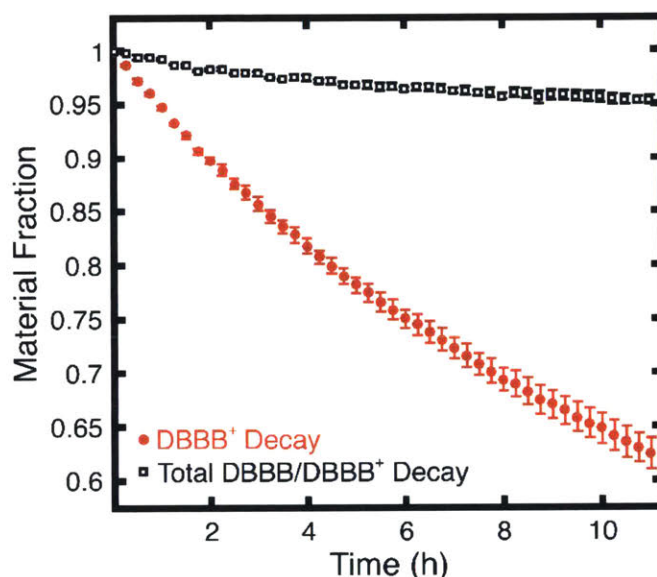
Figure 77: Relative concentration as a function of time for a 0.005 M solution of DBBB in 1 M LiTFSI in PC. For all plots the relative concentration of the radical cation (red circles) and the relative total concentration of redox active material (black squares) were collected in triplicate. Each solution was charged by bulk electrolysis.

It is worth noting that the total material only decayed by ca. 5%, which was shown to be

the maximum error of the measurement for unequal diffusion coefficients. Therefore, square wave

voltammetry, a technique which can be used to determine the total species decay, was used on the

charged solution[212,226]. Using the differential peak current value (proportional to the

concentration), the material decay was determined and compared to the total species decay from

the microelectrode experiments (Figure 78). The square wave voltammetry agrees with the

microelectrode measurements within the variation of the experiments, further validating the use of microelectrodes to measure both the charged and total species decays, simultaneously.
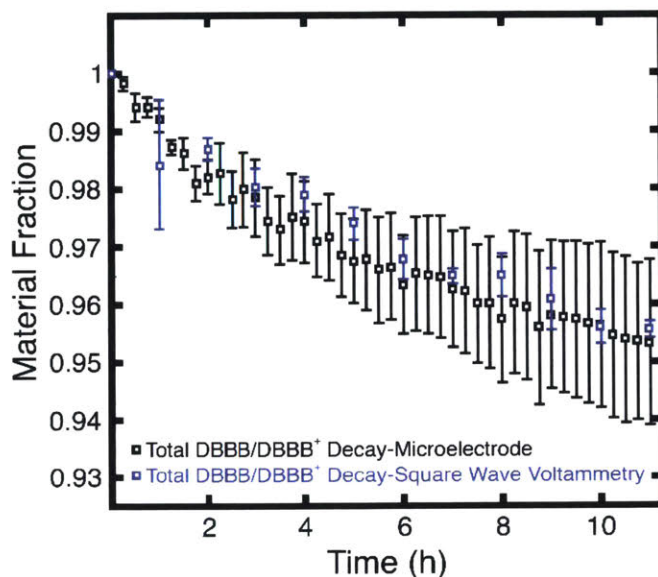
Figure 78: Relative total species concentration as a function of time for a 0.005 M solution of DBBB in 1 M LiTFSI in PC collected by a microelectrode (black squares) every 15 min and collected by square wave voltammetry (blue squares) every hour. All measurements were collected in triplicate. Each solution was charged by bulk electrolysis.

One of the advantages of using the microelectrode to measure the decay is that the materials can be tested at a range of concentrations, which are more realistic for many operating conditions. However, due to the electrochemical charging method used, the maximum concentration that could be tested was around 0.025 M. For example, charging the 0.025 M solution took around 3 h, while the charging time for many of the other solutions were about 1 h. The additional concentrations of DBBB examined were 0.001 M, 0.003 M, and 0.025 M. The lower limit of this microelectrode technique appears to be 0.001 M because below this concentration, the limiting current was on the same order of magnitude as the electrochemical noise of the experiment. Note that with a higher diffusion coefficient (e.g. less viscous solvent) lower concentrations should be measurable. Figure 79 shows the compiled data of DBBB from all of the concentrations tested.
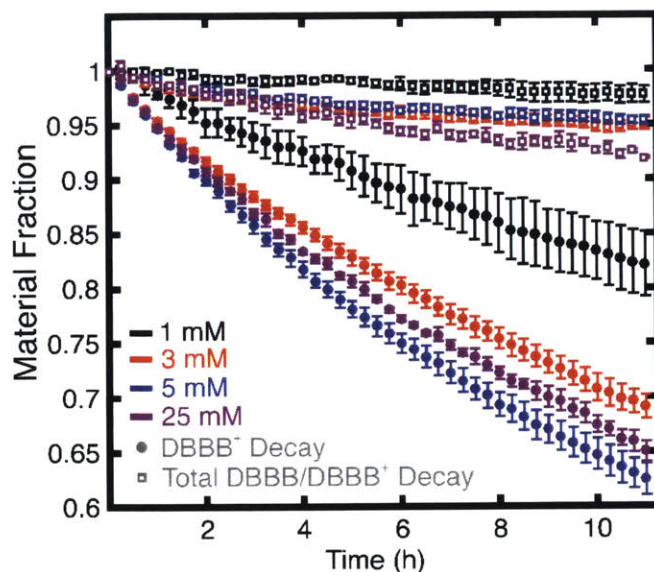
Figure 79: Relative concentration as a function of time for 0.001 M (black), 0.003 M (red), 0.005 M (blue), and 0.025 M (purple) solutions of DBBB in 1 M LiTFSI in PC. The relative concentrations of the radical cation (circles) and the relative total concentrations of redox active material (squares) were collected in triplicate. Each solution was charged by bulk electrolysis.

In general, as the concentration increases the decay rates of both the charged and total materials increase. This is not seen when comparing the decay rate of the charged species at 0.005 M and 0.025 M, but the difference is within the error of the experiment. Additionally, there can be some deviation due to the extra charging time at 0.025 M (4 h of charging rather than 1 h), so additional decay occurs during this time that is not being accounted. This is a limitation of the charging method not the decay technique. Therefore, using other charging methods or starting with the oxidized species could remedy this limitation.

Because this technique gives concentration profiles it is possible to obtain decay rates for the active species as a function of the initial concentration. Figure 80 examines the decay rate for both first order decay, due to its simplicity, and second order decay, which has precedence in the literature[157,158,161]. Even though for this work, an upper concentration limit was set at 0.025 M, much higher concentrations can be probed using a microelectrode. This becomes particularly

relevant when considering the applications of the active material, because the decay rates can be determined at the operating conditions. However, it is worth noting that the decay rate of DBBB$^+$ is realistically more complicated than a second order process, because there are multiple types of reactions occurring (e.g. self-discharge, species decomposition, solvent attack). Because the microelectrode gives a ratio of the concentration to the initial concentration at any time, in practice, other more complicated decay mechanisms can be used to model the decay rate constant(s).
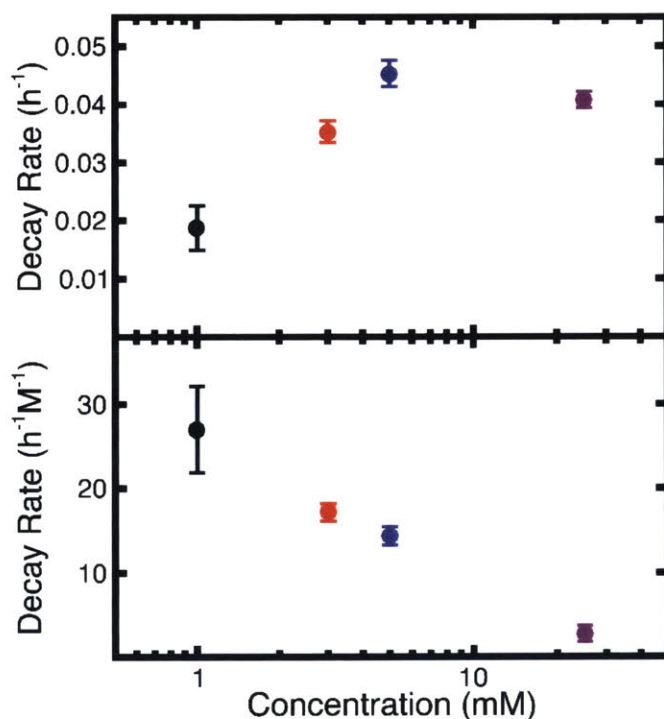
Figure 80: The decay rate as a function of concentration for DBBB$^+$ in 1 M LiTFSI for the 4 concentrations tested (0.001, 0.003, 0.005, 0.025 M), assuming a first order decay (top) and second order decay (bottom). All measurements were completed in triplicate.

9.6   Conclusions

Using a microelectrode as a probing technique is an efficient way to monitor the decay of both the charged material and the total species concentrations, something that is not typically feasible with other decay monitoring techniques. In this work, the ferrocene/ferrocenium couple was first used

to ensure that the measurement process was not causing an artificial decay due to electrode fouling or temperature changes. Once the method was validated, DBBB was used as a model decay compound to examine if the microelectrode could measure the decay rate of both the total species and charged species. Based on the error analysis of the total species decay, square wave voltammetry was used to ensure that the decay behavior obtained using a microelectrode is consistent with accepted methods to measure the decay. Last, the concentration of DBBB was varied to show the range of concentrations usable with the microelectrode.

While the work presented here is limited by the charging method, different charging methods could be used to reach higher concentrations. Additionally, the time frame of this experiment is limited to 14 h. As a material becomes more stable, this timeframe will not be sufficient to measure the decay rate. However, raising the temperature should increase the decay rate and therefore, the decay rate should be detectable[156]. One possible drawback of using a microelectrode as a probing technique, which was not observed here, is if the material decays into a different electrochemically active species in the same potential window of interest. In this case, the electrochemical response could be masked by the newly formed decay product. Overall, microelectrodes show promise as an accessible, inexpensive method to measure decay because multiple decay rates can be measured simultaneously and the measurement is compatible with radicals, oxidations, or reductions.

9.7   List of Variables and Constants

a   Hydrodynamic radius in solution (m)
c   Concentration (mol/cm^3)
c_o Instantaneous concentration of the oxidized species (mol/cm^3)
$C_{o,i}$ Initial concentration of the oxidized species (mol/cm^3)

255

c_r	Instantaneous concentration of the reduced species (mol/cm^3)
$C_{r,i}$	Initial concentration of the reduced species (mol/cm^3)
D	Diffusion coefficient (cm^2/s)
D_o	Diffusion coefficient of the oxidized species (cm^2/s)
D_r	Diffusion coefficient of the reduced species (cm^2/s)
F	Faraday's constant (96485 C/mol)
F_{acc}	Fraction of coulombs accessed in a single microelectrode scan
i_{ss}	Steady state current (A)
$I_{ss,o}$	Initial steady state current of the oxidized species (A)
$i_{ss,o}$	Instantaneous steady state current of the oxidized species (A)
$I_{ss,r}$	Initial steady state current of the reduced species (A)
$i_{ss,r}$	Instantaneous steady state current of the reduced species (A)
k_b	Boltzmann's constant (1.38 × 10^{-23}J/K)
n	Number of electrons transferred
Q_{cyc}	Maximum number of coulombs from a single microelectrode scan (C)
Q_{sol}	Number of coulombs in the solution from the microelectrode (C)
r	Radius of the microelectrode (cm)
R_c	Ratio of the instantaneous total concentration to the initial total concentration
t_{cyc}	Time for one microelectrode scan (s)
T	Temperature (K)
V	Volume of solution in the microelectrode measurement (cm^3)
α	Ratio of the instantaneous steady state currents of the reduced to oxidized species
β	Ratio of the initial steady state currents of the reduced to oxidized species
γ	Ratio of the diffusion coefficients of the reduced to oxidized species
ε	Fractional error for unequal diffusion coefficients
μ	Solution dynamic viscosity (Pa s)

10 Conclusions and Outlook

This concluding section provides my outlook for redox flow battery technology focusing specially on the active materials. This section contains partially reprinted work from "Recent Developments and Trends in Redox Flow Batteries" by Liang Su, **Jeffrey A. Kowalski**, Kyler J. Carroll, and Fikile R. Brushett in <u>Rechargeable Batteries: Materials, Technologies and New Trends</u> (2015, editors: Zhengcheng Zhang and Sheng Shui Zhang). Permission for reproduction of the work was obtained on January 1, 2019 through Copyright Clearance Center's RightsLink® service.

Stationary energy storage systems, in particular electrochemical energy storage systems, will play a pivotal role in the widespread integration of renewable, non-dispatchable energy sources (e.g., solar photovoltaic (PV), wind) and in the improvement of energy efficiency of the electric power sector. Redox flow batteries are particularly attractive for these applications due to their favorable combination of performance, cost, and safety. However, present generation technologies are not cost-competitive, which drives research and development efforts towards new redox chemistries, electrolyte formulations, and cell designs. Analysis by Darling et al. has indicated that both aqueous and nonaqueous RFBs have pathways to meeting long-term objectives for cost-effective energy storage[2]. As mentioned previously, reductions in battery costs ($/kWh) can be achieved via lowering materials cost ($/kg) and increasing materials energy density (kWh/kg). Shifting away from transition metals to organic active materials, may offer a pathway forward through both metrics, because these materials can be synthesized via cost-effective routes and are less dependent on the production and reserves of key elements (e.g., vanadium). Moreover, the electrochemical and physical properties can be tailored via modification of the redox moieties and the surrounding structure[61]. The most common redox cores examined for the posolyte are

dialkoxybenzene, phenothiazine, and TEMPO derivatives. While all of these materials act as a good foundation for molecular modification, none of them are acceptable for implementation.

One of the largest design challenges still facing these molecules is a high redox potential while remaining stable in all accessible states-of-charge[157,158,211,213]. As seen in Subtractive Engineering of Dialkoxybenzenes, Halidization of Dialkoxybenzenes, Impact of Cycling Conditions on Perceived Stability, and Measuring Decay Using a Microelectrode, dialkoxybenzenes have a redox potential at the upper limit of the solvent stability window, but the charged species is not stable for long periods of time in solution. A similar response was seen with phenothiazine derivatives in Multi-property Modifications of Phenothiazines. Here the low redox potential derivatives were stable, but once the potential started to reach the upper stability limit of the electrolyte, the species decayed. Although not discussed in this thesis, TEMPO derivatives suffer from the same challenges[146]. Therefore, research efforts exploring higher potential electrolytes could help stabilize these high potential materials through fewer solvent/active species interactions. It is worth also noting that as materials become more stable, stability testing becomes longer highlighting the need for efficient testing protocols introduced in Measuring Decay Using a Microelectrode.

A second major challenge for active materials in nonaqueous electrolytes is achieving high solubility in all relevant states-of-charge because higher concentrations will lead to more energy dense systems. Although electron concentrations could reach 1 M in Multi-property Modifications of Phenothiazines for one of the phenothiazine derivatives presented here, the highest electron concentration tested in this work was 0.6 M. In addition to the challenge of synthesizing highly soluble active species, high concentration electrochemistry is not well understood and becomes particularly challenging in nonaqueous electrolytes due to the low neat molarity of the solvents

used[168]. For these systems, the active species concentration and solvent concentration will be in the same order of magnitude. In order to optimize flow battery performance, understanding active material behavior at relevant concentrations is crucial, which can be achieved by using high concentration testing methods, modeling high concentration systems, and investigating electrolyte/active species systems together[137,170].

Recent research efforts on active materials have also begun to investigate the use of redox active macromolecules in order to reduce the challenge of using an expensive ion-exchange membrane. By using macromolecules like oligomers[153,227,228], polymers[121,229,230], and colloids[231], inexpensive size selective separators can be used with minimal performance losses due to species crossover. In particular, oligomer active species with polymers of intrinsic microporosity (PIM) membranes[153,227] have shown promise for reducing system costs because the oligomers have similar solution and electrochemical behaviors as the monomer, but is still larger than the PIM pore size.

In addition to active materials, reductions in battery costs may also be achieved through advances in cell design and engineering. High performance electrodes and electroreactors, often inspired by more mature electrochemical technologies (e.g., fuel cells[232]), can reduce reactor size requirements and associated costs. Further, new reactor designs are required to efficiently employ nonaqueous chemistries with low ionic conductivity and high viscosity and voltage. Together with an evolving regulatory environment, these R&D activities are expected to lead to the commercial success of RFB technologies in the near future and to the deployment of a range of new flowable storage concepts.

References

(1)   Su, L.; Kowalski, J. A.; Carroll, K. J.; Brushett, F. R. Recent Developments and Trends in Redox Flow Batteries. In *Rechargeable Batteries*; Zhang, Z., Zhang, S. S., Eds.; Green Energy and Technology; Springer International Publishing, 2015; pp 673–712. https://doi.org/10.1007/978-3-319-15458-9_24.

(2)   Darling, R. M.; Gallagher, K. G.; Kowalski, J. A.; Ha, S.; Brushett, F. R. Pathways to Low-Cost Electrochemical Energy Storage: A Comparison of Aqueous and Nonaqueous Flow Batteries. *Energy Env. Sci* **2014**, *7* (11), 3459–3477. https://doi.org/10.1039/C4EE02158D.

(3)   International Energy Agency. Key World Energy Statistics. 2014.

(4)   Hojjati, B.; Wade, S. H. U.S. Household Energy Consumption and Intensity Trends: A Decomposition Approach. *Energy Policy* **2012**, *48*, 304–314.

(5)   Department of Energy; International Energy Agency. Annual Energy Review 2011 http://www.eia.gov/totalenergy/data/annual/index.cfm/.

(6)   *Rising above the Gathering Storm : Energizing and Employing America for a Brighter Economic Future / Committee on Prospering in the Global Economy of the 21st Century : An Agenda for American Science and Technology ; Committee on Science, Engineering, and Public Policy.*; Washington, D.C. : National Academies Press, c2007., 2007.

(7)   Ehleringer, J. R.; Cerling, T. E.; Dearing, M. D. *A History of Atmospheric CO_2 and Its Effects on Plants, Animals, and Ecosystems / James R. Ehleringer, Thure E. Cerling, and M. Denise Dearing, Editors.*; Ecological studies; New York, NY, USA : Springer, c2005., 2005.

(8)   Stocker, T. F.; Qin, D.; Plattner, G.-K.; Tignor, M. M. B.; Allen, S. K.; Boschung, J.; Nauels, A.; Xia, Y.; Bex, V.; Midgley, P. M. Climate Change 2013: The Physical Science Basis. Climate Change 2013: The Physical Science Basis. 2013.

(9)   International Energy Agency. Energy Technology Perspectives 2012: Pathways to a Clean Energy System. *SourceOECD Energy* **2012**, *2012* (5), 1.

(10)   Chu, S.; Majumdar, A. Opportunities and Challenges for a Sustainable Energy Future. *Nature* **2012**, *488* (7411), 294–303. https://doi.org/10.1038/nature11475.

(11)   US-Department of Energy. Smart Grid System Report. 2010.

(12)   US-Department of Energy. Grid Energy Storage. 2013.

(13)   Akhil, A.; Boyes, J.; Butler, P. Chapter 30: Batteries for Electrical Energy Storage Applications. In *Linden's Handbook of Battery. Editor: T Reddy*; McGraw-Hill: New York, 2010.

(14)   U.S. Department of Energy. Basic Research Needs for Electrical Energy Storage. 2007.

(15)   International Energy Agency. Technology Roadmap: Energy Storage http://www.iea.org/publications/freepublications/publication/name,36573,en.html (accessed Apr 10, 2014).

(16) Electric Power Research Institute. DOE Handbook of Energy Storage for Transmission and Distribution Applications. 2003.

(17) Akhil, A. A.; Huff, G.; Currier, A. B.; Kaun, B. C.; Rastler, D. M.; Chen, S. B.; Cotter, A. L.; Bradshaw, D. T.; Gauntlett, W. D. DOE/EPRI 2013 Electricity Storage Handbook in Collaboration with NRECA. *Ed Albuq. NM Sandia Natl. Lab.* **2013**.

(18) Electric Power Research Institute. Electricity Energy Storage Technology Options.

(19) International Energy Agency. Pumped storage provides grid reliability even with net generation loss http://www.eia.gov/todayinenergy/detail.cfm?id=11991# (accessed Oct 10, 2014).

(20) ARPA-E; U.S. Department of Energy. Grid-Scale Rampable Intermittent Dispatchable Storage.

(21) U.S. Department of Energy,. Joint Center for Energy Storage. 2014.

(22) Shin, S.-H.; Yun, S.-H.; Moon, S.-H. A Review of Current Developments in Non-Aqueous Redox Flow Batteries: Characterization of Their Membranes for Design Perspective. *RSC Adv.* **2013**, *3* (24), 9095–9116. https://doi.org/10.1039/C3RA00115F.

(23) Schwenzer, B.; Zhang, J.; Kim, S.; Li, L.; Liu, J.; Yang, Z. Membrane Development for Vanadium Redox Flow Batteries. *ChemSusChem* **2011**, *4* (10), 1388–1406. https://doi.org/10.1002/cssc.201100068.

(24) Li, X.; Zhang, H.; Mai, Z.; Zhang, H.; Vankelecom, I. Ion Exchange Membranes for Vanadium Redox Flow Battery (VRB) Applications. *Energy Environ. Sci.* **2011**, *4* (4), 1147–1160. https://doi.org/10.1039/C0EE00770F.

(25) Chakrabarti, M. H.; Brandon, N. P.; Hajimolana, S. A.; Tariq, F.; Yufit, V.; Hashim, M. A.; Hussain, M. A.; Low, C. T. J.; Aravind, P. V. Application of Carbon Materials in Redox Flow Batteries. *J. Power Sources* **2014**, *253*, 150–166. https://doi.org/10.1016/j.jpowsour.2013.12.038.

(26) Parasuraman, A.; Lim, T. M.; Menictas, C.; Skyllas-Kazacos, M. Review of Material Research and Development for Vanadium Redox Flow Battery Applications. *Electrochimica Acta* **2013**, *101*, 27–40. https://doi.org/10.1016/j.electacta.2012.09.067.

(27) Li, X.; Sabir, I. Review of Bipolar Plates in PEM Fuel Cells: Flow-Field Designs. *Int. J. Hydrog. Energy* **2005**, *30* (4), 359–371. https://doi.org/10.1016/j.ijhydene.2004.09.019.

(28) Alotto, P.; Guarnieri, M.; Moro, F. Redox Flow Batteries for the Storage of Renewable Energy: A Review. *Renew. Sustain. Energy Rev.* **2014**, *29*, 325–335. https://doi.org/10.1016/j.rser.2013.08.001.

(29) Wang, W.; Luo, Q.; Li, B.; Wei, X.; Li, L.; Yang, Z. Recent Progress in Redox Flow Battery Research and Development. *Adv. Funct. Mater.* **2013**, *23* (8), 970–986. https://doi.org/10.1002/adfm.201200694.

(30) Leung, P.; Li, X.; León, C. P. de; Berlouis, L.; Low, C. T. J.; Walsh, F. C. Progress in Redox Flow Batteries, Remaining Challenges and Their Applications in Energy Storage. *RSC Adv.* **2012**, *2* (27), 10125–10156. https://doi.org/10.1039/C2RA21342G.

(31) Yang, Z.; Zhang, J.; Kintner-Meyer, M. C. W.; Lu, X.; Choi, D.; Lemmon, J. P.; Liu, J. Electrochemical Energy Storage for Green Grid. *Chem. Rev.* **2011**, *111* (5), 3577–3613. https://doi.org/10.1021/cr100290v.

(32) Weber, A. Z.; Mench, M. M.; Meyers, J. P.; Ross, P. N.; Gostick, J. T.; Liu, Q. Redox Flow Batteries: A Review. *J. Appl. Electrochem.* **2011**, *41* (10), 1137–1164. https://doi.org/10.1007/s10800-011-0348-2.

(33) Skyllas-Kazacos, M.; Chakrabarti, M. H.; Hajimolana, S. A.; Mjalli, F. S.; Saleem, M. Progress in Flow Battery Research and Development. *J. Electrochem. Soc.* **2011**, *158* (8), R55–R79. https://doi.org/10.1149/1.3599565.

(34) Viswanathan, V.; Crawford, A.; Stephenson, D.; Kim, S.; Wang, W.; Li, B.; Coffey, G.; Thomsen, E.; Graff, G.; Balducci, P.; et al. Cost and Performance Model for Redox Flow Batteries. *J Power Sources* **2014**, *247*, 1040–1051. https://doi.org/10.1016/j.jpowsour.2012.12.023.

(35) Michaels, K.; Hall, G. *Cost Projections for Redox Energy Storage Systems*; 1980.

(36) Mellentine, J. Performance Characterization and Cost Assessment of an Iron Hybrid Flow Battery. Thesis, 2011.

(37) Zhang, M.; Moore, M.; Watson, J. S.; Zawodzinski, T. A.; Counce, R. M. Capital Cost Sensitivity Analysis of an All-Vanadium Redox-Flow Battery. *J. Electrochem. Soc.* **2012**, *159* (8), A1183–A1188. https://doi.org/10.1149/2.041208jes.

(38) Joerissen, L.; Garche, J.; Fabjan, C.; Tomazic, G. Possible Use of Vanadium Redox-Flow Batteries for Energy Storage in Small Grids and Stand-Alone Photovoltaic Systems. *J. Power Sources* **2004**, *127* (1), 98–104. https://doi.org/10.1016/j.jpowsour.2003.09.066.

(39) Newman, J.; Hoertz, P. G.; Bonino, C. A.; Trainham, J. A. Review: An Economic Perspective on Liquid Solar Fuels. *J. Electrochem. Soc.* **2012**, *159* (10), A1722–A1729. https://doi.org/10.1149/2.046210jes.

(40) Max, S. P.; Klaus, D. T.; Ronald, E. W. Plant Design and Economics for Chemical Engineers. *Int. Ed.* **1991**.

(41) Poonpun, P.; Jewell, W. T. Analysis of the Cost per Kilowatt Hour to Store Electricity. *IEEE Trans. Energy Convers.* **2008**, *23* (2), 529–534. https://doi.org/10.1109/TEC.2007.914157.

(42) International Energy Agency. Key World Energy Statistics. 2012.

(43) http://www.eia.gov/todayinenergy/detail.cfm?id=14671 (accessed Jun 26, 2014).

(44) Eyer, J. M.; Corey, G. P. *Energy Storage for the Electricity Grid: Benefits and Market Potential Assessment Guide: A Study for the DOE Energy Storage Systems Program.*; SAND2010-0815, 1031895; 2010. https://doi.org/10.2172/1031895.

(45) Darling, R. M.; Perry, M. L. The Influence of Electrode and Channel Configurations on Flow Battery Performance. *J. Electrochem. Soc.* **2014**, *161* (9), A1381–A1387. https://doi.org/10.1149/2.0941409jes.

(46) James, B. D.; Moton, J. M.; Colella, W. G.; Inc, S. A. Mass Production Cost Estimation of Direct H2 PEM Fuel Cell Systems for Transportation Applications: 2012 Update.

263

(47) James, B. D.; Moton, J. M.; Colella, W. G.; Inc, S. A. Mass Production Cost Estimation of Direct H2 PEM Fuel Cell Systems for Transportation Applications: 2010 Update.

(48) Mathias, M. F.; Makharia, R.; Gasteiger, H. A.; Conley, J. J.; Fuller, T. J.; Gittleman, C. J.; Kocha, S. S.; Miller, D. P.; Mittelsteadt, C. K.; Xie, T. Two Fuel Cell Cars in Every Garage. *Electrochem Soc Interface* **2005**, *14* (3), 24–35.

(49) Eckroad, S. Vanadium Redox Flow Batteries: An in-Depth Analysis. *Electr. Power Res. Inst. Palo Alto CA* **2007**, *1014836*.

(50) IHS Chemical. Chemical Economics Hanbook. 2011.

(51) Anderson, J. Determining Manufacturing Costs. *Back Basics* 5.

(52) Business Analytic Center. *Propylene Carbonate (PC) (CAS 108-32-7): Market Research Report 2013*; 2013.

(53) Cho, K. T.; Albertus, P.; Battaglia, V.; Kojic, A.; Srinivasan, V.; Weber, A. Z. Optimization and Analysis of High-Power Hydrogen/Bromine-Flow Batteries for Grid-Scale Energy Storage. *Energy Technol.* **2013**, *1* (10), 596–608. https://doi.org/10.1002/ente.201300108.

(54) Carbajales-Dale, M.; J. Barnhart, C.; M. Benson, S. Can We Afford Storage? A Dynamic Net Energy Analysis of Renewable Electricity Generation Supported by Energy Storage. *Energy Environ. Sci.* **2014**, *7* (5), 1538–1544. https://doi.org/10.1039/C3EE42125B.

(55) Nelson, P. A.; Gallagher, K. G.; Bloom, I. D.; Dees, D. W. *Modeling the Performance and Cost of Lithium-Ion Batteries for Electric-Drive Vehicles*; Argonne National Lab.(ANL), Argonne, IL (United States), 2012.

(56) Nelson, P. A.; Gallagher, K. G.; Bloom, I. BatPaC (Battery Performance and Cost) Software. *Argonne Natl. Lab.* **2012**.

(57) Hossain, S.; Linden, D. Handbook of Batteries. *McGraw-Hill N. Y.* **1995**, *70*, 71.

(58) Xu, K. Nonaqueous Liquid Electrolytes for Lithium-Based Rechargeable Batteries. *Chem. Rev.* **2004**, *104* (10), 4303–4418. https://doi.org/10.1021/cr030203g.

(59) Aurbach, D. *Nonaqueous Electrochemistry*; CRC Press, 1999.

(60) Anderman, M.; Kalhammer, F. R.; MacArthur, D. Advanced Batteries for Electric Vehicles: An Assessment of Performance, Cost, and Availability. *Prep. State Calif. Air Resour. Board Sacram. Calif.* **2000**.

(61) Kowalski, J. A.; Su, L.; Milshtein, J. D.; Brushett, F. R. Recent Advances in Molecular Engineering of Redox Active Organic Molecules for Nonaqueous Flow Batteries. *Curr. Opin. Chem. Eng.* **2016**, *13*, 45–52. https://doi.org/10.1016/j.coche.2016.08.002.

(62) LaMonica, M. EnerVault novel battery technology http://www.technologyreview.com/view/512736/startup-enervault-rethinks-flow-battery-chemistry/ (accessed Sep 10, 2014).

(63) Vanysek, P. Electrochemical Series. In *CRC Handbook of Chemistry and Physics. Editor: WM Haynes*; Taylor & Francis Group: Boca Raton, 2014; pp 5–80 to 5–89.

(64) Reid, M. A.; Gahn, R. F. Factors Affecting the Open-Circuit Voltage and Electrode Kinetics of Some Iron/Titanium Redox Flow Cells. May 8, 1977.

(65) Wang, W.; Kim, S.; Chen, B.; Nie, Z.; Zhang, J.; Xia, G.-G.; Li, L.; Yang, Z. A New Redox Flow Battery Using Fe/V Redox Couples in Chloride Supporting Electrolyte. *Energy Environ. Sci.* **2011**, *4* (10), 4068–4073. https://doi.org/10.1039/C0EE00765J.

(66) Lopez-Atalaya, M.; Codina, G.; Perez, J. R.; Vazquez, J. L.; Aldaz, A. Optimization Studies on a Fe/Cr Redox Flow Battery. *J. Power Sources* **1992**, *39* (2), 147–154. https://doi.org/10.1016/0378-7753(92)80133-V.

(67) Skyllas-Kazacos, M.; Grossmith, F. Efficient Vanadium Redox Flow Cell. *J. Electrochem. Soc.* **1987**, *134* (12), 2950–2953. https://doi.org/10.1149/1.2100321.

(68) Zhou, H.; Zhang, H.; Zhao, P.; Yi, B. A Comparative Study of Carbon Felt and Activated Carbon Based Electrodes for Sodium Polysulfide/Bromine Redox Flow Battery. *Electrochimica Acta* **2006**, *51* (28), 6304–6312. https://doi.org/10.1016/j.electacta.2006.03.106.

(69) Skyllas-Kazacos, M. Novel Vanadium Chloride/Polyhalide Redox Flow Battery. *J. Power Sources* **2003**, *124* (1), 299–302. https://doi.org/10.1016/S0378-7753(03)00621-9.

(70) Xue, F.-Q.; Wang, Y.-L.; Wang, W.-H.; Wang, X.-D. Investigation on the Electrode Process of the Mn(II)/Mn(III) Couple in Redox Flow Battery. *Electrochimica Acta* **2008**, *53* (22), 6636–6642. https://doi.org/10.1016/j.electacta.2008.04.040.

(71) Fang, B.; Iwasa, S.; Wei, Y.; Arai, T.; Kumagai, M. A Study of the Ce(III)/Ce(IV) Redox Couple for Redox Flow Battery Application. *Electrochimica Acta* **2002**, *47* (24), 3971–3976. https://doi.org/10.1016/S0013-4686(02)00370-5.

(72) Bartolozzi, M. Development of Redox Flow Batteries. A Historical Bibliography. *J. Power Sources* **1989**, *27* (3), 219–234. https://doi.org/10.1016/0378-7753(89)80037-0.

(73) Hagedorn, N. NASA Redox Storage System Development Project. October 1984.

(74) Zhao, P.; Zhang, H.; Zhou, H.; Yi, B. Nickel Foam and Carbon Felt Applications for Sodium Polysulfide/Bromine Redox Flow Battery Electrodes. *Electrochimica Acta* **2005**, *51* (6), 1091–1098. https://doi.org/10.1016/j.electacta.2005.06.008.

(75) Scamman, D. P.; Reade, G. W.; Roberts, E. P. L. Numerical Modelling of a Bromide–Polysulphide Redox Flow Battery: Part 1: Modelling Approach and Validation for a Pilot-Scale System. *J. Power Sources* **2009**, *189* (2), 1220–1230. https://doi.org/10.1016/j.jpowsour.2009.01.071.

(76) Scamman, D. P.; Reade, G. W.; Roberts, E. P. L. Numerical Modelling of a Bromide-Polysulphide Redox Flow Battery. Part 2: Evaluation of a Utility-Scale System. *J. Power Sources* **2009**, *189* (2), 1231–1239. https://doi.org/10.1016/j.jpowsour.2009.01.076.

(77) Sum, E.; Rychcik, M.; Skyllas-kazacos, M. Investigation of the V(V)/V(IV) System for Use in the Positive Half-Cell of a Redox Battery. *J. Power Sources* **1985**, *16* (2), 85–95. https://doi.org/10.1016/0378-7753(85)80082-3.

(78) Sum, E.; Skyllas-Kazacos, M. A Study of the V(II)/V(III) Redox Couple for Redox Flow Cell Applications. *J. Power Sources* **1985**, *15* (2–3), 179–190. https://doi.org/10.1016/0378-7753(85)80071-9.

(79) Skyllas-Kazacos, M.; Rychcik, M.; Robins, R. G.; Fane, A. G.; Green, M. A. New All-Vanadium Redox Flow Cell. *J. Electrochem. Soc.* **1986**, *133* (5), 1057–1058. https://doi.org/10.1149/1.2108706.

(80) Li, B.; Gu, M.; Nie, Z.; Shao, Y.; Luo, Q.; Wei, X.; Li, X.; Xiao, J.; Wang, C.; Sprenkle, V.; et al. Bismuth Nanoparticle Decorating Graphite Felt as a High-Performance Electrode for an All-Vanadium Redox Flow Battery. *Nano Lett.* **2013**, *13* (3), 1330–1335. https://doi.org/10.1021/nl400223v.

(81) Li, B.; Gu, M.; Nie, Z.; Wei, X.; Wang, C.; Sprenkle, V.; Wang, W. Nanorod Niobium Oxide as Powerful Catalysts for an All Vanadium Redox Flow Battery. *Nano Lett.* **2014**, *14* (1), 158–165. https://doi.org/10.1021/nl403674a.

(82) Kazacos, M.; Cheng, M.; Skyllas-Kazacos, M. Vanadium Redox Cell Electrolyte Optimization Studies. *J. Appl. Electrochem.* **1990**, *20* (3), 463–467. https://doi.org/10.1007/BF01076057.

(83) Li, L.; Kim, S.; Wang, W.; Vijayakumar, M.; Nie, Z.; Chen, B.; Zhang, J.; Xia, G.; Hu, J.; Graff, G.; et al. A Stable Vanadium Redox-Flow Battery with High Energy Density for Large-Scale Energy Storage. *Adv. Energy Mater.* **2011**, *1* (3), 394–400. https://doi.org/10.1002/aenm.201100008.

(84) Kim, S.; Thomsen, E.; Xia, G.; Nie, Z.; Bao, J.; Recknagle, K.; Wang, W.; Viswanathan, V.; Luo, Q.; Wei, X.; et al. 1 KW/1 KWh Advanced Vanadium Redox Flow Battery Utilizing Mixed Acid Electrolytes. *J. Power Sources* **2013**, *237*, 300–309. https://doi.org/10.1016/j.jpowsour.2013.02.045.

(85) Poizot, P.; Dolhem, F. Clean Energy New Deal for a Sustainable World: From Non-CO2 Generating Energy Sources to Greener Electrochemical Storage Devices. *Energy Environ. Sci.* **2011**, *4* (6), 2003–2019. https://doi.org/10.1039/C0EE00731E.

(86) Huskinson, B.; Marshak, M. P.; Suh, C.; Er, S.; Gerhardt, M. R.; Galvin, C. J.; Chen, X.; Aspuru-Guzik, A.; Gordon, R. G.; Aziz, M. J. A Metal-Free Organic-Inorganic Aqueous Flow Battery. *Nature* **2014**, *505* (7482), 195–198. https://doi.org/10.1038/nature12909.

(87) Huskinson, B.; Marshak, M. P.; Gerhardt, M. R.; Aziz, M. J. Cycling of a Quinone-Bromide Flow Battery for Large-Scale Electrochemical Energy Storage. *ECS Trans.* **2014**, *61* (37), 27–30. https://doi.org/10.1149/06137.0027ecst.

(88) Chambers, J. Q. Electrochemistry of Quinones. In *Quinonoid Compounds (1974)*; Patai, S., Ed.; John Wiley & Sons, Ltd., 1974; pp 737–791.

(89) Bailey, S. I.; Ritchie, I. M. A Cyclic Voltammetric Study of the Aqueous Electrochemistry of Some Quinones. *Electrochimica Acta* **1985**, *30* (1), 3–12. https://doi.org/10.1016/0013-4686(85)80051-7.

(90) Huskinson, B.; Nawar, S.; Gerhardt, M. R.; Aziz, M. J. Novel Quinone-Based Couples for Flow Batteries. *ECS Trans.* **2013**, *53* (7), 101–105. https://doi.org/10.1149/05307.0101ecst.

(91) Xu, Y.; Wen, Y.-H.; Cheng, J.; Cao, G.-P.; Yang, Y.-S. A Study of Tiron in Aqueous Solutions for Redox Flow Battery Application. *Electrochimica Acta* **2010**, *55* (3), 715–720. https://doi.org/10.1016/j.electacta.2009.09.031.

(92) Yang, B.; Hoober-Burkhardt, L.; Wang, F.; Prakash, G. K. S.; Narayanan, S. R. An Inexpensive Aqueous Flow Battery for Large-Scale Electrical Energy Storage Based on Water-Soluble Organic Redox Couples. *J. Electrochem. Soc.* **2014**, *161* (9), A1371–A1380. https://doi.org/10.1149/2.1001409jes.

(93) Cappillino, P. J.; Pratt, H. D.; Hudak, N. S.; Tomson, N. C.; Anderson, T. M.; Anstey, M. R. Application of Redox Non-Innocent Ligands to Non-Aqueous Flow Battery Electrolytes. *Adv. Energy Mater.* **2014**, *4* (1), n/a-n/a. https://doi.org/10.1002/aenm.201300566.

(94) Sleightholme, A. E. S.; Shinkle, A. A.; Liu, Q.; Li, Y.; Monroe, C. W.; Thompson, L. T. Non-Aqueous Manganese Acetylacetonate Electrolyte for Redox Flow Batteries. *J. Power Sources* **2011**, *196* (13), 5742–5745. https://doi.org/10.1016/j.jpowsour.2011.02.020.

(95) Chakrabarti, M. H.; Dryfe, R. A. W.; Roberts, E. P. L. Evaluation of Electrolytes for Redox Flow Battery Applications. *Electrochimica Acta* **2007**, *52* (5), 2189–2195. https://doi.org/10.1016/j.electacta.2006.08.052.

(96) Zhang, D.; Lan, H.; Li, Y. The Application of a Non-Aqueous Bis(Acetylacetone)Ethylenediamine Cobalt Electrolyte in Redox Flow Battery. *J. Power Sources* **2012**, *217*, 199–203. https://doi.org/10.1016/j.jpowsour.2012.06.038.

(97) Shinkle, A. A.; Sleightholme, A. E. S.; Griffith, L. D.; Thompson, L. T.; Monroe, C. W. Degradation Mechanisms in the Non-Aqueous Vanadium Acetylacetonate Redox Flow Battery. *J. Power Sources* **2012**, *206*, 490–496. https://doi.org/10.1016/j.jpowsour.2010.12.096.

(98) Mun, J.; Lee, M.-J.; Park, J.-W.; Oh, D.-J.; Lee, D.-Y.; Doo, S.-G. Non-Aqueous Redox Flow Batteries with Nickel and Iron Tris(2,2′-Bipyridine) Complex Electrolyte. *Electrochem. Solid-State Lett.* **2012**, *15* (6), A80–A82. https://doi.org/10.1149/2.033206esl.

(99) Matsuda, Y.; Tanaka, K.; Okada, M.; Takasu, Y.; Morita, M.; Matsumura-Inoue, T. A Rechargeable Redox Battery Utilizing Ruthenium Complexes with Non-Aqueous Organic Electrolyte. *J. Appl. Electrochem.* **1988**, *18* (6), 909–914. https://doi.org/10.1007/BF01016050.

(100) Chakrabarti, M. H.; Roberts, E. P. L.; Bae, C.; Saleem, M. Ruthenium Based Redox Flow Battery for Solar Energy Storage. *Energy Convers. Manag.* **2011**, *52* (7), 2501–2508. https://doi.org/10.1016/j.enconman.2011.01.012.

(101) Liu, Q.; Sleightholme, A. E. S.; Shinkle, A. A.; Li, Y.; Thompson, L. T. Non-Aqueous Vanadium Acetylacetonate Electrolyte for Redox Flow Batteries. *Electrochem. Commun.* **2009**, *11* (12), 2312–2315. https://doi.org/10.1016/j.elecom.2009.10.006.

(102) Liu, Q.; Shinkle, A. A.; Li, Y.; Monroe, C. W.; Thompson, L. T.; Sleightholme, A. E. S. Non-Aqueous Chromium Acetylacetonate Electrolyte for Redox Flow Batteries. *Electrochem. Commun.* **2010**, *12* (11), 1634–1637. https://doi.org/10.1016/j.elecom.2010.09.013.

(103) Shinkle, A. A.; Sleightholme, A. E. S.; Thompson, L. T.; Monroe, C. W. Electrode Kinetics in Non-Aqueous Vanadium Acetylacetonate Redox Flow Batteries. *J. Appl. Electrochem.* **2011**, *41* (10), 1191–1199. https://doi.org/10.1007/s10800-011-0314-z.

(104) Shinkle, A. A.; Pomaville, T. J.; Sleightholme, A. E. S.; Thompson, L. T.; Monroe, C. W. Solvents and Supporting Electrolytes for Vanadium Acetylacetonate Flow Batteries. *J. Power Sources* **2014**, *248*, 1299–1305. https://doi.org/10.1016/j.jpowsour.2013.10.034.

(105) Lee, D.-Y.; Lee, M.-J.; Park, J.-W.; Oh, D.-J.; Mun, J.-Y.; Doo, S.-G. Aromatic Ligand Coordinated Redox Couples & Their Application into Redox Flow Batteries. The International Flow Battery Forum 2011 Edinburgh 2011.

(106) Gagne, R. R.; Koval, C. A.; Lisensky, G. C. Ferrocene as an Internal Standard for Electrochemical Measurements. *Inorg. Chem.* **1980**, *19* (9), 2854–2855. https://doi.org/10.1021/ic50211a080.

(107) Wei, X.; Cosimbescu, L.; Xu, W.; Hu, J. Z.; Vijayakumar, M.; Feng, J.; Hu, M. Y.; Deng, X.; Xiao, J.; Liu, J.; et al. Towards High-Performance Nonaqueous Redox Flow Electrolyte Via Ionic Modification of Active Species. *Adv. Energy Mater.* **2015**, *5* (1), n/a-n/a. https://doi.org/10.1002/aenm.201400678.

(108) Li, Z.; Li, S.; Liu, S.; Huang, K.; Fang, D.; Wang, F.; Peng, S. Electrochemical Properties of an All-Organic Redox Flow Battery Using 2,2,6,6-Tetramethyl-1-Piperidinyloxy and N-Methylphthalimide. *Electrochem. Solid-State Lett.* **2011**, *14* (12), A171–A173. https://doi.org/10.1149/2.012112esl.

(109) Brushett, F. R.; Vaughey, J. T.; Jansen, A. N. An All-Organic Non-Aqueous Lithium-Ion Redox Flow Battery. *Adv. Energy Mater.* **2012**, *2* (11), 1390–1396. https://doi.org/10.1002/aenm.201200322.

(110) Park, S.-K.; Shim, J.; Yang, J.; Shin, K.-H.; Jin, C.-S.; Lee, B. S.; Lee, Y.-S.; Jeon, J.-D. Electrochemical Properties of a Non-Aqueous Redox Battery with All-Organic Redox Couples. *Electrochem. Commun.* **2015**, *59*, 68–71. https://doi.org/10.1016/j.elecom.2015.07.013.

(111) Wei, X.; Xu, W.; Huang, J.; Zhang, L.; Walter, E.; Lawrence, C.; Vijayakumar, M.; Henderson, W. A.; Liu, T.; Cosimbescu, L.; et al. Radical Compatibility with Nonaqueous Electrolytes and Its Impact on an All-Organic Redox Flow Battery. *Angew. Chem. Int. Ed.* **2015**, *54* (30), 8684–8687. https://doi.org/10.1002/anie.201501443.

(112) Kaur, A. P.; Holubowitch, N. E.; Ergun, S.; Elliott, C. F.; Odom, S. A. A Highly Soluble Organic Catholyte for Non-Aqueous Redox Flow Batteries. *Energy Technol.* **2015**, *3* (5), 476–480. https://doi.org/10.1002/ente.201500020.

(113) Duan, W.; Vemuri, R. S.; Milshtein, J. D.; Laramie, S.; Dmello, R. D.; Huang, J.; Zhang, L.; Hu, D.; Vijayakumar, M.; Wang, W.; et al. A Symmetric Organic-Based Nonaqueous Redox Flow Battery and Its State of Charge Diagnostics by FTIR. *J. Mater. Chem. A* **2016**, *4* (15), 5448–5456. https://doi.org/10.1039/C6TA01177B.

(114) Potash, R. A.; McKone, J. R.; Conte, S.; Abruña, H. D. On the Benefits of a Symmetric Redox Flow Battery. *J. Electrochem. Soc.* **2016**, *163* (3), A338–A344. https://doi.org/10.1149/2.0971602jes.

(115) Oh, S. H.; Lee, C.-W.; Chun, D. H.; Jeon, J.-D.; Shim, J.; Shin, K. H.; Yang, J. H. A Metal-Free and All-Organic Redox Flow Battery with Polythiophene as the Electroactive Species. *J. Mater. Chem. A* **2014**, *2* (47), 19994–19998. https://doi.org/10.1039/C4TA04730C.

(116) Winsberg, J.; Hagemann, T.; Muench, S.; Friebe, C.; Häupler, B.; Janoschka, T.; Morgenstern, S.; Hager, M. D.; Schubert, U. S. Poly(Boron-Dipyrromethene)—A Redox-Active Polymer Class for Polymer Redox-Flow Batteries. *Chem. Mater.* **2016**. https://doi.org/10.1021/acs.chemmater.6b00640.

(117) Chen, Z.; Qin, Y.; Amine, K. Redox Shuttles for Safer Lithium-Ion Batteries. *Electrochimica Acta* **2009**, *54* (24), 5605–5613. https://doi.org/10.1016/j.electacta.2009.05.017.

(118) Darling, R.; Gallagher, K.; Xie, W.; Su, L.; Brushett, F. Transport Property Requirements for Flow Battery Separators. *J. Electrochem. Soc.* **2016**, *163* (1), A5029–A5040. https://doi.org/10.1149/2.0051601jes.

(119) Rasmussen, P. G. Electrical Storage Device Utilizing Pyrazine-Based Cyanoazacarbons and Polymers Derived Therefrom. US8080327 B1, December 20, 2011.

(120) Gong, K.; Fang, Q.; Gu, S.; Li, S. F. Y.; Yan, Y. Nonaqueous Redox-Flow Batteries: Organic Solvents, Supporting Electrolytes, and Redox Pairs. *Energy Environ. Sci.* **2015**, *8* (12), 3515–3530. https://doi.org/10.1039/C5EE02341F.

(121) Nagarjuna, G.; Hui, J.; Cheng, K. J.; Lichtenstein, T.; Shen, M.; Moore, J. S.; Rodríguez-López, J. Impact of Redox-Active Polymer Molecular Weight on the Electrochemical Properties and Transport across Porous Separators in Nonaqueous Solvents. *J. Am. Chem. Soc.* **2014**, *136* (46), 16309–16316. https://doi.org/10.1021/ja508482e.

(122) Wei, X.; Xu, W.; Vijayakumar, M.; Cosimbescu, L.; Liu, T.; Sprenkle, V.; Wang, W. TEMPO-Based Catholyte for High-Energy Density Nonaqueous Redox Flow Batteries. *Adv. Mater.* **2014**, *26* (45), 7649–7653. https://doi.org/10.1002/adma.201403746.

(123) Milshtein, J. D.; Barton, J. L.; Darling, R. M.; Brushett, F. R. 4-Acetamido-2,2,6,6-Tetramethylpiperidine-1-Oxyl as a Model Organic Redox Active Compound for Nonaqueous Flow Batteries. *J. Power Sources* **2016**, *327*, 151–159. https://doi.org/10.1016/j.jpowsour.2016.06.125.

(124) Huang, J.; Cheng, L.; Assary, R. S.; Wang, P.; Xue, Z.; Burrell, A. K.; Curtiss, L. A.; Zhang, L. Liquid Catholyte Molecules for Nonaqueous Redox Flow Batteries. *Adv. Energy Mater.* **2014**, n/a-n/a. https://doi.org/10.1002/aenm.201401782.

(125) Huang, J.; Su, L.; Kowalski, J. A.; Barton, J. L.; Ferrandon, M.; Burrell, A. K.; Brushett, F. R.; Zhang, L. A Subtractive Approach to Molecular Engineering of Dimethoxybenzene-Based Redox Materials for Non-Aqueous Flow Batteries. *J. Mater. Chem. A* **2015**, *3* (29), 14971–14976. https://doi.org/10.1039/C5TA02380G.

(126) Narayana, K. A.; Casselman, M. D.; Elliott, C. F.; Ergun, S.; Parkin, S. R.; Risko, C.; Odom, S. A. N-Substituted Phenothiazine Derivatives: How the Stability of the Neutral and Radical Cation Forms Affects Overcharge Performance in Lithium-Ion Batteries. *Chemphyschem Eur. J. Chem. Phys. Phys. Chem.* **2015**, *16* (6), 1179–1189. https://doi.org/10.1002/cphc.201402674.

(127) Kaur, A. P.; Ergun, S.; Elliott, C. F.; Odom, S. A. 3,7-Bis(Trifluoromethyl)-N-Ethylphenothiazine: A Redox Shuttle with Extensive Overcharge Protection in Lithium-Ion

Batteries. *J. Mater. Chem. A* **2014**, *2* (43), 18190–18193. https://doi.org/10.1039/C4TA04463K.

(128) Assary, R. S.; Brushett, F. R.; Curtiss, L. A. Reduction Potential Predictions of Some Aromatic Nitrogen-Containing Molecules. *RSC Adv.* **2014**, *4* (101), 57442–57451. https://doi.org/10.1039/C4RA08563A.

(129) Sevov, C. S.; Brooner, R. E. M.; Chénard, E.; Assary, R. S.; Moore, J. S.; Rodríguez-López, J.; Sanford, M. S. Evolutionary Design of Low Molecular Weight Organic Anolyte Materials for Applications in Nonaqueous Redox Flow Batteries. *J. Am. Chem. Soc.* **2015**, *137* (45), 14465–14472. https://doi.org/10.1021/jacs.5b09572.

(130) Wang, W.; Xu, W.; Cosimbescu, L.; Choi, D.; Li, L.; Yang, Z. Anthraquinone with Tailored Structure for a Nonaqueous Metal–Organic Redox Flow Battery. *Chem. Commun.* **2012**, *48* (53), 6669–6671. https://doi.org/10.1039/C2CC32466K.

(131) Chénard, E.; Sutrisno, A.; Zhu, L.; Assary, R. S.; Kowalski, J. A.; Barton, J. L.; Bertke, J. A.; Gray, D. L.; Brushett, F. R.; Curtiss, L. A.; et al. Synthesis of Pyridine– and Pyrazine–BF$_3$ Complexes and Their Characterization in Solution and Solid State. *J. Phys. Chem. C* **2016**, *120* (16), 8461–8471. https://doi.org/10.1021/acs.jpcc.6b00858.

(132) Carino, E. V.; Diesendruck, C. E.; Moore, J. S.; Curtiss, L. A.; Assary, R. S.; Brushett, F. R. BF3-Promoted Electrochemical Properties of Quinoxaline in Propylene Carbonate. *RSC Adv.* **2015**, *5* (24), 18822–18831. https://doi.org/10.1039/C5RA00137D.

(133) Liang, Y.; Tao, Z.; Chen, J. Organic Electrode Materials for Rechargeable Lithium Batteries. *Adv. Energy Mater.* **2012**, *2* (7), 742–769. https://doi.org/10.1002/aenm.201100795.

(134) Song, Z.; Zhou, H. Towards Sustainable and Versatile Energy Storage Devices: An Overview of Organic Electrode Materials. *Energy Environ. Sci.* **2013**, *6* (8), 2280. https://doi.org/10.1039/c3ee40709h.

(135) Connelly, N. G.; Geiger, W. E. Chemical Redox Agents for Organometallic Chemistry. *Chem. Rev.* **1996**, *96* (2), 877–910. https://doi.org/10.1021/cr940053x.

(136) Boeré, R. T.; Roemmele, T. L. Electrochemistry of Redox-Active Group 15/16 Heterocyles. *Coord. Chem. Rev.* **2000**, *210* (1), 369–445. https://doi.org/10.1016/S0010-8545(00)00349-0.

(137) Su, L.; Ferrandon, M.; Kowalski, J. A.; Vaughey, J. T.; Brushett, F. R. Electrolyte Development for Non-Aqueous Redox Flow Batteries Using a High-Throughput Screening Platform. *J. Electrochem. Soc.* **2014**, *161* (12), A1905–A1914. https://doi.org/10.1149/2.0811412jes.

(138) Cheng, L.; Assary, R. S.; Qu, X.; Jain, A.; Ong, S. P.; Rajput, N. N.; Persson, K.; Curtiss, L. A. Accelerating Electrolyte Discovery for Energy Storage with High-Throughput Screening. *J. Phys. Chem. Lett.* **2015**, *6* (2), 283–291. https://doi.org/10.1021/jz502319n.

(139) Zhang, L.; Zhang, Z.; Redfern, P. C.; Curtiss, L. A.; Amine, K. Molecular Engineering towards Safer Lithium-Ion Batteries: A Highly Stable and Compatible Redox Shuttle for Overcharge Protection. *Energy Environ. Sci.* **2012**, *5* (8), 8204–8207. https://doi.org/10.1039/C2EE21977H.

(140) Huang, J.; A. Shkrob, I.; Wang, P.; Cheng, L.; Pan, B.; He, M.; Liao, C.; Zhang, Z.; A. Curtiss, L.; Zhang, L. 1,4-Bis(Trimethylsilyl)-2,5-Dimethoxybenzene: A Novel Redox Shuttle Additive for Overcharge Protection in Lithium-Ion Batteries That Doubles as a Mechanistic Chemical Probe. *J. Mater. Chem. A* **2015**, *3* (14), 7332–7337. https://doi.org/10.1039/C5TA00899A.

(141) Huang, J.; Azimi, N.; Cheng, L.; Shkrob, I. A.; Xue, Z.; Zhang, J.; Rago, N. L. D.; Curtiss, L. A.; Amine, K.; Zhang, Z.; et al. An Organophosphine Oxide Redox Shuttle Additive That Delivers Long-Term Overcharge Protection for 4 V Lithium-Ion Batteries. *J. Mater. Chem. A* **2015**, *3* (20), 10710–10714. https://doi.org/10.1039/C5TA01326G.

(142) Chen, J.; Buhrmester, C.; Dahn, J. R. Chemical Overcharge and Overdischarge Protection for Lithium-Ion Batteries. *Electrochem. Solid-State Lett.* **2005**, *8* (1), A59–A62. https://doi.org/10.1149/1.1836119.

(143) Zhang, Z.; Zhang, L.; Schlueter, J. A.; Redfern, P. C.; Curtiss, L.; Amine, K. Understanding the Redox Shuttle Stability of 3,5-Di-Tert-Butyl-1,2-Dimethoxybenzene for Overcharge Protection of Lithium-Ion Batteries. *J. Power Sources* **2010**, *195* (15), 4957–4962. https://doi.org/10.1016/j.jpowsour.2010.02.075.

(144) Chen, Z.; Wang, Q.; Amine, K. Understanding the Stability of Aromatic Redox Shuttles for Overcharge Protection of Lithium-Ion Cells. *J. Electrochem. Soc.* **2006**, *153* (12), A2215–A2219. https://doi.org/10.1149/1.2352048.

(145) Deen, W. M. *Analysis of Transport Phenomena, Topics in Chemical Engineering*; Oxford University Press, New York, 1998; Vol. 3.

(146) Buhrmester, C.; Moshurchak, L. M.; Wang, R. L.; Dahn, J. R. The Use of 2,2,6,6-Tetramethylpiperinyl-Oxides and Derivatives for Redox Shuttle Additives in Li-Ion Cells. *J. Electrochem. Soc.* **2006**, *153* (10), A1800–A1804. https://doi.org/10.1149/1.2221860.

(147) Milshtein, J. D.; Kaur, A. P.; Casselman, M. D.; Kowalski, J. A.; Modekrutti, S.; Zhang, P. L.; Attanayake, N. H.; Elliott, C. F.; Parkin, S. R.; Risko, C.; et al. High Current Density, Long Duration Cycling of Soluble Organic Active Species for Non-Aqueous Redox Flow Batteries. *Energy Environ. Sci.* **2016**, *9* (11), 3531–3543. https://doi.org/10.1039/C6EE02027E.

(148) Kowalski, J. A.; Casselman, M. D.; Kaur, A. P.; Milshtein, J. D.; Elliott, C. F.; Modekrutti, S.; Attanayake, N. H.; Zhang, N.; Parkin, S. R.; Risko, C.; et al. A Stable Two-Electron-Donating Phenothiazine for Application in Nonaqueous Redox Flow Batteries. *J. Mater. Chem. A* **2017**, *5* (46), 24371–24379. https://doi.org/10.1039/C7TA05883G.

(149) Hwang, D.-H.; Kim, S.-K.; Park, M.-J.; Lee, J.-H.; Koo, B.-W.; Kang, I.-N.; Kim, S.-H.; Zyung, T. Conjugated Polymers Based on Phenothiazine and Fluorene in Light-Emitting Diodes and Field Effect Transistors. *Chem. Mater.* **2004**, *16* (7), 1298–1303. https://doi.org/10.1021/cm035264+.

(150) Buhrmester, C.; Moshurchak, L.; Wang, R. L.; Dahn, J. R. Phenothiazine Molecules Possible Redox Shuttle Additives for Chemical Overcharge and Overdischarge Protection for Lithium-Ion Batteries. *J. Electrochem. Soc.* **2006**, *153* (2), A288–A294. https://doi.org/10.1149/1.2140615.

271

(151) Moshurchak, L. M.; Buhrmester, C.; Wang, R. L.; Dahn, J. R. Comparative Studies of Three Redox Shuttle Molecule Classes for Overcharge Protection of LiFePO4-Based Li-Ion Cells. *Electrochimica Acta* **2007**, *52* (11), 3779–3784. https://doi.org/10.1016/j.electacta.2006.10.068.

(152) Casselman, M. D.; Kaur, A. P.; Narayana, K. A.; Elliott, C. F.; Risko, C.; Odom, S. A. The Fate of Phenothiazine-Based Redox Shuttles in Lithium-Ion Batteries. *Phys Chem Chem Phys* **2015**, *17* (10), 6905–6912. https://doi.org/10.1039/C5CP00199D.

(153) Hendriks, K. H.; Robinson, S. G.; Braten, M. N.; Sevov, C. S.; Helms, B. A.; Sigman, M. S.; Minteer, S. D.; Sanford, M. S. High-Performance Oligomeric Catholytes for Effective Macromolecular Separation in Nonaqueous Redox Flow Batteries. *ACS Cent. Sci.* **2018**, *4* (2), 189–196. https://doi.org/10.1021/acscentsci.7b00544.

(154) Sevov, C. S.; Samaroo, S. K.; Sanford, M. S. Cyclopropenium Salts as Cyclable, High-Potential Catholytes in Nonaqueous Media. *Adv. Energy Mater.* **2017**, *7* (5), 1602027. https://doi.org/10.1002/aenm.201602027.

(155) Montoto, E. C.; Cao, Y.; Hernández-Burgos, K.; Sevov, C. S.; Braten, M. N.; Helms, B. A.; Moore, J. S.; Rodríguez-López, J. Effect of the Backbone Tether on the Electrochemical Properties of Soluble Cyclopropenium Redox-Active Polymers. *Macromolecules* **2018**, *51* (10), 3539–3546. https://doi.org/10.1021/acs.macromol.8b00574.

(156) Sevov, C. S.; Hickey, D. P.; Cook, M. E.; Robinson, S. G.; Barnett, S.; Minteer, S. D.; Sigman, M. S.; Sanford, M. S. Physical Organic Approach to Persistent, Cyclable, Low-Potential Electrolytes for Flow Battery Applications. *J. Am. Chem. Soc.* **2017**, *139* (8), 2924–2927. https://doi.org/10.1021/jacs.7b00147.

(157) Zhang, J.; Huang, J.; Robertson, L. A.; Shkrob, I. A.; Zhang, L. Comparing Calendar and Cycle Life Stability of Redox Active Organic Molecules for Nonaqueous Redox Flow Batteries. *J. Power Sources* **2018**, *397*, 214–222. https://doi.org/10.1016/j.jpowsour.2018.07.001.

(158) Zhang, J.; Shkrob, I. A.; Assary, R. S.; Tung, S. on; Silcox, B.; Curtiss, L. A.; Thompson, L.; Zhang, L. Toward Improved Catholyte Materials for Redox Flow Batteries: What Controls Chemical Stability of Persistent Radical Cations? *J. Phys. Chem. C* **2017**, *121* (42), 23347–23358. https://doi.org/10.1021/acs.jpcc.7b08281.

(159) Huang, J.; Pan, B.; Duan, W.; Wei, X.; Assary, R. S.; Su, L.; Brushett, F. R.; Cheng, L.; Liao, C.; Ferrandon, M. S.; et al. The Lightest Organic Radical Cation for Charge Storage in Redox Flow Batteries. *Sci. Rep.* **2016**, *6*, 32102. https://doi.org/10.1038/srep32102.

(160) Duan, W.; Huang, J.; Kowalski, J. A.; Shkrob, I. A.; Vijayakumar, M.; Walter, E.; Pan, B.; Yang, Z.; Milshtein, J. D.; Li, B.; et al. "Wine-Dark Sea" in an Organic Flow Battery: Storing Negative Charge in 2,1,3-Benzothiadiazole Radicals Leads to Improved Cyclability. *ACS Energy Lett.* **2017**, *2* (5), 1156–1161. https://doi.org/10.1021/acsenergylett.7b00261.

(161) Zhang, J.; Yang, Z.; Shkrob, I. A.; Assary, R. S.; Tung, S. on; Silcox, B.; Duan, W.; Zhang, J.; Su, C. C.; Hu, B.; et al. Annulated Dialkoxybenzenes as Catholyte Materials for Non-Aqueous Redox Flow Batteries: Achieving High Chemical Stability through Bicyclic Substitution. *Adv. Energy Mater.* **2017**, *7* (21), 1701272. https://doi.org/10.1002/aenm.201701272.

(162) Laramie, S. M.; Milshtein, J. D.; Breault, T. M.; Brushett, F. R.; Thompson, L. T. Performance and Cost Characteristics of Multi-Electron Transfer, Common Ion Exchange Non-Aqueous Redox Flow Batteries. *J. Power Sources* **2016**, *327*, 681–692. https://doi.org/10.1016/j.jpowsour.2016.07.015.

(163) Haynes, W. M. *CRC Handbook of Chemistry and Physics, 92nd Edition.*; CRC Press: Hoboken, 2011.

(164) Pilar, F. L. Rates and Equilibria of Organic Reactions (Leffler, John E.; Grunwald, Ernest). *J. Chem. Educ.* **1964**, *41* (7), 407. https://doi.org/10.1021/ed041p407.1.

(165) Hansch, C.; Leo, A.; Taft, R. W. A Survey of Hammett Substituent Constants and Resonance and Field Parameters. *Chem. Rev.* **1991**, *91* (2), 165–195. https://doi.org/10.1021/cr00002a004.

(166) Carino, E. V.; Staszak-Jirkovsky, J.; Assary, R. S.; Curtiss, L. A.; Markovic, N. M.; Brushett, F. R. Tuning the Stability of Organic Active Materials for Nonaqueous Redox Flow Batteries via Reversible, Electrochemically Mediated Li^+ Coordination. *Chem. Mater.* **2016**, *28* (8), 2529–2539. https://doi.org/10.1021/acs.chemmater.5b04053.

(167) Bachman, J. E.; Curtiss, L. A.; Assary, R. S. Investigation of the Redox Chemistry of Anthraquinone Derivatives Using Density Functional Theory. *J. Phys. Chem. A* **2014**. https://doi.org/10.1021/jp5060777.

(168) Zhang, J.; Corman, R. E.; Schuh, J. K.; Ewoldt, R. H.; Shkrob, I. A.; Zhang, L. Solution Properties and Practical Limits of Concentrated Electrolytes for Nonaqueous Redox Flow Batteries. *J. Phys. Chem. C* **2018**, *122* (15), 8159–8172. https://doi.org/10.1021/acs.jpcc.8b02009.

(169) Fujita, H.; Kishimoto, A.; Matsumoto, K. Concentration and Temperature Dependence of Diffusion Coefficients for Systems Polymethyl Acrylate and N-Alkyl Acetates. *Trans. Faraday Soc.* **1960**, *56*, 424. https://doi.org/10.1039/tf9605600424.

(170) Su, L.; Ferrandon, M.; Barton, J. L.; de la Rosa, N. U.; Vaughey, J. T.; Brushett, F. R. An Investigation of 2,5-Di-Tertbutyl-1,4-Bis(Methoxyethoxy)Benzene in Ether-Based Electrolytes. *Electrochimica Acta* **2017**, *246*, 251–258. https://doi.org/10.1016/j.electacta.2017.05.167.

(171) Kissa, E. *Fluorinated Surfactants and Repellents*; CRC Press, 2001; Vol. 97.

(172) Chen, Z.; Amine, K. Degradation Pathway of 2,5-Di-Tert-Butyl-1,4-Dimethoxybenzene at High Potential. *Electrochimica Acta* **2007**, *53* (2), 453–458. https://doi.org/10.1016/j.electacta.2007.06.073.

(173) Li, T.; Xing, L.; Li, W.; Peng, B.; Xu, M.; Gu, F.; Hu, S. Theoretic Calculation for Understanding the Oxidation Process of 1,4-Dimethoxybenzene-Based Compounds as Redox Shuttles for Overcharge Protection of Lithium Ion Batteries. *J. Phys. Chem. A* **2011**, *115* (19), 4988–4994. https://doi.org/10.1021/jp2004584.

(174) Jones, J.; Anouti, M.; Caillon-Caravanier, M.; Willmann, P.; Sizaret, P.-Y.; Lemordant, D. Solubilization of SEI Lithium Salts in Alkylcarbonate Solvents. *Fluid Phase Equilibria* **2011**, *305* (2), 121–126. https://doi.org/10.1016/j.fluid.2011.03.007.

(175) W. Hamann, T.; A. Jensen, R.; F. Martinson, A. B.; Ryswyk, H. V.; T. Hupp, J. Advancing beyond Current Generation Dye -Sensitized Solar Cells. *Energy Environ. Sci.* **2008**, *1* (1), 66–78. https://doi.org/10.1039/B809672D.

(176) Wang, Q.; Zakeeruddin, S. M.; Wang, D.; Exnar, I.; Grätzel, M. Redox Targeting of Insulating Electrode Materials: A New Approach to High-Energy-Density Batteries. *Angew. Chem. Int. Ed.* **2006**, *45* (48), 8197–8200. https://doi.org/10.1002/anie.200602891.

(177) Huang, Q.; Li, H.; Grätzel, M.; Wang, Q. Reversible Chemical Delithiation/Lithiation of LiFePO 4 : Towards a Redox Flow Lithium-Ion Battery. *Phys. Chem. Chem. Phys.* **2013**, *15* (6), 1793–1797. https://doi.org/10.1039/C2CP44466F.

(178) Escalante-García, I. L.; Wainright, J. S.; Thompson, L. T.; Savinell, R. F. Performance of a Non-Aqueous Vanadium Acetylacetonate Prototype Redox Flow Battery: Examination of Separators and Capacity Decay. *J. Electrochem. Soc.* **2015**, *162* (3), A363–A372.

(179) Takechi, K.; Kato, Y.; Hase, Y. A Highly Concentrated Catholyte Based on a Solvate Ionic Liquid for Rechargeable Flow Batteries. *Adv. Mater.* **2015**, *27* (15), 2501–2506. https://doi.org/10.1002/adma.201405840.

(180) Ergun, S.; Elliott, C. F.; Kaur, A. P.; Parkin, S. R.; Odom, S. A. Overcharge Performance of 3,7-Disubstituted N-Ethylphenothiazine Derivatives in Lithium-Ion Batteries. *Chem Commun* **2014**, *50* (40), 5339–5341. https://doi.org/10.1039/C3CC47503D.

(181) Ergun, S.; Elliott, C. F.; Kaur, A. P.; Parkin, S. R.; Odom, S. A. Controlling Oxidation Potentials in Redox Shuttle Candidates for Lithium-Ion Batteries. *J. Phys. Chem. C* **2014**, *118* (27), 14824–14832. https://doi.org/10.1021/jp503767h.

(182) Odom, S. A.; Ergun, S.; Poudel, P. P.; Parkin, S. R. A Fast, Inexpensive Method for Predicting Overcharge Performance in Lithium-Ion Batteries. *Energy Environ. Sci.* **2014**, *7* (2), 760–767. https://doi.org/10.1039/C3EE42305K.

(183) Aaron, D. S.; Liu, Q.; Tang, Z.; Grim, G. M.; Papandrew, A. B.; Turhan, A.; Zawodzinski, T. A.; Mench, M. M. Dramatic Performance Gains in Vanadium Redox Flow Batteries through Modified Cell Architecture. *J. Power Sources* **2012**, *206*, 450–453. https://doi.org/10.1016/j.jpowsour.2011.12.026.

(184) Liu, Q. H.; Grim, G. M.; Papandrew, A. B.; Turhan, A.; Zawodzinski, T. A.; Mench, M. M. High Performance Vanadium Redox Flow Batteries with Optimized Electrode Configuration and Membrane Selection. *J. Electrochem. Soc.* **2012**, *159* (8), A1246–A1252. https://doi.org/10.1149/2.051208jes.

(185) Chen, Q.; Gerhardt, M. R.; Hartle, L.; Aziz, M. J. A Quinone-Bromide Flow Battery with 1 W/Cm2 Power Density. *J. Electrochem. Soc.* **2016**, *163* (1), A5010–A5013. https://doi.org/10.1149/2.0021601jes.

(186) Chen, Q.; Eisenach, L.; Aziz, M. J. Cycling Analysis of a Quinone-Bromide Redox Flow Battery. *J. Electrochem. Soc.* **2016**, *163* (1), A5057–A5063. https://doi.org/10.1149/2.0081601jes.

(187) Park, M.-S.; Lee, N.-J.; Lee, S.-W.; Kim, K. J.; Oh, D.-J.; Kim, Y.-J. High-Energy Redox-Flow Batteries with Hybrid Metal Foam Electrodes. *ACS Appl. Mater. Interfaces* **2014**, *6* (13), 10729–10735. https://doi.org/10.1021/am5025935.

(188) Dennison, C. R.; Agar, E.; Akuzum, B.; Kumbur, E. C. Enhancing Mass Transport in Redox Flow Batteries by Tailoring Flow Field and Electrode Design. *J. Electrochem. Soc.* **2016**, *163* (1), A5163–A5169. https://doi.org/10.1149/2.0231601jes.

(189) Lewandowski, A.; Osińska, M.; Swiderska-Mocek, A.; Galinski, M. A Cryptate Reference Electrode for Ionic Liquids. *Electroanalysis* **2008**, *20* (17), 1903–1908. https://doi.org/10.1002/elan.200804267.

(190) Dahn, J. R.; Jiang, J.; Moshurchak, L. M.; Fleischauer, M. D.; Buhrmester, C.; Krause, L. J. High-Rate Overcharge Protection of LiFePO4-Based Li-Ion Cells Using the Redox Shuttle Additive 2,5-Ditertbutyl-1,4-Dimethoxybenzene. *J. Electrochem. Soc.* **2005**, *152* (6), A1283–A1289. https://doi.org/10.1149/1.1906025.

(191) Lee, C.; Yang, W.; Parr, R. G. Development of the Colle-Salvetti Correlation-Energy Formula into a Functional of the Electron Density. *Phys. Rev. B* **1988**, *37* (2), 785–789. https://doi.org/10.1103/PhysRevB.37.785.

(192) Becke, A. D. Density-Functional Exchange-Energy Approximation with Correct Asymptotic Behavior. *Phys. Rev. A* **1988**, *38* (6), 3098–3100. https://doi.org/10.1103/PhysRevA.38.3098.

(193) Becke, A. D. Density-functional Thermochemistry. III. The Role of Exact Exchange. *J. Chem. Phys.* **1993**, *98* (7), 5648–5652. https://doi.org/10.1063/1.464913.

(194) Tomasi, J.; Mennucci, B.; Cammi, R. Quantum Mechanical Continuum Solvation Models. *Chem. Rev.* **2005**, *105* (8), 2999–3094. https://doi.org/10.1021/cr9904009.

(195) Kim, J.-H.; Kim, K. J.; Park, M.-S.; Lee, N. J.; Hwang, U.; Kim, H.; Kim, Y.-J. Development of Metal-Based Electrodes for Non-Aqueous Redox Flow Batteries. *Electrochem. Commun.* **2011**, *13* (9), 997–1000. https://doi.org/10.1016/j.elecom.2011.06.022.

(196) Cosimbescu, L.; Wei, X.; Vijayakumar, M.; Xu, W.; Helm, M. L.; Burton, S. D.; Sorensen, C. M.; Liu, J.; Sprenkle, V.; Wang, W. Anion-Tunable Properties and Electrochemical Performance of Functionalized Ferrocene Compounds. *Sci. Rep.* **2015**, *5*, 14117.

(197) Kopera, J.; Armitage, A. K. Comparison of Some Pharmacological Properties of Chlorpromazine, Promethazine and Pethidine. *Br. J. Pharmacol. Chemother.* **1954**, *9* (4), 392–401.

(198) Casey, J. F.; Lasky, J. J.; Klett, C. J.; Hollister, L. E. Treatment of Schizophrenic Reactions with Phenothiazine Derivatives: A Comparative Study of Chlorpromazine, Triflupromazine, Mepazine, Prochlorperazine, Perphenazine, and Phenobarbital. *Am. J. Psychiatry* **1960**, *117*, 97–105. https://doi.org/10.1176/ajp.117.2.97.

(199) Taylor, K.; Holtby, H. Methylene Blue Revisited: Management of Hypotension in a Pediatric Patient with Bacterial Endocarditis. *J. Thorac. Cardiovasc. Surg.* **2005**, *130* (2), 566. https://doi.org/10.1016/j.jtcvs.2005.01.001.

(200) Treat, N. J.; Sprafke, H.; Kramer, J. W.; Clark, P. G.; Barton, B. E.; Read de Alaniz, J.; Fors, B. P.; Hawker, C. J. Metal-Free Atom Transfer Radical Polymerization. *J. Am. Chem. Soc.* **2014**, *136* (45), 16096–16101. https://doi.org/10.1021/ja510389m.

(201) Discekici, E. H.; Treat, N. J.; Poelma, S. O.; Mattson, K. M.; Hudson, Z. M.; Luo, Y.; Hawker, C. J.; Alaniz, J. R. de. A Highly Reducing Metal-Free Photoredox Catalyst: Design and Application in Radical Dehalogenations. *Chem. Commun.* **2015**, *51* (58), 11705–11708. https://doi.org/10.1039/C5CC04677G.

(202) Grätzel, M. Materials Science: Ultrafast Colour Displays. *Nature* **2001**, *409* (6820), 575–576. https://doi.org/10.1038/35054655.

(203) Yen, H.-J.; Liou, G.-S. Enhanced Near-Infrared Electrochromism in Triphenylamine-Based Aramids Bearing Phenothiazine Redox Centers. *J. Mater. Chem.* **2010**, *20* (44), 9886–9894. https://doi.org/10.1039/C0JM01889A.

(204) Wu, W.; Yang, J.; Hua, J.; Tang, J.; Zhang, L.; Long, Y.; Tian, H. Efficient and Stable Dye-Sensitized Solar Cells Based on Phenothiazine Sensitizers with Thiophene Units. *J. Mater. Chem.* **2010**, *20* (9), 1772–1779. https://doi.org/10.1039/B918282A.

(205) Otwinowski, Z.; Minor, W. Processing of X-Ray Diffraction Data Collected in Oscillation Mode; Enzymology, B.-M. in, Ed.; Macromolecular Crystallography Part A; Academic Press, 1997; Vol. 276, pp 307–326.

(206) Krause, L.; Herbst-Irmer, R.; Sheldrick, G. M.; Stalke, D. Comparison of Silver and Molybdenum Microfocus X-Ray Sources for Single-Crystal Structure Determination. *J. Appl. Crystallogr.* **2015**, *48* (1), 3–10. https://doi.org/10.1107/S1600576714022985.

(207) Sheldrick, G. M. SHELXT– Integrated Space-Group and Crystal-Structure Determination. *Acta Crystallogr. Sect. Found. Adv.* **2015**, *71* (1), 3–8. https://doi.org/10.1107/S2053273314026370.

(208) Gritzner, G.; Kuta, J. Recommendations on Reporting Electrode Potentials in Nonaqueous Solvents (Recommendations 1983). *Pure Appl. Chem.* **1984**, *56* (4), 461–466. https://doi.org/10.1351/pac198456040461.

(209) Olah, G. A.; Spear, R. J. Stable Carbocations. CLXXX. Carbon-13 and Proton Nuclear Magnetic Resonance Spectroscopic Study of Phenyl-, Methyl-, and Cyclopropyl-Substituted Alkenyl (Allyl) Cations. Further Studies of the Trend of Charge Distribution and the Relative Delocalization Afforded by Phenyl, Methyl, and Cyclopropyl. *J. Am. Chem. Soc.* **1975**, *97* (6), 1539–1546. https://doi.org/10.1021/ja00839a044.

(210) Li, Z.; Bally, T.; Houk, K. N.; Borden, W. T. Variations in Rotational Barriers of Allyl and Benzyl Cations, Anions, and Radicals. *J. Org. Chem.* **2016**, *81* (20), 9576–9584. https://doi.org/10.1021/acs.joc.6b01530.

(211) Goulet, M.-A.; Aziz, M. J. Flow Battery Molecular Reactant Stability Determined by Symmetric Cell Cycling Methods. *J. Electrochem. Soc.* **2018**, *165* (7), A1466–A1477. https://doi.org/10.1149/2.0891807jes.

(212) Bard, A. J.; Faulkner, L. R. *Electrochemical Methods: Fundamentals and Applications*; Wiley: New York, 2001.

(213) Armstrong, C. G.; Toghill, K. E. Stability of Molecular Radicals in Organic Non-Aqueous Redox Flow Batteries: A Mini Review. *Electrochem. Commun.* **2018**, *91*, 19–24. https://doi.org/10.1016/j.elecom.2018.04.017.

(214) Leung, P.; Shah, A. A.; Sanz, L.; Flox, C.; Morante, J. R.; Xu, Q.; Mohamed, M. R.; Ponce de León, C.; Walsh, F. C. Recent Developments in Organic Redox Flow Batteries: A Critical Review. *J. Power Sources* **2017**, *360*, 243–283. https://doi.org/10.1016/j.jpowsour.2017.05.057.

(215) Zhang, J.; Huang, J.; Robertson, L. A.; Assary, R. S.; Shkrob, I. A.; Zhang, L. Elucidating Factors Controlling Long-Term Stability of Radical Anions for Negative Charge Storage in Nonaqueous Redox Flow Batteries. *J. Phys. Chem. C* **2018**, *122* (15), 8116–8127. https://doi.org/10.1021/acs.jpcc.8b01434.

(216) Carney, T. J.; Collins, S. J.; Moore, J. S.; Brushett, F. R. Concentration-Dependent Dimerization of Anthraquinone Disulfonic Acid and Its Impact on Charge Storage. *Chem. Mater.* **2017**, *29* (11), 4801–4810. https://doi.org/10.1021/acs.chemmater.7b00616.

(217) Huang, J.; Cheng, L.; Assary, R. S.; Wang, P.; Xue, Z.; Burrell, A. K.; Curtiss, L. A.; Zhang, L. Liquid Catholyte Molecules for Nonaqueous Redox Flow Batteries. *Adv. Energy Mater.* **2015**, *5* (6), n/a-n/a. https://doi.org/10.1002/aenm.201401782.

(218) Brushett, F. R.; Vaughey, J. T.; Jansen, A. N. An All-Organic Non-Aqueous Lithium-Ion Redox Flow Battery. *Adv. Energy Mater.* **2012**, *2* (11), 1390–1396. https://doi.org/10.1002/aenm.201200322.

(219) Compton, R. G.; Banks, C. E. *Understanding Voltammetry*; World Scientific, 2011.

(220) Radke, S. M.; Alocilja, E. C. A High Density Microelectrode Array Biosensor for Detection of E. Coli O157:H7. *Biosens. Bioelectron.* **2005**, *20* (8), 1662–1667. https://doi.org/10.1016/j.bios.2004.07.021.

(221) Llaudet, E.; Botting, N. P.; Crayston, J. A.; Dale, N. A Three-Enzyme Microelectrode Sensor for Detecting Purine Release from Central Nervous System. *Biosens. Bioelectron.* **2003**, *18* (1), 43–52. https://doi.org/10.1016/S0956-5663(02)00106-9.

(222) Pletcher, D.; Valdes, E. M. Studies of a Microelectrode Sensor for Monitoring Chlorine in Water Supplies. *Anal. Chim. Acta* **1991**, *246* (2), 267–273. https://doi.org/10.1016/S0003-2670(00)80960-5.

(223) Pletcher, D.; Sotiropoulos, S. Towards a Microelectrode Sensor for the Determination of Oxygen in Waters. *Anal. Chim. Acta* **1996**, *322* (1), 83–90. https://doi.org/10.1016/0003-2670(95)00599-4.

(224) Yeh, N.-H.; Medcalf, M.; Moeller, K. D. Organic Electrochemistry and a Role Reversal: Using Synthesis To Optimize Electrochemical Methods. *J. Am. Chem. Soc.* **2018**, *140* (24), 7395–7398. https://doi.org/10.1021/jacs.8b02922.

(225) Graaf, M. D.; Marquez, B. V.; Yeh, N.-H.; Lapi, S. E.; Moeller, K. D. New Methods for the Site-Selective Placement of Peptides on a Microelectrode Array: Probing VEGF–V107 Binding as Proof of Concept. *ACS Chem. Biol.* **2016**, *11* (10), 2829–2837. https://doi.org/10.1021/acschembio.6b00685.

(226) Oh, Y.; Heien, M. L.; Park, C.; Kang, Y. M.; Kim, J.; Boschen, S. L.; Shin, H.; Cho, H. U.; Blaha, C. D.; Bennet, K. E.; et al. Tracking Tonic Dopamine Levels in Vivo Using Multiple Cyclic Square Wave Voltammetry. *Biosens. Bioelectron.* **2018**, *121*, 174–182. https://doi.org/10.1016/j.bios.2018.08.034.

(227) Doris, S. E.; Ward, A. L.; Baskin, A.; Frischmann, P. D.; Gavvalapalli, N.; Chénard, E.; Sevov, C. S.; Prendergast, D.; Moore, J. S.; Helms, B. A. Macromolecular Design Strategies for Preventing Active-Material Crossover in Non-Aqueous All-Organic Redox-Flow Batteries. *Angew. Chem. Int. Ed.* **2017**, *56* (6), 1595–1599. https://doi.org/10.1002/anie.201610582.

(228) Baran, M. J.; Braten, M. N.; Montoto, E. C.; Gossage, Z. T.; Ma, L.; Chénard, E.; Moore, J. S.; Rodríguez-López, J.; Helms, B. A. Designing Redox-Active Oligomers for Crossover-Free, Nonaqueous Redox-Flow Batteries with High Volumetric Energy Density. *Chem. Mater.* **2018**, *30* (11), 3861–3866. https://doi.org/10.1021/acs.chemmater.8b01318.

(229) Montoto, E. C.; Nagarjuna, G.; Moore, J. S.; Rodríguez-López, J. Redox Active Polymers for Non-Aqueous Redox Flow Batteries: Validation of the Size-Exclusion Approach. *J. Electrochem. Soc.* **2017**, *164* (7), A1688–A1694. https://doi.org/10.1149/2.1511707jes.

(230) Janoschka, T.; Martin, N.; Martin, U.; Friebe, C.; Morgenstern, S.; Hiller, H.; Hager, M. D.; Schubert, U. S. An Aqueous, Polymer-Based Redox-Flow Battery Using Non-Corrosive, Safe, and Low-Cost Materials. *Nature* **2015**, *527* (7576), 78–81. https://doi.org/10.1038/nature15746.

(231) Montoto, E. C.; Nagarjuna, G.; Hui, J.; Burgess, M.; Sekerak, N. M.; Hernández-Burgos, K.; Wei, T.-S.; Kneer, M.; Grolman, J.; Cheng, K. J.; et al. Redox Active Colloids as Discrete Energy Storage Carriers. *J. Am. Chem. Soc.* **2016**, *138* (40), 13230–13237. https://doi.org/10.1021/jacs.6b06365.

(232) Forner-Cuenca, A.; Manzi-Orezzoli, V.; Biesdorf, J.; Kazzi, M. E.; Streich, D.; Gubler, L.; Schmidt, T. J.; Boillat, P. Advanced Water Management in PEFCs: Diffusion Layers with Patterned Wettability I. Synthetic Routes, Wettability Tuning and Thermal Stability. *J. Electrochem. Soc.* **2016**, *163* (8), F788–F801. https://doi.org/10.1149/2.0271608jes.